UNIVERSITY OF SOUTHAMPTON

FACULTY OF NATURAL AND ENVIRONMENTAL SCIENCES

Ocean and Earth Sciences

The Behaviour of Chromium and its Isotopes in Nickel Laterites

by

Jens C. Krüger

Thesis for the degree of Doctor of Philosophy

April 2019

UNIVERSITY OF SOUTHAMPTON

ABSTRACT

FACULTY OF NATURAL AND ENVIRONMENTAL SCIENCES

Ocean and Earth Sciences

Doctor of Philosophy

THE BEHAVIOUR OF CHROMIUM AND ITS ISOTOPES IN NICKEL LATERITES

By Jens Carsten Krüger

Ni laterites are important metal deposits that form by oxidative weathering of exposed ultramafic rocks in the Critical Zone; a key process for element cycling and supergene metal enrichment. Most continental chromium is hosted in ultramafic rocks and redox–dependent Cr release during laterite formation largely contributes to the Cr budget and the isotope signal that is transported via rivers into the oceans. However, the fractionation behaviour of Cr isotopes during Cr oxidation, in particular during the passage from rock to soil, is poorly understood. The aim of this study is to identify the major driving factors that govern Cr isotope fractionation during ultramafic rock weathering and subsequent Ni laterite formation. Three Ni laterites (Çaldağ, Karaçam, São João do Piauí) were investigated to evaluate the impact of the geochemical composition, the mineralogy, and the conditions of formation on the Cr isotopic composition. This study also presents the first comprehensive characterisation of the São João do Piauí Ni deposit and reveals that weathering under semi–arid climates can lead to the formation of a valuable Ni laterite given a distinct chemical composition of the parent rock. The results show that the total range of Cr isotopic compositions in modern (Cenozoic to Mesozoic) Ni laterites can be highly variable ($\Delta^{53/52}Cr$ = 0.26 to 1.58 ‰) and that the isotopic evolution is primarily controlled by the distribution of the Cr between silicates and oxides. The early stages of weathering are characterised by a significant loss of Cr from silicates, which is accompanied by a large Cr isotope fractionation, whereas loss of Cr from oxides only occurs in the later stages. Based on these findings, a Cr isotope fractionation model was formulated that includes the chemical composition of Cr–bearing minerals of the parent rock and uses a Cr isotope fractionation factor that was estimated from the Cr isotopic composition of analysed pore water ($\delta^{53}Cr$ = 4.31 ‰). Secondary controls that influence the Cr isotopic compositions of Ni laterites include the Mn content of the rock and the external conditions of laterite formation, such as the height of the water table and the evolution of the local relief.

Table of Contents

Table of Tables

Table of Figures

Academic Thesis: Declaration of Authorship

I, Jens Carsten Krüger, declare that this thesis entitled **the behaviour of Cr and its isotopes in Ni laterites** and the work presented in it are my own and has been generated by me as the result of my own original research.

I confirm that:

1. This work was done wholly or mainly while in candidature for a research degree at this University;
2. Where any part of this thesis has previously been submitted for a degree or any other qualification at this University or any other institution, this has been clearly stated;
3. Where I have consulted the published work of others, this is always clearly attributed;
4. Where I have quoted from the work of others, the source is always given. With the exception of such quotations, this thesis is entirely my own work;
5. I have acknowledged all main sources of help;
6. Where the thesis is based on work done by myself jointly with others, I have made clear exactly what was done by others and what I have contributed myself;
7. None of this work has been published before submission.

Signed: .....

Date: .....

Acknowledgements

First, an enormous thanks to my supervisors Rachael James, Christopher Pearce and Stephen Roberts. I am especially indebted to Rachael for her invaluable amount of help, patience, and energy, in particular during times when my private life distracted me on finishing this project. I am very grateful for her time and expertise she spent during the write–up phase of this work, always trying to focus me on relevant aspects and the bigger meaning behind the data. I would like to thank Chris and Stephen for their great support in the labs and that their doors were always open to come by.

A very special thank is dedicated to Richard Herrington, who provided the sample material from the Çaldağ and Karaçam Ni laterite as well as realised microprobe measurements at the Natural History Museum in London that were substantial for the development of the Cr isotope fractionation model. Next, I would like to thank Heather Goring-Harford, Andy Milton, and Matthew Cooper, who were a great support during the lab work and basically helped me to evolve my analytical skills. They always gave me a save back–up when things went wrong. Heather taught me so many essential (clean) lab skills that I adopted for the Cr isotope chemistry of my rock samples and she greatly contributed to the analysis of the water samples. I have to particularly thank Andy, because of his ridiculously large endurance in spending time with me on the mass spectrometer and teaching me how to measure Cr isotopes. And on top of that, he was always in good mood.

I am grateful to my supervisors and Richard Herrington for making it possible to participate on the 'CoG^{3}' field trip to the São João do Piauí Ni deposit in NE Brazil. It was a great experience. Further, I would like to thank Anne and Mike Oxley for hosting me at their demonstration plant site and for giving me all the support during my stay, but particularly for being interested in isotope geochemistry as potential tool to improve the mining industry. My thanks also go to Ailton Miranda for assisting me with the shipment of the samples and for having a great lunch before suffering on rice and beans at the base camp for four weeks.

Next, I would like to thank Ian Croudace for his advices during the whole–rock sample preparation and for conducting the XRF analysis of the samples, but in particular I want to thank him for his guidance and help during the preparation of the chrysotile–rich samples. I want to thank Daniel Doran for teaching me how to properly cut my rock samples and for the preparation of the thin sections. A huge thanks goes to Ross Williams and Richard Pearce for the XRD analysis and some microprobe measurements. A big thanks also goes to Shir Akbari for his help and guidance during the carbon and loss of ignition measurements.

Acknowledgements

I would like to give a high five to Tom Skiggs, who supported this work as part of his Master`s thesis. I am particular excited about his meticulous optical microscope work of these ‘not so beautiful rocks’ and the basic, however, very challenging characterisation of the São João do Piauí laterite. I really appreciate our discussions, in particular because I received an impression of how it will be to supervise a student at some point (maybe).

Next, I would like to give a very huge thank to Ghylaine Quitté for the opportunity to analyse Ni isotopes at the IRAP in Toulouse, thereby greatly improving the significance of this thesis. I am especially grateful for teaching me very valuable lab skills and in general, for showing me how to measure Ni isotopes. I also want to give thanks to Maria Cristina Castillo for her lovely support during my four week–long visit and the excellent Mexican tequila we shared.

I owe a lot to My ‘IsoNose’ fellows including Rasesh Pokharel, Daniel Frick, Xu Zhang, Marie Küßner, Ann–Kristin Kalveram, Nils Suhr, Carolina Rosca, Ruben Gerrits, Maria Cristina Castillo Alvarez, Franziska Stamm, Grant Craig, Danijela Mavrić, their supervisors, and Maja Tesmer for the great time we spent together in workshops, conferences and especially during our free time. I want to highlight Maja because she greatly initiated my participation on this PhD project and because of her generous support of cigarettes in times of nicotine shortage. I am particularly grateful to Friedhelm von Blanckenburg, who initiated this outstanding project and gave me a work place at the GFZ Potsdam during my write–up phase. The last but not at all the least thank goes to David Fries, my ‘co–IsoNose fellow’ at the University of Southampton, for the countless more or less scientific discussions, the mutual help, but foremost for the exceptionally good time that I had during my time in Southampton.

The innermost circle comes last; my mother and my friends, Benno, Martin, Silvio and Rolf. All my love to you for accompanying me on my way, always being there, never doubting.

Official thanks are directed to the vast majority of the European tax payers, who allow me to write the following sentence: The research leading to the results of the work presented in the following thesis has received funding from the People Programme (Marie Curie Actions) of the European Union`s Seventh Framework Programme FP7/2007-2013/ under REA grant agreement n^0 [608069].

Definitions and Abbreviations

~	Circa or about
%	per cent (10^2)
‰	per mille (10^3)
°C	Degree Celsius
α	alpha (isotope fractionation factor)
Al	Aluminium
Al_2O_3	Aluminium oxide
Ag	Silver
amo	amorphous phase
As	Arsenic
Au	Gold
$AuCl_4^-$	Tetrachloroaurate
Ba	Barium
Ca	Calcium
CaO	Calcium oxide
Ce	Cerium
chl	Chlorite
CIA	Chemical index of alteration
cm	Centimetre (10^{-2} m)
CMM	Cold month mean temperature
Co	Cobalt
CO_2	Carbon dioxide
Cr	Chromium
$CrCl_2^+$	Chromium chloride

$Cr(OH)_2^+$	Chromium hydroxide
CrO_4^-	Chromate
crs	Cristobalite
Cu	Copper
$CuSO_4^{2-}$	Copper(II)–sulphate
δ	Delta (lower case letter; notation of isotope ratio normalised to a reference material)
Δ	Delta (upper case letter; difference between two δ–values)
Dy	Dysprosium
ε	fractionation factor equivalent to Δ; defined as $\delta_{product} - \delta_{educt}$. **ε** is related to α by $\varepsilon \approx 1000 \cdot \ln\alpha$.
E	East
E_h	Reduction potential (also known as redox potential), given in volts {V}
EPMA	Electron probe micro–analyser (or –analysis)
Er	Erbium
Eu	Europium
f	fraction (between 0 and 1)
Fe	Iron
Fe_2O_3	Iron(III)–oxide
g	gram(s)
Gd	Gadolinium
h	hour(s) (60 min)
HCl	Hydrochloric acid
$HClO_4$	Perchloric acid
$HCrO_4^-$	Bichromate
H_2CrO_4	Dichromate

hem	Hematite
HF	Hydrofluoric acid
Hf	Hafnium
HNO_3	Nitric acid
Ho	Holmium
ICP–MS	Inductively coupled plasma mass spectrometry
ICP–OES	Inductively coupled plasma optical emission spectroscopy
In	Indium
IOL	Index of lateritisation
K	Potassium
K_2O	Potassium oxide
kln	kaolinite
kV	Kilovolt
kW	Kilowatt
kyr	Kilo year (duration)
l	Litre
La	Lanthanum
ln	Natural logarithm (to the base of the mathematical constant e)
LOI	loss of ignition
LOD	Limit of detection
LOQ	Limit of quantification
Lu	Lutetium
m	Metre
Ma	Million years (10^6 yr) ago
mag	Magnetite

MAP	Mean annual precipiation
MC–ICP–MS	Multicollector inductively coupled plasma mass spectrometer
mgs	Magnesite
MIA	Mafic index of lateritisation
min	Minute(s)
miqtz	Micro–crystalline quartz
µg	microgram(s) (10^{-6} g)
mg	Milligram(s) (10^{-3} g)
Mg	Magnesium
MgO	Magnesium oxide
ml	Millilitre (10^{-3} l)
µm	micrometre (10^{-6} m)
mm	Millimetre (10^{-3} m)
Mn	Manganese
MnO	Manganese oxide
Myr	Million years (10^{6} yr; duration)
N	North
N	equivalent concentration or normality (chemistry)
nA	Nanoampere (10^{-9} ampere)
Na	Sodium
Na_2O	Sodium oxide
Nb	Niobium
Nd	Neodymium
ng	Nanogram(s) (10^{-9} g)
Ni	Nickel

NIST	National Institute of Standards and Technology
pH	decimal logarithm of the reciprocal of the hydrogen ion activity in an aqueous solution
ppb	Parts per billion (10^9)
PPL	Plane–polarised light
ppm	Parts per million (10^6)
Pr	Praseodymium
qtz	Quartz
R^2	Coefficient of determination
Rb	Rubidium
REE	Rare earth element(s)
Rh	Rhodium
rpm	revolutions per minute
∑	Sigma (sum over the set of terms; here elements)
s	second(s)
S	South
Sc	Scandium
SD	Standard deviation
SE	Standard error
SEM	Standard error of the mean
Si	Silicon
SiO_2	Silicon dioxide
Sm	Samarium
sme	Smectite
Sr	Strontium
SRM	Standard Reference Material

srp	Serpentine
τ	Tau (reported as fractions)
θ	Theta (incident angle, X–ray diffraction)
Tb	Terbium
Th	Thorium
Ti	Titanium
TiO_2	Titanium dioxide
tlc	Talc
Tm	Thulium
TOC	Total organic content
trd	Tridymite
U	Uranium
UMIA	Ultramafic index of alteration
V	Volt(s)
V	Vanadium
vol%	Volume percent
vs.	versus
W	West
WMM	Warm month mean temperature
wt%	Weight percent
XPL	Cross–polarised light
XRD	X–Ray diffraction
XRF	X–Ray fluorescence
Y	Yttrium
Yb	Ytterbium

yr	year (duration)
Zn	Zinc
Zr	Zirconium

Chapter 1 Introduction

1.1 Laterites: definition and terminology

The term *laterite* first appears in the work of Buchanan (1807) who described an indurated clay–rich material with a red to yellow colour that is soft, but becomes hard when exposed to the air. It is a vesicular or nodular rock that is porous, bears many cavities, and contains large quantities of iron in form of various ochres. Buchanan (1807) coined the term *laterite* from the Greek *later*, which means brick (**Fig. 1.1**). Since then, the term laterite has been used to describe various ferruginous clay–rich upper crustal materials, often different from the material that Buchanan originally described (Hamming, 1968; Paton and Williams, 1972). Around 150 years later a more precise definition was presented by Prescott and Pendleton (1952) that a laterite is: 'a massive, vesicular or concretionary ironstone formation'. This covers the most important structural and compositional characteristics of a laterite in general. Investigation of weathering cycles of rocks and the need of metal supply from surficial deposits led to a better understanding of laterites and provided a basis for a more accurate definition, which can be broadly summarised in the two following sentences: Laterites are chemically stratified weathering profiles that are 20 to 500 m thick. They develop through intense rock weathering in a humid to semi–arid climate under present or past climate conditions over several million years (Tardy, 1993; Tardy et al., 1988). Compositionally, laterites represent the residual derivate from the alteration of rock landmasses. In general, there are two main types of laterites, which are derived from either the weathering of alumo–silicate rocks (laterite *sensu stricto*) or from weathering of carbonate rocks (karst–bauxite–laterite). Characteristics of laterites are controlled by their mineralogy and the interaction between geologic and climatic factors, such as geomorphological history, drainage, structure, seasonality, lithology, tectonic setting, and time. They are exclusively found in the *Critical Zone* (Tandarich, 1994), with a few exceptions that are considered to be paleo–deposits, which formed in the geologic past and are now deeply buried or had been transported (Herrington et al., 2007; Berger et al., 2011). The *Critical Zone* is the thin complex outer layer of the Earth that is composed of air, water, biota, organic matter, soil and surficial rock lithologies. Igneous metal–bearing rocks that were formed deep in the Earth are subject to alteration, when they are transported into the *Critical Zone* by tectonic uplift, denudation or obduction. The interplay between physical, chemical, geologic, and biologic processes at the *Critical Zone* interface, which act on different timescales and with variable intensities, are responsible for the formation of laterite deposits.

Fig. 1.1 a) Laterite rock parcels (bricks) are dug up and cut into shape with a pick axe for later use as building material. **b)** Road made from laterite material. Photos from *Werner Schellmann* and *Dorothy Voorhees* (https://en.wikipedia.org/wiki/Laterite).

There is no single definition of the term *laterite* and it is variably used in different scientific fields, such as geology, mineralogy, pedology and engineering. Scientists from many different disciplines are interested in laterite formation, and this has often created confusion about their genesis, definition and nomenclature. As this study has a geochemical and mineralogical focus, laterites are classified according to their geologic and mineralogical characteristics. A 'semi–genetic' definition has been given by Schellmann (1982, 1983): "Laterites are products of intense sub–aerial weathering. They consist predominantly of mineral assemblages of goethite, hematite, aluminium hydroxides, kaolinite minerals and quartz". Geologically, the term *laterite* refers to regolith material that contains a stratified weathering profile. *Laterite* defines no specific horizon, rather than is a generic term to describe the entire profile from the parent rock upwards to the soil horizon. In this study, a genetic distinction between *ferricrete* and *laterite* is also adopted (Widdowson, 2007), in which a *laterite* is defined as an in–situ alteration product and has an autochthonous origin, whereas *ferricrete* represents transported material and has an allochthonous origin.

Nickel laterites represent a sub–group of laterites that are derived from the weathering of ultramafic rock material and often contain significant amounts of nickel and cobalt, which are usually enriched in specific horizons within the Ni laterite profile. These are in the focus of this study. Laterites of granitic or carbonate origin differ in their chemical composition, in particular in the amount of iron, which strongly demarcates them from nickel laterites.

1.2 Nickel laterites

Nickel laterites are a sub–group of laterites that are residual products of ultramafic, Mg–rich rocks, in particular peridotites and serpentinites. In general, ultramafic rocks that are subject to lateritic weathering are of ophiolitic origin or have an intrusive character (e.g. Brand et al., 1998; Butt and Cluzel, 2013). Ophiolites are seafloor segments of (ultra)mafic composition, which have been obducted on continental margins. Their occurrence is widespread, however, they are relatively rare, covering only 3% of the surface of the Earth (Guillot and Hattori, 2013). Ni laterites that developed from non–ophiolitic peridotites include ultramafic rock intrusions or layered igneous complexes (Butt and Cluzel, 2013). The initial Ni content of the parent rock that underlies a typical Ni laterite ranges from 0.2 to 0.4 wt% (Brand et al., 1998), which allows an economically relevant Ni (and often Co) enrichment in overlying weathering products during laterite formation. Laterites with Ni concentrations higher than 1.0 wt% are considered 'mineable' (Butt and Cluzel, 2013). Ni is hosted in a variety of secondary Fe–oxy–hydroxides, hydrous Mg–silicates and smectite–clays. In general, a Ni laterite consists of many or all of the following horizons from the bottom to the top (**Fig. 1.2**): parent rock, saprock, saprolite, plasmic zone, mottled zone, lateritic residuum, and soil (Eggleton et al., 1987; Eggleton, 2001). A common feature among all Ni laterites is the pronounced loss of mobile elements, in particular the alkali and alkali–earth elements, during early phases of laterite formation. The so–called *Mg–discontinuity* marks a steep decrease in the Mg concentration and separates the weathering profile into an upper part that is characterized by a strongly leached Fe–rich saprolite, an overlying plasmic zone and is capped by an indurated duricrust or a topsoil horizon. Below the Mg–discontinuity the profile exhibits a relatively unleached Mg–rich saprolite horizon that is underlain by the saprock and bedrock horizon. The lower saprolite shows textural and structural elements of the protolith and contains partly unaltered bedrock fragments, whereas the saprolite above the Mg–discontinuity becomes more homogenous and the protolith characteristics are gradually replaced up to the plasmic zone, where no original textural elements are present. The position of the Mg–discontinuity varies among different Ni laterites and the main Ni ore is situated either below or above the Mg–discontinuity, which depends on the type of the Ni laterite (Brand et al., 1998). Furthermore, Ni laterites often evolve under climatic conditions that change throughout the formation time, thereby replacing the existing ore type or producing a new ore type mineralogy (Freyssinet et al., 2005: Golightly, 2010).

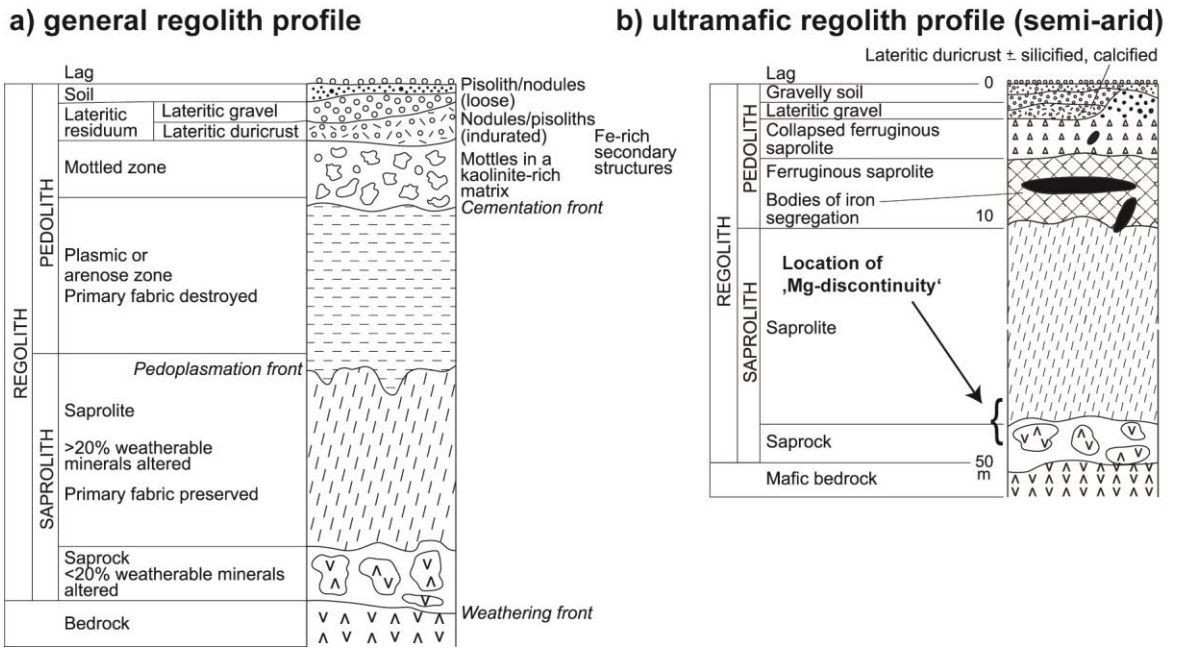

Fig. 1.2 a) Generalised laterite weathering profile. The regolith is divided into saprolith and pedolith that are further divided into sub–units based on the textural variations in the weathering profile. **b)** Example of a Ni laterite profile overlying mafic bedrock that developed under semi–arid climate conditions from the North Yilgarn craton (Eggleton et al., 2001).

1.2.1 Classification

Various classification schemes have been established for nickel laterites based on different characteristics, such as alteration of the host rock, climate, drainage, geomorphological history, variations in the degree of serpentinisation of the parent rock, chemical composition of the laterite column, and dominant ore type mineral assemblage (e.g. Butt and Zeegers, 1992; Golightly, 1981; Alcock 1988; Brand et al., 1998). However, the most commonly used classification is based on the mineralogy of the main Ni host (Brand et al., 1998; Gleeson et al., 2004; Freyssinet et al., 2005). Ni minerals that form during laterite formation include oxides, hydrous Mg–silicates, and clays (**Table 1.1**) that have different levels of magnesium, iron, and silica (Dalvi et al., 2004; Elias, 2002). Three main types of nickel laterite deposits are commonly distinguished (**Fig. 1.3**). These mineralogical subtypes are confined to different horizons or layers of the same weathering profile. In general, most nickel laterites are mixed deposits that contain two ore types; first, an oxide component in shallow horizons and second, a hydrous Mg–silicate or a smectite component in deeper horizons (Brand et al., 1998; Berger et al., 2011).

Table 1.1. Principal Ni–bearing minerals in different types of Ni laterites (Butt and Cluzel, 2013).

mineral	mineral family	chemical formula	Ni content
		oxide ores	
goethite	oxyhydroxide	α–(Fe^{3+})O(OH)	2 wt%
asbolane	oxyhydroxide	(Ni^{2+},Co^{3+})$_x$$Mn^{4+}(O,OH)_4$·nH2O	16 wt%
lithiophorite	oxyhydroxide	(Al, Li)$Mn^{4+}O_2(OH)_2$	1 wt%
		hydrous Mg–silicate ores	
Ni lizardite	serpentine	$(Mg,Ni)_3Si_2O_5(OH)_4$	6–33 wt%
7Å garnierite	serpentine	Variable, poorly defined	15 wt%
nimite	chlorite	$(Ni_5Al)(Si_3Al)O_{10}(OH)_8$	17 wt%
14Å garnierite	chlorite	Variable, poorly defined	3 wt%
falcondoite	sepiolite	$(Ni,Mg)_4Si_6O_{15}(OH)_2·6H_2O$	24 wt%
kerolite–willemseite	talc	$(Ni,Mg)_3Si_4O_{10}(OH)_2$	16–27 wt%
10Å garnierite	talc	Variable, poorly defined	20 wt%
		clay silicate ores	
nontronite	smectite	$Na_{0.3}Fe_2^{3+}(Si,Al)_4O_{10}(OH)_2·nH_2O$	~4 wt%
saponite	smectite	$(0.5Ca,Na)_{0.3}(Mg,Fe^{2+})_3(Si,Al)_4O_{10}(OH2)·4H_2O$	~3 wt%

These three mineralogical types represent ‘end–members’ in naturally occurring Ni laterite formations. Deposits of a ‘pure’ end–member subtype are rare and their classification is based on the most abundant Ni–bearing mineral of the weathering profile. The following classification emphasises the mineralogical variability among Ni laterites and is not intended to serve as a scheme for general discrimination.

1.2.1.1 Oxide nickel deposit

Oxide deposits (**Fig. 1.3a**) that are also referred as *limonite* deposits are dominated by the presence Fe–oxyhydroxides (**Table 1.1**). The uppermost horizon typically consists of a ferruginous duricrust that may contain solution voids (Thorne, 2011). Below, a Fe–rich clay horizon (plasmic zone) is typically present over a ferruginous saprolite horizon. Goethite dominates the profile mineralogy from the plasmic zone down to the mid saprolite and is typically the main Ni ore. Manganese oxides (e.g. asbolane, lithiophorite) are common and can also bear economic Ni concentrations. Downwards, the transition to the underlying lower saprolite and saprock is marked by a sharp increase of the MgO content (Mg–discontinuity). The saprock horizon overlies the weathered protolith. The boundary between parent rock and saprock is often not sharp and more diffuse. There is a gradual change from the protolith to the saprolite horizon that is characterised by oxidised mineral veins, whose abundance increases towards the saprolite. Many oxide deposits contain abundant secondary silica. Insufficient drainage and the low Al content of ultramafic rocks, in particular in dunites and serpentinised dunites, lead to an absence of clay formation during weathering, partial retention and secondary precipitation of mobilised SiO_2.

This re–silification process generally stabilises the weathering profile and an indurated silica cap as ultimate residue of lateritic weathering often preserves the underlying laterite from erosion and denudation (Lacinska and Styles, 2013; Butt, 2014). The average nickel grade of oxide deposits ranges between 1.0 and 1.6 wt% (Brand et al., 1998). Oxide deposits are the most common type among Ni laterites. They represent about 66% of the total Ni resources (7629 million tonnes) with over 60 identified Ni deposits worldwide (Berger et al., 2011).

1.2.1.2 Hydrous Mg–silicate deposit (garnierite deposit)

Hydrous Mg–silicate deposits (**Fig. 1.3b**) are characterized by a two–step Ni enrichment. Ni is mobilised and transported from secondary, Ni–bearing Fe–oxyhydroxides (e.g. goethite) from the plasmic zone down to the saprolite zone, below the Mg–discontinuity, where it re–combines with secondary hydrous Mg–silicates (**Table 1.1**). The mineable ore horizon is dominated by nickeloan varieties of serpentine, talc, chlorite, and sepiolite, commonly referred as *garnierite* (Butt and Cluzel, 2013). *Garnierite* varieties are characterised by a variable greenish colour and are found in different textural assemblages. Hydrous Mg–silicate deposits can be described as 're–worked' oxide deposits, as they are chemically similar to oxide deposits. Tectonically active regions of high relief allow a high water flow through the laterite profile (i.e. low water table). Ni is mobilised from the limonite horizon, then translocated downwards, and finally re–combined with the original silicate assemblage into secondary silicate phases. Field observations indicate a significant role of active brittle tectonics for garnierite formation, in which faults, gaps, or crevices serve as pathways for Ni–rich fluids (Villanova-de-Benavent et al., 2014). Most hydrous Mg–silicate deposits develop on serpentinised peridotites and show the highest Ni grades among all three types with mean Ni concentrations of between 1.8 wt% and 3.0 wt% (Brand et al., 1998). The richest deposits with Ni concentrations exceeding 3.0 wt% form, where the oxide–rich regolith has been uplifted and Ni is leached downwards to concentrate in neo–formed hydrous Mg–silicates in the saprolite. Hydrous Mg–silicate deposits represent about 32% of the total Ni laterite resources (4077 million tonnes) with over 40 identified Ni deposits worldwide (Berger et al., 2011).

1.2.1.3 Clay–silicate deposit (smectite deposit)

Clay–silicate Ni laterite deposits (**Fig. 1.3c**) have only recently been recognised as an individual ore type, although the presence of Ni–bearing clays (**Table 1.1**) that developed over serpentinite is long known (Butt and Cluzel, 2013). These deposits are characterised by the dominance of Ni–rich smectite, which is a general term to describe a group of dioctrahedal and trioctahedral clays that includes nontronite, saponite, montmorillonite, and beidellite (Odom, 1984; **Table 1.1**). The main ore horizon is situated in the saprolite and the upper boundary of the ore overlaps approximately with the Mg–discontinuity, above which the goethite horizon lies. The plasmic zone is often capped by a hematite–rich duricrust, equivalent to the oxide–type mineralisation. In general, clay–silicate deposits show an elevated Al content compared to hydrous Mg–silicate– and oxide–deposits. The formation of clay–silicate deposits is associated with areas of low relief or low drainage (Freyssinet et al, 2005), when Si is partially retained, and when the protolith has an initial Al content that allows the formation of aluminosilicates (e.g. Al–rich peridotites, troctolite). The deposits generally have the lowest Ni grades among all ore types ranging from 1.0 wt% to 1.5 wt% Ni with small tonnages compared to oxide and hydrous silicate deposits. They account for 8% of the worldwide Ni resources (879 million tonnes) with about 10 identified Ni deposits worldwide (Berger et al., 2011).

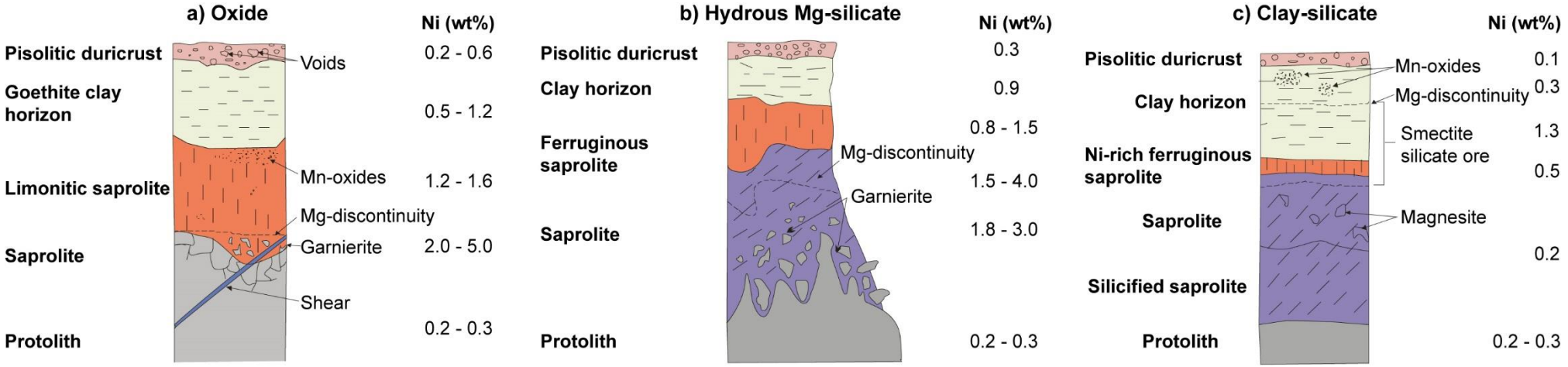

Fig. 1.3. Classification of nickel laterites based on the dominant ore type after Freyssinet et al., (2005) and from Thorne (2011); **a)** oxide deposit, **b)** hydrous Mg–silicate deposit, **c)** clay–silicate deposit. The average Ni concentration of individual horizons is given to the right of the respective weathering profile.

1.2.2 Worldwide distribution

Ni laterite deposits are dominantly located around the equatorial belt, in central Western Australia or the humid areas of Eastern Europe (Elias, 2002). On a global scale most laterite deposits are found around the tropical and sub–tropical regions of the equator between the 35°N and 35°S latitude (Anand and Paine, 2002). Deposits from outside this zone (e.g. NW Australia, USA, the Balkans, Turkey, Ural) are considered to be paleo–deposits that formed under past climate conditions (Thorne et al., 2012). Ni laterite deposits are distributed worldwide (**Fig. 1.4**) and can cover large areas (e.g. New Caledonia, the Philippines, Indonesia, Australia, Brazil, the Caribbean, Western Africa).

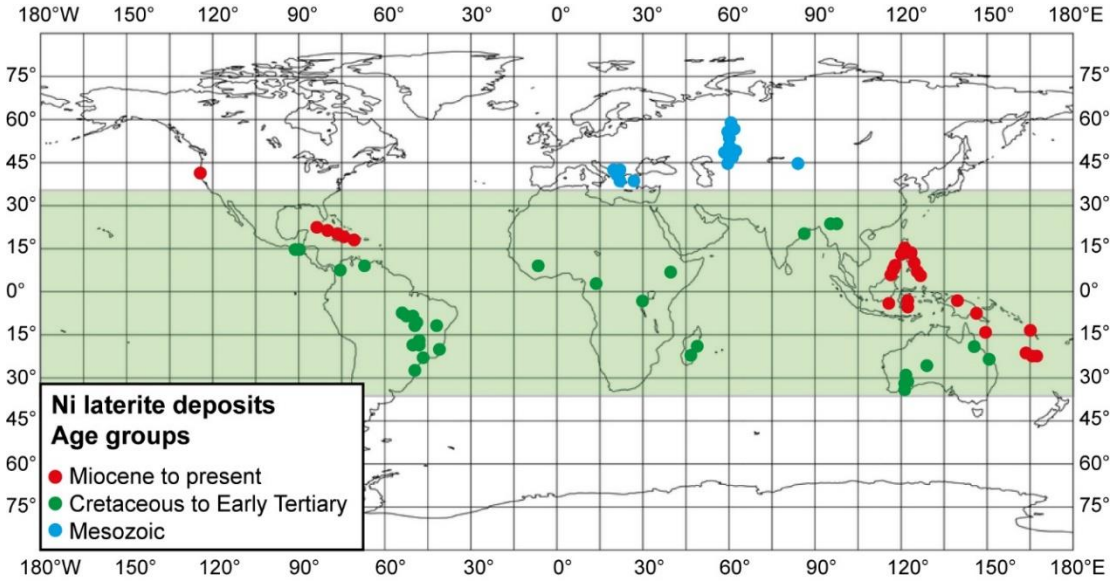

Fig. 1.4. World map of explored Ni–Co laterite deposits of different age redrawn from Berger et al. (2011). The green shaded area represents the zone, where recent climatic conditions are conducive for Ni laterite formation.

Favourable topographic landforms on which Ni laterites generally form are peneplain areas, plateaus, or gentle slopes, and spurs. Hydrous Mg–silicate deposits are found in tropical humid climates, whereas clay–silicate dominated deposits tend to be found in semi–arid climatic regions. Oxide deposits can occur in both tropical and semi–arid climates and are often the dominant ore type in tropical regions. Laterite formation is often accompanied by an inversion of the local relief, as many deposits develop an indurated ferruginous or siliceous cover, which protects the underlying laterite from denudation, while the surrounding country rocks are often less resistant to erosion and thus, denudated throughout time (Butt and Cluzel, 2013; Lacinska and Styles, 2013; Butt, 2014).

Some of the oldest laterites are found in the Precambrian shields of Australia and Brazil, which developed on komatiites and layered complexes in Archean and Proterozoic greenstone belts (e.g. Barros de Oliveira et al., 1992; Brand et al., 1998). The development of broad semi–desert plains and low relief hills is, for instance, typical for Australian laterites (e.g. Prider, 1970). Smaller alpine type intrusives have formed laterites in Guatemala, Columbia, Central Europe, India, and Burma (Dalvi et al., 2004). Tertiary and Mesozoic obducted ophiolite complexes and continental collision zones that formed laterite deposits are found in New Caledonia, Cuba, Indonesia, the Philippines, Turkey, and Greece (**Fig. 1.4**). A period of very intense weathering, due to the favourable climate during the last 100 Ma, is responsible for most of the present Ni laterite deposits (Retallack, 2010).

1.2.3 Economic significance

The economic significance of Ni laterites first and foremost results from their high nickel concentration (1.3 wt% Ni on average) compared to the average concentration of the crust (0.002 – 0.006 wt% Ni; McLennan and Xiao, 1998; Dalvi et al., 2004). By–products from mining Ni laterites can include cobalt, scandium, and Ni–rich silica varieties, such as chrysoprase, that is used as gemstone (Elias, 2002; Dalvi et al., 2004; Mudd, 2010). Today, nickel is an important metal, however, it had been used in alloys for millennia before it was formerly identified by the Swedish chemist *Axel Fredrik Cronstedt* in 1751. In modern industry, the majority of mined Ni is manufactured to stainless steel (58%), followed by nickel–based alloys (14%), casting and alloy steels (9%), electroplating (9%), and rechargeable batteries (Mudd, 2010). Economic Ni resources are found either in massive sulfide–hosted deposits or in Ni laterites. The bulk of historic Ni production is derived from sulfide ores, whereas the majority of known Ni reserves are situated in laterite ores (Schnebele, 2017). As a metal, mining of Ni is intrinsically unsustainable, as it is 'extracted' from the surface of the Earth and the recycling process of 'existing, already manufactured Ni' is, yet, not capable to fulfil worldwide Ni demand alone. Therefore, the exploration of new Ni deposits is essential and the primary issue with Ni is the cost effective processing of the Ni–bearing ore into the final product. Energy requirements, environmental impacts and economic costs determine the viability of a deposit and reflect the historic preference for Ni mining from sulfide deposits over laterite deposits. Ni production from laterite ores is generally relatively complex and requires large open cut areas due to the shallow nature of the ore.

Production of nickel from laterites started about 150 years ago with the discovery of the Ni deposit in New Caledonia in 1863 by *Jules Garnier*, who found a new Ni–rich mineral later named *garnierite* after him. Production of Ni, the so called 'white metal' (*allaige blanc*), started in 1875 and the French Ni company quickly became the world`s largest Ni producer. However, the exploration of the Sudbury sulfide hosted Ni deposit in Canada in the 20th century caused a shift in Ni ore production leading to a dominance of Ni mined from massive sulfide deposits (**Fig. 1.5**). However, new processing and refining technologies that reduced energy demands and environmental impacts combined with a steady increase in Ni demand means that a large number of known Ni laterites deposits have become economically viable over the past decades, which triggered a new growth in Ni mining from laterites since then.

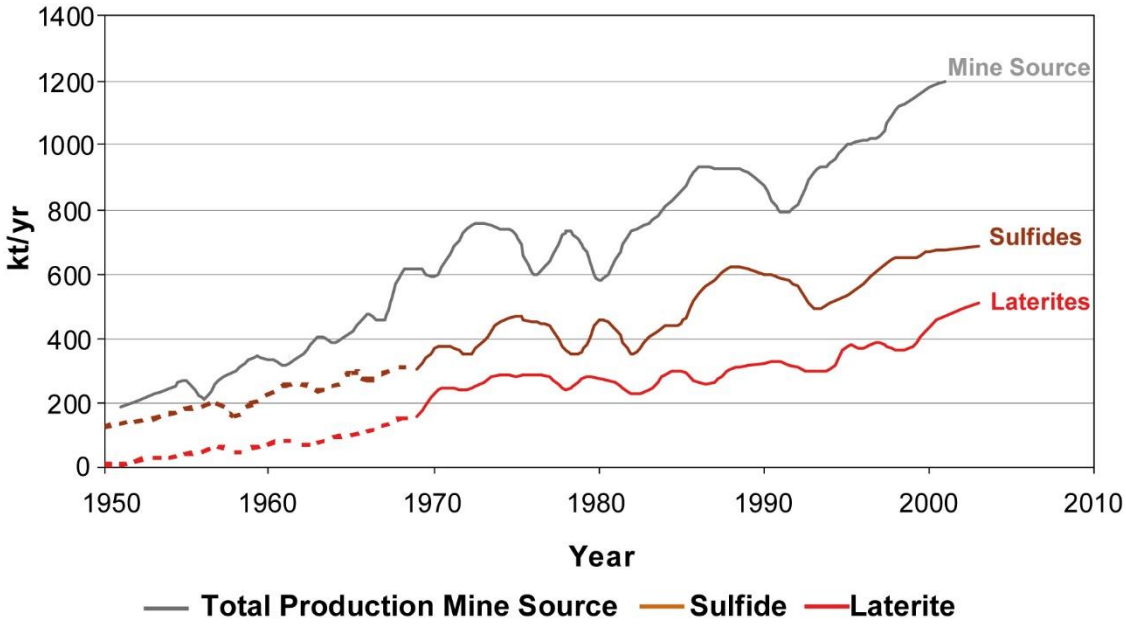

Fig. 1.5. Annual world nickel production from 1950 to 2003. Adapted from Dalvi et al. (2004).

Extensive Ni resources are also found in hydrothermal systems as well as in manganese nodules and crusts on the ocean floor (e.g. Post, 1999; Pelleter et al., 2017). However, economic deep–sea mining is yet to be implemented in the metal supply chain. Identified onshore Ni resources contain at least 130 million tons of nickel with about 70% in laterites, however, laterites currently only account for ~40% of the annual, global Ni production (**Fig. 1.6**) The total world Ni production in 2016 was 2.25 million tons (Schnebele, 2017).

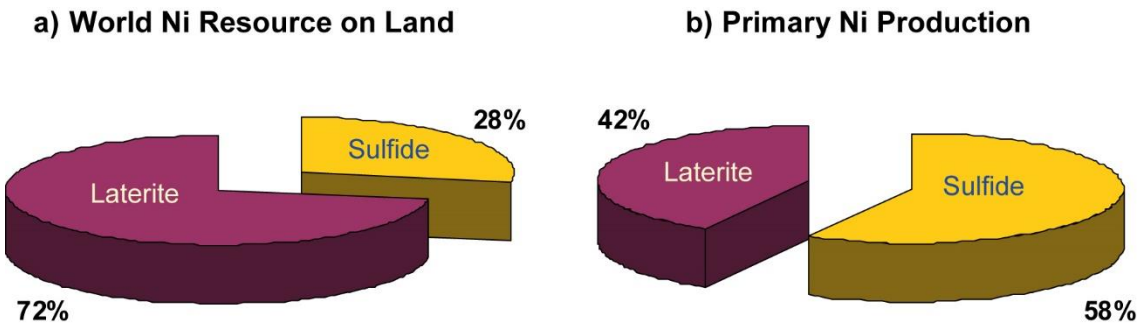

	Mt Resource	% Ni	Mt Ni	% of Total
Sulfide	10500	0.58	62	27.8%
Laterite	12600	1.28	161	72.2%
Total	23100	0.97%	223	100

Fig. 1.6 a) Land–based world Ni resources showing the distribution between laterite– and sulfide–hosted deposits. **b)** Primary Ni production from laterites and sulfides. Graphs and table from Dalvi et al. (2004). Mt: million tonnes.

1.3 Weathering: The basis for Ni laterite formation

Weathering is the physical and chemical alteration of rocks and minerals under Earth`s surface conditions via a combination of physical, chemical, and biological processes (Pope et al., 2002). The conditions (e.g. temperature, pressure, oxygen fugacity) at the surface are different from the conditions of mineral formation in the deep Earth, hence, minerals become unstable and tend to ‘weather’. Chemical weathering is the major driving factor for laterite formation (**Fig. 1.7**). The thermodynamic disequilibrium at the mineral surface leads to a transformation by dissolution of primary mineral components and formation of secondary minerals that are stable under surficial conditions. Physical weathering plays an important, however, rather subordinate role and needs to be generally low during laterite formation via the movement of rock material due to stress gradients that are induced by physical (e.g. gravity, friction, phase transformation), chemical (e.g. mineral precipitation, hydration, oxidation), and biological processes (flora growth, burrowing fauna).

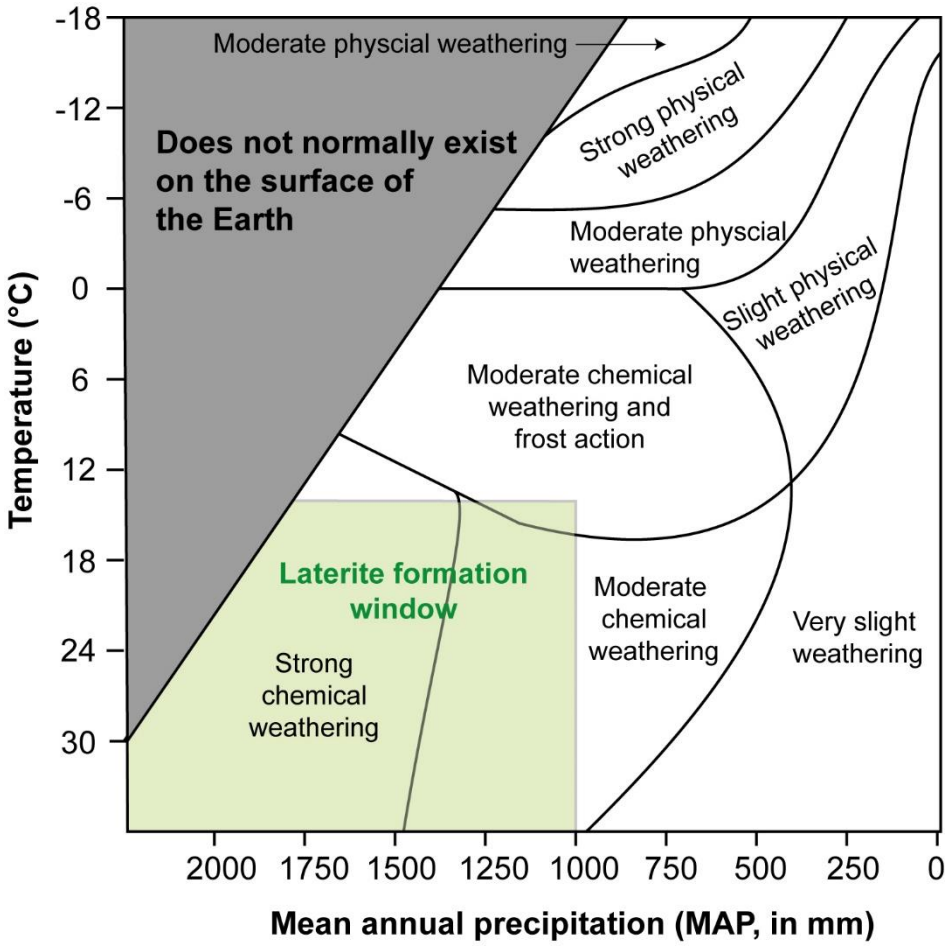

Fig. 1.7. Relative importance of physical and chemical weathering as a function of precipitation and temperature after Peltier (1950). Laterites form in tropical to sub–tropical areas around the equatorial belt where temperature and precipitation are high, therefore, chemical weathering is moderate to strong. Physical weathering, in particular erosion, usually plays a subordinate role during in–situ laterite formation. The green shaded area approximately marks the laterite formation window (LFW), in which the climatic conditions are conducive for Ni laterite formation (Thorne et al., 2012).

The weathering process begins with the alteration of compact rock material and ultimately ends with the formation of a loose soil. The major factors that dominate during weathering and control laterite formation are parent rock mineralogy, climate, and erosion (Dupré et al., 2003). Weathering profiles consist of stratified horizons that are well–developed at the surface and become progressively less developed with depth (April et al., 1986). These horizons form sequentially from a progenitor similar to that immediately beneath it. The transformation from rock to soil encompasses intermediate steps that define the *Critical Zone*, which describes the uppermost layer of the surface of the Earth that is in direct contact to the atmosphere (**Fig. 1.8**).

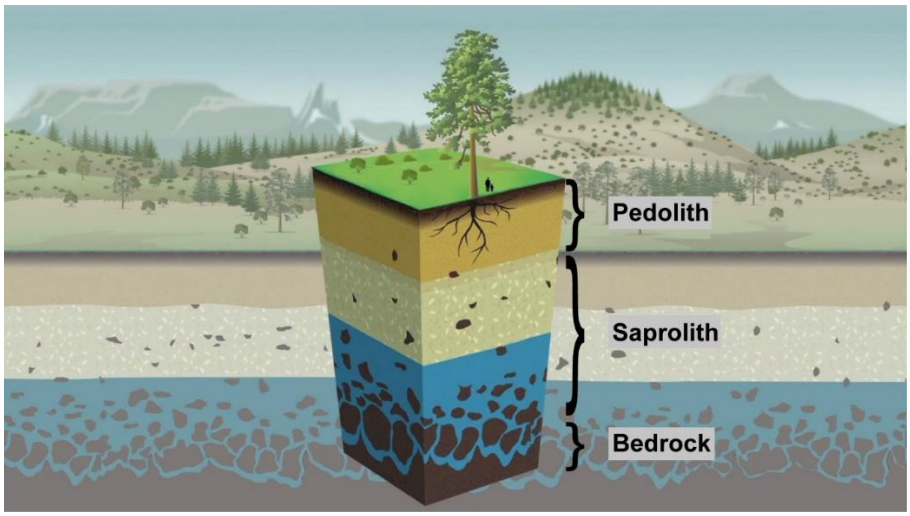

Fig. 1.8. Schematic diagram of the *Critical Zone*. At the base of the Critical Zone, there is a layer of bedrock, which progressively decomposes towards the top. Above this horizon lies the saprolith horizon, which is in turn overlain by the pedolith horizon. The pedolith horizon is characterised by a high proportion of soil minerals and the presence of biota. Processes operating within the *Critical Zone* are responsible for the geomorphology of the surface of the Earth. From the *University of Arizona College of Science (Mountain Lemmon Science Tour)* and *Catalina-Jemez Critical Zone Observatory*.

On a macroscopic level, weathering starts along joints, cracks, and fractures on the surface of a rock mass and propagates into its interior. On a microscopic scale, incipient weathering propagates along grain boundaries, fractures and inter–crystalline discontinuities (e.g. in olivine) and cleavage– or twin–planes (e.g. in pyroxene or plagioclase).

Water is essential for the weathering process, as it acts as transport media, dissolving agent, oxygen and microorganism supply, and governs chemical reactions. Vertical and lateral infiltration of water on a microscopic level eventually leads to the formation of a macroscopic network of channels in the percolated rock. Most chemical reactions during weathering are not solid–solid reactions, hence the presence of a fluid is crucial for the re–equilibration of the system and allows dissolution of primary minerals and the formation of secondary minerals. There are several chemical reactions during weathering that occur at the mineral–fluid interface, in particular dissolution, oxidation, hydrolysis, alkalinolysis (weathering in a strongly alkaline environment), acidolysis (weathering in a strongly acidic environment), and transformation. Hydrolysis and oxidation are the most important weathering mechanisms in the *Critical Zone* under conditions that predominate on the Earth`s surface and are the major driving factors that determine the evolution of a laterite weathering profile. Oxidation only follows or accompanies reactions with water, which in turn is pH dependent. In most weathering environments pH is between 5 and 9 and the usual reaction, in particular for silicates, is hydrolysis (Butt and Zeegers, 1992).

Weathering also leads to physical changes in rock volume. Soluble elements, in particular alkali and alkali–earth elements, are mobilised and extracted from the weathering profile. Residual elements form secondary phases, which replace the primary mineral assemblage. Secondary mineral phases tend to have a lower density and thus, occupy a larger volume, which compensates for the loss of soluble elements. Therefore, early stages of laterite formation are characterized by isovolumetric weathering, whereas later stages are dominated by physical compensation and shrinking due to the progressive loss of elements and the increasing pore space that eventually leads to a failure of the internal coherence of the rock and thus, to a collapse of the weathering profile (Millot and Bonifas, 1955).

1.3.1 Weathering controls on Ni laterite formation

Climate is an essential factor for Ni laterite formation, as it largely influences ore grade, mineralogy, regolith depth, and drainage. Climate covers various factors, including temperature, precipitation, seasonality, and vegetation, which are responsible for the evolution of Ni laterites on ultramafic substrates and the formation of different Ni–ore types. Laterite formation requires that the rate of chemical weathering, which is directly controlled by precipitation and temperature, exceeds the rate of physical erosion to develop an in–situ, stratified regolith profile. In general, exposed ultramafic rocks that receive more than 1000 mm/yr precipitation are conducive to the development of an economically relevant Ni laterite profile (**Fig. 1.9**). Furthermore, cold month mean temperatures (CMM) and warm month mean temperatures (WMM) need to range from 15 to 27°C and from 22 to 31°C, respectively (Thorne et al., 2012). Therefore, tropical to semi–arid regions around the equatorial belt are the most favoured regions on a global scale for the formation of Ni laterites. Deposits that have been found outside this favourable zone are considered to be paleo–deposits, which formed in warmer, more humid environments in the geologic past. Seasonality also influences the type of ore mineralisation (Thorne, 2011). High precipitation induced drainage can lead to saturation of the weathering profile, which hampers the formation of secondary Ni–rich silicates and promotes the formation of an oxide dominated deposit. However, a pronounced seasonality with months of no or little precipitation results in a low water table and precipitation of garnierite (e.g. Freyssinet et al., 2005; Thorne, 2011; Thorne et al., 2012). The rate of lateritisation strongly depends on local climate and vegetation. Large lateritic regoliths can develop within 100 kyr with thickening rates of 3 to 60 m/Myr (e.g. Nahon, 1986; Retallack, 2010).

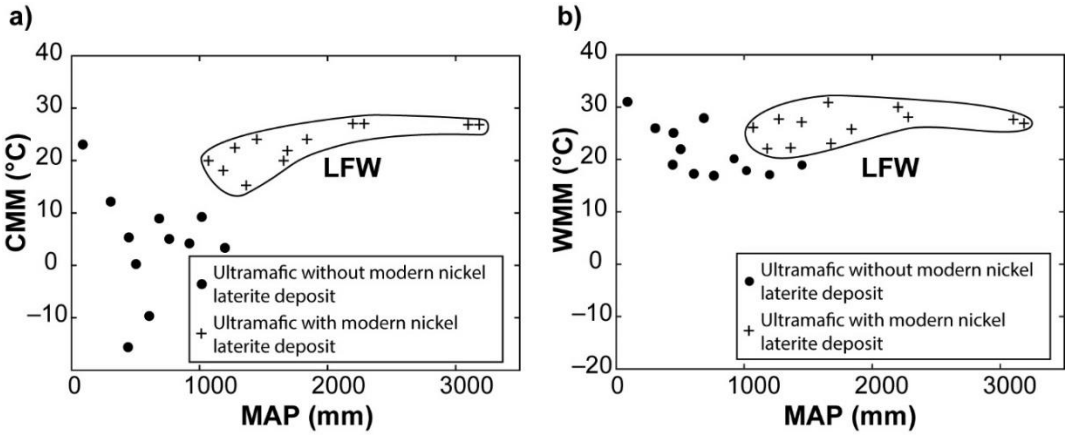

Fig. 1.9. Climatic conditions under which exposed ultramafic lithologies are suitable for Ni laterite formation from Thorne et al. (2012). **a)** Graph illustrating the dependency between cold month mean temperatures (CMM) and mean annual precipitation (MAP). **b)** Graph illustrating the dependency between warm month mean temperatures (WMM) and mean annual precipitation (MAP). Significant Ni laterite formation is restricted to areas that receive a precipitation of more than 1000 mm/year.

Vegetation can also play an important role and depends on the regional and local climate. Tropical forests have a dense and deep root network, whereas semi–arid areas are generally sparsely vegetated and the root network only penetrates the uppermost layers of the weathering profile. Vegetation is responsible for leaching and removal of certain elements from the underlying weathering profile. Plants take up elements for nutrition supply and growth from soils, in particular metals and metalloids, which can enhance rock leaching and accelerates weathering rates by a factor of 2 to 5 (Beukes et al., 2002). For instance, chromium uptake by plants promotes growth, increases yield, and plants can show a Cr concentration of up to 200 ppm compared to 200 to 5000 ppm in soils derived from the weathering of serpentinites (Oze, 2003; Peralta-Videa et al., 2009). Iron leaching can occur in deposits with a high content of organic matter and a deep penetrating root system. Silica uptake by vegetation is capable of removing significant amounts of SiO_2 over a geologically short period of time (Lovering, 1959). The presence of organic material lowers pH due to the formation of organic acids and reduces the E_h of the local environment. Percolating rainwater becomes slightly acidic because of interaction with the overburden vegetation (Freyssinet and Farah, 2000). Vegetation density and especially root penetration depth is important and facilitates drainage. Abundant surface biomass production allows dissolution and transport of transition metals by organic acids in wet seasons and accumulation of metal–bearing hydroxides in dry seasons (e.g. Beukes et al., 2002). Vegetation also influences the geological stability of a laterite profile. Generally, it stabilises the profile and prevents erosion. However, laterite formations with a resistant iron– or silica–rich cap can be destabilised by penetrating roots, which eventually allows rainwater to enter and erosion to denudate the profile.

1.3.2 The laterite formation process: the geochemical enrichment and depletion of elements

The first geochemical explanation for weathering induced enrichment and depletion of elements was given by Goldschmidt (1937). 'The ionic potential of an element defines its affinity for leaching or retention'. Elements form either water–soluble compounds (cations or complex anions) that are readily evacuated or low–soluble compounds (oxy–hydroxides) that tend to be retained. Geochemically, the process of laterite formation can be summarised as selective mobilisation, which includes leaching and partial precipitation of mobile elements on one hand, and hydration, retention and residual accumulation of immobile elements on the other. Mg and Ca are the most mobile elements that readily go into solution, whereas Fe and Al define their counterparts by often being immobile and form oxy–hydroxides of low solubility (Goldschmidt, 1937). However, the majority of elements, in particular most transition metals show an intermediate mobility and do not form individual hydroxides.

Laterite formation includes supergene enrichment, which describes the process of metal mobilisation from primary minerals, its redistribution in the weathering profile and the accumulation of mobile metals (e.g. Cu, Ni, Cr, Zn, Ag, Au, and U) in secondary ore minerals. Supergene metal enrichment is a result of three major processes (Dill, 2015): (1) Electrochemical oxidation of metals in primary minerals and accompanied mobilisation; (2) Transport of liberated metals as water–soluble metal species (e.g. $CuSO_4^{2-}$, CrO_4^{2-}, $AuCl_4^-$); (3) Accumulation of metals in secondary minerals and formation of economically mineable ore grades in specific horizons. Different processes lead to supergene enrichment, including reductive immobilisation (e.g. Cr^{6+} to Cr^{3+}), super–saturation (e.g. Mg^{2+} in magnesite deposits), cation exchange (e.g. Ni^{2+} exchange for Mg^{2+} in smectite and serpentine minerals), and sorption of elements on mineral surfaces (e.g. Ni on Fe–oxyhydroxides).

1.3.3 Ni laterite formation: The behaviour of major elements during weathering

A typical ultramafic rock is composed of all or at least one of the following constituents in order of increasing weathering resistance: glass, olivine, plagioclase, pyroxene, metal–oxide (Eggleton et al., 1987). Eventually, laterite formation (lateritisation) leads to the development of soil minerals, which are phyllo–silicates, Fe–oxides, and Fe–hydroxides (Rasmussen et al., 2010). Lateritisation can be broadly summarised by a sequence of mineral transformations and element enrichment and depletion processes that are based on incongruent mineral dissolution due to differential element mobility during primary mineral dissolution. The progress of lateritisation can be monitored based on the relative amounts of primary and secondary minerals and their chemical composition. According to Nesbitt and Wilson (1992) the degree of lateritisation can be divided into four stages.

In the first, the *incipient stage* (leaching stage), the rock is dominated by the primary mineral assemblage that shows no or little textural transformation into secondary minerals. Weathering starts with the hydrolysis of primary minerals, such as olivine, pyroxene, serpentine, and chlorite, and leaching of incorporated alkali, alkali–earth elements and transition metals, in particular Mg, Ca, Ni, Co, Mn, and Cr (**Fig. 1.10**). Significant amounts of mobile elements are lost, whereas Al and Fe are predominantly retained and start to form oxy–hydroxides (e.g. Babechuck, 2015).

In the *intermediate stage*, hydrolysis and oxidation fully dissolve primary silicates. Mobile silica can combine with Fe– and Al–oxy–hydroxides to form clay minerals (smectite or illite) that adsorb elements, such as Ni, from percolating weathering solutions. Some primary minerals still remain, but the majority of minerals are of secondary origin.

In the *advanced stage*, clay formation is followed by partial and variable leaching of less mobile components, such as Si, Al, and partly Ti, which strongly depends on drainage, temperature, and the presence of biota (Cornu et al., 1999; Aiuppa et al., 2000; Du et al., 2012; Lacinska and Styles, 2013). Primary minerals are completely transformed into clays and predominant reactions are the decomposition of smectite and illite and the formation of tertiary minerals (kaolin, oxides, and hydroxides).

In the *extreme stage*, laterites, in particular in well–drained environments, often show a significant desilification and a complete replacement of pedogenetic phyllosilicates by Fe–oxyhydroxides (e.g. Hill et al., 2000a). In Al–poor progenitors, clay formation is significantly hampered due to the lack of Al and Fe–oxyhydroxides usually form directly from the breakdown of the primary mineral assemblage (Butt and Cluzel, 2013).

Climate is the principal control on Ni laterite evolution and leads to the variability between Ni laterite deposits, mainly manifested in different Ni ore types, however, it also determines silica mobility during weathering. A humid climate with a well–drained weathering profile leads to the formation of an oxide dominated Ni laterite with goethite or hematite as the main Ni ore due to the evacuation of silica. On the other hand, a dry climate and a poorly–drained profile leads to a clay dominated Ni laterite with nontronite and saponite as main Ni ores due to the residual character of silica under these climate conditions. The behaviour of the transition elements, such as Ni, Co, Mn, and Cr, is more complex because of their sensitivity to redox– and sorption–processes as well as their affinity to incorporate into both silicate and oxide phases (Driese, 2004).

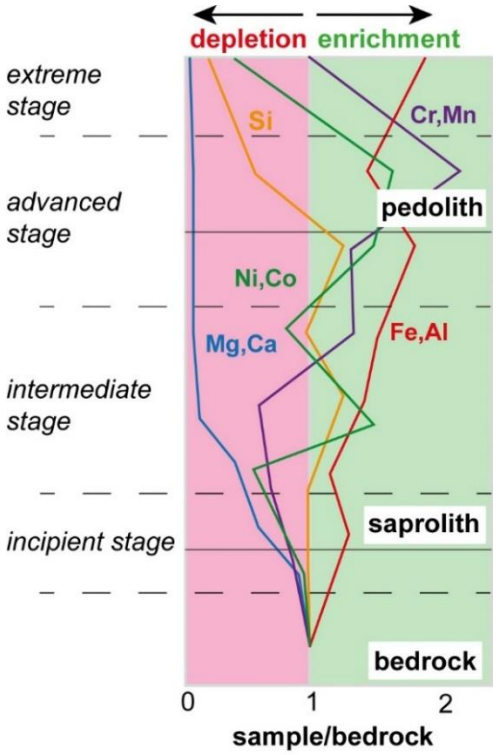

Fig. 1.10. Schematic diagram summarising the principal behaviour of major and some trace elements during laterite formation. Element concentrations are shown normalised to the bedrock concentration. Mobile elements (Mg, Ca trend) are readily extracted from the profile, which is shown by a strong decrease in concentration relative to bedrock in the lower saprolith (Mg–discontinuity). Immobile elements (Fe, Al trend) are predominantly retained in the solid phase. They accumulate in the profile, although their behaviour can be variable, depending on the local conditions. Elements that are characterised by intermediate mobility (Cr, Mn and Ni, Co trend) show a more complex behaviour, which is controlled by redox–processes, ligand–promoted processes, etc. Their enrichment pattern along the profile strongly varies among Ni laterites and is determined by protolith mineralogy, shrinking of the profile, drainage, temperature, seasonality, and secondary mineral formation. The behaviour of Si is strongly controlled by the local drainage and temperature. Arid conditions lead to retention, whereas humid conditions lead to high mobility and evacuation of Si.

1.4 Chromium in ultramafic rocks and its behaviour during weathering

Chromium is a compatible element during magmatic activity and therefore, mainly resides in oxide phases and to a lower extent in silicates (Oze, 2003). In ultramafic rocks, Cr–bearing minerals are mainly chromite and magnetite, followed by pyroxene, serpentine, and olivine, which show by far lower concentrations compared to Cr–bearing oxides (Oze, 2004). The average Cr concentration in ultramafic rocks ranges between 2400 ppm and 3000 ppm (Stueber and Goles, 1967; Shiraki, 1997). However, Cr concentrations in their weathering products, in particular in Ni laterites and serpentine soils, is up to 6.0 wt%. In serpentine soils, about 10% of the total Cr is hosted in silicates, whereas 90% is hosted in oxides (Oze, 2003). In general, spinel hosts the majority of Cr with chromite as the most important mineral followed by Cr–rich magnetite (e.g. Oze et al., 2007; Garnier et al., 2008). Chromite and Cr–rich magnetite have Cr concentrations of up to 45 wt% (Oze, 2004). Cr–bearing silicates are pyroxene, serpentine, and olivine, which can contain up to 8 wt% Cr (Grapes, 1981; Treloar, 1987; Challis et al., 1995). Serpentinisation of ultramafic rocks leads to the formation of serpentine and magnetite, and hydrothermal alteration and CO_2 metasomatism can produce relatively unusual Cr–bearing silicate phases including fuchsite/mariposite (mica), uvarovite (garnet), tawmawite (epidote), and kämmerite (chlorite). These minerals have variable Cr concentrations and Cr isomorphically substitutes for octahedral Al (Oze, 2003). The heterogeneous distribution of Cr between oxide and silicate minerals directly affects its mobility during weathering and is responsible for the widely held opinion that Cr is residually enriched during laterite and soil formation. The behaviour of Cr during lateritisation is determined by (1) the distribution of Cr between individual silicate and oxide phases, (2) the availability of oxidants (e.g. Mn–oxides) that leads to mobile Cr^{6+}, (3) the availability of reductants (e.g. organic matter or Fe^{2+}) or sorbents (clays or oxy–hydroxides) that immobilise mobile Cr^{6+} and (4) the structural development of the weathering profile (e.g. collapse, dilation, fracture propagation).

Peridotites and serpentinites often form the bedrock of Ni laterites. In these rocks, most Cr is hosted in Cr–spinel, if present, and therefore, the Cr concentration is very sensitive to the amount of chromite. However, chromite is extremely resistant to chemical weathering and dissolves incongruently retaining Cr. The net enrichment of Cr during alteration is attributed to the loss of Fe, Mg and Al (Oze, 2003; Banerjee et al., 2015). Serpentinisation is associated with the hydration of olivine that leads to oxidation of Fe^{2+} and the formation of magnetite that grows around primary chromite (Moody, 1976). Dissolution traces (i.e. small linear cavities) inside magnetite rims and inside the enclosed chromite, however, suggest that chromite slowly releases Cr during weathering, which leads to a long–term, more diffuse source of Cr (Garnier et al., 2008).

Furthermore, chromite dissolution during weathering and magnetite formation increases the specific surface area, which potentially enhances the role of chromite and Cr–magnetite as sources of Cr. However, chromite weathering is sluggish, hence, the majority of mobile Cr is derived from the breakdown of Cr–bearing silicate phases, in particular during early stages of lateritisation (Oze et al., 2007). Weathering of primary silicates, although low in Cr compared to chromite, accounts for most of the mobile Cr during the incipient and intermediate stages of lateritisation.

Mobilisation of Cr primarily occurs due to the oxidation of trivalent Cr to hexavalent Cr, a process, which tends to be dominantly driven by Mn–bearing oxy–hydroxides in rock regolith–systems (Nakayama et al., 1985; Eary and Rai, 1987; Richard and Bourg, 1991; Economou-Eliopoulos et al., 2014). Therefore, proximal Mn–availability on grain boundaries may largely affect Cr–mobility. Mobile Cr is either extracted from the weathering profile as Cr^{6+} or is incorporated as Cr^{3+} into secondary Fe–oxides and clay minerals and substituted for Al^{3+} and Fe^{3+}, which depends on sorption capacity and pH (e.g. Fendorf, 1995; Oze, 2004; Adegoke et al., 2014). Chromium enrichment during lateritisation is the product of two different processes. Shrinking of the weathering profile tends to be the major process by which Cr is residually enriched, which is the result of collapse of the rock body induced by voids from the dissolution of primary minerals and the evacuation of mobile elements. This physical shrinking of the rock profile leads to a relative enrichment of Cr. The second process is chemical enrichment, which results from the mobilisation of Cr due to the breakdown of primary Cr–bearing silicates and oxides, redistribution of Cr in the profile, retention and accumulation in secondary Cr–bearing mineral phases. Physical and chemical enrichment are responsible for Cr accumulation during lateritisation and pedogenesis, in which physical collapse can play an important role in medium stages of lateritisation, whereas chemical enrichment may start with incipient lateritisation and can persist throughout even the extreme stages of lateritisation (e.g. Zeissink, 1969; Esson, 1983; Som and Joshi, 2002). In general, chromite-rich weathering profiles that collapsed during lateritisation tend to show an overall Cr enrichment, whereas chromite–poor profiles that did not collapse tend to be depleted in Cr (e.g. Schellmann, 1986; Bardossy and Aleva, 1990; McAlister and Smith, 1997; Hill et al., 2000b).

1.4.1 Chromium geochemistry

In 1797 *Nicolas–Louis Vauquelin* discovered Cr in the mineral crocoite (Burns and Burns, 1975). The name *chromium* is derived from the Greek *chroma*, which translates to *colour* referring to the chromophore nature of many Cr–bearing compounds. Chromium is a transition metal and it occurs in two valence states on the surface of the Earth, which are reduced, trivalent Cr (denoted Cr^{3+} hereafter), and oxidised, hexavalent Cr (denoted Cr^{6+} hereafter). Cr^{3+} is weakly mobile and non–hazardous, whereas Cr^{6+} is highly mobile and toxic to living organisms (Daugherty, 1992; Cohen et al., 1993; James et al., 1997). The valence state of Cr is controlled by the prevailing redox potential (E_h) and pH conditions (**Fig. 1.11**). Under Earth`s surface conditions Cr^{6+} is mobile in most aquatic environments and is always bound with oxygen in form of the soluble chromate species, H_2CrO_4 (dichromate), $HCrO_4^-$ (bichromate), and CrO_4^{2-} (chromate). All Cr^{6+} species behave as divalent anions rather than hexavalent cations (Kimbrough et al., 1999). Cr^{3+} is present in solids, such as silicates and oxides, or as various Cr–hydroxide complexes, which are fairly immobile and adsorbing, hence, forming stable surface complexes (Beverskog and Puigdomenech, 1997). Experimental studies show that the long–term thermodynamic stability of Cr–bearing hydroxide precipitates is lower than that of Cr_2O_3 precipitates, which favours chromite as the ultimate stable phase under atmospheric conditions and implies possible secondary formation of chromite (Oze, 2003). During oxidative weathering within the *Critical Zone*, Cr^{3+} in minerals can be directly oxidised by O_2 to form Cr^{6+}, however, this reaction is slow and the Cr oxidation process in natural systems is largely triggered in the presence of manganese oxides (Eary and Rai, 1987; Zasoski and Fendorf, 1992; Economou-Eliopoulos et al., 2014). Cr^{6+} is fluid mobile and migrates into rivers and eventually into the oceans. In the modern ocean, Cr^{3+} and Cr^{6+} are both present, however, Cr^{6+} is the dominant species (Van der Weijden and Reith, 1982; Connelly et al., 2006).

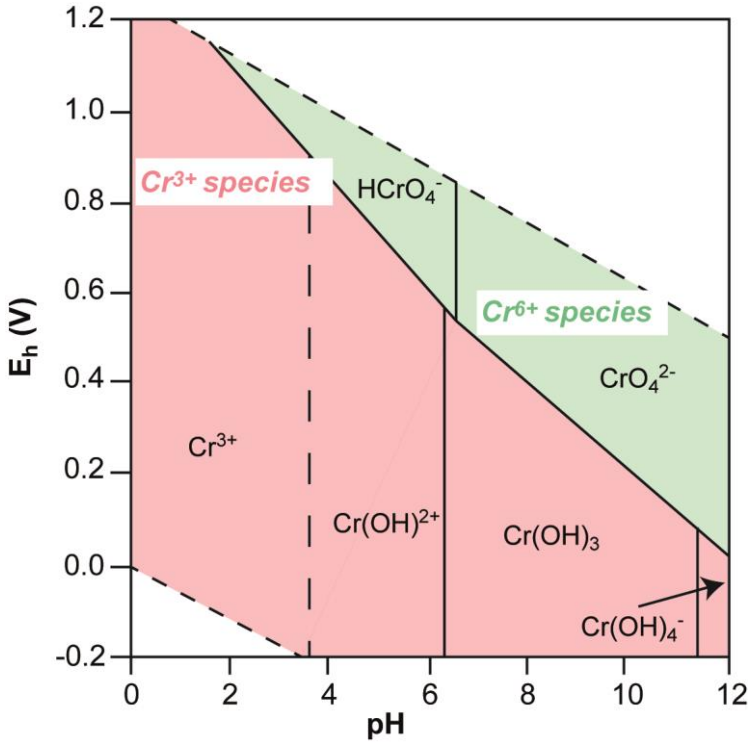

Fig. 1.11. Pourbaix diagram (redox potential vs. pH) for Cr at ambient temperature and atmospheric pressure and $[Cr(aq)]_{total} = 10^{-6}$. Green shaded areas show that Cr^{6+} is the dominant Cr species. Red shaded areas show that Cr^{3+} is the dominant Cr species. The figure shows that apart from the local redox–conditions the prevailing pH has a large control on the predominant Cr species. From Larsen et al. (2016) and Giménez-Forcada et al. (2017).

1.4.2 Chromium isotopes

Chromium has four naturally occurring stable isotopes, ^{50}Cr, and ^{52}Cr, ^{53}Cr, and ^{54}Cr, with natural abundances of 4.35 %, 83.79 %, 9.50 %, and 2.36 %, respectively (Rosman and Taylor, 1998). Among Cr isotopes, ^{50}Cr, ^{52}Cr, and ^{54}Cr are non–radiogenic, whereas ^{53}Cr is the radiogenic product of the extinct ^{53}Mn nuclide that had a half–life of 3.7 Myr (Honda and Imamura, 1971). Chromium isotope variations in terrestrial samples are reported using the ^{53}Cr/^{52}Cr ratio, expressed in the conventional delta notation (*equation 1.1*) relative to NIST SRM 979, which is an artificial Cr–nitrate ($Cr(NO_3)_3 \cdot 9 \cdot H_2O$) from the *National Institute of Standards and Technology*.

$$\delta^{53}Cr(‰) = \left(\frac{\left(\frac{^{53}Cr}{^{52}Cr}\right)_{sample}}{\left(\frac{^{53}Cr}{^{52}Cr}\right)_{standard}} - 1 \right) \times 1000 \quad (1.1)$$

Cr isotopes are utilised to track planetary formation processes, environmental contamination, mantle and core evolution of the Earth, paleo–environmental evolution, and biogeochemical cycling of Cr on land and in the oceans (Qin and Wang, 2017 and references therein). The earliest work on Cr isotopes in natural materials focused on cosmochemical processes, in particular the analysis of ^{53}Cr produced from the decay of the short–lived, extinct ^{53}Mn to date early solar system events (Birck and Allègre, 1984, 1988; Rotaru et al., 1992), and the analysis of ^{54}Cr in meteorites produced by nucleosynthetic processes (Birck and Allègre, 1984; Trinquier et al., 2007; Qin et al., 2011). More recently, Cr isotopes have been used to monitor Cr^{6+} as an environmental contaminant, because it is a known carcinogen and is hazardous to living organisms, including humans (e.g. James et al., 1997). Anthropogenic inputs of Cr^{6+} to the environment stem from industrial processes, such as electrical plating and leather tanning (Agrawal et al., 2006). In catchments underlain by Cr–rich ultramafic rocks, non–anthropogenic sources may predominate and geogenic pollution is induced by weathering of Cr-rich minerals (Godgul and Sahu, 1995). Reduction of mobile Cr^{6+} to immobile Cr^{3+} removes Cr from groundwater by various methods such as, natural attenuation (Palmer and Puls, 1994), active remediation (Mohan and Pittman, 2006; Frei and Polat, 2013) and biostimulation (Benazir et al., 2010; Dong et al., 2013). Cr isotopes can be used to monitor the reduction of Cr^{6+} because light Cr isotopes are preferentially reduced and incorporated into the precipitate, leaving the remaining Cr^{6+} pool enriched in heavy Cr isotopes (e.g. Ellis et al., 2002; Frei et al., 2014).

Mass–dependent Cr isotope fractionation in high–temperature settings is much less understood, which currently limits the application of Cr isotopes to trace igneous and large scale planetary processes. However, such studies are crucial, as they constrain the Cr isotope inventory of major terrestrial reservoirs (**Fig. 1.12**), which is critical for the interpretation of Cr isotope behaviour in low–temperature settings. Schoenberg et al. (2008) investigated mantle xenoliths, ultramafic rocks, as well as oceanic and continental basalts and found that they share a similar Cr isotopic composition with an average δ^{53}Cr value of –0.12±0.10 ‰, which is consequently proposed as the Cr isotopic composition of the bulk silicate Earth (BSE, **Fig 1.12**). However, a recent study by Xia et al. (2017) reveals that there is indeed significant Cr isotope heterogeneity among mantle xenoliths from diverse geological settings, including various peridotites, pyroxenite veins and associated basalts, with δ^{53}Cr values that range between –1.36±0.04 ‰ and 0.75±0.05 ‰ (**Fig. 1.12**). This indicates either the presence of different mantle reservoirs with a specific Cr isotope signature, or a single heterogeneous mantle source implying Cr isotope fractionation during partial melting of mantle peridotites. δ^{53}Cr values of ultra–high P–T metamorphic rocks, however, do not differ from bulk–silicate–Earth (BSE) values and are indistinguishable from their magmatic precursors (Schoenberg et al., 2008; Zheng et al., 2008; Wang et al., 2013). The isotopic similarity compared to their magmatic precursors could be explained by the absence of fluids during metamorphism that alter the Cr isotopic composition (Shen et al., 2015), because serpentinised oceanic crust partly shows a significant enrichment in heavy Cr isotopes with δ^{53}Cr values of up to 1.22±0.02 ‰, which is interpreted to reflect reduction of isotopically heavy Cr^{6+}–bearing fluids during serptinisitation (Farkaš et al., 2013; Wang et al., 2016; Xia et al., 2017).

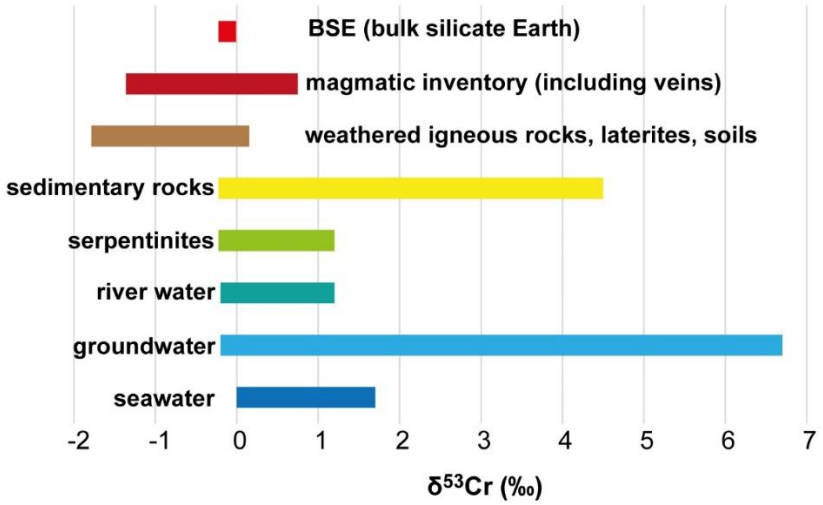

Fig. 1.12. Cr isotopic composition of different terrestrial reservoirs adapted from Qin and Wang (2017), with the bulk silicate earth (BSE) value from Schoenberg et al. (2008), and magmatic inventory data from Xia et al. (2017). Cr isotopic compositions of weathered rocks and soil include data from this study (see chapter 2 and 4).

More recently, Cr isotopes have been utilised to trace past atmospheric oxygenation events (e.g. Frei et al., 2009; Crowe et al., 2013; Berger and Frei, 2014; Planavsky et al., 2014; Cole et al., 2016; Gilleaudeau et al., 2016) and, consequently, to assess the linkages between the early redox history of the Earth and the evolution of life. The application of Cr isotopes as paleo–redox tracer follows the basic idea that variations of $\delta^{53}Cr$ in Precambrian sedimentary rock successions reflect Cr mobility due to redox–controlled processes that fractionate Cr isotopes.

In an O_2–rich atmosphere Cr^{3+} in rocks will be oxidised by manganese oxides, which leads to an enrichment of ^{53}Cr in the mobile Cr^{6+} pool. In a fully oxygenated atmosphere, the Cr isotopic composition of sedimentary rocks is determined by redox–controlled processes that remove Cr^{6+} from fluids by reductive immobilisation and incorporate isotopically light Cr^{3+} into the sediment, thereby enriching seawater in heavy Cr isotopes (Reinhard et al., 2013, 2014). Hence, Cr isotopes may be used to track the redox–evolution of the oceans. However, hydrothermal inputs of Cr also have to be considered (Holmden et al., 2016).

In an O_2–poor atmosphere, Cr is not oxidised and either transported as detrital Cr or as dissolved Cr^{3+}, in which no isotope fractionation occurs (Konhauser et al., 2011). However, recent results from Babechuk et al. (2018) point out that non–redox dependent Cr^{3+} isotope fractionation pathways (e.g. ligand promoted dissolution, ligand exchange, adsorption of Cr^{3+}) may contribute to $\delta^{53}Cr$ variations in hydrothermal systems or during laterite formation.

1.4.3 Behaviour of Cr isotopes during weathering

Weathering of rocks under atmospheric conditions leads to dissolution of Cr–bearing minerals which produces a Cr isotope signature in the weathered rock that is different from the protolith. Weathering products tend to be depleted in heavy Cr isotopes and have a lower $\delta^{53}Cr$ value in respect to the unweathered protolith (e.g. Frei et al., 2009, 2014; Crowe et al., 2013; Frei and Polat, 2013; Berger and Frei, 2014; Paulukat et al., 2015; Novak et al., 2017; Wille et al., 2018). Weathering profiles developed on ultramafic substrates have been shown to have $\delta^{53}Cr$ values of between –1.8 ‰ and 0.2 ‰ (Qin and Wang, 2017 and references therein). In contrast, the underlying ultramafic bedrock usually shows a $\delta^{53}Cr$ value within the range of BSE (−0.12±0.10 ‰; Schoenberg et al., 2008). The total Cr isotopic range $\Delta^{53/52}Cr$ is defined as the difference between the most positively fractionated $\delta^{53}Cr$ value and the most negatively fractionated $\delta^{53}Cr$ value ($\delta^{53}Cr_{max} - \delta^{53}Cr_{min}$) of a weathering profile. In modern laterites $\Delta^{53/52}Cr$ is generally between 0.2 ‰ and 0.6 ‰, however, Precambrian paleosols tend to show higher isotope ranges of up to 0.8 ‰ with $\delta^{53}Cr$ values as low as –1.0 ‰ (Crowe et al., 2013; Frei and Polat, 2013; Paulukat et al., 2015; Frei et al., 2016; Gilleaudeau et al., 2016).

Berger and Frei (2014) mimicked Cr–bearing mineral dissolution of tonalitic rock powders from a lateritic weathering profile under different pH conditions. Under acid conditions, Cr^{3+} is released from the dissolution of Cr in sulfides and the Cr isotopic composition of the leachate was isotopically indistinguishable from the protolith. However, under neutral and basic conditions, Cr^{6+} was released from the hydrolysis of Cr in silicates and the $\delta^{53}Cr$ value of the leachate was higher than that of the protolith. A high pH lowers the E_h–threshold, which leads to a more readily oxidation of Cr^{3+} to Cr^{6+} (**Fig. 1.11)** This indicates that the observed $\delta^{53}Cr$ variations within the profile resulted from the oxidation of Cr^{3+} to Cr^{6+}.

Infiltrating water is the most important source of dissolved O_2 during weathering, but other potential oxidants include O_3, PbO_2, H_2O_2, and MnO_2. The direct oxidation of Cr^{3+} by oxygen at room temperature is slow and concurrent reactions, such as precipitation and sorption, predominate (Nakayama et al., 1985). Oxidation of Cr^{3+} in laterites tends to be dominantly driven by Mn–bearing oxide phases that rapidly oxidise Cr (Eary and Rai, 1987). The formation of Mn–oxides requires the presence of molecular O_2 and microorganisms to catalyse the reaction between reduced Mn^{2+} in the rock and oxygen that ingresses by weathering solutions (Tipping et al., 1984). Fractured serpentinites and their weathering products provide favourable conditions for Cr^{3+} oxidation on the surface of Mn–oxides in the weathering profile. The rate of Cr^{6+} production depends on the rate of Cr^{3+} diffusion to Mn–oxide surfaces, so the distance between the Cr–bearing solid and the Mn–oxide is an important factor that determines the rate of Cr^{6+} production.

For instance, if the distance between hydrated Cr^{3+} ($Cr(OH)_3$) and birnessite (Mn^{4+}–oxide) increases from 10 nm to 100 nm, then the diffusion rate decreases by an order of magnitude (Hausladen and Fendorf, 2017). This spatial control on Cr–oxidation is, in turn, dependent on the textural relationship between the bedrock and the overlying regolith. Mn–oxides are present as grain–coatings, finely disseminated grains or along small fissures within the rock texture. The mineralogical form of the Mn will also ultimately affect the extent of Cr isotope fractionation (**Table 1.2**).

The rate of Cr^{3+} release by dissolution determines the amount of available Cr for oxidation. Cr–bearing spinels, in particular chromite, have by far the highest Cr concentrations, followed by much lower concentrations of Cr in silicates (e.g. pyroxene, serpentine, olivine). Therefore, Cr–oxides are the main Cr source in ultramafic rocks, although Cr release from silicates will dominate during incipient and intermediate stages of lateritisation. Cr dissolution from oxides is sluggish and provides a more variable long–term Cr source (Garnier et al., 2008). However, Cr release from chromite can be increased in the presence of birnessite (Mn–oxide) that produces aqueous Cr^{6+} within hours with formation rates of between 0.5 and 6.2 nM h^{-1}, depending on pH (**Fig. 1.13**). On the other hand, chromite dissolution in the absence of birnessite yielded insignificant Cr mobilisation over 450 h (Martin et al., 2013). The 'Mn–oxide–boosted' dissolution and oxidation of Cr from chromite implies that other Cr–oxide minerals, in particular spinel and Cr–rich magnetite, may show similar Cr^{6+} formation rates in the presence of Mn–oxides. This means that birnessite is not only an oxidant of Cr in laterites, but it also drastically enhances Cr dissolution from oxides.

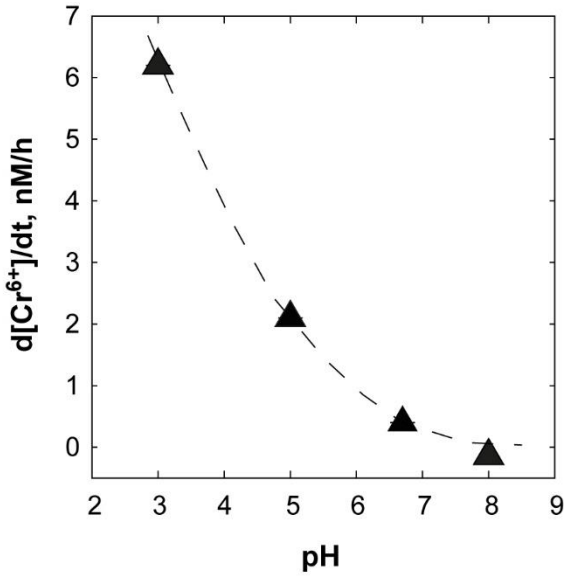

Fig. 1.13. Chromite dissolution rate (nM/h) in the presence of birnessite under different pH conditions (Oze et al., 2007). The rate of dissolution increases with decreasing pH, which indicates that release of Cr from chromite is higher in the later stages of laterite formation when the pH is below 7. The early stages of lateritisation are dominated by the breakdown of Cr–bearing Mg–silicates, which shifts pH and supresses chromite dissolution.

Theoretical calculations show that an oxidised Cr^{6+}–complex tends to have a higher $\delta^{53}Cr$ value than a substance containing Cr^{3+} (Schauble et al., 2004; Zink et al., 2010; Wang et al., 2015). Cr isotope variations in terrestrial samples result from equilibrium isotope fractionation and kinetic isotope fractionation processes that are based on different physical laws. Equilibrium isotope fractionation results from zero–point energy differences that reflect vibrational modes, which is a quantum mechanical effect. Kinetic isotope fractionation, on the other hand, can be described by classical mechanics as the result of motion (Bigeleisen and Mayer, 1947; Urey, 1947; Young et al., 2002). Theoretically– and laboratory–derived fractionation factors predict an equilibrium isotope fractionation of about 6.0 ‰ and a redox–controlled kinetic isotope fractionation that varies between –1.0 and 4.6 ‰ under ambient temperature (Ellis et al., 2002; Schauble et al., 2004; Bain and Bullen, 2005; Ottonello and Zuccolini, 2005; Zink et al., 2010; Wanner and Sonnenthal, 2013; Basu et al., 2014; Wang et al., 2015).

Equilibrium Cr isotope fractionation occurs when Cr^{3+} and Cr^{6+} co–exist and there is isotope exchange between the two Cr species (i.e. isotope exchange on fluid–rock interface). Heavy Cr isotopes are favourably incorporated into the Cr^{6+} fraction because they form stiffer bonds than lighter isotopes in the Cr^{6+} pool (Schauble et al., 2004). At isotopic equilibrium the $\delta^{53}Cr$ value of the Cr^{6+} species is about 6.0 ‰ higher than the co–existing Cr^{3+} species (**Table 1.2**).

Kinetic isotope fractionation is typically observed for systems that undergo a fast forward reaction with a backward reaction that is negligible (unidirectional process; DePaolo, 2011). For example, reduction of Cr^{6+} by organic matter or Fe^{2+} leads to favourable incorporation of light Cr isotopes into the Cr^{3+}precipitate, as bonds with heavy Cr in Cr^{6+} are stronger and therefore, are less easily broken (**Table 1.2**).

On the other hand, Cr^{3+} oxidation was also observed to enrich the resulting Cr^{6+} pool in heavy Cr isotopes (e.g. Zink et al., 2010). However, Cr isotope fractionation during oxidation remains poorly understood, mainly because of equivocal experimental results that show fractionation of heavy isotopes into the Cr^{6+} product (up to 1.0 ‰) on one hand, and fractionation of light isotopes into the Cr^{6+} product (up to –2.5 ‰) on the other hand (Bain and Bullen, 2005; Ellis et al., 2008; Zink et al., 2010). A possible explanation for these contrasting results is attributed to the complex nature of Cr oxidation that involves multiple electron transfers, different reaction pathways, and disproportionation of Cr species, which could in turn lead to a variable Cr isotope fractionation (Banerjee and Nesbitt, 1999; Zink et al., 2010).

Furthermore, theoretical– and laboratory–derived Cr fractionation factors represent results from idealised chemical systems and the influence of complex natural factors (e.g. availability of Cr, presence of reducing or oxidising agents, moving water table, passivation of reaction surface) will likely have a variable influence on the Cr isotopic composition. However, accumulation of isotopically light Cr in the resulting Cr^{6+} product may play a subordinate role during Cr oxidation in natural systems, as $\delta^{53}Cr$ values of stream waters, rivers, and the oceans clearly reflect heavy Cr isotope enrichments in fluids (e.g. Bonnand et al., 2013; Farkaš et al., 2013; Goring-Harford, 2017; Novak et al., 2017; Goring-Harford et al., 2018).

Table 1.2. Laboratory–derived Cr isotope fractionation ($\delta^{53}Cr_{product} - \delta^{53}Cr_{reactant}$) by different mechanisms that may occur during Ni laterite formation.

Reagent	Isotope fractionation	Reference
Reduction of Cr^{6+}		
magnetite	–3.5±0.1 ‰	Ellis et al. (2002)
Fe^{2+}–bearing goethite	–3.9±0.2 ‰	Basu and Johnson (2012)
Biotic reagents[a]	–4.6 to –0.4 ‰	Xu et al. (2015),Han et al. (2012)
dissolved Fe^{2+}	–3.6 to –1.5 ‰	Døssing et al. (2011)
Oxidation of Cr^{3+}		
pyrolusite (β–MnO_2)	≤ +1 ‰	Ellis et al. (2008)
birnessite (δ–MnO_2)[b]	–2.5 to +0.7 ‰	Bain and Bullen (2005)
Non-redox processes		
aqueous Cr^{3+} – Cr^{6+} exchange[c]	5.8±0.5 ‰ (Cr^{6+} isotopically heavier)	Wang et al. (2015)
Cr^{3+}–Cl–H_2O system exchange[d]	+1 to +2 ‰ (Cr^{3+} isotopically lighter)	Babechuk et al. (2018)

Note: The '–' and '+' sign of isotope fractionation denotes that the product is respectively isotopically lighter or heavier with respect to the reactant. **a)** Shown is the range of Cr isotope fractionation of numerous biotic reagents (e.g. Shewanella oneidensis). **b)** Birnessite encompasses a fractionation range, where the product can be either isotopically lighter or heavier. **c)** aqueous Cr^{3+} – Cr^{6+} exchange refers to a multi–step interaction between dissolved Cr^{6+} (i.e. $HCrO_4^-$, CrO_4^{2-}) and Cr^{3+}–hydroxide (i.e. $CrOH_2^+$, $Cr(OH)_2^+$, $Cr(OH)_3$ in chemical equilibrium involving Cr^{5+} as intermediate species at pH between 4 and 9 as proposed by Altman and King (1961). **d)** Cr^{3+}–Cl–H_2O system consists of $CrCl_2^+$, $CrCl^{2+}$, and Cr^{3+}.

Equilibrium and kinetic Cr isotope fractionation processes both enrich the Cr^{6+} fraction in heavy Cr isotopes, which leads to a decrease of the $\delta^{53}Cr$ value in the Cr^{3+} fraction. Thus, the 'relatively slow' equilibrium isotope exchange has the potential to 'overprint' Cr isotope variations that originate from 'relatively fast' kinetic Cr isotope fractionation processes. However, in natural weathering settings, in particular during laterite formation, equilibrium isotope exchange may play a secondary role, as reduced and oxidised Cr need to stay in contact for years to establish significant isotope exchange. Wang et al. (2015) calculated that during weathering (where the Cr^{6+} concentration is initially low and the and Cr^{3+} concentration is initially high) significant isotopic differences can occur within 20 years, which is usually longer than an individual Cr^{6+} ion will stay in the weathering profile; Cr^{6+} is highly mobile and recall that laterite formation requires significant annual variations in rainfall (Thorne, 2011; Thorne et al., 2012). Passivation of the mineral–fluid interface by competing ions further hampers the isotope exchange between solid–bound Cr^{3+} and aqueous Cr^{6+}. Thus, it is likely that redox–controlled Cr isotope fractionation will be dominantly responsible for the observed $\delta^{53}Cr$ variations in natural samples, in particular oxidation of Cr^{3+} during rock weathering (Cole et al., 2018).

Nonetheless, other competing processes can result in Cr isotope fractionation, such as sorption or ligand exchange. Adsorption of Cr^{6+} on the surface of goethite was initially characterised by preferential uptake of light Cr isotopes, but no fractionation was observed after 24 hours (Ellis et al., 2004). Ligand exchange experiments in the Cr^{3+}–Cl–H_2O system yielded a Cr isotope fractionation of up to 2 ‰ between Cr^{3+} species implying that Cr inter–species transformation may lead to $\delta^{53}Cr$ variations in systems that are temporarily stable, such as laterite formations (Babechuk et al., 2018). However, their contribution to the whole–rock Cr isotopic composition of weathered rock is considered low, as Cr^{3+}–species are very insoluble and tend to stay in the rock. In order to produce a significant $\delta^{53}Cr$ variation, fractionated Cr has to leave the bulk rock. Redox–controlled Cr conversion and Cr inter–species transformations represent the chemical processes that affect Cr during laterite formation, which leads to a general depletion of heavy Cr isotopes in the weathered rock material and accumulation of heavy Cr isotopes in rivers and groundwater. However, there are certain horizons in laterites that do not appear to follow this 'first–order weathering trend'. These weathering horizons exhibit a higher $\delta^{53}Cr$ value than the underlying 'fresh' bedrock (e.g. Berger and Frei, 2014; Crowe et al., 2013; Frei and Polat, 2013; Frei et al., 2014; Crowe et al., 2016) and have accumulated isotopically heavy Cr that was derived from an isotopically heavy Cr^{6+} pool, which likely originates from the oxidation of Cr^{3+} from higher parts of the weathering profile. Retention of transported Cr^{6+} is determined by comparison of Cr contents between the affected rock and the unaffected rock (e.g. fresh bedrock).

Normalisations to elements, in particular the so–called 'immobile elements' that are characterised by a very low mobility during weathering (e.g. Ti, Zr, Al, Th, Nb), help to separate leaching effects from physical effects, such as shrinking or dilation of the weathering profile, and simplify the determination of the processes that are responsible for residual induced Cr enrichments and/or depletions. Chemically induced Cr enrichment can result from reductive immobilisation of a mobile Cr^{6+} pool that moves with the water table and stems from the breakdown of Cr–bearing minerals from upper parts of the weathering profile. Reduction of Cr^{6+} initially shifts the Cr isotopic composition of remaining Cr^{6+} towards higher $\delta^{53}Cr$ values. The process follows a simple Rayleigh distillation and if reduction is not complete, Cr enriched zones retain a ^{53}Cr depleted isotope signature, whereas the $\delta^{53}Cr$ of the residual mobile Cr^{6+} pool is further increased. On the other hand, if reduction of Cr^{6+} is significant, the $\delta^{53}Cr$ value of the rock may become higher than the unweathered bedrock. Cr enrichment zones are typically located in the saprolite or lower soil portions of the weathering profile, where high amounts of Fe–oxides and organic compounds are present (e.g. Paulukat et al., 2015).

In conclusion, Cr isotope fractionation during weathering of rocks under atmospheric surface conditions is a complex process that is predominantly driven by the redox–controlled interconversion of Cr^{3+} and Cr^{6+} that have different solubilities. The behaviour of Cr isotopes is affected by: (1) the permeability and pore space of the rock that influences the flux of water and determines the surface area for fluid–rock interactions; (2) the dissolution rate of individual Cr–bearing minerals that incongruently dissolve and therefore produce a variable Cr^{3+} flux; (3) the availability of Mn–oxides, in particular the distance between Cr^{3+} and Mn^{4+}, and the mineralogical form; (4) the presence of reducing agents (e.g. Fe^{2+}, organic matter) that may lead to secondary retention of Cr, and (5) the interplay among these factors within the laterite profile and as the laterite evolves.

1.5 Content of thesis

The following work consists of three individual chapters followed by a chapter summarising the principle outcomes of this doctoral thesis and giving perspectives for future research.

Chapter 2 presents the Cr geochemistry, in particular focused on the Cr isotopic compositions, of the Çaldağ and Karaçam Ni laterite deposits in West Turkey, which are both oxide–dominated nickel laterite deposits that developed under past tropical climates and are thus, considered to be paleo Ni laterite deposits. The behaviour of Cr during oxidative weathering and laterite formation is investigated in depth and its impact on the Cr isotopic composition in the weathering profiles. Furthermore, the role of Mn–oxides as trigger for Cr oxidation and subsequent Cr isotope fractionation is discussed and implications are drawn in order to utilise Cr isotopes as paleo–pH tracers revealing in which portions of the weathering profiles the conditions for supergene Ni enrichments are favourable.

Chapter 3 presents the geochemistry and mineralogy of the São João do Piauí Ni laterite deposit in Northeast Brazil focused on a general characterisation of the Ni laterite deposit, deciphering the mineralogical evolution in the laterite and discussing the tectonic and in particular the climatic conditions of its formation. The chapter investigates in depth the processes that led to supergene Ni enrichment, silicification of the laterite, and the formation of a siliceous top horizon that caps the Ni deposit.

Chapter 4 presents the Cr and Ni isotopic compositions of the São João do Piauí Ni laterite as well as the Cr isotopic compositions of interstitial pore waters and catchment waters and investigates the pathways of Cr and Ni during weathering and Ni laterite formation. The chapter includes a Cr isotope fractionation model that describes the evolution of the Cr isotopic compositions in the profile based on the Cr mineralogy of the underlying bedrock.

The final chapter 5 presents the most important findings of the aforementioned three chapters and gives a general perspective on future research and ideas related to open questions and problems that arouse during this research.

Chapter 2 Chromium isotope geochemistry of the Çaldağ and Karaçam nickel laterite deposits, W. Turkey

2.1 Abstract

The Çaldağ and Karaçam nickel laterites in West Turkey are paleo–deposits that developed under past tropical climates between the Late Cretaceous and the Early Eocene. The purpose of this study is to investigate the evolution of the Cr isotopic composition during ultramafic rock weathering and Ni laterite formation to get a better understanding of the geochemical Cr cycle on the continents, as Ni laterites are important sources of Cr on the continents and account for large amounts of Cr transported via rivers into the oceans. Furthermore, redox–controlled Cr isotope fractionation may reveal insights into the pH–dependent supergene Ni enrichment process. The chromium isotopic compositions of the Çaldağ and Karaçam Ni laterites are variable and show a total Cr isotope range ($\Delta^{53/52}Cr$) between, respectively –0.14 and 0.12 ‰ and –0.61 and –0.08 ‰. Both weathering profiles are characterised by a net loss of Cr during weathering, which is accompanied by a preferential loss of heavy Cr isotopes into the fluid phase, thereby enriching the residual weathering products in light Cr isotopes. Oxidised Cr^{6+} from the hydrolysis of the primary mineral assemblage is taken up by weathering solutions and is transported down through the profile preferentially along clay–filled veins that are present in both laterite profiles and can be retained deeper in the profile, thereby overprinting the primary Cr isotopic composition that originates from initial Cr loss in these horizons. Correlations between the Mn abundance and $\delta^{53}Cr$ value in the profile indicate that Cr oxidation is catalysed by reduction of Mn^{4+}–oxides and that the extent of Cr isotope fractionation may depend on the concentration of Mn. Rayleigh fractionation calculations reveal considerably small Cr isotope fractionation factors of $10^3 \cdot \ln\alpha \approx \varepsilon = \Delta^{53/52}Cr_{(Cr^{6+}-Cr^{3+})}$ of 0.09 ‰ (Çaldağ) and 0.06 ‰ (Karaçam). Low $\delta^{53}Cr$ values correlate with Ni enriched laterite horizons indicating that Cr isotope fractionation under alkaline pH conditions is higher than under acid pH conditions.

2.2 Introduction

Nickel laterite deposits contain 60% of the land–based Ni reserves and account for about 40% of global nickel production (Kuck, 2010; Mudd, 2010; Schnebele, 2017). They are formed by intense oxidative weathering of ultramafic rocks exposed in tropical to semi–arid regions (Butt and Cluzel, 2013), involving the dissolution of primary Mg–silicates and the formation of Fe–oxyhydroxides. If temperature, precipitation, and seasonality are conducive, then economic Ni grades can develop in specific horizons (Thorne et al., 2012). Primary mineral phases are selectively 'leached', and form residual clay and oxide components due to removal of mobile elements (e.g. Mg, Ca, Na) that are taken up by percolating meteoric water and the enrichment of elements that have a low mobility (e.g. Fe, Al). The infiltration of rain water transports mobilised elements through faults and fractures of the laterite, which leads to a progressive downwards migration of the weathering front and eventually to deeply weathered regolith profiles, in which redox–controlled mobilisation, redistribution and accumulation of elements are dominantly responsible for the geochemical evolution of the laterite profile. Oxidative weathering leads to a change in the oxidation state of redox–sensitive elements, predominantly mobilising species that are highly soluble in their oxidised form.

Chromium is abundant in ultramafic rocks and mainly resides in oxide phases and to a lesser extent in silicates. Chromite and magnetite are the principal Cr–bearing minerals, followed by significantly lower concentrations in pyroxene, serpentine, and olivine (Grapes, 1981; Challis et al., 1995; Hanson and Jones, 1998; Righter et al., 2003; Oze et al., 2004; Garnier et al., 2008). The average Cr concentration in ultramafic rocks ranges between 2400 ppm and 3000 ppm, although the Cr concentration in their weathering products, in particular in Ni laterites and serpentine soils, can reach up to 6 wt% (Stueber and Goles, 1967; Shiraki, 1997; Lee et al., 2004). In serpentine soils, about 10% of the total Cr is hosted in silicates, whereas 90% is hosted in oxides (Oze, 2003). The heterogeneous distribution of Cr between oxides and silicate minerals directly affects its mobility during weathering, and it is usually assumed that Cr is relatively immobile and is residually enriched during laterite and soil formation. Indeed, some laterite profiles show significant Cr enrichment that can exceed even Fe–enrichment (e.g. Schellmann, 1986; Bardossy and Aleva, 1990; Hill et al., 2000b). However, other laterites are depleted in Cr during weathering (e.g. McAlister and Smith, 1997).

The behaviour of Cr during lateritisation is mainly determined by: (1) the distribution of Cr between individual silicate and oxide phases; (2) the availability of manganese oxides that are principally responsible for oxidation of Cr^{3+} to Cr^{6+} (Richard and Bourg, 1991; Economou-Eliopoulos et al., 2014); (3) the availability of abiotic and biotic reductants, such as Fe^{2+}, sulfides, microbes, and organic acids (Fendorf et al., 2000), or sorbents (clays or oxy–hydroxides) that immobilise Cr^{6+}, (4) the local pH conditions that influence the redox–potential and (5) the structural development of the weathering profile (e.g. collapse, dilation, fracture propagation) that determines physical (residual) Cr enrichment. The redox behaviour of Cr in laterites is controlled by the competition between hydration, complexation, dissolution/precipitation, and adsorption/desorption of Cr^{3+} and Cr^{6+}. The redox–sensitivity of Cr and the associated Cr isotope fractionation provides important insights into the redox evolution of laterite profiles and may help to understand the processes that lead to Ni enrichment. Chromium isotope compositions are expressed as $^{53}Cr/^{52}Cr$ ratios normalised to the NIST SRM 979 Cr isotope standard using the common delta (δ) notation:

$$\delta^{53}\mathrm{Cr}(‰) = 1000 \times \left\{ \left[\frac{\left(\frac{^{53}Cr}{^{52}Cr}\right)_{sample}}{\left(\frac{^{53}Cr}{^{52}Cr}\right)_{SRM979}} \right] - 1 \right\} \quad (2.1)$$

Cr mobility and solubility are mainly dependent on oxidation state. Cr^{6+} is highly soluble, whereas Cr^{3+} tends to be immobile (Beverskog and Puigdomenech, 1997; James et al., 1997). Weathering of ultramafic rocks under atmospheric conditions leads to a Cr isotope signature in the weathered rock that is different from the protolith. Weathering products tend to be depleted in heavy Cr isotopes and have a lower $\delta^{53}Cr$ value compared to the unweathered protolith (Frei et al., 2009, 2014; Crowe et al., 2013; Frei and Polat, 2013; Berger and Frei, 2014; Paulukat et al., 2015; Novak et al., 2017; Wille et al., 2018). However, the availability of Cr isotope data for weathered continental rocks, in particular for Ni laterite deposits, is yet sparse. Moreover, as Cr derived from weathering of ultramafic provinces accounts for 80% of the global Cr input from the continents into the oceans (McClain and Maher, 2016), a better understanding of Cr cycling in modern ultramafic weathering profiles is essential for interpretation of records of seawater $\delta^{53}Cr$ that are currently used as paleo–redox tracers (Frei et al., 2009, 2014, 2017; Konhauser et al., 2011; Crowe et al., 2013; Frei and Polat, 2013; Paulukat et al., 2015).

This chapter presents the Cr geochemistry of the Çaldağ and Karaçam nickel oxide deposits in West Turkey. We show that oxidative weathering leads to a decrease of the $\delta^{53}Cr$ value in the regolith units, which results from removal of isotopically heavy Cr in the weathered rock compared to the unweathered protolith. Furthermore, clay–filled fractures that are emplaced in the regolith units and developed during the course of laterite formation serve as pathways for mobilised Cr that can be transported into the lower part of the profile. Furthermore, Cr isotopes could maybe utilised as a paleo–pH tracer to indicate in which portions of the weathering profile the conditions for Ni enrichment were favourable, as Cr isotope fractionation is likely be influenced by local pH conditions that also control Ni mobilisation from primary minerals and retention onto secondary minerals, which ultimately leads to supergene Ni enrichment in laterites.

2.3 Geologic setting

Turkey has numerous paleo–laterite Ni deposits that have formed from tropical weathering of serpentinised peridotite material that was uplifted during the closure of the Tethys and was subsequently exposed to surficial weathering during the Mesozoic and the Cenozoic (Herrington et. al., 2016). The Çaldağ and Karaçam Ni laterite deposits developed on oceanic fragments of the northern ophiolite belt, one of three major belts that separate the main tectonic units of Turkey (**Fig. 2.1**).

The Çaldağ Ni laterite deposit is located close to Manisa city about 60 km from Izmir in NW Turkey. It is situated at the northern edge of the Menderes Massif and overlies serpentinised peridotite that was tectonically emplaced on Triassic dolomites in the Late Cretaceous about 93±2 Ma (Önen and Hall, 2000). The deposit is located on a horst structure and is partly overlain by continental and lacustrine sediments of Eocene age that protected the laterite from erosion (Thorne et al., 2009). The Çaldağ deposit is the largest nickel resource in Turkey, with ore reserves of 29.7 million tonnes and an average concentration of 1.14 wt% Ni. The Çaldağ laterite is well documented by Thorne et al. (2009) and Tavlan et al. (2011), who made detailed mineralogical studies and characterised the Ni laterite as an oxide–dominated Ni deposit that developed under an aggressive weathering environment (high temperature, high precipitation) with a high standing water table. A high silica concentration throughout most of the laterite indicates a preferred retention of mobilised SiO_2 from initial silicate breakdown, which is often associated with a change towards a more arid climate (Lacinska and Styles, 2013) and is therefore, interpreted to reflect an increasing seasonality in the Eocene with longer dry periods and less precipitation.

The Çaldağ protolith was subject to weathering under an increasingly warm, tropical climate for about 15 – 20 Myr from the Late Cretaceous until the Early– to Mid–Eocene, when the climate became cooler (Thorne et al., 2012). The formation was exposed until the Late Miocene when the deposit was overlain by lacustrine sediments (Kaya et al., 2004). Tavlan et al. (2011) combined the exhumation history of the Çaldağ protolith with available climate data and constrained a total period of about 50 Myr when the climate was conducive for Ni laterite formation.

The Karaçam Ni laterite deposit is located about 50 km north of Ankara in Central Turkey at the northern margin of the Anatolide–Tauride Block about 300 km Northeast of Çaldağ (**Fig. 2.1**). The laterite developed on a serpentinised peridotite slab that was emplaced between the Anatolide–Taurides and the Sakarya Zone during Mesozoic times (Okay et al., 2001; Okay 2011). The Karaçam (also known as Adatepe) laterite is a relatively small Ni deposit and has only about 6 million tonnes ore with an average concentration of 0.6 wt% Ni. The deposit is relatively unknown, because of its small size and low Ni content, and it is only briefly described by Boyalı (1985), Karaoğlu and Gümüş (1997), and Girgin et al. (2011). The first comprehensive characterisation of the Karaçam Ni laterite was made by Herrington et al. (*in preparation*), who studied mineralogy and geochemistry of the weathering profile and found evidence for late, low pH groundwater that lead to remobilisation of Ni, Al, Cr, and Sc and transformed the laterite from a clay–dominated into a more oxide–dominated Ni deposit. The Karaçam protolith was exposed to oxidative weathering from the Late Cretaceous until the Early to Mid–Eocene, which led to the formation of a deep weathering profile, although the exact timing of lateritisation is unknown.

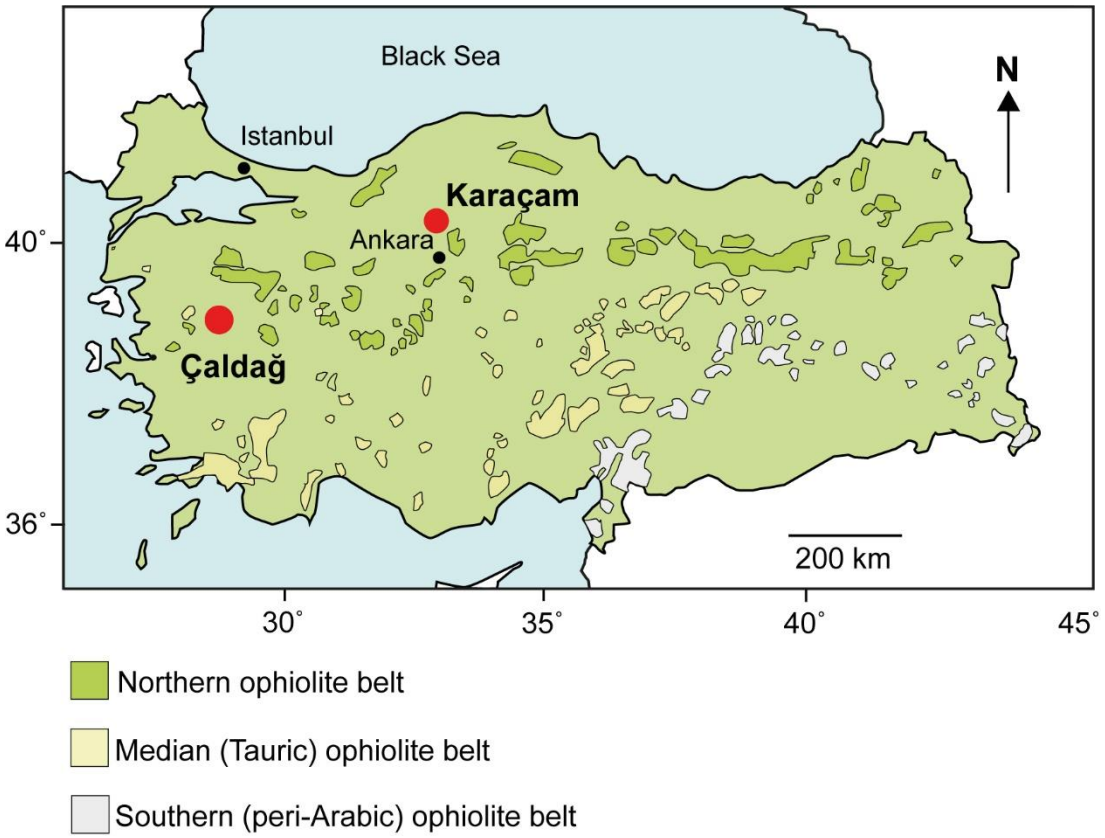

Fig. 2.1. Geologic map illustrating the main tectonic units of Turkey and the location of the Çaldağ and Karaçam Ni laterite deposits. Figure from Thorne (2011).

2.4 Characterisation of the Çaldağ and Karaçam Ni laterite deposits

2.4.1 Çaldağ

Three weathering profiles have been sampled within the Çaldağ Ni laterite deposit (Thorne et al., 2009), and the Hematite Pit is subject of this study (**Fig. 2.2**). The Hematite Pit weathering profile can be divided into five major zones based on the dominant mineralogy and rock texture. The laterite shows a complete weathering profile with serpentinite at the bottom of the profile overlain by a limonitic saprolite, followed by a lower and an upper limonite horizon, and an indurated siliceous horizon at the top. The protolith (PB1, PB5) is a light–brown to green serpentinite that consists of a mineral assemblage of lizardite, montmorillonite, and quartz, with brown goethite veins that penetrate into the overlying regolith at the sharp contact between serpentinite and saprolite. The saprolite horizon (PB2) is characterised by an increasing amount of goethite towards the top compared to the underlying serpentinite and a gradual replacement of the primary rock texture. The limonite zone (PB3, PB4) that is the dominant unit of the laterite profile is generally yellowish brown, shows only relic primary mineral textures, and is characterised by a high amount of fine–grained goethite. The limonite horizon becomes gradually enriched in silica towards the top of the profile, which consists of an indurated, virtually pure silica cap. Economic Ni enrichments are present in the upper limonitic saprolite and the lower limonite with Ni concentrations of up to 2.5 wt%. The Ni laterite is an oxide deposit with goethite as the main Ni ore. The weathering profile has experienced a significant degree of internal collapse that was induced by incongruent mineral dissolution and the loss of soluble elements, in particular Mg and Ca, which eventually led to shrinking of the regolith column. Slight dilation occurred at the serpentinite–saprolite boundary due to the volume increase caused by the formation of low density secondary mineral phases. Throughout the rest of the profile, shrinking predominates and this partly accounts for economic Ni enrichments within the limonitic saprolite. Chromite is the main Cr–bearing mineral and is present throughout the regolith profile. Chromite generally has a very low weathering susceptibility, however, individual crystals in the laterite show dissolution textures. Clay–filled fractures (PB6) penetrate the upper parts of the weathering profile, in particular the limonite and in the silicified limonite horizon that consist of a mixture of montmorillonite, kaolinite, saponite, nontronite, chromite, and goethite. In hand specimen, the clayey material appears dark green to blue and is highly soluble in water. Based on the classification of (Brand et al., 1998), the Çaldağ laterite is an oxide–dominated Ni deposit.

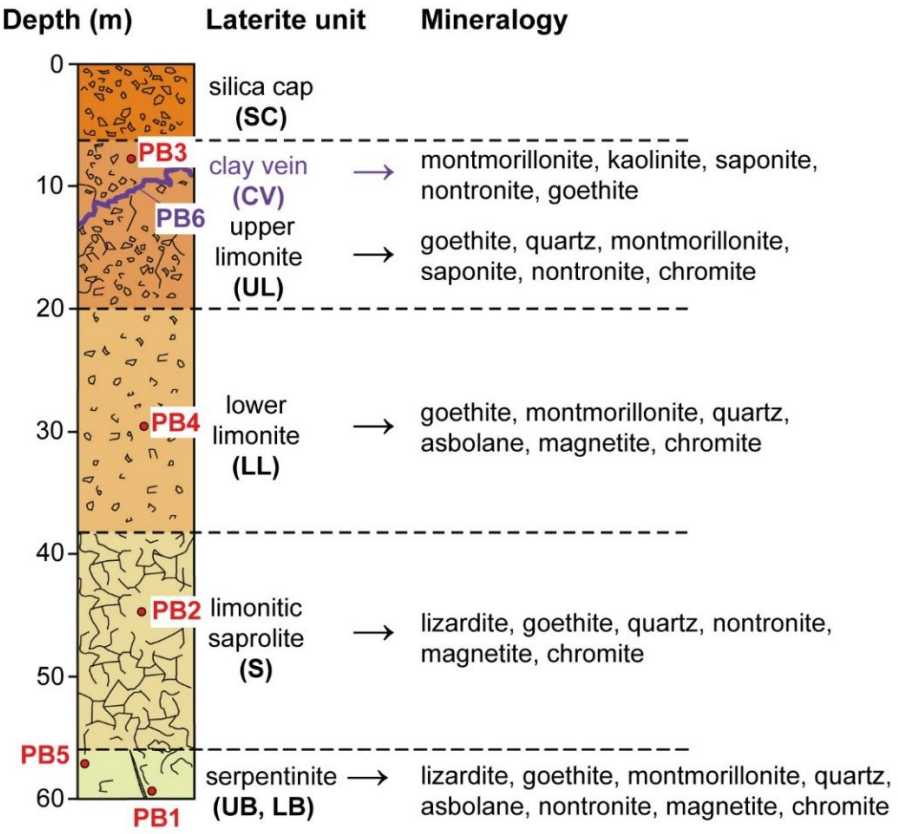

Fig. 2.2. Schematic stratigraphic profile of the Çaldağ Ni laterite. The main laterite units are indicated by different colours and the dominant mineralogy is given to the right of the laterite unit. Locations of bulk samples are indicated by red circles and locations of vein samples are shown in purple, blue and green. LB = lower bedrock, UB = upper bedrock, S = saprolite, LL = lower limonite, UL = upper limonite, SC = silica cap, CV = clay vein.

2.4.2 Karaçam

The Karaçam Ni laterite does not exhibit a complete weathering profile down to the unweathered protolith, however, a distinct saprolite zone at the base of the deposit indicates that the profile formed in–situ and does not originate from the transport of lateritic material from higher depths (Herrington et al., *in preparation*). The weathering profile can be divided into five major zones based on the dominant mineralogy and rock texture (**Fig. 2.3**). The protolith (KC1) is a green serpentinised peridotite with relict textures, which confirms its cumulate origin, and mainly consists of a mineral assemblage of lizardite with minor goethite, and montmorillonite. The serpentinite is not entirely 'fresh', which is shown by the presence of clay filled inter–granular fractures and a relatively high loss of ignition (LOI; **Table 2.2**) of 16.2 wt%. Nevertheless, the bulk of the protolith contains unaltered serpentine and euhedral spinel.

The saprolite (KC2, KC6) is dominated by pale green minerals with variable Ni contents, which are present in patches and along fractures. The saprolite contains the mineral takovite ($Ni_6Al_2(CO_3,OH)(OH)_{16}\cdot 4H_2O$) that appears bright green in the weathering profile and contains up to 51 wt% Ni. The presence of takovite is responsible for the highly elevated Ni concentration of the saprolite sample KC6. The primary mineral assemblage is mostly replaced by secondary phases, such as montmorillonite, nontronite, and goethite, although the original rock structure is still preserved.

The limonite horizon (KC3, KC4, KC5, KC10) is characterised by a yellowish–brown goethite dominated mineral assemblage with fine–grained goethite fingers that penetrate down into the upper saprolite. The upper limonite is characterised by a reddish–brown colour, which reflects its high amount of hematite. Economic Ni enrichments are present between the saprolite zone and the upper limonite with Ni concentrations that range from 1.8 to 3.0 wt%. Locally, the whole–rock Ni concentration can be as high as 8.7 wt% where takovite is present (KC6). However, the main Ni ore in the saprolite and limonite horizon is goethite.

The weathering profile shows characteristics of a significant re–silification event and the SiO_2 concentration increases towards the top of the profile and is as high as 99 wt% in the chromite–mottled cap that contains loosely amorphous aggregated silica. Silica has a massive glassy texture, which indicates precipitation as silica gel during laterite formation. Chromite is the main Cr mineral and is present throughout the profile, although in lower relative proportions than in the Çaldağ laterite samples. Distinctive blue and green clay–filled fractures (KC11, KC12) in the upper limonite are identified as a Cr–rich mineral assemblage that consists of montmorillonite, saponite, nontronite, and small quantities of kaolinite. The Cr concentration of these clay–filled fractures is as high as 4.2 wt%, which indicates significant Cr mobilisation and subsequent retention in localised zones during laterite formation. Based on the classification of Brand et al. (1998), the Karaçam laterite is an oxide–dominated Ni deposit with goethite as Ni main ore. However, the saprolite horizon also contains Ni–rich takovite, which reflects Al mobility due to the presence of low pH groundwater (Herrington et al., *in preparation*). The removal of Al from the limonite units is likely responsible for the absence of Ni–bearing clays in the Karaçam laterite deposit. Hence, late low pH fluids may have rejuvenated an existing Ni laterite deposit that subsequently led to the development of an oxide–dominated Ni laterite formation. The Çaldağ Ni laterite deposit may represent and extreme end–member of this rejuvenation process, which is supported by a complete absence of As in the profile that is mobile at low pH (Herrington et al., *in prepartion*).

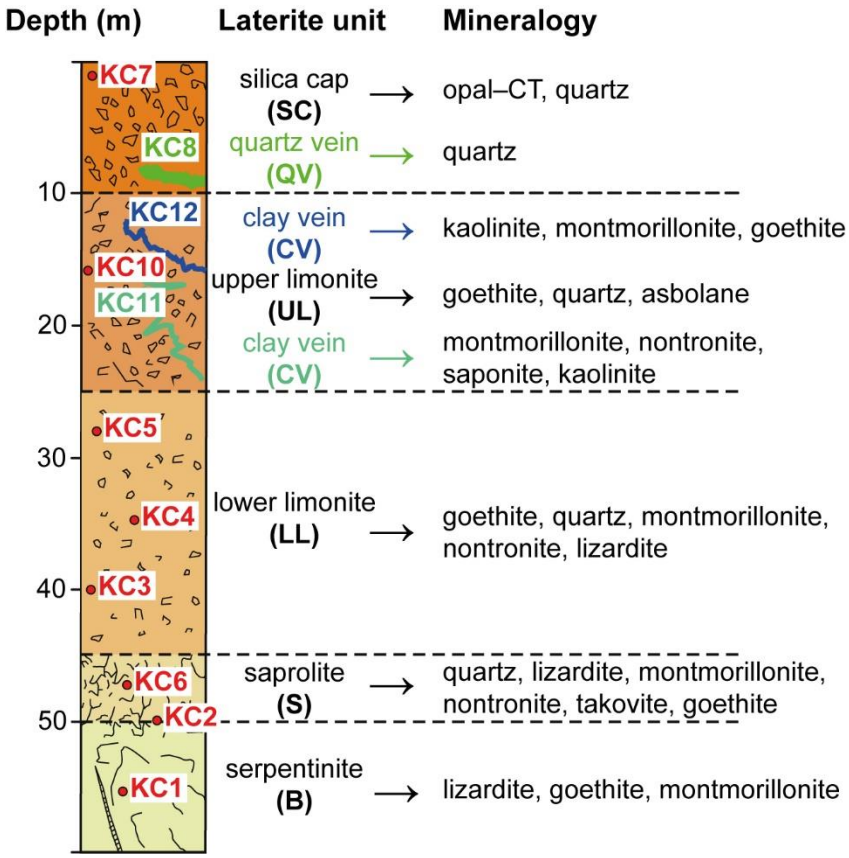

Fig. 2.3. Schematic stratigraphic profile of the Karaçam Ni laterite. The main laterite units are indicated by different colours and the dominant mineralogy is given to the right of the laterite unit. Locations of bulk samples are indicated by red circles and locations of vein samples are shown in purple, blue and green. B = bedrock, S = saprolite, LL = lower limonite, UL = upper limonite, SC = silica cap, CV = clay vein, QV = quartz vein.

2.5 Methods

The Çaldağ samples were collected from the Hematite Pit by Thorne (2011) and major element, trace element, and rare earth element (REE) concentrations were determined by a Master student (Brown, 2014, MSc Thesis, Imperial College London, unpublished). Rock samples (PB1, PB2, PB3, PB4, PB5) are bulk rock samples representative of each of the individual laterite units. One clay vein sample (PB6) was collected from within the upper part of the silicified limonite horizon. The Karaçam samples were collected by Herrington et al. (*in prepartion*). Rock samples (KC1, KC2, KC3, KC4, KC5, KC6, KC7, KC10) are bulk rock samples representative of the different laterite units, and one quartz vein sample (KC8) and two clay vein samples (KC11, KC12) were collected, respectively, within the silica cap and in the upper limonite.

2.5.1 Major, trace and rare earth elements

The chemical compositions of the Çaldağ and Karaçam samples were determined by inductively coupled plasma optical emission spectroscopy (ICP–OES) and inductively coupled plasma mass spectrometry (ICP–MS) at the *Natural History Museum, London*.

Major elements and some trace elements were measured by ICP–OES (**Table 2.1** – **2.4**). Homogenised sample material was mixed with a lithium–tetraborate flux, and then fused in platinum crucibles. The fused sample discs were chipped and then dissolved, respectively in dilute HNO_3 (Çaldağ samples) and in a mixture of HF and $HClO_4$ (Karaçam samples) and were later analysed by a *Varian Vista–Pro CCD Simultaneous* ICP–OES. The certified rock standards MA-N, PCC-1, SU-1 were used for ICP–OES and ICP–MS analysis. The accuracy of all major elements, Ni, and Sr of the rock standard material is better than 5% compared to recommended values (Govindaraju, 1994, 1995). The reproducibility of ICP–OES measurements is given by the relative standard deviation (RSD; Hayes, 1994), and is usually better than 10% for all major elements, Ni, and Sr.

All other trace elements and the rare earth elements (REE) were measured by ICP–MS (**Table 2.3** – **2.6**). Homogenised sample material was totally digested in HF and $HClO_4$ and then taken up in 10% HNO_3 for analysis. The concentrations of the trace elements were then determined on a *Varian 810* ICP–MS and by ICP–OES as required. Results are accurate to 10 % and the precision of replicate measurements is better than 10% (RSD) for all trace elements and the REE.

Cr concentrations of the Çaldağ and Karaçam samples were determined by ICP–OES. However, the Cr content of the sample material was reconfirmed at the University of Southampton by ICP–MS and by isotope dilution (ID) on a MC–ICP–MS. A comparison of the Cr concentrations determined by ICP–OES and (MC)–ICP–MS is found in **Table 2.7** and **2.8**. A discussion about the reliability of the data and its implications for this study is presented in **Chapter 2.5.4**.

2.5.2 Sample preparation and Cr concentration analysis for Cr isotope measurements

For Cr isotope analysis, about 100 mg of homogenised sample material was dissolved using a multiple–step acid dissolution that consisted of: (1) aqua regia (mixture of HCl and HNO_3 in a 3:1 ratio) digestion at 160°C for 24 h, followed by; (2) HF/$HClO_4$ digestion at 170°C for at least 7 days (14 days for spinel–rich samples), and (3) $HClO_4$ digestion at 180°C for 2 – 4 days. The sample solutions were evaporated to incipient dryness after each individual digestion step. After acid dissolution the sample material was re–dissolved in HCl and heated at 130°C for 48 h to reduce low solubility fluorides that may have formed during the second acid dissolution step. This relatively long dissolution was applied, as most samples contained significant amounts of chromite or Cr–rich magnetite that are extremely resistant to acid dissolutions, which yields in an incomplete Cr recovery (e.g. Jain et al., 2000). The long digestion in HF/$HClO_4$ ensures a full dissolution of Cr–oxides. A complete Cr–recovery of the samples was confirmed by the simultaneously processed rock standards JP-1 and DTS-2b. Both rock standards are chromite–rich ultramafic rocks that underwent the same dissolution procedure.

From all sample solutions that showed no evidence for residues after centrifuging for 15 min at 3000 rpm, a small aliquot was taken between two glass plates to re–check for small undissolved mineral grains under a microscope (10x magnification). Samples that showed no evidence of residues under the microscope (i.e. complete clear sample solution without tiny floating particles) then underwent a total digestion. Samples were evaporated to incipient dryness and taken up in 7M HCl to create stock solutions for subsequent Cr concentration and Cr isotope analysis. Cr concentration analysis was performed at the *University of Southampton* on a *Thermo Scientific ELEMENT 2* ICP–MS to facilitate accurate spiking of the samples for Cr isotope and concentration (ID) analysis on the MC–ICP–MS. The internal calibration standard was made from a single Cr element standard in a 3% HNO_3 matrix with Rh and In to correct for possible matrix effects. Samples were analysed in the same 3% HNO_3 matrix. The certified reference materials JP-1 and DTS-2b that contain chromite were used as an external standards. The results of replicate measurements of the JP-1 and DTS-2b reference material are accurate to 6 % (Mukherjee et al., 2012; Robin-Popieul et al., 2012; Day et al., 2015) and the precision of replicate measurements is better than 10% (RSD).

Table 2.1. Major element concentrations of the Çaldağ Ni laterite samples.

Depth (m)	Sample	Laterite unit	SiO_2 (wt%)	TiO_2 (wt%)	Al_2O_3 (wt%)	Fe_2O_3 (wt%)	MnO (wt%)	MgO (wt%)	CaO (wt%)	LOI[b] (wt%)	Total[c] (wt%)
LOQ[a]			1.00	0.009	0.05	0.10	0.008	0.005	0.03		
8	PB3	Upper limonite	5.22	0.011	1.33	64.5	0.125	0.299	0.07	26.0	74.0
11	PB6*	Clay vein	45.8	0.009	19.2	10.7	0.040	1.65	0.79	17.8	82.2
31	PB4	Lower limonite	12.4	0.010	1.41	63.7	1.06	0.637	0.15	17.7	82.3
43	PB2	Saprolite	33.4	0.014	0.83	34.6	0.452	15.9	0.32	11.4	88.6
57	PB5	Upper bedrock	35.3	0.034	1.07	20.1	0.105	27.1	0.09	14.4	85.6
60	PB1	Lower bedrock	33.0	<	0.31	8.46	0.116	34.0	5.93	17.5	82.5

<	Determined values are below the limit of quantification (LOQ). LOQ = Blank mean + 10·SD (Blank)
a	Limit of quantification.
b	Calculated as {100 wt% – Total (wt%)}.
c	Total includes the concentration of all major elements, trace and rare earth elements.
*****	Clay–rich fracture filling/vein. All other samples are bulk rock.
Note	Concentrations determined by ICP–OES. Na_2O, K_2O, and P_2O_5 data are not shown as the concentrations were below the LOQ for all samples. Data are from Brown, 2014 (MSc Thesis, Imperial College London).

Table 2.2. Major element concentrations of the Karaçam Ni laterite samples.

Depth (m)	Sample	Laterite unit	SiO_2 (wt%)	TiO_2 (wt%)	Al_2O_3 (wt%)	Fe_2O_3 (wt%)	MnO (wt%)	MgO (wt%)	CaO (wt%)	LOI[b] (wt%)	Total[c] (wt%)
LOQ[a]			0.1	0.01	0.1	0.01	0.005	0.01	0.001		
0	KC7	Silica cap	97.6	0.02	0.5	0.43	0.006	0.07	0.150	1.0	99.0
10	KC8*	Quartz vein	98.6	0.02	0.7	0.41	0.013	0.15	0.118	0.0	100.4
12	KC12*	Clay vein	36.4	<	24.9	11.18	0.006	0.43	0.448	21.7	78.3
13	KC11*	Clay vein	51.0	0.03	16.6	7.47	0.008	3.39	1.40	14.4	85.6
15	KC10	Upper limonite	10.8	<	1.1	65.25	1.12	0.56	0.012	17.6	82.4
28	KC5	Lower limonite	37.9	<	1.0	44.83	0.463	0.57	0.032	12.9	87.1
35	KC4	Lower limonite	65.1	<	<	21.61	2.02	2.73	<	6.0	94.0
40	KC3	Lower limonite	51.5	<	<	11.58	0.713	22.5	<	11.3	88.7
48	KC6	Saprolite	53.6	<	8.5	13.27	0.016	1.19	0.394	14.1	85.9
50	KC2	Saprolite	63.8	<	0.2	10.51	0.192	13.8	0.152	8.5	91.5
55	KC1	Bedrock	40.3	0.01	1.3	7.53	0.103	33.3	0.912	16.2	83.8

<	Determined values are below the level of quantification (LOQ). LOQ = Blank mean (ppm) + 10·SD (Blank)
a	Level of quantification.
b	Calculated as {100 wt% – Total (wt%)}..
c	Total includes the concentration of all major elements, trace and rare earth elements.
*****	Fracture filling/ mineral vein. Samples without asterisk refer to bulk rock laterite samples.
Note	Concentrations determined by ICP–OES. Data from Herrington et al., (*in preparation*). Na_2O, K_2O, and P_2O_5 data are not shown as the concentrations were below the LOQ in all samples.

Table 2.3. Trace element concentrations of the Çaldağ Ni laterite samples.

Depth (m)	Sample	Laterite unit	As (ppm)	Ba (ppm)	Co (ppm)	Cu (ppm)	Hf (ppm)	Ni[b] (ppm)	Rb (ppm)	Sc (ppm)	Sr[b] (ppm)	V (ppm)	Y (ppm)	Zn (ppm)	Zr (ppm)
LOQ[a]			0.07	0.11	0.006	0.01	0.03	150	0.02	0.06	5	0.07	0.003	0.16	0.04
8	PB3	Upper limonite	91.3	75.4	114	378	0.06	662	3.17	13.3	<	207	0.681	116	4.95
11	PB6*	Clay vein	48.1	27.5	116	133	<	8810	1.16	199	21.4	63.5	0.604	156	0.88
31	PB4	Lower limonite	31.9	398[c]	1640	170	<	21400	1.50	36.4	11.8	62.4	3.57	404	0.99
43	PB2	Saprolite	18.5	426[c]	1100	11.1	0.05	24600	3.31	5.58	16.2	16.6	1.51	363	1.78
57	PB5	Upper bedrock	29.9	73.6	682	10.8	0.15	11000	5.64	5.35	<	15.6	1.45	105	4.79
60	PB1	Lower bedrock	2.19	50.0	128	3.34	<	2040	0.18	4.60	29.8	11.1	0.077	40	0.22

<	Determined values are below the level of quantification (LOQ). LOQ = Blank mean (ppm) + 10·SD (Blank)
a	Level of quantification.
b	Determined by ICP–OES.
*****	Clay–rich fracture filling/vein. Samples without asterisk refer to bulk rock laterite samples.
Note	The shown dataset is determined by ICP–MS unless otherwise stated. Data are from Brown, 2014, (MSc Thesis, Imperial College London).

Table 2.4. Trace element concentrations of the Karaçam Ni laterite samples.

Depth (m)	Sample	Laterite unit	As[b] (ppm)	Ba (ppm)	Co (ppm)	Cu (ppm)	Hf (ppm)	Ni[b] (ppm)	Rb (ppm)	Sc (ppm)	Sr[b] (ppm)	V (ppm)	Y (ppm)	Zn (ppm)	Zr (ppm)
LOQ[a]			40	0.02	0.07	0.02	0.004	50	0.004	0.08	35	0.03	0.001	0.03	0.006
0	KC7	Silica cap	86.4	10.8	10.2	44.0	0.138	184	7.23	2.6	58	6.60	0.45	330	2.34
10	KC8*	Quartz vein	<	6.33	6.91	252	0.156	292	5.06	3.4	<	53.9	0.08	369	2.70
12	KC12*	Clay vein	<	106	74.2	26.7	0.011	6950	0.53	300	182	210	20.8	131	0.57
13	KC11*	Clay vein	<	90.5	436	8.35	0.015	25500	1.26	160	91	256	5.24	157	0.69
15	KC10	Upper limonite	1100	94.6	1520	3.13	0.020	30600	2.19	17.6	68	24.2	31.4	566	0.54
28	KC5	Lower limonite	<	24.0	712	3.45	0.029	19000	1.63	27.7	42	50.2	5.68	216	2.07
35	KC4	Lower limonite	700	106	1950	4.30	0.004	21700	2.70	2.1	42	8.03	2.02	79	0.20
40	KC3	Lower limonite	<	36.5	632	11.2	0.016	20600	0.97	4.0	<	9.41	0.32	72	0.52
48	KC6	Saprolite	45.7	19.1	239	13.5	0.007	87700	1.06	74.4	45	4.72	4.59	203	0.15
50	KC2	Saprolite	<	21.2	931	15.3	0.008	26100	0.54	2.9	<	8.07	9.17	389	0.23
55	KC1	Bedrock	175	10.4	109	15.1	0.008	2170	0.10	6.9	58	37.3	0.12	47	0.23

a Level of quantification.
b Determined by ICP–OES.
***** Fracture filling/ mineral vein. Samples without asterisk refer to bulk rock laterite samples.
Note The shown dataset is from Herrington et al., (*in preparation*).and has been determined by ICP–MS unless otherwise stated

Table 2.5. REE, Th and U concentrations of the Çaldağ Ni laterite samples.

Depth (m)	Sample	Laterite unit	La (ppm)	Ce (ppm)	Pr (ppm)	Nd (ppm)	Sm (ppm)	Eu (ppm)	Gd (ppm)	Tb (ppm)	Dy (ppm)	Ho (ppm)	Er (ppm)	Tm (ppm)	Yb (ppm)	Lu (ppm)	Th (ppm)	U (ppm)
LOQ[a]			0.003	0.011	0.004	0.008	0.002	0.001	0.001	0.001	0.001	0.001	0.002	0.001	0.002	0.001	0.06	0.003
8	PB3	Upper limonite	0.818	1.98	0.227	0.859	0.187	0.044	0.161	0.025	0.148	0.032	0.088	0.016	0.116	0.018	0.60	1.99
11	PB6*	Clay vein	0.411	0.217	0.128	0.505	0.114	0.030	0.112	0.017	0.110	0.023	0.063	0.012	0.094	0.017	1.31	15.9
31	PB4	Lower limonite	3.81	4.96	0.920	3.49	0.628	0.145	0.629	0.086	0.519	0.108	0.339	0.055	0.396	0.061	0.14	10.1
43	PB2	Saprolite	0.982	1.97	0.240	0.923	0.237	0.056	0.215	0.036	0.235	0.050	0.166	0.031	0.260	0.038	0.21	4.98
57	PB5	Upper bedrock	1.52	2.94	0.390	1.46	0.316	0.075	0.297	0.046	0.282	0.059	0.196	0.031	0.217	0.033	0.52	1.30
60	PB1	Lower bedrock	0.025	0.056	0.008	0.025	0.006	0.002	0.007	0.001	0.009	0.002	0.009	0.001	0.018	0.003	<	4.41

<	Determined values are below the level of quantification (LOQ). LOQ = Blank mean (ppm) + 10·SD (Blank)
a	Level of quantification.
*****	Clay–rich fracture filling/vein. Samples without asterisk refer to bulk rock laterite samples.
Note	The shown dataset is determined by ICP–MS. Data are from Brown, 2014 (MSc Thesis, Imperial College London)

Table 2.6. REE, Th and U concentrations of the Karaçam Ni laterite samples.

Depth (m)	Sample	Laterite unit	La (ppm)	Ce (ppm)	Pr (ppm)	Nd (ppm)	Sm (ppm)	Eu (ppm)	Gd (ppm)	Tb (ppm)	Dy (ppm)	Ho (ppm)	Er (ppm)	Tm (ppm)	Yb (ppm)	Lu (ppm)	Th (ppm)	U (ppm)
LOQ[a]			$3\cdot10^{-4}$	$5\cdot10^{-4}$	$1\cdot10^{-4}$	$9\cdot10^{-4}$	$9\cdot10^{-4}$	$2\cdot10^{-4}$	$6\cdot10^{-4}$	$3\cdot10^{-4}$	$6\cdot10^{-4}$	$3\cdot10^{-4}$	$7\cdot10^{-4}$	$3\cdot10^{-4}$	$6\cdot10^{-4}$	$4\cdot10^{-4}$	$1.2\cdot10^{-3}$	$2\cdot10^{-4}$
0	KC7	Silica cap	0.647	1.19	0.129	0.509	0.104	0.030	0.105	0.015	0.096	0.017	0.046	0.006	0.033	0.004	0.412	0.080
10	KC8*	Quartz vein	0.139	0.316	0.028	0.105	0.022	0.006	0.021	0.003	0.016	0.004	0.009	0.001	0.008	0.001	0.088	0.260
12	KC12*****	Clay vein	2.35	4.61	1.30	7.18	3.88	1.55	6.43	1.12	7.54	1.49	4.63	0.745	5.91	0.863	<	<
13	KC11*****	Clay vein	0.300	0.213	0.183	1.08	0.588	0.249	1.13	0.217	1.54	0.340	1.06	0.160	1.18	0.176	0.413	1.64
15	KC10	Upper limonite	1.60	1.02	0.291	1.48	0.659	0.322	2.34	0.409	3.02	0.739	2.15	0.249	1.46	0.214	0.080	1.57
28	KC5	Lower limonite	0.541	0.701	0.136	0.643	0.235	0.097	0.532	0.096	0.723	0.174	0.549	0.074	0.518	0.075	0.032	1.05
35	KC4	Lower limonite	0.318	0.476	0.046	0.201	0.050	0.020	0.137	0.020	0.144	0.037	0.103	0.012	0.066	0.010	0.053	2.75
40	KC3	Lower limonite	0.101	0.173	0.014	0.058	0.012	0.003	0.020	0.002	0.016	0.004	0.013	0.002	0.012	0.002	0.012	2.57
48	KC6	Saprolite	0.159	0.304	0.059	0.336	0.207	0.093	0.451	0.089	0.688	0.161	0.523	0.081	0.635	0.091	0.008	7.66
50	KC2	Saprolite	0.392	1.21	0.164	0.874	0.493	0.223	1.10	0.223	1.63	0.363	1.14	0.158	1.12	0.166	0.044	1.98
55	KC1	Bedrock	0.069	0.140	0.014	0.061	0.014	0.005	0.018	0.003	0.018	0.005	0.017	0.003	0.024	0.005	0.036	0.007

<	Determined values are below the level of quantification (LOQ). LOQ = Blank mean (ppm) + 10·SD (Blank)
a	Level of quantification.
*****	Fracture filling/ mineral vein. Samples without asterisk refer to bulk rock laterite samples.
Note	The shown dataset is determined by ICP–MS. Data from Herrington et al., (*in preparation*).

2.5.3 Cr isotope measurements

Subsample aliquots containing 2 µg of Cr were taken from the stock solutions for Cr separation and subsequent Cr isotope analysis. An appropriate amount of a $^{50}Cr/^{54}Cr$ enriched double spike was added and samples were evaporated to incipient dryness. Samples were re–dissolved in 7M HCl and Cr was purified using a two–step chromatographic separation using *Bio-Rad AG1-X8* resin to separate Fe and *Bio-Rad AG50W-X12* to separate Ti and V (Bonnand et al., 2011). Purified Cr samples were taken up in 3% HNO_3. The Cr isotopic compositions of the samples and the Cr standard material *SRM 979* were determined at the *University of Southampton*, on a *Thermo Scientific Neptune* multicollector inductively coupled plasma mass spectrometer (MC–ICP–MS) operated in medium resolution mode and using an *Aridus* desolvator for sample injection. Sample aliquots (1 ppm Cr) were diluted 8 times (125 ppb Cr) to give a 10 – 15 V signal on the ^{52}Cr Faraday cup. The procedural Cr blank was lower than 10 ng and is negligible compared to the Cr content of each sample (2000 ng). Individual sample analyses consisted of 100 isotope ratio measurements with an integration time of 8 s. The background signal was measured using the same 3% HNO_3 solution that was used for the standard and sample solutions and was subtracted during deconvolution of the data from the sample signal. The injector wash time between individual samples was 12 min to avoid cross contamination and to ensure low background signals. The long–term instrumental reproducibility was determined by measuring a spiked *SRM 979* Cr standard. The $\delta^{53}Cr$ values recovered by the double–spike technique are within an error of 0 ‰, however the average value is slightly positive, with $\delta^{53}Cr = 0.02 \pm 0.06$ ‰ (2SD, n = 71). The results of the Cr isotope analysis and the Cr ID concentration measurements are shown in **Table 2.7** (Çaldağ) and **2.8** (Karaçam).

Table 2.7. Cr isotopic compositions and Cr concentrations of the Çaldağ laterite samples.

		MC–ICP–MS							**ICP–MS**				**MC–ICP–MS**				**Reference value[d]** (ICP–OES)
Depth	Sample	$\delta^{50}Cr$	$2\sigma_($	**$\delta^{53}Cr$**	**$2\sigma_{(m)}$**	$\delta^{54}Cr$	$2\sigma_{(m)}$	$^{56}Fe/^{54}Cr$	Cr[a]	1SD[c]	No. of replicates	No. of digests	Cr[b]	1SD[c]	No. of replicates	No. of digests	Cr
m		‰		‰		‰			ppm				ppm				ppm
8	PB3	0.29	0.05	**-0.14**	**0.06**	-0.28	0.05	0.03	22900	1480	7	5	21300	2000	4	2	14900
11	PB6*	-0.34	0.18	**0.17**	**0.08**	0.33	0.17	0.06	31200	5070	6	4	32600	2800	2	2	36000
31	PB4	0.16	0.01	**-0.08**	**0.06**	-0.15	0.01	0.03	5960	1480	6	4	5520	210	2	1	7100
43	PB2	-0.25	0.08	**0.12**	**0.06**	0.24	0.08	0.03	3210	650	8	5	3100	350	4	2	4600
57	PB5	0.22	0.06	**-0.11**	**0.06**	-0.21	0.05	0.25	5950	1370	9	6	5730	650	3	2	5600
60	PB1	0.14	0.14	**-0.07**	**0.07**	-0.13	0.14	0.05	4900	1150	8	4	5120	610	3	2	6600
Standard rock material																	
	JP-1	0.57	0.02	**-0.28**	**0.06**	-0.55	0.02	0.01	2070	100	11	6	2270	–	1	1	n.d.
	DTS2b	0.19	0.12	**-0.09**	**0.07**	-0.18	0.09	0.01	14900	600	5	4	15400	900	2	2	n.d.

* Vein sample within the whole–rock laterite unit.

a Cr concentration determined by single collector ICP–MS (from Chapter 3). Given concentrations are average values that were obtained from multiple individual measurements. The quantity of measurements is given as No. replicates.

b Cr concentration determined by multicollector (MC) ICP–MS by isotope dilution. Given concentrations are average values from multiple individual measurements. The quantity of measurements is given as No. of replicates.

c 1SD refers to the standard deviation of the average concentration from replicate measurements of the samples and the given number describes the deviation of the last digits of the corresponding concentration. The standard deviation (SD) is given as rounded values, so that it only affects the first three significant figures (SF) of corresponding concentrations, deduced from the reproducibility of processed reference materials (i.e. DTS-2b).

d Data are from Brown, 2014, (MSc Thesis, Imperial College London) and were determined by ICP–OES from fused rock powders that were dissolved in a nitric acid solution.

Note $2\sigma(m)$ is the sample standard error of the mean (SEM) of two individual analyses, where $2\sigma(m)= 2SD/(N)0.5$ (N = number of measurements). The standard deviation of a single analysis is smaller than $2\sigma(m)$ and ranges between 0.01 and 0.03‰. The long–term reproducibility of the SRM 979 standard was chosen for samples that have a $2\sigma_{(m)}$ that is lower than 0.06.

Table 2.8. Cr isotopic compositions of the Karaçam laterite samples.

		MC–ICP–MS							ICP–MS				MC–ICP–MS				Reference value[d] (ICP–OES)
Depth	Sample	$\delta^{50}Cr$	$2\sigma_($	**$\delta^{53}Cr$**	**$2\sigma_{(m)}$**	$\delta^{54}Cr$	$2\sigma_{(m)}$	$^{56}Fe/^{54}Cr$	Cr[a]	1SD[c]	No. of replicates	No. of digests	Cr[b]	1SD[c]	No. of replicates	No. of digests	Cr
m		‰		‰		‰			ppm				ppm				ppm
Laterite samples																	
0	KC7	0.16	0.20	**-0.08**	**0.09**	-0.16	0.19	0.05	1290	700	7	4	1230	100	3	2	928
10	KC8*	0.34	0.08	**-0.17**	**0.06**	-0.33	0.07	0.04	2820	197	4	3	2720	80	3	2	5057
12	KC12*	0.75	0.13	**-0.37**	**0.06**	-0.72	0.12	0.02	42100	9100	6	3	39700	400	2	1	44200
13	KC11*	0.30	0.01	**-0.14**	**0.06**	-0.29	0.01	0.04	30200	4600	5	2	33900	900	2	1	41730
15	KC10	0.36	0.58	**-0.29**	**0.11**	-0.35	0.56	0.04	1550	360	7	4	1550	60	2	1	1763
28	KC5	0.22	0.07	**-0.11**	**0.06**	-0.21	0.06	0.03	3150	520	10	5	2920	<10	2	1	5603
35	KC4	0.48	0.10	**-0.23**	**0.06**	-0.46	0.10	0.05	1610	192	7	4	1550	150	3	2	1908
40	KC3	0.39	0.05	**-0.19**	**0.06**	-0.38	0.05	0.05	2600	1200	9	5	2780	<10	2	1	5564
48	KC6	0.82	0.01	**-0.40**	**0.06**	-0.80	0.01	0.07	732	270	6	4	776	1	2	1	799
50	KC2	0.44	0.07	**-0.21**	**0.06**	-0.42	0.07	0.03	1740	600	9	5	1870	<10	2	1	2919
55	KC1	1.26	0.11	**-0.61**	**0.06**	-1.22	0.11	0.03	1860	203	8	4	1790	<10	2	1	2694
Standard rock material																	
	JP-1	0.57	0.02	**-0.28**	**0.06**	-0.55	0.02	0.01	2070	100	11	6	2270	–	1	1	n.d.
	DTS2b	0.19	0.12	**-0.09**	**0.07**	-0.18	0.09	0.01	14900	600	5	4	15400	900	2	2	n.d.

* Vein sample within the whole–rock laterite unit.

a Cr concentration determined by single collector ICP–MS (from Chapter 3). Given concentrations are average values that were obtained from multiple individual measurements. The quantity of measurements is given as No. replicates.

b Cr concentration determined by multicollector (MC) ICP–MS by isotope dilution. Given concentrations are average values from multiple individual measurements. The quantity of measurements is given as No. of replicates.

c 1SD refers to the standard deviation of the average concentration from replicate measurements of the samples and the given number describes the deviation of the last digits of the corresponding concentration. The standard deviation (SD) is given as rounded values, so that it only affects the first three significant figures (SF) of corresponding concentrations, deduced from the reproducibility of processed reference materials (i.e. DTS-2b).

d Data are from Herrington et al. (*in preparation*) and were determined by ICP–OES on fused rock powders that were dissolved in a nitric acid solution.

Note $2\sigma(m)$ is the sample standard error of the mean (SEM) of two individual analyses, where $2\sigma(m)= 2SD/(N)0.5$ (N = number of measurements). The standard deviation of a single analysis is smaller than $2\sigma(m)$ and ranges between 0.01 and 0.03‰. The long–term reproducibility of the SRM 979 standard was chosen for samples that have a $2\sigma_{(m)}$ that is lower than 0.06.

2.5.4 Comparison of Cr concentrations determined by previous authors: Implications for reliability and accuracy of Cr isotopic compositions

Cr concentrations of the Çaldağ and Karaçam nickel laterite samples that were used in this study were previously determined by other authors. The Çaldağ and Karaçam samples were both processed at the National History Museum, London, and the results were used in a Master Thesis by Brown (2014) and by Herrington et al., (*in preparation*). Powdered sample material was fused in platinum crucibles, then sample discs were broken into small glass chips, and eventually dissolved in, respectively, HNO_3 (Çaldağ) and in a mixture of HF and $HClO_4$ (Karaçam). Unfortunately, no further analytical details were given regarding the number of individual replicate measurements, the number of different digests, or the exact conditions of the digestion process (e.g. time, temperature, etc.). Cr measurements were performed with diluted sample aliquots on a *Varian Vista–Pro CCD* Simultaneous ICP–OES.

In this study, a relatively long dissolution procedure was applied comprising treatment of sample powders with a mixture of aqua regia, HF, and $HClO_4$ for about 14 days at about 170 – 180°C. Two international rock standards JP-1 and DTS-2b were processed alongside during the sample dissolutions using the very same procedure as applied for the sample material. Both standard materials consist of chromite–rich peridotite that closely resembles the mineralogy of the parent rock of both laterite weathering profiles and are thus, excellently eligible to serve as reference materials. The here applied procedure was preferred over a dissolution using 'digestion bombs' or fusing of sample powder with subsequent acid dissolution, as some samples contain significant amounts of chromite or Cr–rich magnetite, in particular the Çaldağ samples, which are extremely resistant to common acid dissolution procedures and fusing (e.g. Jain et al., 2000). This generally yields in an incomplete Cr recovery given the common time span for a general rock sample dissolution procedure that usually ranges between 24 and 72 h.

Sample digestion is a critical step in elemental analysis, due to the risk of contamination and analytical losses, contributing for systematic analysis errors or incomplete element recovery (e.g. Fuente and Juàrez, 1995; Zachariadis et al., 1995). Therefore, the aforementioned dissolution procedure was carried out multiple times (**Table 2.8**) for the sample material (number of digests = 2 to 5) as well as for the standard materials (number of digests = 4 to 6) that were used as external reference in order to receive accurate and reliable data for subsequent Cr isotope analyses and Cr ID concentration measurements.

The average Cr concentration (determined by ICP–MS) of JP-1 and DTS-2b is, respectively, 2070±100 ppm and 14900±600 ppm, which is in excellent agreement with certified values from the GeoReM database (Jochum et al., 2007) that range from 1250 to 3300 ppm and from 14053 to 15932 ppm, respectively. Published values for the DTS-2b standard material span a relatively narrow range of about 9 % (RSD), whereas the relatively large Cr concentration range of the JP-1 standard (RSD = 64 %) may result from heterogeneous sample material and/or systematic differences between different analytical methods. For instance, highest reported Cr concentrations of JP-1 were usually determined by XRF, while lower concentrations were measured on ICP–MS.

A comparison between Cr concentrations of the Çaldağ and Karaçam samples that were determined in this study by ICP–MS and by isotope dilution (ID) on the MC–ICP–MS reveals a good overlap and Cr concentrations only deviate slightly with a RSD ≤ 8%, which indicates a reliable degree of accuracy between both methods. However, it has to be noted that this is no general conformation that determined concentrations represent the 'true value', as both methods used aliquots from same stock solutions and thus, represent no independent measurements, rather than they confirm internal consistency between the two analyses.

A comparison between Cr ID concentrations determined during this study and Cr concentrations that were previously determined by Brown (2014) and Herrington et al. (*in preparation*) by ICP–OES, however, show partly large relative standard deviations (RSD; **Fig. 2.4**) of up to 28 % (Çaldağ) and 47 % (Karaçam) between the results.

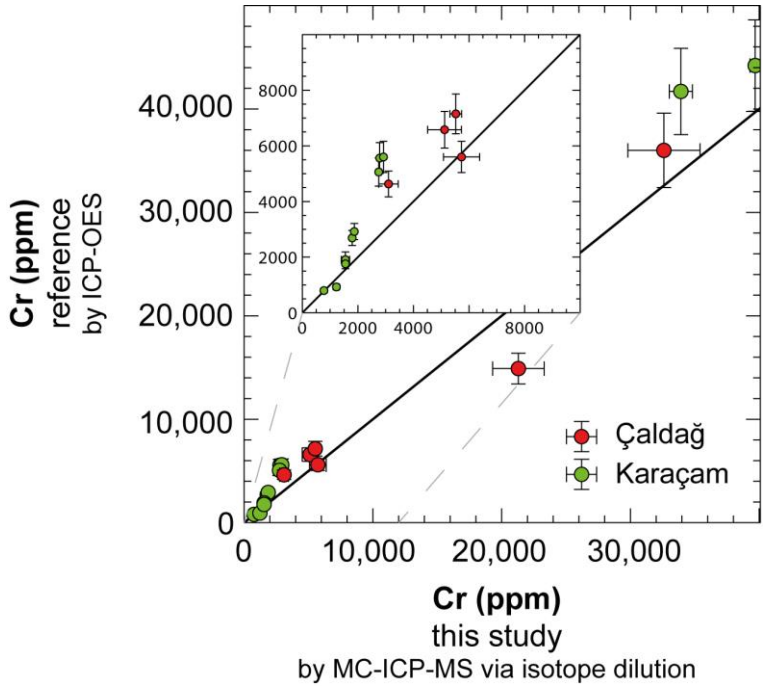

Fig. 2.4. Cr concentrations of the Çaldağ (red circles) and Karaçam (green circles) laterite samples determined by isotope dilution on a MC–ICP–MS (x–axis) over Cr concentrations of the same sample material determined by previous authors (Brown, 2014, MSc Thesis; Herrington et al., (*in preparation*). Errors of shown results are given in 1SD (standard deviation between independent sample measurements; MC–ICP–MS from this study) and 10 % RSD (ICP–OES from previous authors).

Two of the Çaldağ samples (i.e. PB5, PB6) show good agreements between results from the MC–ICP–MS and the ICP–OES analysis with Cr concentrations that overlap within their errors. Remaining four samples show larger relative standard deviations of between 18 and 28%. Samples PB1, PB2, and PB4 have lower and PB3 has a higher Cr concentration compared to previously determined values on the ICP–OES.

Five of the Karaçam samples (i.e. KC4, KC6, KC10, KC11, KC12) show good agreements between results from the MC–ICP–MS and the ICP–OES analysis with Cr concentrations that overlap within their errors. However, 6 samples (i.e. KC1, KC2, KC3, KC5, KC7, KC8) show larger variations of between 20 to 47 % (RSD). There is a general trend that ICP–OES results show higher Cr concentrations compared to results from this study via isotope dilution on MC–ICP–MS.

Possible explanations include the use of heterogeneous sample material for the digestion process (i.e. 'nugget effect'; Agterberg et al., 2010), which is rendered likely, as Ni laterites that developed from peridotite material often show cumulate textures in their parent rock due to the mantle–derived origin. Oxide–rich parts or so called 'nests' in the rock lead to an inhomogeneous spatial distribution of elements, in particular of Fe, Cr, Al, and Ti, in the overlying laterite formation (e.g. Oze et al., 2004; Venturelli et al., 2016) and thus, to analytical errors determining a representative concentration result from a small quantity of sample material (~50 – 200 mg).

Further sources of deviations between Cr concentrations determined by (MC)–ICP–MS and ICP–OES can result from (1) matrix effects and (2) spectral interferences using ICP–OES; the latter being the biggest problem. Spectral overlap of elements, each emitting an average of about 300 spectral lines, can result in cluttered spectra particularly for the transition elements including Cr (Olesik, 1991).

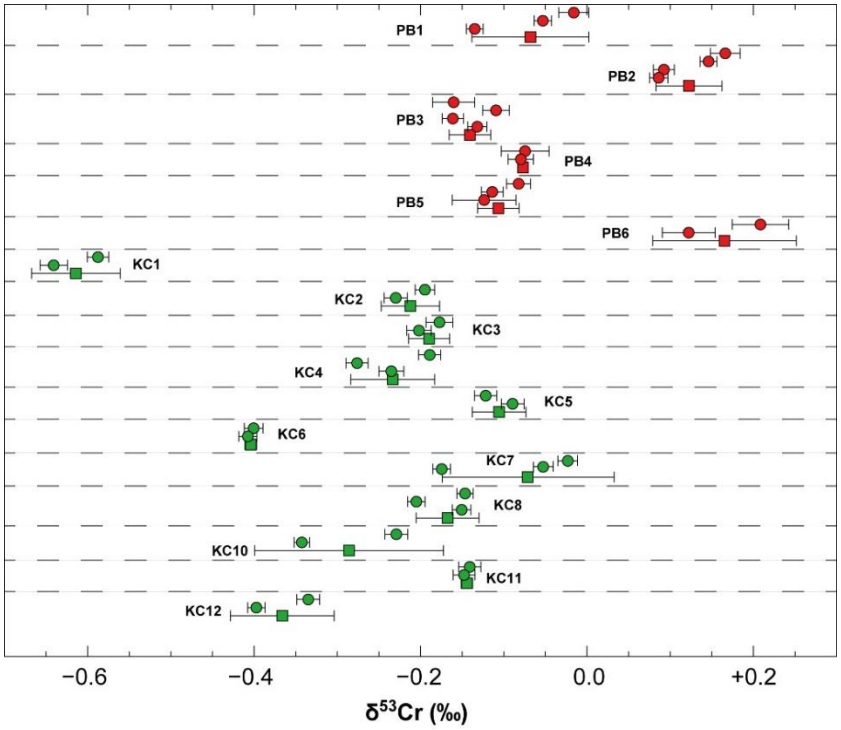

Fig. 2.5. Cr isotope compositions of the Çaldağ (red) and Karaçam (green) samples. Each circle represents an individual Cr isotope measurement, whereas the squares represent the average value with a $2\sigma_{(m)}$ corresponding to the standard error of the mean (SEM) that is calculated according to $2\sigma_{(m)} = 2SD/(N)^{0.5}$ (N = number of measurements). For samples that have a $\delta^{53}Cr$ value with a $2\sigma_{(m)}$ that is lower than 0.06 ‰, the $2\sigma_{(m)}$ was replaced by the long–term reproducibility of the SRM 979 (2SD = 0.06 ‰).

Another possibility includes an incomplete Cr–recovery during the digestion method that was applied in this study, which is, however, unlikely due to the excellent agreement of measured Cr concentrations for reference materials, in particular for DTS-2b, with published values. However, if the dissolution procedure did not lead to complete dissolution of Cr–bearing oxides, in particular not completely dissolving the innermost parts of tiny chromite grains, the here presented Cr isotopic compositions may 'over–represent' the Cr isotope signal of the silicate fraction in respect to the whole–rock mineralogy.

Unweathered chromites generally tend to have a Cr isotopic composition of –0.08±0.06 ‰ (Schoenberg et al., 2008). Assuming that only a fraction of the chromite grains in the processed sample material was fully dissolved; this would shift the Cr isotopic compositions of chromite–rich samples that show a low δ^{53}Cr value towards higher values and therefore, narrowing the total Cr isotope range to a value of –0.08 ‰. Given a generous relative amount of not dissolved chromite–bound Cr of about 30% (that was unaffected by isotope fractionation); this would have a variable effect on Cr isotopic compositions of the Çaldağ and Karaçam samples depending on how close the determined value deviates from –0.08 ‰. This effect would be relatively insignificant, for instance, for samples KC8, KC5, PB5, PB4, and PB1, as their determined δ^{53}Cr value is close to –0.08 ‰ (**Fig. 2.5**). Largest effects would occur for δ^{53}Cr values of KC1, PB6, KC6, and KC12 (**Fig. 2.5**), which show highly fractionated values compared to a δ^{53}Cr value of –0.08 ‰. For example, the 'original δ^{53}Cr value' of KC1 is –0.61 ‰, whereas the 'corrected value' would be –0.45 ‰.

However, although the possible incomplete Cr–recovery from the dissolution procedure may minimises the total Cr isotopic range in the Ni laterite profiles, this has no general effect, which would alter following interpretations and implications for the behaviour of Cr and its isotopes in this study. In the following chapters, the Cr concentrations determined by ICP–MS are used, as (1) there is only a minimal deviation to values determined by isotope dilution (ID) of <10 % RSD, and (2) Cr concentration results from the ICP–MS analysis are based on more independent digests and are therefore, considered to be more robust.

2.6 Results

2.6.1 Choice of a suitable immobile element

Laterite formations are residual weathering products that are characterised by significant losses of mobile elements, such as Mg, Ca, and Na, and relative enrichments of elements that are characterised by a low mobility during lateritisation (e.g. Fe, Al, Ti, Zr, Nb). Commonly, the latter are referred as 'immobile elements' that are retained during the weathering process, as they (1) are hosted in weathering resistant mineral phases (e.g. V, Ti or Zr in Cr–spinel, chromite, zircon, baddeleyite) or (2) are compatible elements that are efficiently taken up into secondary minerals (e.g. Fe or Al in goethite, gibbsite), or (3) form complexes that are insoluble in their oxidised form, such as Th, Sc, and Nb (e.g. Middelburg et al., 1988; Braun and Pagel, 1994; Hill et al., 2000a; Pearce, 2014). The use of immobile marker elements is crucial for the interpretation of gains and losses of other elements, and for the interpretation of Cr isotopic compositions, as regolith weathering profiles that overlie ultramafic substrates experience physical changes, such as shrinking or dilation during their evolution, which has a strong influence on element concentrations.

Ni laterite profiles generally show significant differences between the actual thickness of individual laterite units (e.g. saprolite, limonite) and the original thickness of the progenitor unit from which they formed (Brand et al., 1998; Butt and Cluzel, 2013). The uppermost units of a lateritic profile are strongly depleted in mobile elements, in particular in Mg, which results in solution voids and internal collapse (shrinking). On the other hand, units that are close to the protolith (e.g. saprock, saprolite) usually show no significant change from the original thickness, which is a result of the balance between incipient loss of mobile elements and the formation of secondary low density mineral phases that compensate this loss (i.e. isovolumetric weathering; e.g. Anand and Gilkes, 1984; Braucher et al., 2002). The physical effects of compaction of the weathering profile can be removed by normalising geochemical data to an immobile element (Brimhall et al., 1991; Oh and Richter, 2005; Amundson, 2013). Recent work by Gong et al. (2011) indicates that Ti and Nb are the least mobile elements in modern oxidative weathering environments. However, Ti and Nb concentrations of the laterite samples are low and often below the detection limit. Other elements that are frequently used include Al, Th, Zr, Sc, and V, that are considered to be immobile under most weathering conditions (Eggleton et al., 1987; Braun et al., 1993; Braun and Pagel, 1994; van der Weijden and van der Weijden, 1995; MacLean et al., 1997; Brown et al., 2003; Berger and Frei, 2014; Pearce, 2014; Babechuk et al., 2017).

Fe^{2+} is nearly quantitatively converted to Fe^{3+} during oxidative weathering and is predominantly retained in weathering profiles (Babechuk et al., 2017).

The distribution of an immobile element along the profile needs to resemble the physical effects of laterite formation. The Çaldağ and Karaçam Ni laterite experienced a significant degree of shrinking, in particular in the upper limonite units. Therefore, the concentration of the immobile marker element should increase towards the top of the profile. Furthermore, the choice of the immobile element strongly depends on the individual mineralogical evolution of the laterite profile. For instance, the Çaldağ and Karaçam profiles show a significant degree of re–silification, in particular in the upper parts of the profiles, which implies Si mobility during the lateritisation process. Therefore, Si cannot be used as immobile element. Similarly, the presence of takovite (Al–rich hydrotalcite) demonstrates Al mobility and therefore, prohibits an element normalisation based on Al.

Profiles of Sc, Zr, V, and Fe_2O_3 concentrations in Çaldağ and Karaçam are shown in **Fig. 2.6** and **2.7**, respectively. Sc concentrations are relatively constant with depth in Çaldağ, with a local enrichment within the lower limonite (**Fig. 2.6**). Zr is significantly enriched at the protolith–saprolite boundary, with relatively low Zr abundances in the saprolite and lower limonite, and higher Zr concentrations towards the top of the profile. The abundance of V and Fe_2O_3 steadily increases from the base of the profile towards the top (**Fig. 2.6**). Therefore, V and Fe_2O_3 seem to best reflect the physical shrinking of the profile, particularly in the uppermost parts. Thus hereafter, these elements are utilised as (quasi) immobile maker elements to discuss the Cr geochemistry and the Cr isotopic composition of the Çaldağ laterite samples.

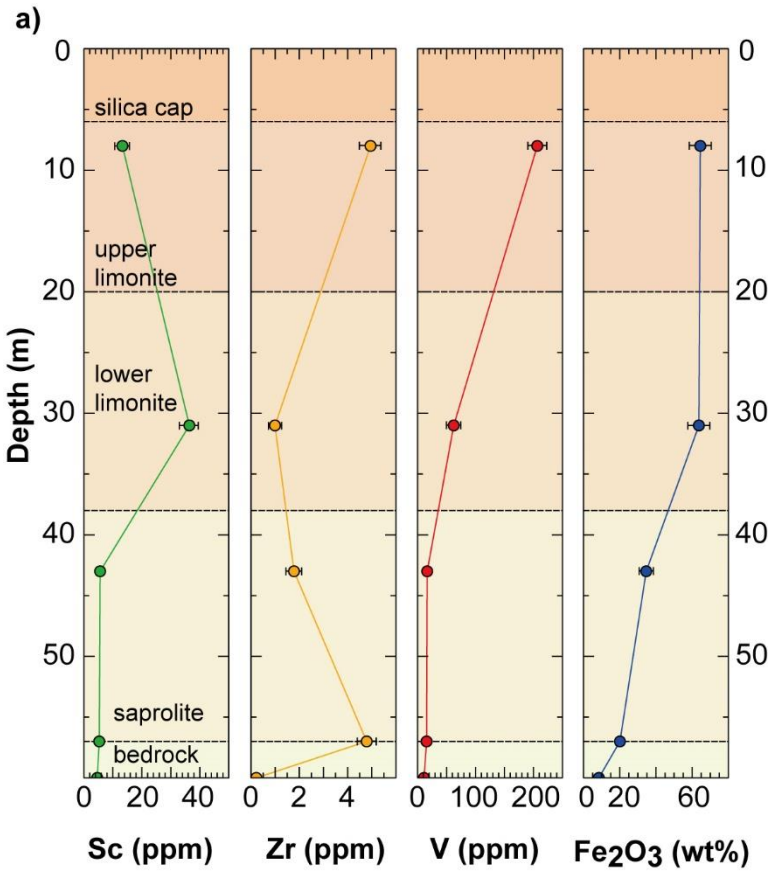

Fig. 2.6. Concentrations of potential immobile marker elements in the Çaldağ and **b)** Ni laterite deposit. Horizontal dashed lines show the boundaries of individual laterite units from the stratigraphic profiles shown in **Fig. 2.2**. The physical evolution of the profile that is mainly characterised by shrinking is best reflected by V and Fe_2O_3 for the Çaldağ profile.

For the Karaçam profile (**Fig. 2.7**), the Fe_2O_3 and Zr concentration best reflect the shrinking of the profile, in particular in the limonite units. The Sc concentration is variable and shows a local anomaly within the saprolite zone (KC6). The presence of takovite with a modal abundance of up to 50 vol% in sample KC6 correlates with an increase in Sc, which indicates Sc mobility similar to Al. The V concentration in the Karaçam profile shows a local depletion in the lower parts compared to the protolith concentration and therefore, may not accurately reflect the physical shrinking of the laterite. Consequently, the Fe_2O_3 and Zr concentration shows the most conservative pattern along the profile and they are considered to be the least mobile elements and will be both used for subsequent discussion of the Cr geochemistry and the Cr isotopic composition of the Karaçam laterite profile.

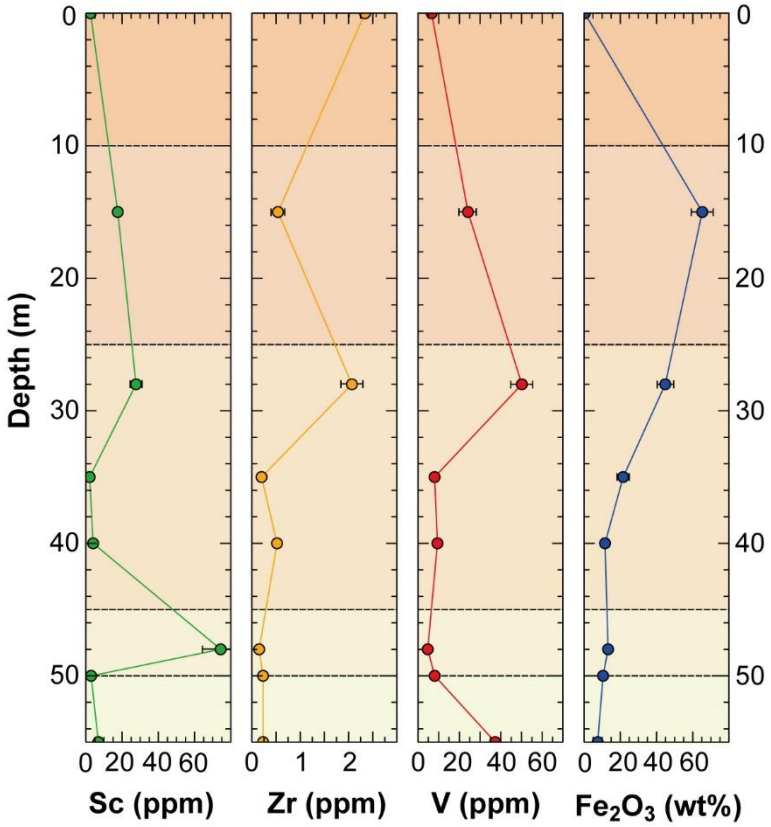

Fig. 2.7. Concentrations of potential immobile marker elements in the Karaçam Ni laterite deposit. Horizontal dashed lines show the boundaries of individual laterite units from the stratigraphic profiles shown in **Fig. 2.3**. The physical evolution of the profile that is mainly characterised by shrinking is best reflected by Zr and Fe_2O_3 for the Karaçam profile.

2.6.2 Degree of lateritisation

There are various geochemical indices that can be used to estimate the degree of weathering in different rock types. The upwards loss of mobile elements in Ni laterites that overlie ultramafic rock material is best quantified by the mafic index of alteration (MIA; Babechuk et al., 2014). The mafic index of alteration (MIA) is a chemical weathering index that considers the redox–sensitivity of Fe and includes the Mg content of the sample, which is of particular importance when estimating the degree of weathering in Mg–rich rocks. Basically, the MIA is an indicator of progressive Mg removal and residual Fe enrichment due to formation of secondary Fe–rich oxides. However, dilution of residual elements by secondary processes, such as re–silification, cannot be monitored.

The Çaldağ and Karaçam Ni laterites developed by surficial weathering under oxidising conditions, hence, Fe is considered to be present as Fe^{3+} (Babechuk et al., 2017) and the MIA calculation for oxidative weathering is used (Babechuk et al., 2014):

$$MIA(ox) = 100 \times \frac{Al_2O_3 + Fe_2O_3}{Al_2O_3 + Fe_2O_3 + MgO + CaO^* + Na_2O + K_2O} \quad (2.2)$$

Concentrations are in molar units and CaO* is total CaO less that in apatite and carbonate. The studied profiles show no presence of apatite and bear only traces of carbonate material, thus it is assumed that CaO* = CaO. Mineralogically, the MIA represents the relative amounts of Fe– and Al–oxyhydroxides compared to other mineral phases and therefore, determines the degree of lateritisation. In ultramafic rocks, low MIA values indicate a high abundance of MgO that is associated with the dominant presence of primary Mg–silicates (e.g. olivine, pyroxene, serpentine) and thus, represent unaltered rock. Increasing index values represent progressively more altered rock material by removal of mobile elements and a value of 100 indicates complete removal of MgO, CaO, Na_2O, and K_2O and the dominant presence of Fe– and Al–bearing minerals.

MIA values of the Çaldağ laterite (**Fig. 2.8a**) increase upwards from the unaltered serpentinite (6 – 17), through the saprolite (36) towards the lower limonite (96) and upper limonite (98), which is typical for deeply weathered laterite profiles and reflects the gradual replacement of primary silicate minerals (i.e. serpentine, chlorite) by secondary clays (i.e. montmorillonite, nontronite, asbolane) and oxyhydroxide phases (i.e. goethite). Hydration and subsequent decomposition of Mg–silicates lead to the loss of soluble elements, such as Mg, Ca, and Na, and to higher MIA values. The characteristic Mg–discontinuity (sharp drop of MgO concentration) is situated at the saprolite–lower limonite boundary. The high MIA value of the lower and upper limonite units indicates virtually complete removal of mobile elements, which demonstrates a strong degree of weathering that is mineralogically expressed by the dominant presence of goethite and the absence of Mg–silicates.

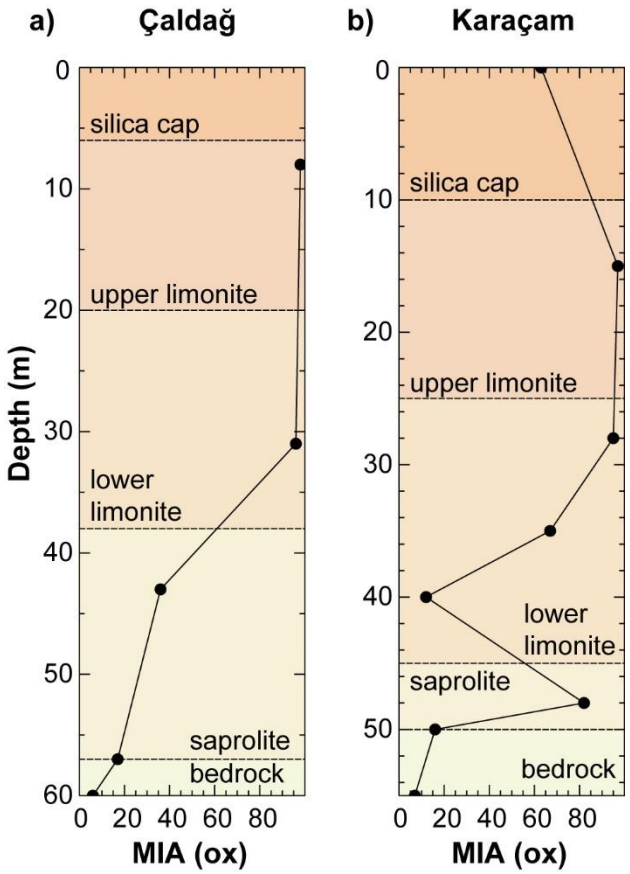

Fig. 2.8. The mafic index of alteration (MIA) in the **a)** Çaldağ and **b)** Karaçam Ni laterite. Horizontal dashed lines show the boundaries between individual laterite units from the stratigraphic profiles given **Fig. 2.2** and **2.3**.

MIA values in the Karaçam laterite (**Fig. 2.8b**) are more variable, with a protolith value of 7 and a saprolite value of between 16 and 82. The high MIA value of KC6 (MIA = 82) results from the high amount of Ni–bearing Al–rich takovite, whose formation is associated with Al mobility (Taylor, 1984). The lower and upper limonite units show a relatively large MIA range of between 12 and 97, with a sharp increase in MIA values in the lower limonite and a narrow zone with very high MIA values (95 – 97) towards the upper limonite. Due to the presence of takovite in the saprolite, the position of the Mg–discontinuity is ambiguous. However, it is likely located in the upper part of the lower limonite. Similarly to the Çaldağ laterite samples, increasing MIA values reflect the gradual replacement of primary Mg–silicates (i.e. lizardite) by secondary clays (i.e. montmorillonite, kaolinite, takovite, nontronite, asbolane) and Fe–rich oxides (i.e. goethite) in the Karaçam laterite. The chromite–mottled silica cap shows a moderate MIA value of 63, which is associated with an elevated CaO content that may result from aeolian inputs.

In summary, the Çaldağ and Karaçam Ni laterite weathering profiles both developed from lizardite–rich serpentinite and show a high loss of mobile components that led to significant clay and Fe–oxide mineralisation and the formation of deep weathered regolith profiles. However, the presence of takovite and a more variable MIA trend of the Karaçam laterite indicate a more complex evolution of the profile, probably due to influx of late stage low pH fluids that induced re–cycling of elements such as Ni, Al, Cr, and Sc *(*Herrington et al., *in preparation*.)

2.6.3 Cr behaviour in the weathering profile

Chromium concentrations in the Çaldağ laterite profile generally increase from the base towards the top (**Fig. 2.9a**) with Cr concentrations of between 4900 and 5950 ppm in the protolith, and a slightly lower Cr concentration of 3210 ppm in the saprolite. The lower limonite has a Cr concentration of 5960 ppm that drastically increases towards the upper limonite (22900 ppm Cr). The clay–rich vein sample (PB6) that is located within the upper limonite is strongly Cr–enriched and shows a concentration of 31200 ppm Cr. The general increase in Cr towards the top of the profile can be attributed to (1) the weathering resistance of chromite, which is the major Cr–bearing mineral in the laterite, and (2) the shrinking of the profile that leads to residual enrichment of Cr in the upper parts of the laterite. However, Cr concentrations normalised to V and Fe_2O_3 (**Fig. 2.10a**) indicate that Cr is significantly depleted in the saprolite and throughout the upper parts of the weathering profile, with a relative Cr loss of up to 84 % in respect to the unaltered bedrock. The high Cr loss results from effective Cr removal from Mg–silicates and suggests Cr mobilisation from chromite, which is shown by SEM–images that indicate progressive dissolution of individual chromite crystals (**Fig. 2.11**) similar to the observations of Garnier et al., (2008). The vein sample PB6 is relatively enriched in Cr by 110 % relative to V, and 500 % relative to Fe_2O_3. The vein mainly consist of clays and a small portion of relict chromite, hence the high Cr content indicates significant Cr retention in secondary clays.

Cr concentrations in the Karaçam laterite range from 732 ppm to 3150 ppm (**Fig. 2.9b**) and are significantly lower than Cr concentrations in the Çaldağ laterite. The Cr content within the protolith unit is relatively stable (1740 – 1860 ppm), slightly decreases in the takovite–rich sample (732 ppm) in the saprolite and increases towards the lower limonite, which shows a slight Cr enrichment (1610–3150 ppm) compared to the bedrock. The upper limonite is slightly Cr depleted with respect to the bedrock (1550 ppm Cr), and the silica cap has a Cr concentration of 1290 ppm.

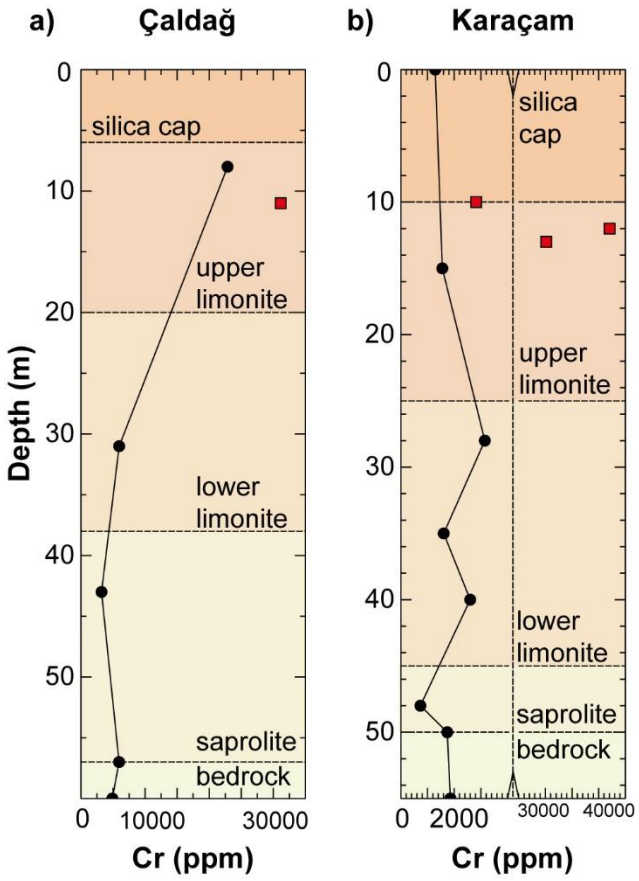

Fig. 2.9. Profile of Cr concentrations in the **a)** Çaldağ and **b)** Karaçam Ni laterite deposits. Black circles represent bulk rock laterite samples and red squares are vein samples. The x–axis is broken at 4000 ppm (vertical dashed line) and starts again at 25000 ppm (b). Horizontal dashed lines show the boundaries between individual laterite units from the stratigraphic profiles given in **Fig. 2.2** and **2.3**.

The clay–rich vein samples KC11 and KC12 from the upper parts of the weathering profile are strongly Cr–enriched, with Cr concentrations respectively, of 3.02 and 4.21 wt%. The vein sample KC8 predominantly consists of quartz and has a moderate Cr concentration of 2820 ppm. Cr concentrations normalised to Fe_2O_3 and Zr reveal a general depletion in Cr within the saprolite unit, and a Cr depletion up to 90% in the lower limonite compared to the bedrock (**Fig. 2.10b**). The clay–veins are significantly Cr enriched, from 500% (Zr normalised) to 1600% (Fe_2O_3 normalised) higher than the bedrock value, which demonstrates significant Cr mobilisation from the breakdown of primary Mg–silicates as well as suggesting input of Cr from chromite dissolution.

Cr is a compatible element that is mainly hosted in the oxide fraction (e.g. chromite, Cr–bearing magnetite) of ultramafic rocks with a minor amount of Cr that is incorporated in Mg–silicates (olivine, pyroxene) and their metamorphic equivalents (serpentine minerals). Chromite is present in both laterite profiles as a major Cr–bearing mineral, however, it is likely that the majority of mobile Cr was derived from the breakdown of primary Cr–bearing silicates, as chromite weathering is sluggish and chromite can be found even at the top of the profile, in particular in the chromite–mottled silica cap of the Karaçam laterite. Hence, incipient Cr loss in units below the Mg–discontinuity (e.g. protolith, saprolite, ± limonite) is interpreted to mainly stem from silicate–derived Cr, whereas Cr loss in units that are situated above the Mg–discontinuity may include the sluggish dissolution of Cr–bearing oxides. However, in the presence of Mn–oxides, chromite weathering can be significantly enhanced (Oze et al., 2007; Hausladen and Fendorf, 2017) and, as Cr^{6+} is highly mobile, this may contribute to significant loss of Cr in both weathering profiles.

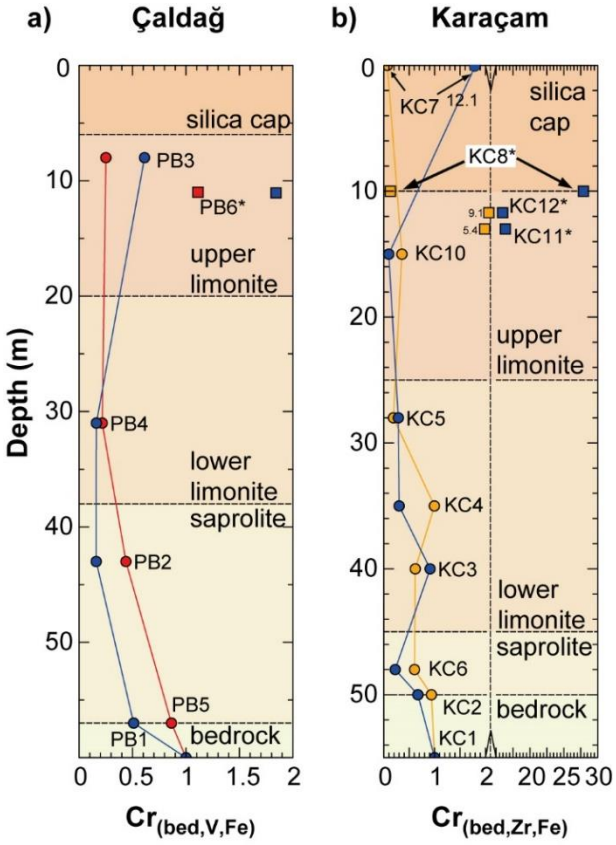

Fig. 2.10 a) Cr concentration normalised to V (red) and Fe_2O_3 (blue) in the Çaldağ weathering profile. **b)** Cr concentration normalised to Zr (yellow) and Fe_2O_3 (blue) in the Karaçam weathering profile. Horizontal dashed lines show the boundaries of individual laterite units from the stratigraphic profiles shown in **Fig. 2.2** and **2.3**. The asterisks mark vein material that was emplaced in the laterite.

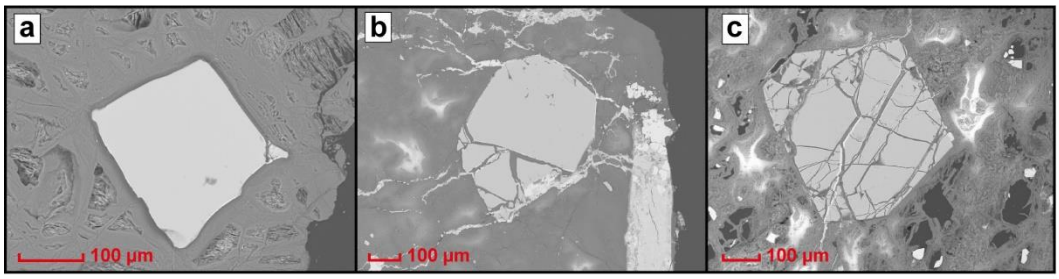

Fig. 2.11. SEM pictures illustrating the progressive dissolution of chromite from the **a)** protolith, to the **b)** saprolite, and the **c)** limonite of the Çaldağ laterite samples. The scale bars equal 100 µm.

2.6.4 Cr isotopes

The change in the Cr isotopic composition with depth in the Çaldağ and Karaçam weathering profiles is shown in **Fig. 2.12**. There is relatively little variation in $\delta^{53}Cr$ in the Çaldağ laterite weathering profile, ranging from $\delta^{53}Cr$ = –0.14±0.06 ‰ in the most weathered sample PB3 from the upper limonite (MIA = 98) to $\delta^{53}Cr$ = 0.12±0.06 ‰ in the saprolite sample PB2 (MIA = 42). The serpentinite protolith has a $\delta^{53}Cr$ value of –0.07±0.07 ‰, which lies within the range of the Cr isotope igneous inventory ($\delta^{53}Cr$ = –0.12±0.10 ‰; Schoenberg et al., 2008, 2016). Most laterite samples have a $\delta^{53}Cr$ value that is lower than the bedrock value, which indicates preferential loss of heavy Cr isotopes under oxidative weathering conditions; in support of this, normalised Cr concentrations in the laterite samples are lower than those in the protolith (**Fig. 2.10a**). The saprolite sample PB2 and the clay–rich vein sample PB6 have positive $\delta^{53}Cr$ values of, respectively, 0.12±0.06 ‰ and 0.17±0.08 ‰, higher than the bedrock $\delta^{53}Cr$ value. The clay vein (PB6) has a high Cr concentration and is strongly Cr enriched, which indicates retention of mobile Cr with a positively fractionated $\delta^{53}Cr$ value. The saprolite sample (PB2) is relatively Cr depleted compared to the bedrock. However, this does not exclude addition of Cr from a fluid phase, as the initial Cr loss in the saprolite could have been higher than indicated by the normalised Cr abundance in PB2.

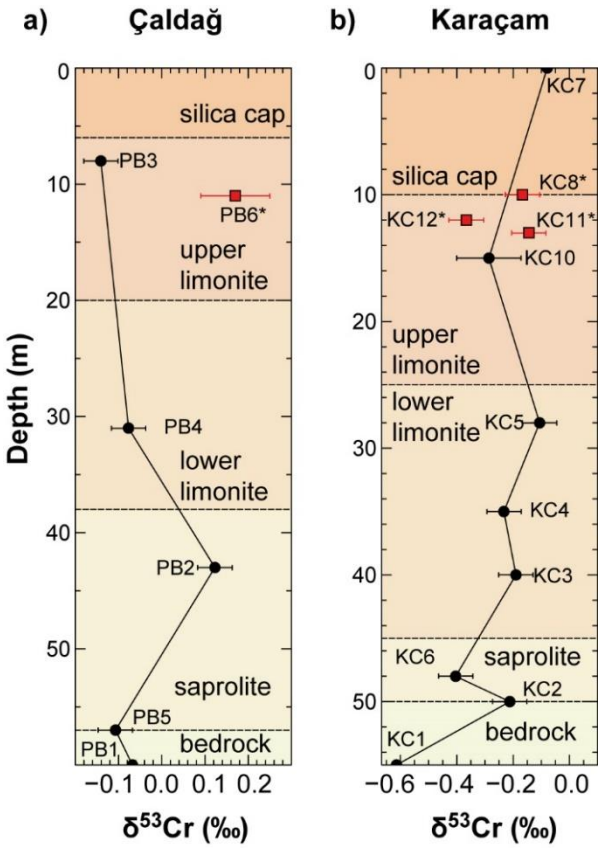

Fig. 2.12. Profiles of Cr isotopic compositions in the **a)** Çaldağ and **b)** Karaçam Ni laterite deposits. Bulk rock samples are black circles and vein samples are red squares.

The range of $\delta^{53}Cr$ values in the Karaçam laterite profile is higher than in the Çaldağ laterite, from $\delta^{53}Cr$ = –0.61±0.06 ‰ in the protolith (KC1) to –0.08±0.09 ‰ in the silica cap (KC7). The $\delta^{53}Cr$ value of the protolith is significantly lower than the Cr isotopic composition of the igneous inventory (Schoenberg et al., 2008, 2016). Low $\delta^{53}Cr$ values are commonly interpreted to be indicative of loss of isotopically heavy Cr, however, the protolith has a relatively low MIA value of 7, which may suggests that the low $\delta^{53}Cr$ value originates from secondary processes prior to weathering (see **Chapter 2.7**). The saprolite unit that overlies the protolith has $\delta^{53}Cr$ values of between –0.40 and –0.21 ‰, and the lower limonite shows $\delta^{53}Cr$ values of between –0.23 and –0.11 ‰. The upper limonite sample KC10 has a slightly lower $\delta^{53}Cr$ value of –0.29±0.11 ‰ compared to the underlying lower limonite, and the uppermost silica–rich cap has $\delta^{53}Cr$ = –0.08±0.09 ‰ (KC7). Vein samples KC8, KC11, and KC12 that are emplaced in the upper limonite show $\delta^{53}Cr$ values of between –0.37 and –0.14 ‰. The quartz vein KC8 ($\delta^{53}Cr$ = –0.17±0.06 ‰) and the clay–rich vein KC11 ($\delta^{53}Cr$ = –0.14±0.06 ‰) are slightly enriched in heavy Cr compared to the enclosing upper limonite unit ($\delta^{53}Cr$ = –0.29±0.11 ‰), whereas the other clay–rich vein KC12 has a lower $\delta^{53}Cr$ value of –0.37±0.06 ‰.

2.7 Discussion

Low $\delta^{53}Cr$ values of modern regolith profiles that overlie ultramafic substrates are usually interpreted to reflect weathering under oxidising conditions, which is common for weathered continental samples and this trend has been documented in numerous studies (e.g. Crowe et al., 2013; Berger and Frei, 2014; Frei et al., 2009, 2014). Corresponding Cr^{6+}–rich fluids are generally enriched in heavy Cr isotopes compared to the residual Cr^{3+} in the rock (e.g. Frei et al., 2014; Novak et al., 2017). The enrichment of heavy isotopes in the Cr^{6+} pool during oxidative weathering is in principle a result of two processes.

Firstly, Cr isotopes directly fractionate during the oxidation of Cr^{3+} to Cr^{6+}. This process is poorly understood, however, it likely has a large kinetic component (Zink et al., 2010). Laboratory experiments show a general trend of heavy Cr enrichment in the Cr^{6+} pool and residual Cr^{3+} fractions roughly plot along a decreasing Rayleigh–type trend during Cr oxidation (Zink et al., 2010).

Secondly, Cr isotopes fractionate when solid Cr^{3+} and aqueous Cr^{6+} stay in contact (isotope exchange) for a long time. This process is driven by equilibrium isotope fractionation and is considerably well investigated. It can lead to significant heavy Cr isotope enrichment in the Cr^{6+} pool of up to 5.6 ‰ (Schauble et al., 2004; Wang et al., 2015). Equilibrium isotope fractionation is potentially important in systems where Cr^{3+} and Cr^{6+} stay in contact for several years or longer (Wang et al., 2015). The impact of Cr isotope exchange in modern weathering profiles remains unclear, however, it may be not significant, as seasonality leads to phases of evaporation and a low or fluctuating water table (Thorne et al., 2012), thus higher parts of the profile will periodically dry out and may not stay in contact with Cr–rich fluids over a long period of time (several years).

Both fractionation processes lead to low $\delta^{53}Cr$ values in the weathered rock and high $\delta^{53}Cr$ values in the corresponding Cr–rich fluid. Initial Cr isotope variations that originated by Cr^{3+} oxidation may be overprinted by later isotope exchanges between solid Cr^{3+} and aqueous Cr^{6+}(Wang et al., 2015).

2.7.1 Çaldağ

Most of the Çaldağ laterite samples have negative $\delta^{53}Cr$ values that are lower than the $\delta^{53}Cr$ value of the bedrock (PB1). The silicified limonite (PB3) at the top of the weathering profile is the most weathered laterite sample (MIA = 98) and shows the lowest $\delta^{53}Cr$ value of –0.14±0.06 ‰. However, the total Cr isotope range among laterite samples that have lower $\delta^{53}Cr$ values than the bedrock is only 0.07 ‰. This extremely narrow Cr isotope range indicates a limited isotope fractionation during oxidative weathering, as experimental studies imply a Cr isotope fractionation during oxidation between 0.2 and 0.7 ‰ (Bain and Bullen, 2005; Ellis et al., 2008; Zink et al., 2010). Furthermore, this indicates that a significant portion of mobilised Cr did not fractionate during oxidative Cr removal. Possible reasons that can lead to a limited Cr isotope fractionation include (1) the so–called 'rind effect', where each micro–layer of Cr^{3+}–(oxy)hydroxide particles is essentially completely oxidised, which 'shields' the particle surface and hampers isotope exchange, (2) a small amount of surface active Cr^{3+} and a low abundance of adsorbed Cr^{6+} on Cr^{3+}–bearing mineral surfaces (e.g. Wang et al., 2015), and (3) low pH conditions that increase E_h, which leads to a lower Cr oxidation rate and thus, likely hamper Cr isotope fractionation (e.g. Berger and Frei, 2014).

In general, a small to negligible Cr isotope fractionation is consistent with the weathering resistivity of chromite that prevents mobilisation and subsequent oxidation of large quantities of Cr^{3+}. However, Cr normalised concentrations indicate a significant Cr loss of up to 80% upwards the profile that generally correlates with high MIA values; thus it is likely that Cr was lost from phases in addition to Mg–silicates. SEM pictures of individual chromite crystals from different laterite units imply that breakdown of chromite is rather slow, but may account for a distinct fraction of mobile Cr (**Fig. 2.11**). The upper limonite (PB3) has lost between 39 and 75% of its Cr compared to the bedrock, which implies that the sluggish breakdown of chromite accounts at least for a fraction of the Cr that was lost during laterite formation.

Chromite weathering can be drastically enhanced in the presence of Mn–oxides (Oze et al., 2007; Hausladen and Fendorf, 2017) that are generally abundant in nickel laterites (Butt and Cluzel, 2013). Lab experiments demonstrated accelerated dissolution of chromite in the presence of birnessite (Mn^{4+}–oxide) and subsequent oxidation of Cr^{3+} to aqueous Cr^{6+} (Oze et al., 2007). The experiments mimicked chromite dissolution in serpentine soils under ambient temperatures at pH of between 3 and 8 in an acetate buffered solution. The results show a production of aqueous Cr^{6+} within hours with formation rates of between 0.5 and 6.2 nM h^{-1}, whereas chromite dissolution in the absence of birnessite yielded insignificant Cr mobilisation over 450 h.

This implies that chromite weathering may represent a relatively constant, but more diffuse long–term source of Cr that persists during the entire course of laterite formation. Therefore, it is likely that chromite dissolution contributed to the overall Cr loss of the laterite during the weathering process.

The saprolite sample (PB2) and the vein sample (PB6) have positive $\delta^{53}Cr$ values of, respectively, 0.12 and 0.09 ‰, which indicates incorporation of Cr from a fluid phase that was enriched in heavy Cr isotopes. Cr mobilisation due to the breakdown of Mg–silicates and Cr–bearing oxides leads to release of mobile and isotopically heavy Cr^{6+} that can migrate downwards the weathering profile through local fractures and fissures that have formed during the alteration process. It is likely that some parts of the weathering profile that allow through–flow of mobile Cr have reacted with this Cr pool and are not only affected by loss of isotopically heavy Cr. Therefore, all parts of the profile can potentially be affected by secondary processes including sorption and reductive immobilisation of Cr and/or interaction with mobile Cr from overlying regolith units down to the weathering front at the bedrock transition. Hence, only the uppermost part of a weathering profile is likely to reflect the first–order Cr isotope signature due to oxidative weathering. The silicified limonite sample PB3 belongs to the uppermost laterite horizon of the Çaldağ profile and although the limonite has experienced secondary re–silification processes, it can be assumed that this sample has been least affected by secondary processes that altered the Cr isotopic composition.

Under the premise that the upper limonite sample PB3 and the bedrock sample PB1 were not affected by secondary processes that disturbed the first–order Cr isotope signature, Cr isotope fractionation during oxidative weathering can be approximated by a Rayleigh–type trend for residual Cr^{3+} fractions in the profile, similar to Zink et al. (2010), and an 'effective fractionation factor under natural conditions' can be estimated. The per cent loss of Cr (relative to V and Fe_2O_3) in PB3 is recast as the fraction of Cr^{3+} (fCr^{3+}_s) that remains in the laterite after the loss of aqueous Cr^{6+} and ranges from 0.25 (V normalised) to 0.61 (Fe_2O_3 normalised). Assuming a Rayleigh–type behaviour for this model calculation, then the fractionation factor between aqueous Cr^{6+} and solid Cr^{3+}, which is defined as $\Delta^{53/52}Cr_{(Cr^{6+}-Cr^{3+})} = \varepsilon \approx 1000 \cdot \ln\alpha$, is 0.07 to 0.10 ‰ (**Fig. 2.13**).

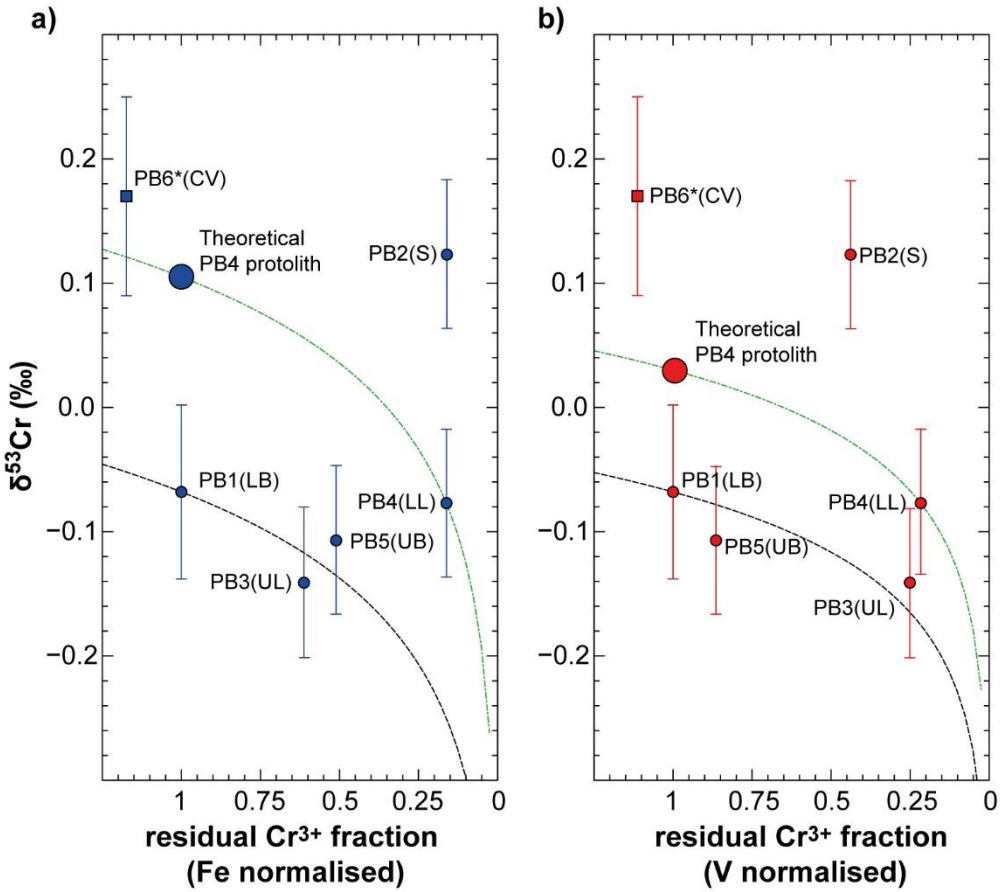

Fig. 2.13. $\delta^{53}Cr$ vs. Cr concentration normalised to **a)** V and **b)** Fe for the Çaldağ laterite. The black dotted lines represent modelled Rayleigh fractionation curves between the most weathered sample (PB3) and the least weathered sample (PB1) to determine the effective Cr fractionation factor. The green dotted lines are modelled Rayleigh fractionation curves that define a theoretical progenitor of sample PB4, assuming that this sample was not affected by secondary Cr processes (*see text*). B = bedrock, LB = lower bedrock, UB = upper bedrock, S = saprolite, LL = lower limonite, UL = upper limonite, SC = silica cap, CV = clay vein, QV = quartz vein.

The fractionation factor is lower than the experimentally determined value of Zink et al. (2010) that ranges between 0.2 and 0.6 ‰, however it can be argued that Cr oxidation and isotope fractionation may be less efficient in natural settings due to effects that limit Cr isotope fractionation, such as the 'rind effect', a low abundance of surface active Cr^{3+}, or a low concentration of aqueous Cr^{6+}. Furthermore, the presence of oxidants different from H_2O_2 may also have a strong impact on the Cr isotope fractionation. In nature, Cr oxidation is driven by manganese–oxides that are considered as the most important oxidising agents during rock weathering (Richard and Bourg, 1991; Economou-Eliopoulos et al., 2014).

Moreover, type and concentration of MnO_2 presumably affect the Cr oxidation reaction pathway (Silvester et al., 1995) and $\delta^{53}Cr$ values of aqueous Cr^{6+} vary between –2.5 and 0.7 ‰ (Bain and Bullen, 2005) during Cr^{3+} oxidation experiments using birnessite (δ–MnO_2), which highlights the complex nature of Cr isotope fractionation during Cr oxidation. However, it is unlikely that isotopically light Cr^{6+} with $\delta^{53}Cr$ as low as –2.5 ‰ is relevant for the global Cr cycle, as modern rivers are either richer in heavy Cr isotopes or overlap with the Cr isotopic composition of the bedrock source (Frei et al., 2014; D'Arcy et al., 2016).

The vein sample PB6 is a product of secondary in–situ clay formation and is enriched in Cr relative to the bedrock, by between 110 and 500 % (respectively, relative to V and Fe_2O_3). The Cr content of this sample likely consists of (1) residual Cr with a Cr isotopic signature that is similar to the enclosing limonite unit (PB3), and (2) Cr that was mobilised during weathering of the upper parts of the profile and was transported downwards through the veins. The Cr isotopic composition of the mobile Cr pool can be estimated by mass balance as follows:

$$\delta^{53}Cr(WR) = fCr_{res,norm} \times \delta^{53}Cr(res) + fCr_{mobile,norm} \times \delta^{53}Cr(mobile) \quad (2.3)$$

with:

$\delta^{53}Cr(WR) = Cr\ isotope\ composition\ of\ the\ whole\text{–}rock\ (WR)$

$\delta^{53}Cr(res) = Cr\ isotope\ composition\ of\ residual\ (initial)\ Cr$

$\delta^{53}Cr(mobile) = Cr\ isotope\ composition\ of\ mobile\ (external)\ Cr$

$fCr(res)_{norm} = fraction\ of\ resdiual\ (initial)\ Cr$

$fCr(mobile)_{norm} = fraction\ of\ mobile\ (external)\ Cr$

Rearranging equation (2.3) to $\delta^{53}Cr(mobile)$ and assuming:

$$fCr(res)_{norm} + fCr(mobile)_{norm} = fCr(total)_{norm} \quad (2.4)$$

yields in:

$$\delta^{53}Cr(mobile) = \frac{fCr(total)_{norm} \times \delta^{53}Cr(WR) - fCr(res)_{norm} \times \delta^{53}Cr(res)}{fCr(total)_{norm} - fCr(res)_{norm}} \quad (2.5)$$

with:

$$fCr(total)_{norm} = fCr(PB6)$$

$$\delta^{53}Cr(WR) = \delta^{53}Cr(PB6)$$

$$fCr(res)_{norm} = fCr(PB3)$$

$$\delta^{53}Cr(res) = \delta^{53}Cr(PB3)$$

Equation 2.4 yields in a δ^{53}Cr value of the mobile Cr fraction (*$\delta^{53}Cr(mobile)$*) between 0.21 and 0.26 ‰, depending on which element is utilised as the immobile element. These values are higher than the predicted initial Cr isotopic composition of Cr^{6+} (0.00 – 0.03 ‰) using an effective fractionation factor of $\Delta^{53/52}Cr_{(Cr^{6+}-Cr^{3+})}$ = ε =0.07 to 0.10 ‰ and starting from the Cr isotopic composition of unweathered bedrock sample PB1 (δ^{53}Cr = –0.07 ‰). This implies that a part of the mobile Cr^{6+} pool was retained during the passage downwards through the weathering profile, likely by reductive immobilisation that further increases the δ^{53}Cr value of the remaining Cr^{6+} in the mobile Cr pool (Ellis et al., 2002, 2004; Jamieson-Hanes et al., 2012; Kitchen et al., 2012; Šillerová et al., 2014).

The Cr isotopic composition of the saprolite sample PB2 may reflect this successive increase of the δ^{53}Cr value of the Cr^{6+} pool as it is transported through the profile. The saprolite unit is strongly enriched in Ni and developed economic grades during the lateritisation process. The enrichment is a result of Ni leaching and translocation from higher parts of the profile and subsequent retention on goethite (Beukes et al., 2000; Gleeson et al., 2004). The clay–rich veins (e.g. sample PB6) that developed in the laterite formation serve as pathways that are responsible for the supergene Ni enrichment in the saprolite. Cr translocation may occur in the same way as Ni enrichment, with partial retention of Cr as it is transported through the profile. Cr retention may occur due to reduction of mobile Cr^{6+} to Cr^{3+} by biotic (Losi et al., 1994) or abiotic agents (Buerge and Hug, 1997; Patterson et al., 1997; Sedlak and Chan, 1997). Bacteria may be the principal means by which Cr^{6+} is converted to Cr^{3+} in aerobic environments, such as in well–drained laterites and soils (Fendorf et al., 2000). In the saprolite horizon, a significant amount of Cr from the percolating Cr^{6+} pool may had been reductively immobilised, which has led to a relatively high δ^{53}Cr value of 0.16 ‰ in the saprolite sample PB2. Sorption of isotopically heavy Cr^{6+} is rendered unlikely due to the high pH conditions in this horizon (Ajouyed et al., 2010).

The lower limonite sample PB4 has a $\delta^{53}Cr$ value of –0.08±0.06 ‰ that is indistinguishable from the $\delta^{53}Cr$ value of the bedrock sample PB1 ($\delta^{53}Cr$ = –0.07±0.07 ‰). The lower limonite (PB4) has a high MIA value of 96, which indicates a virtually complete loss of mobile elements due to oxidative weathering. The lack of a Cr isotopic response to weathering can be explained in a number of ways.

Firstly, the loss of 84% of the Cr compared to the protolith value may be due to ligand exchange reactions between Cr–hydroxides and Cr–chlorides (e.g. between $Cr(OH)_2^+$ and $CrCl_2^+$), which increases the mobility of Cr^{3+} without Cr oxidation (Katz and Salem, 1993). However, ligand exchange experiments in the Cr^{3+}–Cl–H_2O system suggest that ligand exchange results in Cr isotope fractionation of up to 2‰ between the different Cr^{3+} species that can be expected to change the $\delta^{53}Cr$ value of the bulk rock (Babechuk et al., 2018), which is not observed for sample PB4.

Secondly, PB4 is possibly derived from a bedrock unit that had a $\delta^{53}Cr$ value that was different from the $\delta^{53}Cr$ value of the unaltered bedrock sample PB1. Seafloor alteration can account for mineralogical and chemical heterogeneities of the protolith, such as patchy distribution of Fe–oxides and epidote, and localised K enrichments (Babechuk et al., 2013). Seafloor alteration has to be considered as a potential mechanism to alter the Cr chemistry of the protolith, as it can result in redistribution of Cr from primary magmatic minerals into phases, such as chlorite (e.g. Schandl and Wicks, 1993; Barnes, 2000; Oze et al., 2004; Merlini et al., 2009), and this is likely accompanied by a change of the Cr isotopic composition of the protolith (Farkaš et al., 2013). Assuming the same Cr isotope fractionation factor, $\Delta^{53/52}Cr_{(Cr^{6+} - Cr^{3+})} = \varepsilon$= 0.07‰ to 0.10‰, the $\delta^{53}Cr$ value of the unaltered bedrock unit from which PB4 theoretically formed would have been between 0.03 and 0.10 ‰ (**Fig. 2.13**). In support of this, several authors (Farkaš et al., 2013; Wang et al., 2016; Novak et al., 2017) have shown that serpentinised ultramafic rocks can have positive $\delta^{53}Cr$ signatures.

However, a third explanation is that PB4 represents a mixture between a first order weathering Cr isotope signature generated by preferential loss of heavy Cr isotopes from a bedrock with a $\delta^{53}Cr$ value similar to PB1, followed by Cr uptake from a mobile Cr pool enriched in heavy Cr isotopes that was produced in the overlying laterite unit. This latter idea is supported by the presence of isotopically heavy Cr enriched samples (PB2, PB6) in the profile, as there is no clear evidence from the chemistry or mineralogy of PB4 that indicates a heterogeneous bedrock composition.

2.7.2 Karaçam

The regolith units (saprolite, limonite) in the Karaçam weathering profile generally have higher $\delta^{53}Cr$ values (average $\delta^{53}Cr$ = –0.22 ‰) than the underlying protolith unit that has an unusually low $\delta^{53}Cr$ value of –0.61±0.06 ‰. Despite its low $\delta^{53}Cr$ value, the protolith appears fresh in hand specimen and shows only minor alteration features, such as traces of secondary clays and Fe–hydroxides. A MIA value of 7 for the protolith indicates that the majority of the Mg–silicates in the rock are unaffected by oxidative weathering. However, the lack of Cr in the primary silicate fraction (**Table 2.9**) of the rock implies that Cr may have been lost during incipient weathering; if this is the case then the low $\delta^{53}Cr$ value of the bulk rock mainly reflects the Cr isotopic composition of the Cr–bearing oxide fraction (i.e. chromite). However, chromite–rich rocks tend to have $\delta^{53}Cr$ values of about –0.08±0.06 ‰ (Schoenberg et al., 2008), suggesting that heavy Cr isotopes may be preferentially lost from silicate bound Cr prior to exposure at the Earth`s surface, as chromite in the protolith sample shows no signs of weathering induced decomposition.

The possible absence of Cr in primary Mg–silicates (i.e. lizardite) in KC1 lowers the Cr isotopic composition of the rock of about 0.15 ‰, assuming a $\delta^{53}Cr$ value of 0.14 ‰ for Cr–bearing serpentine (Farkaš et al., 2013) and a generous modal Cr abundance of about 20 % in the silicate fraction. Mass balance considerations yield a $\delta^{53}Cr$ value of –0.46 ‰ for the protolith, which is much lower than reported for unweathered serpentinite. This raises the possibility that there is an, as yet unidentified, Cr reservoir that is depleted in heavy Cr isotopes. Several studies have reported serpentinised mantle xenoliths with positive $\delta^{53}Cr$ values (e.g. Farkaš et al., 2013; Wang et al., 2016; Novak et al., 2017) and it has been suggested that seafloor serpentinisation leads to increasing $\delta^{53}Cr$ values with increasing degree of serpentinisation (Qin and Wang, 2017 and references therein). However, the Cr isotope signature of the Karaçam bedrock (KC1) may provide evidence for a corresponding heavy Cr isotope depleted serpentinite reservoir that originates from seafloor serpentinisation of peridotites.

The saprolite unit has a $\delta^{53}Cr$ value that ranges from –0.40 to –0.21 ‰. The occurrence of takovite (Ni–rich Al clay) in the saprolite sample KC6 reflects strongly oxidising conditions and significant mobilisation of alkali elements that buffer the pH and allows takovite to precipitate (Taylor, 1984). The low $\delta^{53}Cr$ value of –0.40 ‰ reflects the optimal conditions (high E_h, high pH) for oxidation of Cr^{3+} to Cr^{6+} with loss of between 40 (Cr wt% normalised to Zr) to 78 % (Cr wt% normalised to Fe_2O_3) of Cr to solution compared to the underlying protolith.

The MIA value of the laterite units generally increases towards the top (**Fig. 2.8b**; except for KC6) and the upper limonite sample KC10 has a MIA value of 97 that indicates a near complete loss of the mobile element pool (e.g. Mg, Ca, Na). However, there is no obvious relationship between MIA and δ^{53}Cr (**Fig. 2.14**), as would be expected, although there is a tendency to increasing δ^{53}Cr values upwards in the lower limonite (**Fig. 2.12**).

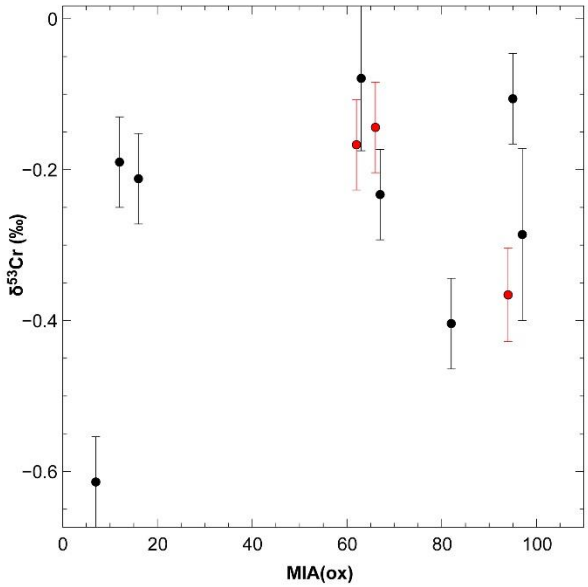

Fig. 2.14. δ^{53}Cr vs. MIA of the Karaçam laterite samples. Black circles are bulk rock samples and red circles represent vein samples. The samples show no clear trend between degree of weathering (i.e. MIA) and the loss of heavy Cr isotopes.

The economic Ni enrichment of the Karaçam laterite is situated in the lower limonite and similarly to the Çaldağ profile it seems likely that the supergene enrichment not only led to Ni redistribution and accumulation in the lower limonite, but it also transported isotopically heavy Cr downwards and this may overprinted the first–order Cr isotope weathering signal. The upper limonite sample has a relatively low δ^{53}Cr value (–0.29±0.11 ‰) compared to the underlying limonite (–0.11 to –0.19 ‰) and saprolite unit (–0.21±0.06 ‰). Similarly to the Çaldağ laterite, it can be argued that the uppermost laterite sample below the silica cap (sample KC10) likely best represents the first–order Cr isotope weathering signal.

Table 2.9. Microprobe analysis of representative mineral grains from selected Karaçam laterite bulk rock and vein samples. Data from Herrington et al. (*in preparation*). Data is given in wt%.

	KC1(bedrock)			KC12(clay vein)			KC11(clay vein)			
	mont.	goethite	lizardite	Cr–mont.	Fe–Cr–mont.	goethite	nontronite	Fe–Al–saponite	saponite	mont.
K_2O	0.01	0.01	b.d.	b.d.	b.d.	b.d.	0.11	0.05	0.01	0.02
Na_2O	b.d.	b.d.	b.d.	0.06	0.06	0.01	0.04	0.04	0.10	0.07
CaO	0.24	0.24	0.04	1.51	0.65	0.19	1.68	1.29	2.16	0.55
MgO	17.57	3.62	36.84	0.57	0.41	0.09	2.58	2.21	1.46	18.91
Al_2O_3	0.02	0.02	0.28	24.40	22.21	1.79	7.43	15.17	26.38	9.50
SiO_2	27.66	5.25	45.56	46.19	34.76	5.06	44.95	54.71	51.44	51.89
MnO	0.03	0.19	0.05	b.d.	0.01	0.02	b.d.	b.d.	b.d.<	b.d.
Cr_2O_3	0.65	0.10	0.02	12.64	10.88	0.41	1.42	5.39	7.29	2.31
FeO	34.76	82.75	7.68	0.31	12.34	67.75	22.76	10.01	3.15	5.57
CoO	0.06	0.01	0.04	b.d.	0.01	0.02	0.17	0.05	0.03	0.04
NiO	4.81	0.70	2.50	0.42	1.16	1.20	7.84	2.99	1.23	2.26
Total	85.81	93.02	93.01	86.15	82.54	76.57	88.99	91.91	93.25	91.14
b.d.	below detection limit									
Note	mont. = montmorillonite									

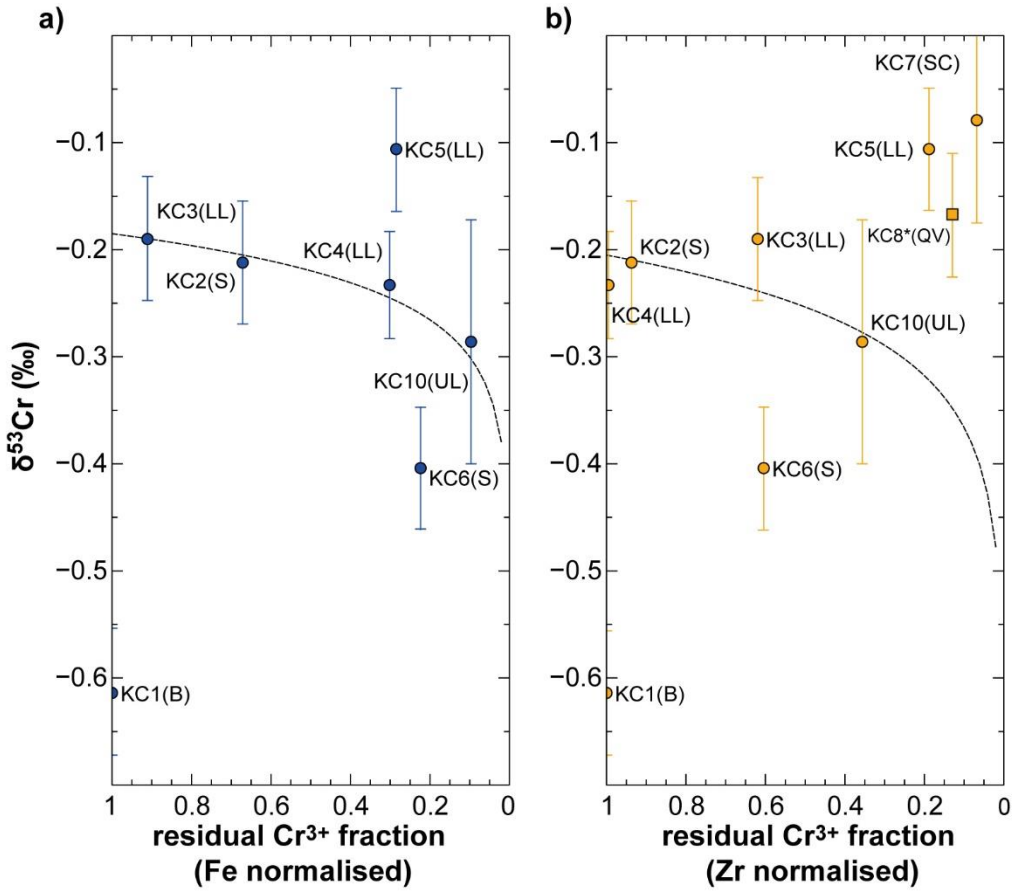

Fig. 2.15. $\delta^{53}Cr$ vs. Cr concentration normalised to **a)** Fe_2O_3 and **b)** Zr in the Karaçam laterite. The black dotted lines represent modelled Rayleigh fractionation curves between the most weathered sample (KC10) and the least weathered sample (KC2) to determine the effective Cr fractionation factor. B=bedrock, UB=upper bedrock, S=saprolite, LL=lower limonite, UL=upper limonite, SC=silica cap, QV=quartz vein.

The effective fractionation factor for Cr oxidation can be estimated by comparing the $\delta^{53}Cr$ values and Cr contents of the weathered and unweathered samples. Normally, the bedrock is considered to be the unweathered protolith; however, as discussed above it is likely that the Cr content and $\delta^{53}Cr$ signature of sample KC1 have likely been affected by serpentinisation processes that lead to removal of heavy Cr prior to weathering. Thus, the Cr isotopic composition of sample KC1 may not be representative for the progenitors from which the overlying laterite has formed. Therefore, the saprolite sample KC2 is chosen as the least weathered sample. Assuming a Rayleigh–type behaviour for Cr oxidation between KC2 and KC10 (upper limonite), then the fractionation factor ($\Delta^{53/52}Cr_{(Cr^{6+}-Cr^{3+})}$ = ε is approximately between 0.05 (Fe normalised; **Fig. 2.15a**) and 0.07 ‰ (Zr normalised; **Fig. 2.15b**).

The majority of the regolith samples that were not obviously affected by secondary processes (e.g. takovite formation) plot along the Rayleigh fractionation trend. The estimated fractionation factor (0.06±0.01 ‰) is comparable with the fractionation factor that was determined for the majority of the Çaldağ laterite samples (0.09±0.02 ‰). The clay–rich veins (KC11, KC12) within the upper limonite formed due to through–flow of meteoric water and are used to transport mobilised elements; as a result, they have high Ni concentrations of between 0.6 wt% and 2.5 wt%. They also have an extremely high Cr enrichment of up to 1600% (**Fig. 2.10b**) compared to the bedrock, with Cr concentrations of between 3.02 and 4.21 wt%. These Cr concentrations are far higher than those recorded in the enclosing upper limonite unit (1550 ppm), which indicates uptake of Cr from a Cr–rich fluid derived from the uppermost parts of the weathering profile. However, there is no systematic shift in Cr isotopic compositions to higher δ^{53}Cr values, as it is observed for the Çaldağ profile, although clay vein samples from both profiles have very similar mineralogies, consisting principally of montmorillonite and kaolinite.

Sample KC12 has a high Cr content in the clay–silicate fraction, whereas sample KC11 has relatively low Cr in the clays (**Table 2.9**). This implies that Cr in the clay–fraction of sample KC12 accounts for the lower δ^{53}Cr value of –0.40 ‰ compared to KC11. A simple isotope mixing calculation shows that Cr in the clays has a δ^{53}Cr value of –0.95 ‰, assuming that only addition of Cr from a fluid is responsible for the different Cr isotopic composition between KC11 and KC12, as inferred from mineral chemistry. KC12 has a strongly elevated Ce content and a low U concentration, which indicates strongly oxidising conditions that allow Ce precipitation and U removal. It is likely that the low whole–rock δ^{53}Cr value of KC12 results from oxidative removal of isotopically heavy Cr from the clay fraction, leaving behind a strongly heavy Cr isotope depleted residue, as indicated by the calculated δ^{53}Cr value of –0.95 ‰ of the clay fraction. The isotopically heavy fluid may then have been transported downwards and partly retained in the upper portions of the lower limonite, as indicated by the relative high δ^{53}Cr value of KC5 (**Fig. 2.12b**).

It should be noted that the mass balance calculations and the determination of the ‘effective Cr isotope fractionation factors under natural conditions’ discussed above require basic assumptions that may only be partially fulfilled in natural settings. Firstly, Cr loss is calculated by normalising the Cr concentration to an immobile marker element, which takes no account of, for example, removal of tiny particles of fractured Cr–bearing minerals such as Cr–bearing oxides. Secondly, the calculations do not take into account allochthonous Cr sources that may be important at the top of the laterite profile. However, in W. Turkey this effect is considered minimal as the Ni laterite profiles have an indurated silica cap that prevented erosion and denudation.

Thirdly, elements are only assumed to be transported upwards or downwards through the weathering profile, however, lateral water movements (e.g. groundwater) may also be significant.

Another possibility is that Cr is removed by late stage low pH fluids that mobilise Cr without significant Cr isotope fractionation (e.g. Berger and Frei, 2014). The presence of takovite in the saprolite reflects the mobility of Al and Ni, whereas Si remains associated with goethite in the overlying oxide zone. This evolution indicates interaction with low pH fluids, which is supported by the presence of kaolinite in the clay–rich vein samples in the upper parts of the profile. Goethite can contain more than 1 wt% As that constrains the pH of the fluid between approximately pH 4 and pH 6 (Herrington et al., *in preparation*). Thus, the Karaçam laterite profile appears to have had a more complex chemical evolution than the Çaldağ laterite. It is also likely that the protolith from which the laterite developed had a heterogeneous Cr isotopic composition that further complicates interpretation of the chemical evolution of the weathering profile.

Finally it has to be mentioned that the weathering profiles are also affected by incongruent dissolution of mineral phases that have a different initial $\delta^{53}Cr$ values. Cr–bearing silicates, in particular serpentine, tend to have a higher $\delta^{53}Cr$ value than Cr–bearing oxides (Farkaš et al., 2013). Weathering starts to primarily decompose silicate phases, which will likely lead to an incongruent release of heavy Cr isotopes between oxide and silicate phases. The determined fractionation factors and the here presented Rayleigh fractionation model only assumes a homogeneous fractionation behaviour of the rock, similar to a monomineralic substance, and does not respect the individual mineralogy. Therefore, the presented Rayleigh model is a simplification that only provides a basic insight when describing Cr isotope fractionation during ultramafic rock weathering under natural conditions. Mineral groups, in particular silicates and oxides, have a significantly different weathering resistivity, which likely leads to a more complex Cr isotope fractionation behaviour that also changes during the weathering cycle. A Cr isotope fractionation model that is based on incongruent mineral dissolution of the parent rock mineralogy is presented and in depth discussed in **Chapter 4**.

2.7.3 Role of Mn–oxides in Cr isotope fractionation

Oxidation of Cr^{3+} in laterites is dominantly driven by Mn–bearing oxides that rapidly oxidise trivalent Cr to its hexavalent form (Eary and Rai, 1987; Richard and Bourg, 1991; Fandeur et al., 2009; Economou-Eliopoulos et al., 2014). Mn^{4+}–oxides (e.g. birnessite, pyrolusite) are the major oxidising agents for Cr^{3+} in natural weathering environments and Cr isotope fractionation is strongly influenced by the presence, availability, and possibly by the mineralogical occurrence of these Mn–oxides (Hausladen and Fendorf, 2017). Mn–oxides form in the presence of molecular O_2 and microorganisms that catalyse the oxidation of Mn^{2+} (Tipping et al., 1984; Tebo et al., 2004), which makes the infiltration of oxygen–replete water into the rock profile a pre–requisite for oxidation of Cr^{3+}. Oxidation of Cr^{3+} to Cr^{6+} reduces virtually immobile Mn^{4+} to soluble Mn^{2+}, hence, laterites that have experienced a high degree of oxidative weathering (low $\delta^{53}Cr$ value) may have a low MnO abundance.

The Çaldağ samples show a partly significant correlation (R^2 = 0.85 normalised to V; R^2 = 0.24 normalised to Fe_2O_3) between $\delta^{53}Cr$ value and Mn content, which implies that oxidation of Cr is indeed accompanied by re–conversion of Mn^{4+} to mobile Mn^{2+} and potentially by subsequent removal (**Fig. 2.16**). Some samples have higher normalised MnO compared to the bedrock; these samples are likely to have experienced secondary replenishment by Mn–bearing fluids that originated from Cr oxidation in the uppermost parts of the weathering profile, with subsequent downwards migration of the Mn^{2+} that forms. Samples with low Mn also have low U concentrations, which is indicative of U removal due to oxidising conditions of in–situ formed laterites (Eliopoulos and Economou-Eliopoulos, 2000) and supports the idea that Mn mobilisation is triggered by redox–controlled reactions with Cr. Furthermore, it is likely that fluids enriched in Mn^{2+} also transport isotopically heavy Cr^{6+}, and precipitation of Cr and/or Mn from this fluid will overprint the primary weathering signals. In this connection, Mn–enriched samples (PB2, PB4) deviate from the modelled Rayleigh fractionation curve in **Fig. 2.13**.

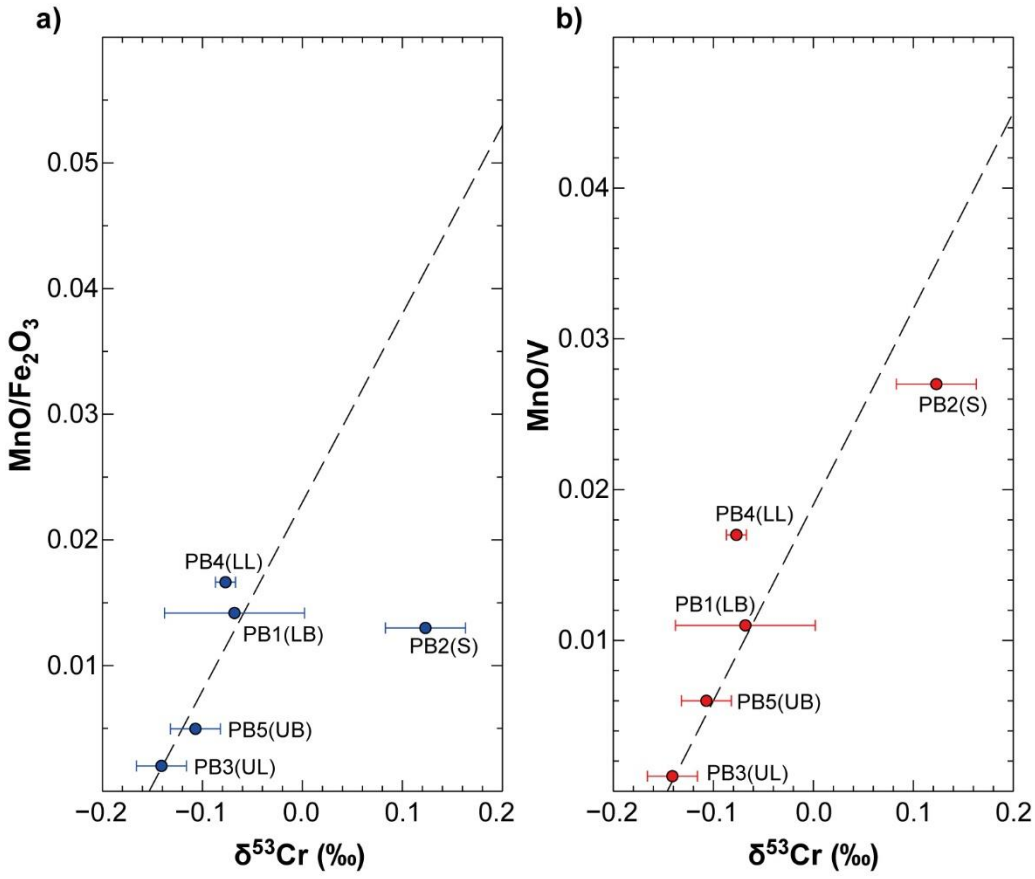

Fig. 2.16. MnO content normalised to **a)** Fe_2O_3 and **b)** V vs. $\delta^{53}Cr$ values of Çaldağ bulk laterite samples. The relationship between Mn content and $\delta^{53}Cr$ shows a statistical relevance for MnO normalised to V (R^2 = 0.85, p–value: 0.03), whereas MnO normalised to Fe_2O_3 shows a poor correlation and is not statistically relevant (R^2 = 0.24, p–value = 0.40). A p–value lower than 0.05 is considered to be statistically relevant (Shaver, 1993). B = bedrock, LB = lower bedrock, UB = upper bedrock, S = saprolite, LL = lower limonite, UL = upper limonite.

The Karaçam laterite samples do not show any statistically relevant relationship between Mn and $\delta^{53}Cr$ (**Fig. 2.17**). However, sample KC6 that contains takovite, which only forms under strongly oxidising conditions, has very a low Mn content and a low $\delta^{53}Cr$ value. Only a few of the Karaçam samples are depleted in Cr relative the bedrock, and it thus appears that the primary weathering signals are strongly overprinted by secondary processes, such as from the infiltration of Cr– (and Mn–) rich fluids from upper parts of the weathering profile.

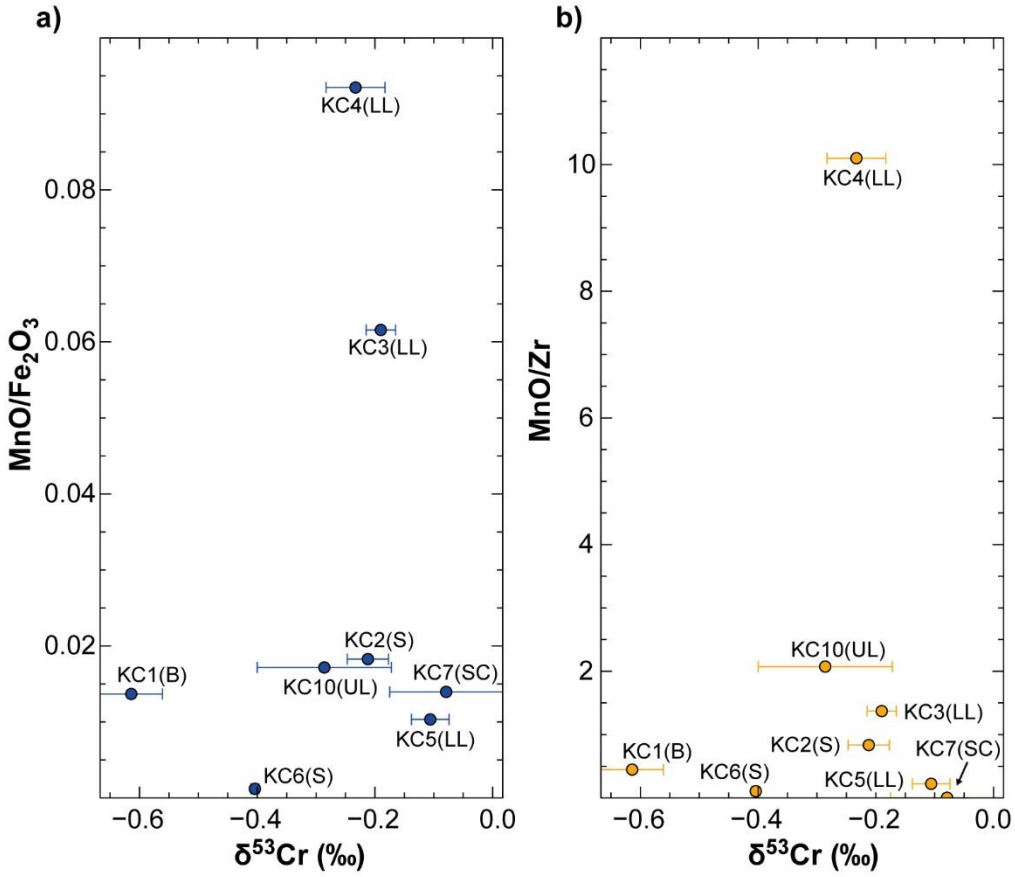

Fig. 2.17. MnO content normalised to **a)** Zr and **b)** Fe_2O_3 vs. $\delta^{53}Cr$ values of the Karaçam laterite. B = bedrock, LB = lower bedrock, UB = upper bedrock, S = saprolite, LL = lower limonite, UL = upper limonite, SC = silica cap, CV = clay vein, QV = quartz vein.

2.7.4 Implications for supergene Ni enrichment

The Çaldağ and Karaçam weathering profiles are both characterised as oxide–dominated Ni laterite deposits with goethite as main Ni ore, however, the Karaçam laterite shows an additional Ni mineralisation in form of takovite (Herrington et al., *in preparation*; Thorne et al., 2009). Ni retention on goethite and takovite formation are favoured at high pH conditions (Taylor, 1984; Beukes et al., 2000). Initial Ni mobilisation generally occurs under alkaline conditions, which likely results from primary serpentine dissolution and accompanied Mg release that increases pH (Golightly, 1981; Barnes et al., 1973). Therefore, mobilised Ni can be retained in–situ onto newly formed goethite, as a product of primary mineral dissolution.

Ni contents (normalised to the bedrock value) of the Çaldağ and Karaçam laterite indicate a substantial Ni enrichment in the upper bedrock and saprolite (Çaldağ; **Fig. 2.18**), and in the lower limonite and saprolite (Karaçam; **Fig. 2.19**) due to supergene Ni mobility. Mobile Ni is transported downwards in episodes of low pH after initial dissolution of primary serpentine (i.e. during formation of secondary Al–poor clays) and is retained deeper in the profile, where alkaline conditions predominate, in particular at the weathering front that is situated close to or within the saprolite (Butt and Cluzel, 2013). Phases of low pH, in particular in the Karaçam laterite, are supported by the presence of takovite in the saprolite (KC6), whose formation requires Al–mobility that constrains the pH of percolating Al–bearing fluids between pH 4 and pH 6 (Herrington et al., *in preparation*). In general, Ni retention increases with pH and laboratory experiments revealed a maximum retention of aqueous Ni^{2+} at pH 9 (Beukes et al., 2000). Berger and Frei (2014) performed Cr leaching experiments under different pH and demonstrated that Cr isotopes fractionate under alkaline conditions producing isotopically heavy Cr^{6+}, whereas under acid conditions, Cr is only mobilised, with no change of the Cr isotopic composition of the leachates with respect to the solid.

The lack of isotope fractionation under acid conditions could be explained by a relatively high E_h threshold (voltage potential with respect to the standard hydrogen electrode; Beverskog and Puigdomenech, 1997) that prevents mobilised Cr^{3+} to be oxidised even in the presence of a suitable oxidising agent (e.g. Mn–oxide). There is no experimental data on the E_h dependence of Cr isotope fractionation, however, it can be hypothesised that the Cr–Mn redox–pairing leads to an E_h lower than or equal to 0.5 V, by which Cr oxidation is only possible under neutral to alkaline conditions (**Fig. 2.20**). Therefore, low $\delta^{53}Cr$ values in the weathering profile may reflect more alkaline conditions, which correlates with highly Ni–enriched samples (**Fig. 2.18** and **2.19**).

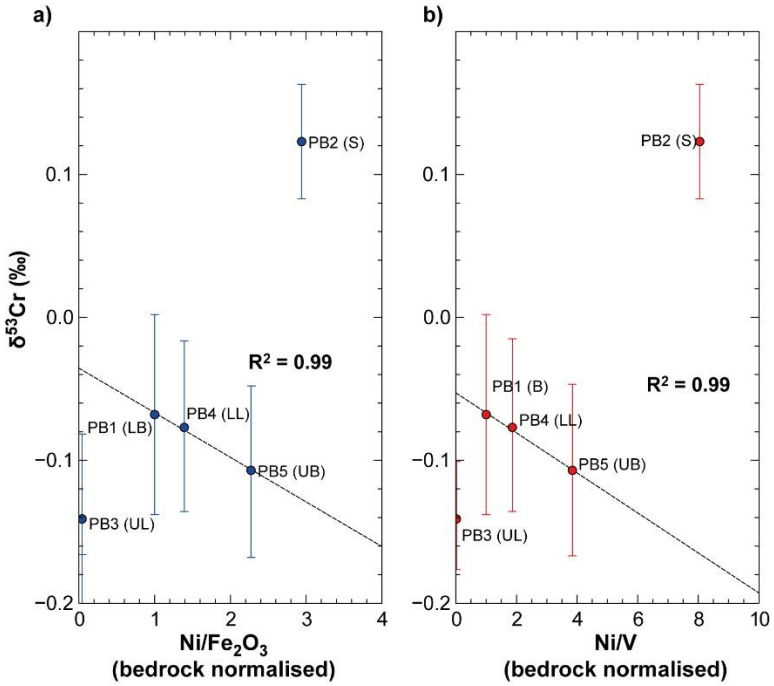

Fig. 2.18. $\delta^{53}Cr$ vs. Ni content normalised to **a)** Fe_2O_3 and **b)** V of the Çaldağ laterite. Note: Samples PB3 and PB2 are not included in the regression line (see text).

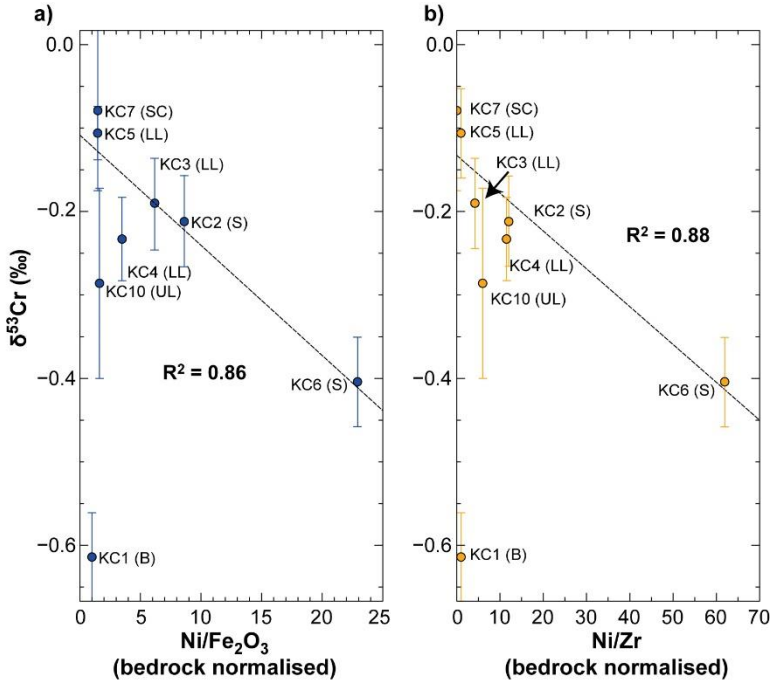

Fig. 2.19 $\delta^{53}Cr$ vs. Ni content normalised to **a)** Fe_2O_3 and **b)** Zr of the Karaçam laterite. Note: Samples KC10 and KC1 are not included in the regression line (see text).

Some of the Çaldağ samples (PB1, PB4, PB5) show an exceptionally good linear correlation between $\delta^{53}Cr$ and Ni enrichment (R^2 = 0.99; **Fig. 2.18**). Samples PB3 (UL) and PB2 (S) were excluded from the regression, as the upper limonite (PB3) was dominated by Ni leaching rather than Ni enrichment (i.e. lower Ni content normalised to bedrock) and the low $\delta^{53}Cr$ value of PB3 likely originates from initial Ni mobilisation during incipient weathering. The saprolite (PB2) has a positive $\delta^{53}Cr$ value that indicates retention of heavy Cr from fluids, which probably resulted from reductive immobilisation (e.g. Cr^{6+} reduction by Fe^{2+} or organic matter). In conclusion, only samples that show a Ni enrichment and a Cr isotopic composition that was not obviously affected by secondary Cr gains from a mobile pool show a statistic relevant correlation between Ni enrichment and $\delta^{53}Cr$ value in the Çaldağ profile.

The Karaçam samples also show a linear good correlation between a low $\delta^{53}Cr$ value and a high Ni enrichment (R^2 = 0.86 to 0.88; **Fig. 2.19**). Samples KC1 (B) and KC10 (UL) were excluded from the regression, as the sample KC1 may represent a bedrock portion that had an initially different Cr isotopic composition compared to the progenitor of the regolith units (i.e. saprolite, limonite). KC10 (UL) was excluded from the regression under the expectation that the Cr isotopic composition predominantly originates from initial mineral dissolution under alkaline conditions, similar to sample PB3 (UL). However, including KC10 yields only a slightly lower R^2 of between 0.6 and 0.7.

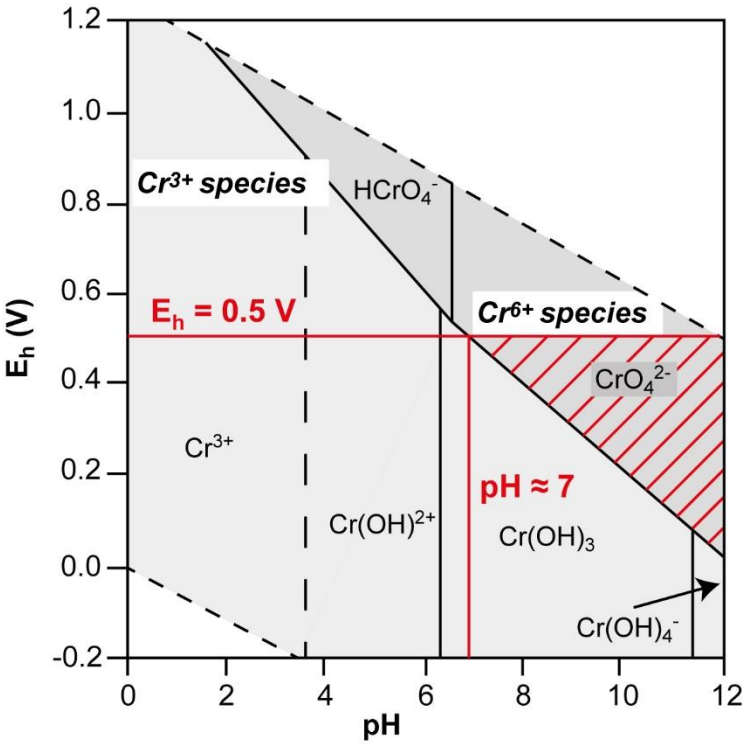

Fig. 2.20. Pourbaix diagram for chromium and $[Cr(aq)]_{total} = 10^{-6}$ mol at 25 ºC and 1atm for the Cr–O–H system after Giménez-Forcada et al. (2017). The Cr concentrations are total concentration (i.e. the sum of all aqueous species containing Cr at each coordinate point; E_h/pH).

In summary, correlations between $\delta^{53}Cr$ and Ni enrichment in the Çaldağ and Karaçam profiles likely reflect predominating alkaline conditions that favour Cr isotope fractionation and retention of mobile Ni onto Fe–oxyhydroxides. In support of this, it is possible that kinetic effects that limit Cr isotope fractionation, such as the 'rind effect' (i.e. shielding of mineral surface) are less significant in Ni–enriched samples, as Cr^{6+} adsorption decreases with increasing pH (Richard and Bourg, 1991), which may lead to a higher overall Cr isotope fractionation.

2.8 Conclusion

The geochemical and Cr isotopic composition of the Çaldağ and Karaçam Ni laterite deposits are a result of intense oxidative weathering that allowed the formation of deeply weathered regolith profiles overlying serpentinised peridotites that were exposed by obduction of sea–floor fragments during the closure of the Tethys. The laterites are ideal for studying the effects of intense weathering on Cr and Cr isotopes, which are summarised below.

(1) Oxidative weathering of exposed Cr–rich ultramafic rocks leads to preferential loss of heavy Cr isotopes leaving behind the regolith with low $\delta^{53}Cr$ values compared to the unweathered protolith, and progressively increasing MIA values. Incipient weathering involves the breakdown of primary Mg–silicates and preferential Cr release from the silicate fraction. Cr loss from chromite weathering is rather long–term and chromites may represent a source of Cr for the entire duration of laterite and soil formation. Cr continues to be lost from the regolith even in the upper part of the weathering profile, where weathering of chromite is likely enhanced in the presence of Mn–oxides that oxidise Cr^{3+} to mobile Cr^{6+}.

(2) Mobile Cr^{6+} that forms by oxidative weathering is transported down through the weathering profile in pre–existing local fractures and fissures and accumulates in clay–filled veins. Precipitation of Cr from these fluids can overprint the first–order signatures of oxidative weathering, producing $\delta^{53}Cr$ values higher than the $\delta^{53}Cr$ value of the underlying bedrock.

(3) There is a weak positive correlation between Mn abundance and $\delta^{53}Cr$ of the samples that strongly indicates that Cr oxidation is catalysed by reduction of Mn^{4+}–oxides under certain conditions (i.e. high standing water table). Oxidation leaves the residue enriched in light Cr isotopes, and depleted in Mn, as Mn^{2+} is soluble whereas Mn^{4+}–oxides are insoluble.

(4) Ni laterites are residual products of weathering of ultramafic substrate in tropical regions, which leads to the formation of Fe–rich regolith material. Supergene Ni enrichment in these weathering profiles necessitates mobilisation, translocation, and ultimately accumulation of Ni, which implies that the weathering profiles are also strongly affected by secondary processes. Similarly, the Cr isotope signature of these Ni laterite profiles is also affected by secondary processes, with accumulation of Cr within clay-rich veins derived from fluids transported from the upper parts of the weathering profile. Only the uppermost laterite samples immediately below the silica cap exhibit a least disturbed first–order weathering signature.

(5) Rayleigh fractionation calculations suggest that the extent of apparent Cr isotope fractionation during laterite formation is relatively small ($10^3 \cdot \ln\alpha \approx \varepsilon = \Delta^{53/52}Cr_{(Cr^{6+}\text{-}Cr^{3+})} = 0.06\pm0.01$ ‰ [Karaçam] and 0.09 ± 0.02 ‰ [Çaldağ]). Furthermore, the relative narrow total Cr isotope range in the two studied weathering profiles suggests that relatively large shifts in $\delta^{53}Cr$ values compared to the underlying bedrock cannot be generated by Cr oxidation alone and are most likely due to back reduction of Cr^{6+} that was mobilised in other parts of the weathering profile.

(6) Low $\delta^{53}Cr$ values correlate with Ni enriched samples, which indicates that Cr isotope fractionation under alkaline pH conditions is more favoured than under acid pH conditions. A high pH leads to a low E_h threshold that allows a more readily oxidation of Cr. Furthermore, oxidised Cr^{6+} is more mobile under high pH, as it is less retained on mineral surfaces, which minimises kinetic effects (i.e. 'rind' effect) and therefore, leads to a higher Cr isotope fractionation. Thus, Cr isotopes may provide a tracer of the predominant pH conditions of the laterite units that prevailed during the course lateritisation and to distinguish between supergene and residual Ni enrichment.

Chapter 3 Mineralogy and geochemistry of the São João do Piauí Ni laterite deposit and implications for its formation

3.1 Abstract

The São João do Piauí nickel laterite is the most important Ni deposit in Northeast Brazil, with 72 million tonnes of ore that has mean grades of 1.0 wt% Ni and 0.05 wt% Co. The regolith units developed from weathering of an underlying dunite that belongs to the ultramafic Brejo Seco Complex, which was exposed in the Early Cenozoic. Strong serpentinisation of the parent rock led to residual Ni enrichment in primary serpentine and a later phase of uplift in the Middle to Late Cenozoic induced Ni migration, which in turn led to economic enrichments in altered serpentine minerals in the lower laterite. Smectite–rich veins and layers are abundant in the laterite and likely originate from weathering of Al–rich troctolite that occurs as intercalations in the dunite parent rock. Ni–rich fluids from weathering of shallow soil horizons were preferentially channelled through smectite–rich zones, which resulted in very high Ni concentrations of up to 5.0 wt%. Since the exposure of the protolith, rainfall has been relatively low (less than 1000 mm/yr), below the expected minimum threshold for Ni laterite formation defined by the laterite formation window (LFW). However, a short intense rainy season of three to four months combined with a low water table due to a relief inversion allows continued weathering of the lower part of the profile. As a result, the laterite formation rates are very slow, between 0.1 and 0.8 m/Myr. The long dry season led to massive retention of secondary silica, and precipitation of secondary silica from oversaturated fluids in the wet season. Iron and aluminium were removed from shallow laterite units by circulating low pH fluids, driving residual silica accumulation on the top of the profile. The São João do Piauí Ni deposit exemplifies that Ni laterites can also form in areas that receive less than 1000 mm/yr rainfall, which widens the climatic regions that are conducive to develop Ni–rich regoliths that overlie ultramafic rocks of dunitic composition. Furthermore, it means that exploration of Ni laterite deposits may be extended to arid regions that experience short, but intense, rainy seasons.

3.2 Introduction

Nickel laterites account for about 70% of the worldwide nickel reserves and over the past decades there has been a general growth in Ni mining from laterites due to a steady increase in demand (Elias, 2002; Dalvi et al., 2004). Technical improvements in processing and refining mean that a large number of small Ni laterite deposits have become economically viable (Mudd, 2009, 2010; Kuck, 2010), and these deposits are ideal for studying ultramafic rock weathering and laterite formation. Ni laterites are residual products of intense weathering of ultramafic rock material that developed economically significant Ni (and Co) concentrations in one or more horizons. Laterites with Ni concentrations higher than 1.0 wt% are considered 'mineable' (Butt and Cluzel, 2013).

Weathering of ultramafic rock material leads to mobilisation of soluble mineral components (i.e. Mg, Ca, Na, K, Sr) due to hydrolysis of Mg–silicates (i.e. olivine, serpentine, pyroxene), which are then partly redistributed, and eventually removed from the rock profile. By contrast, mineral components with low solubility (i.e. Al, Fe, Ti, Th, Nb, Zr, rare earth elements) are mostly retained during weathering, which leads to a residual enrichment. The loss of mobile elements is associated with an increasing perforation of the rock with solution voids until the porosity reaches a threshold and the profile collapses. This shrinking process typically occurs in shallower horizons of the profile and residually enriches Ni together with other less mobile elements. Ni enrichments in deeper parts of the profile, in particular near the weathering front (Mg–discontinuity), rather result from Ni migration in fluids that were transported from shallow horizons of the laterite (Golightly, 1979; Burger, 2000; Butt and Cluzel, 2013).

The evolution of a Ni laterite and its mineralogy mainly depend on protolith chemistry, climate, topography, and overburden vegetation (e.g. Golightly, 1979; Golightly, 1981; Burger, 2000; Elias, 2002; Gleeson et al., 2003; Freyssinet et al., 2005; Berger et al., 2011; Butt and Cluzel, 2013). The chemical composition of the parent rock is the most important factor, as it determines if rock weathering can lead to a Ni–rich regolith. Ni concentrations of parent rocks that underlie modern and paleo–Ni laterites typically range from 0.2 to 0.4 wt% (Brand et al., 1998). Hence, most in–situ formed Ni laterites are situated on ophiolite complexes and a few on ultramafic intrusions, which predominantly consist of various types of peridotites and their metamorphic equivalents (Elias, 2002).

Climate is the second most important factor, as Ni laterite formation occurs in a specific temperature– and precipitation–window, the so–called 'laterite formation window' (LFW; Thorne et al., 2012). Ni laterites favourably form in hot and humid climates in areas that have temperatures higher than 25°C and precipitation >1000 mm/yr. Therefore, most Ni laterites are found around the equatorial belt between the 35°N and 35°S latitude (Anand and Paine, 2002). Deposits outside this zone (e.g. Australia, USA, the Balkans, Turkey, Urals) are considered to be paleo–deposits that formed under favourable, past climate conditions. This interdependency is also utilised to support past climate reconstructions in areas where Ni laterites occur. Climate conditions also control the mineralogy of the Ni–ore (e.g. Tardy and Nahon, 1985; Taylor et al., 1992; Elias, 2002). Humid conditions favour the formation of oxides, whereas dry conditions lead to silicate–dominated deposits due to silica retention. Most Ni laterites occur in tectonically stable (inactive) regions with a low relief, where mechanical erosion is low and chemical weathering dominates.

Ni laterite deposits can form in tectonically active regions, however, their occurrence is restricted to specific areas, such as dissected plateaus, crests, upper slopes, and terraces (Butt and Cluzel, 2013). Rock weathering is a slow process and the landscapes in which Ni laterites occur form over long time periods with changing climates. Ni laterites have rarely been directly dated, but it appears that it can take several millions years to form a deep regolith (e.g. Bourman, 1993; Lima, 2008). In stable cratonic settings with low relief and low rainfall (e.g. West Africa, Australia, Northern Brazil), regolith thickening rates are in the range of 3 – 15 m/Myr (e.g. Golightly, 1981; Peulvast et al., 2008). On the other hand, in active regions with intense rainfall thickening rates can be as high as 60 m/Myr (Freyssinet and Farah, 2000; Retallack, 2010). The tectonic and morphologic evolution of a Ni laterite can be complex due to the long time it takes to form a deep regolith profile, in which changing climate or variable tectonic activity can lead to different drainage conditions and a change in the height of the water table. This multi–stage formation is often associated with different Ni–ore types, and thus a large number of Ni laterites show more than one Ni–rich mineral in the profile. In principle, there are three types of Ni–ore (Brand et al., 1998); (1) oxides (goethite, asbolane, lithiophorite), (2) hydrous Mg–silicates (serpentine, chlorite, talc, sepiolite), and (3) clay–silicates (smectites).

Mineralogy and geochemistry of the São João do Piauí Ni laterite deposit and implications for its formation

Ni laterites that formed over (serpentinised) dunite parent rocks usually develop oxide deposits, irrespective of the local drainage conditions (Butt and Cluzel, 2013). Prominent examples are found in New Caledonia (Tiebaghi, Goro), Australia (Cawse, Murrin Murrin, Ravensthorpe), and Brazil (Onça, Puma). These Ni laterite deposits often contain abundant secondary silica, mainly chalcedony and quartz, because the lack of Al hampers clay formation, which results in dilution of bulk Ni. In particular in arid climates with short wet seasons, dunites retain most of their silica and develop a protecting siliceous cap (Challis et al., 1995). The origin and significance of these caps for the lateritisation process is yet not clear. It has been suggested that silica–rich caps on Ni laterites are the product of earlier arid phases, which occurred prior to laterite formation (Golightly, 2010). However, other studies suggest that the formation of silica caps are an important part of the laterite formation process (Lacinska and Styles, 2013; Butt, 2014) and may also have a control on the Ni enrichment process.

The São João do Piauí Ni laterite is located in Northeast Brazil and developed on a serpentinised dunite of the Brejo Seco Complex (BSC), which is a layered magmatic intrusion of Precambrian age (Salgado et al., 2016). It is situated in the state of Piauí, about 300 km to the west of Petrolina, and is a relatively small Ni deposit with 72 million tonnes of ore with a mean grade of 1.0 % Ni and 0.05% Co (Brazilian Nickel Limited, 2017). The deposit was prospected by *Vale S.A.*, and commercial operation started in 2016 by *Brazilian Nickel Limited (BRN)*. Ni is extracted using low pressure heap leaching and is purified using an ion exchange technique (Oxley and Smith, 2013; Oxley et al., 2016). The São João do Piauí laterite is the most important Ni deposit in northeast Brazil but it has not been well studied, likely due to its small size and relatively low Ni concentrations (Berbert, 1977; Almeida, 1978; Trescases et al., 1981; Barros de Oliveira et al., 1992). The deposit was firstly described by Berbert (1977) and later investigated by Almeida (1978) for its economic relevance. Trescases et al. (1981) discussed the historical development of Ni laterites in Brazil and assigned the exposure of the parent rock formation to the South American erosion cycle in the Eocene (e.g. King, 1956; Bezerra et al., 2008). Barros de Oliveira et al. (1992) described the Ni laterite as a coarse saprolite–dominated Ni deposit with massive transformations to smectite as the main Ni ore. However, no detailed petrographic and geochemical characterisation of the Ni laterite exists to date.

Here we present the geochemistry and mineralogy of a profile sampled from an excavated pit (‘open pit’) that is located on the gently–sloping flank of a local hill that hosts the deposit. The data are used to: (1) characterise the type of the Ni laterite deposit; (2) decipher its mineralogical evolution including the types of Ni–ore, and (3) estimate the conditions of Ni laterite formation, in particular the Ni-enrichment and silicification processes.

3.3 Geology

3.3.1 Regional geological setting

The geology of Northeast Brazil is composed of reworked Archean basement, Proterozoic metasediments and metavolcanics that were amalgamated during the Brasiliano–Pan–Africa orogeny in the Precambrian (Brito Neves et al., 2000). The breakup of Pangea in the Late Jurassic marks the last major tectonic event of Northeast Brazil and from the Late Cretaceous until the present day sedimentation, uplift and, in particular, major erosional events, started to shape the geomorphology, which resulted in a low–lying, pediplain surface with a few elevated areas that originate from differential erosion (Matos, 1992; Peulvast et al., 2006, 2008; Bezerra et al., 2008; IBGE, 2009; Ross, 2013). The Brejo Seco Complex (BSC) is a small Precambrian intrusion (903±20 Ma) of the 'alpine' type, which is comprised of different layers of mafic and ultramafic rocks that were strongly serpentinised during the Brasiliano–Pan–Africa orogeny (Barros de Oliveira et al., 1992; Salgado et al., 2016). The BSC represents an isolated part of the 'alpine serpentine belt' that consists of small ultramafic massifs situated in long alignments in the states of Goiás, Pará, Bahia, and Minas Gerais (Melfi et al., 1988). It is located in the Morro Branco Complex (MBC) that lies at the north–western edge of the Riacho do Pontal orogen north of the São Francisco Craton (**Fig. 3.1**). The uplift of the South American continent led to a period of erosion (South American erosion cycle) from the Early Cenozoic (Eocene) onwards, which was responsible for an extensive pediplansiation of Northeast Brazil (e.g. King, 1956; Bezerra et al., 2008). The erosion cycle led to the exposure of large areas of the Precambrian alpine serpentine belt including the BSC, which triggered the formation of the São João do Piauí Ni deposit (Trescases et al., 1981). A thermochronologic study at the São Francisco Craton concluded that an interval of 20 Myrs was enough to form the regional pediplain after the last uplift event (Japsen et al. 2012). Thus, the formation of the São João do Piauí Ni laterite likely started between 56 and 36 Ma.

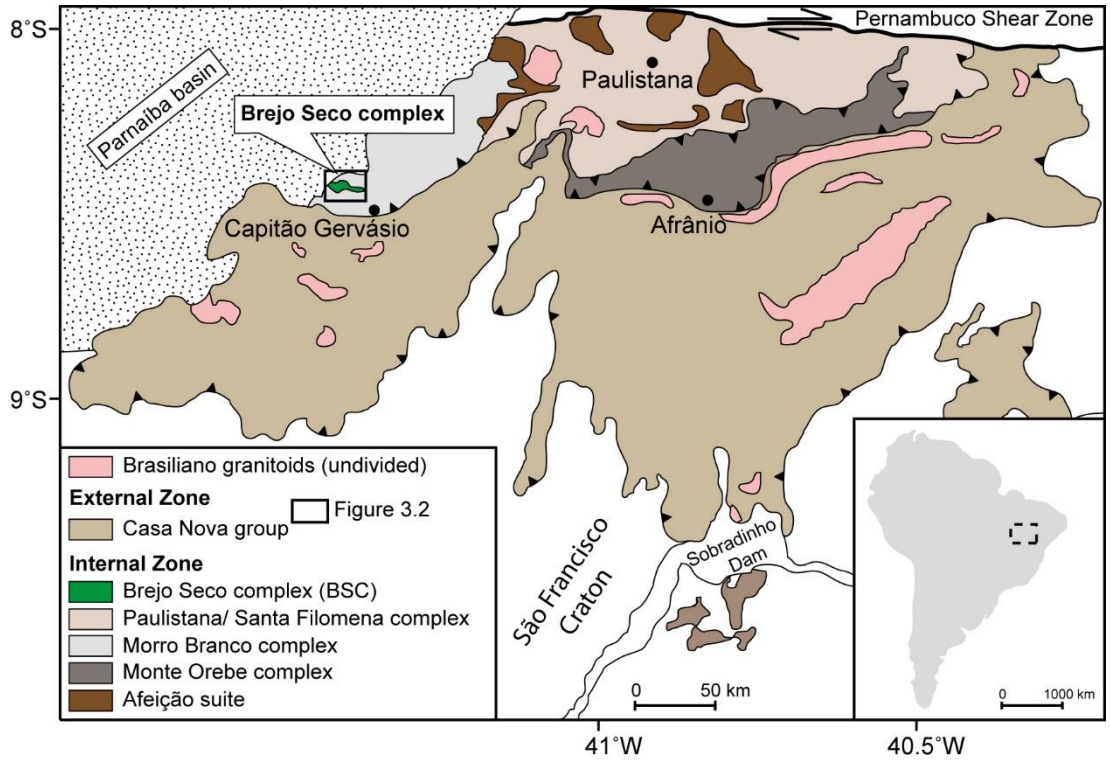

Fig. 3.1. Regional geological map of the Riacho do Pontal orogen after Salgado et al. (2016) and simplified from Caxito et al. (2014). The BSC intruded into the south–western edge of the Precambrian Morro Branco complex and is located at the south–eastern border of the Parnaíba basin. A local geologic map of the BSC and its magmatic layers is shown in **Fig. 3.2**.

The Brejo Seco Complex crops out on the south–western edge of the Morro Branco Complex (MBC) and its exposure level reveals an E–W trending intrusion that is overlain by sediments of the Parnaíba basin to the West and covered by Cenozoic sediments to the East (**Fig. 3.2**). The complex tectonically overlies the Precambrian Rajada granite to the South and is overlain by Late Cenozoic sediments and units of the MBC to the North.

The BSC is a layered intrusion that is composed of four major zones: (1) the Lower Mafic Zone (LMZ; mainly troctolite); (2) the Ultramafic Zone (UZ, serpentinised dunite with troctolite intercalations); (3) the Transitional Mafic Zone (TMZ; mainly troctolite); and (4) the Upper Mafic Zone (UMZ; gabbro and minor anorthosite, troctolite, and ilmenite magnetitite). In the Middle to Late Cenozoic, the mafic zones (LMZ, TMZ, and UMZ) were levelled to the same topographic height as the country rock by the Velhas erosion cycle, leaving only the Ultramafic Zone (UZ) exposed as a 3.5 km wide and 9 km long, partly dissected hill with the overlying São João do Piauí Ni laterite (**Fig. 3.3**; Barros de Oliveira et al., 1992; Salgado et al., 2014).

Despite the high abundance of mafic and ultramafic rocks in the states of Bahia and Piauí, only the São João do Piauí Ni deposit has a preserved weathering profile due to its protective siliceous cap. Other Ni deposits in Northeast Brazil, such as those in Serra das Marrecas and Andorinha, are fully dismantled, and the topography has been levelled to the country rocks such that only relicts of former Ni laterite deposits are preserved (Schobbenhaus, 1976; Barros de Oliveira et al., 1992).

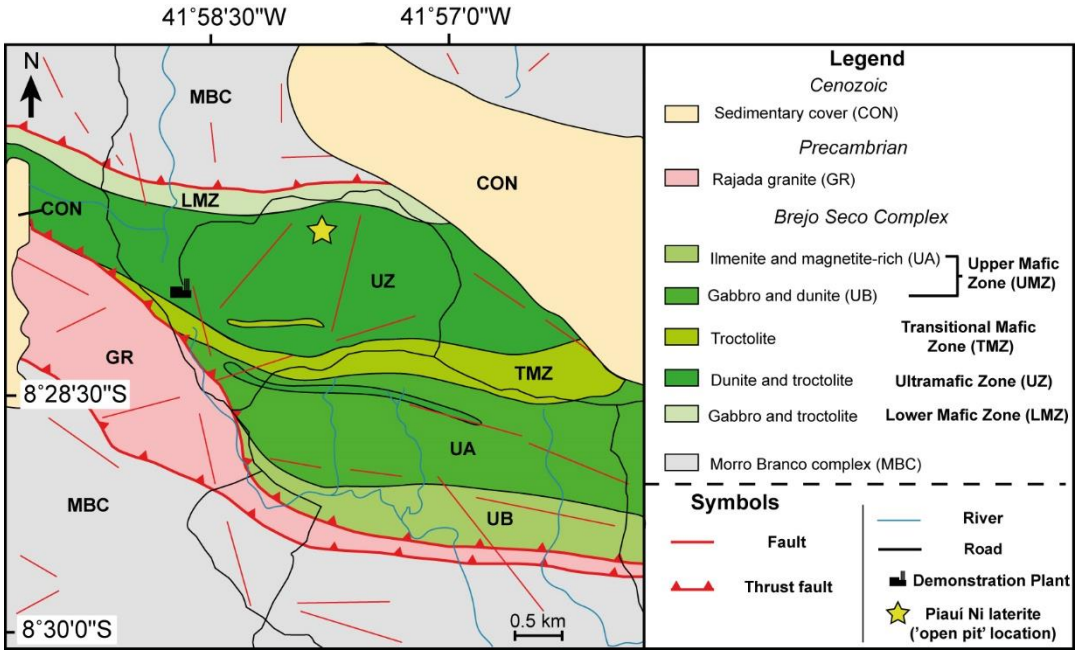

Fig. 3.2. Local geological map of the Brejo Seco complex (BSC) and its adjacent tectonic units modified after Salgado et al. (2016). The layered magmatic body was inverted during the Brazilian Orogeny and was later amalgamated on units of the Morro Branco massif and the Rajada granite in a thrust–fold belt tectonic setting. The yellow star marks the position of the studied laterite weathering profile, which is situated on the lower lands of the tabular hill (**Fig. 3.3**).

3.3.2 Climate

The present day climate of Northeast Brazil is semi–arid with an average temperature of between 24 and 26 ºC, and a precipitation of about 800 mm/yr, which falls mainly between December and March, while largely absent the rest of the year (Ramos, 1975). The predominantly dry climate is related to the presence of moderate to strong El Niño events that control the regional climate of Northeast Brazil (Gurgel et al., 2013). The vegetation is characterised by thorny shrubs and dry bush land, commonly referred as 'caatinga' (de Albuquerque et al., 2007). In the Eocene, as lateritisation started with the exposure of the BSC, the paleo–climate of Northeast Brazil was warmer and probably slightly more humid. Studies combining $\delta^{18}O$ data with ancient CO_2 levels, changes in the Andean surface elevation and other geomorphic and climatic features revealed that the average annual temperature on the South American continent was likely about 1 to 5 ºC higher. Furthermore, El Niño events were less intense or absent, which favoured longer rainy periods and led to a generally more humid climate that lasted until the onset of the Velhas erosion cycle in the Middle to Late Cenozoic (Louise Jeffery et al., 2012; Gurgel et al. 2013).

3.3.3 The Ni laterite

The São João do Piauí Ni deposit is a 8 to 30 m thick weathering mantle that consists of variably silicified regolith material and abundant clay–rich veins and layers that are embedded in the regolith profile. The Ni laterite developed from weathering of underlying serpentinised dunite and a laterite profile is present above most of the Ultramafic Zone (UZ), except on steep slopes (Berbert, 1977; Barros de Oliveira et al., 1992). The laterite only consists of saprolite material that shows a variable, but generally high degree of silicification. A limonite horizon is absent. The saprolite can be divided into three main horizons. A narrow saprock horizon overlies the dunite parent rock, followed by a thick, coarse saprolite, which represents the main laterite horizon, and an argillaceous saprolite horizon towards the top. The uppermost regolith unit consists of a ferruginous siliceous cover, which is common among Ni laterite deposits that originate from dunites (e.g. Butt and Cluzel, 2013; Butt, 2014).

3.3.4 The ‘open pit’ weathering profile

The ‘open pit’ weathering profile is situated on the north–facing gentle slope of a small hill in the central area of the Northern part of the UZ (**Fig. 3.3a, b**). The ‘open pit’ was excavated during the demonstration phase of mining by *Brazilian Nickel Ltd.* and it provided Ni ore for the first production process. Sampling took place about two weeks after the excavation. The ‘open pit’ is about 27 m deep and it exposes all of the laterite horizons that are characteristic of the São João do Piauí Ni deposit (**Fig. 3.4**). The profile mainly consists of heterogeneously silicified saprolite material (23 m) that overlies a ~3 m thick saprock horizon. The saprock is pale grey to brown and has a noticeably low density. The saprolite is pale yellow to deep red in colour, due to variable amounts of Fe–oxyhydroxides. The lower saprolite (15 – 22 m) consists of millimetre– to decimetre–scale coarse blocks that show spheroidal weathering structures and are strongly silicified in the form of vein– or web–like networks. There are zones in the coarse saprolite that consist almost entirely of secondary silica. The upper saprolite is composed of argillaceous, less coarse rock material (6 – 9 m) that consists of variable mixtures of authigenic weathering products and brecciated laterite material from the top of the hill. Magnesite is present with accretions of talc and occurs as veins of variable size, particularly in the argillaceous saprolite.

The Ni laterite is characterised by the presence of clay–rich veins and layers that are of variable thickness, from a few centimetres to several meters. The veins and layers occur throughout the weathering profile, creating a network that provides a drainage pathway for meteoric water. The veins and layers are similarly orientated, creating a preferred fluid–flow pathway through the profile. Unlike the host laterite, the embedded clay–rich veins and layers show no signs of silicification. In the deeper parts of the profile, the veins are pale green to dull black in colour and have a rigid and blocky appearance. Bends in the clay–rich rock layers indicate strike–slip movements relative to the surrounding, rather brittle, saprolite.

At lower depths, or close to the main water pathway, veins appear pale green to grey, have a smaller grain size, and show higher amounts of clays. The rock is loose and is soil–like. In places, the profile shows a high degree of mixing between the host laterite and clay–rich material, which suggests a heterogeneous collapse of the parent body. Green to teal chrysoprase veins are present in some parts of the lower saprolite. The majority of chrysoprase occurs in 1 to 20 cm thick veins. Veins grade from white pure magnesite to green wetstone with quartz and magnesite, to pure gem–quality chrysoprase.

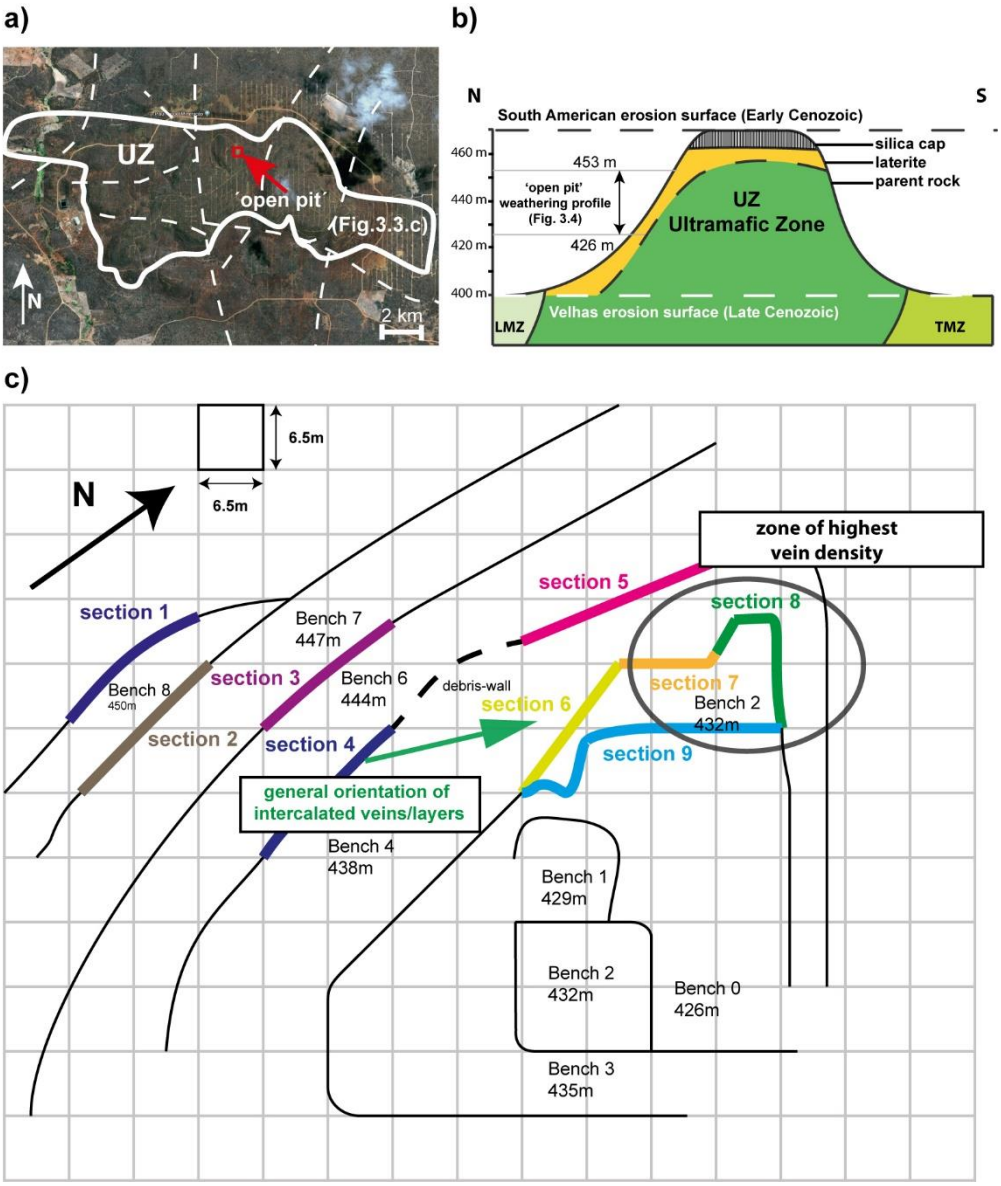

Fig. 3.3 a) Satellite image (Google Earth; imagery date 09/10/2010) of the Ultramafic Zone (UZ, white line) that emerges as a dissected hill surrounded by a flat–lying, pediplain country rock horizon (Velhas erosion surface). The area is characterised by major normal faults (km–size, white stippled lines) that cross the mountain ranges including the laterite and the underlying bedrock. The red square indicates the location of the investigated laterite weathering profile. **b)** Simplified geological cross section of the São João do Piauí Ni laterite deposit (orange) overlying the UZ parent rock. The 'open pit' weathering profile is situated on a gentle, northward dipping slope of the dissected tabular hill. The hill represents an erosional residue that formed during the Velhas cycle and persisted due to the formation of a siliceous cap, which protected the underlying rock from erosion. The height of the hill is enlarged relative to its diameter. Figure compiled from King (1956), Trescases et al. (1981), Barros de Oliveira et al. (1992), and Salgado et al. (2016). **c)** Schematic top view on the 'open pit' that was excavated in March 2016. The pit is about 27 m deep and divided into 8 benches with Bench 0 situated at the bottom. Geologic profiles were drawn from 9 sections of the W–facing wall of the pit and re–combined to give a single profile that presents the main characteristics of the studied profile. The Ni laterite has abundant clay–rich veins and layers. The general orientation of these veins and layers and their relative abundance in the 'open pit' is indicated in the figure by a green arrow.

Field observations reveal that progression of the weathering front is rather undulated throughout the laterite, which likely results from the abundance of intercalated clay–rich veins and layers that mainly determine the fluid–flow path of infiltrating meteoric water. Therefore, sampling of the profile took into consideration the inclined main flow path within the laterite (see **Fig. 3.4** for positions of individual samples). The investigated profile consists of two saprock samples (SR), 9 saprolite samples (CS1 – 7 and AS1, AS2), one magnesite vein (V1) that originated from weathering of the parental dunite, three clay–rich vein samples from different depths (V2, V3, V4), and three serpentinised dunite samples (B1, B2, B3) that were sampled close to the ‘open pit’.

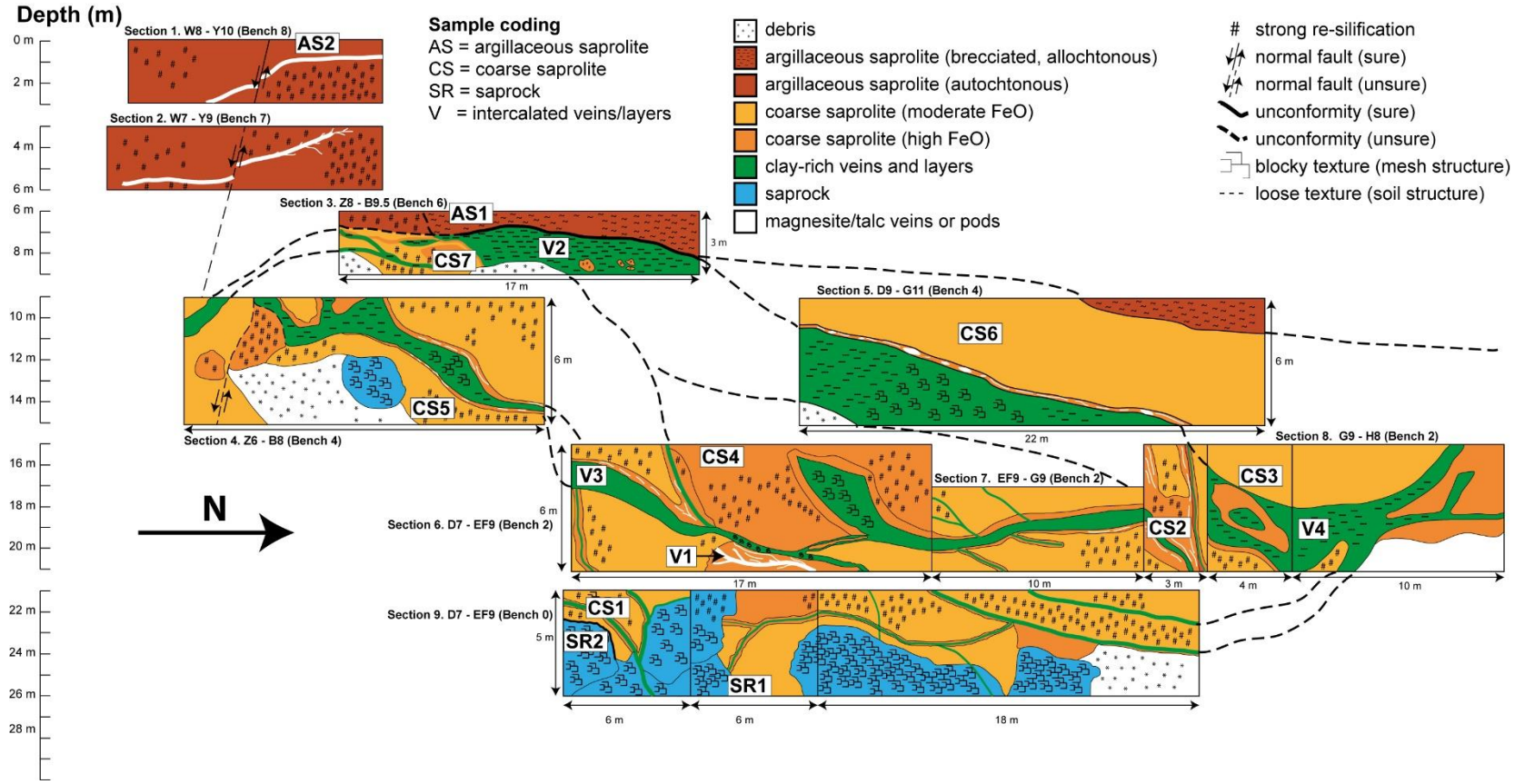

Fig. 3.4. Schematic geologic profile of the West wall of the excavated 'open pit' laterite weathering profile consisting of 9 individual sections (**Fig. 3.3.c**). Each section is aligned according to its relative position in the pit. The stippled lines in between the sections show the suspected course of clay–rich veins and layers between the sections. The squares with sample coding show the sampling positions. The local bedrock did not outcrop in the 'open pit' and was sampled nearby. Coarse saprolite material adjacent to veins and layers is often characterised by a more reddish colouration, which is due to a higher amount of oxidised Fe (hematite). The presence of saprock boulders in section 4 implies strike–slip movements within the laterite formation probably along intercalated veins and layers.

3.4 Methods

3.4.1 Sampling

The rock samples were collected from the excavated 'open pit' of the São João do Piauí Ni laterite during a four week long site visit. All rock samples were taken from the West wall of the 'open pit' (**Fig. 3.4**). Samples were collected from the profile using a hammer and ~1.0 kg of rock material for each sample was transferred into waterproof, high grade cloth bags (polyester) and sealed with drawstrings and subsequently put into large, air tight polyethylene sample bags to prevent any cross contamination among the samples during transport. Rock samples were broken into chips using a hand–operated rock splitter and dried at 100°C overnight. The chips were then ground in an agate mortar for about 3 min to reduce the grain size to <100 µm and homogenise the rock powder. The powder was dried at 105°C overnight.

Chrysotile–rich samples (i.e. bedrock, saprock) underwent a special treatment under safety precautions to prevent any contamination (and inhalation) with/of fine chrysotile crystals (asbestos needles) during rock sample preparation. The chipping was done with triple–bagged (polyethylene) sample material and quantitative material transfers for grinding and subsequent analyses were conducted in a fume hood with an air exhaust. A portable particle counter was placed next to the work bench for air monitoring during all procedures. A tacky mat was placed in front of the fume hood together with the use of an ad hoc vacuum cleaner to remove any particles that potentially escaped from the fume hood. Personal protective equipment (PPE) was worn including safety glasses, dust mask (FFP3), two pairs of gloves, sleeve covers, and lab coat. Expendable materials were separately collected and were disposed to the asbestos waste stream.

All measurements were done at the *University of Southampton*, except the microprobe measurements that were performed at the *Natural History Museum, London*. Results of major, trace, and rare–earth element analyses of various international rock standards that were analysed alongside the samples are given in **Table A.1** (Appendix).

3.4.2 X–ray fluorescence spectroscopy (XRF)

Concentrations of SiO_2, Al_2O_3, Fe_2O_3, MnO, MgO, CaO, K_2O, Na_2O, Ti, Zn, Cu, and V were determined by wavelength dispersive X–ray fluorescence spectroscopy (XRF) on fused glass discs (beads) and on pressed powder pellets for Ti concentration measurements. Beads were prepared by mixing sample powders with a lithium metaborate flux (10:1 flux to sample ratio) and heating in platinum crucibles at ~1100 ºC until the mixture was completely molten and homogenised. Element concentrations were measured on a *Philips MagiX–Pro* automatic sequential wavelength dispersive XRF spectrometer using a 4 kW rhodium end–window tube. Concentrations of certified rock reference materials (JP-1, NIM-P) were accurate to within <±6 % (1SD) for major elements (> 1 wt%) and within <±20 % (1SD) for minor elements compared to certified values (Chatterjee and Lassiter, 2016; Hughes et al., 2016; Bénard et al., 2017). The external precision was better than ±5 % (1SD). The limit of detection (LOD) for all elements was approximately 0.5 ppm (TiO_2 = 50 ppm). The results of the XRF analysis are shown in **Table 3.1**.

3.4.3 Inductively coupled plasma mass spectrometry (ICP–MS) analysis

Rock samples were digested using a method adopted from Babechuk et al. (2010). About 100 mg of sample powder was weighed in a *Savillex* vial and dissolved in 3.5 ml HF and 1 ml concentrated HNO_3 at 130 ºC for at least 60 h and then brought to incipient dryness. The dried samples were repeatedly re–dissolved in 3 ml concentrated HNO_3 and dried down. Then, samples were re–dissolved in 3 ml 3N HNO_3 and refluxed on a hotplate overnight at 130 ºC. Sample solutions were transferred into centrifuge tubes and the *Savillex* vial was washed with another 3 ml 3N HNO_3. Solutions were centrifuged for 15 min at 3000 rpm, checked for residues, and clear solutions were transferred into clean *Savillex* vials. The process was repeated for samples with residues until they were fully dissolved. The samples were diluted with 3N HNO_3 to give a total volume of ~12 ml. This stock solution was diluted 2000 times for analysis of trace elements and the REE. Concentrations were determined using a *Thermo Fisher Scientific X–SERIES 2* ICP–MS. The instrument was calibrated using certified rock reference materials JB-1a, JB-3, JGb-1, BIR-1, BHVO-2, and the certified reference materials DTS-2B, JP-1, and JA-2 were measured as unknowns with blanks bracketing the samples and using In and Re as internal standards to correct for matrix effects.

Obtained concentrations of reference materials were accurate to better than ±20 % (1SD) for all trace elements and the REE compared to certified values (Imai et al., 1995; Babechuk et al., 2010; Day et al., 2015). The precision of replicate measurements of the same sample was better than ±10 % (1SD), except for Sm, Eu, Tb, Yb, Lu, Th (<±20 %). Detection limits vary between 0.01 ppb and 1 ppm and are given with the results of the trace element and REE analyses in **Table 3.2**. and **3.3**.

3.4.4 Loss on ignition and carbon analysis (TOC, CO_2)

The loss on ignition (LOI) was determined by sequential heating of 5 g of dried sample powder in a muffle furnace up to 1050 ºC for about 3 h (Bengtsson and Enell, 1986). The loss of ignition was then calculated by the relative mass difference prior and after igniting. Obtained LOI values for certified reference material JP–1 were accurate to <±11 % (1SD) compared to certified values (Bénard et al., 2017). The precision of replicate measurements was <±5 % (1SD).

Total carbon concentrations were determined on 5 mg aliquots of dried sample powder using an *Elementar Vario EL* CHNS analyser. Carbonate–bound carbon was determined on the CHNS analyser on a separate aliquot of the same sample powder that was combusted in a muffle furnace at 550 °C for 1 h (Dean, 1974). The total organic matter content (TOC) was calculated as the difference between the total carbon concentration and the carbonate–bound carbon concentration. Obtained values for the reference material Citin OAS were accurate to within ±0.1 % (1SD) compared to the certified concentration and the internal precision of replicate measurements was better than ±0.5 % (1SD). The detection limit (LOD) for carbon was 0.12 wt%. The results of the LOI and carbon analysis are given in **Table 3.1**.

3.4.5 X–ray diffraction (XRD)

Identification of mineral phases was performed by X–ray powder diffraction (XRD). Rock powder was mixed with a corundum spike in a 3:1 ratio and homogenised in a *McCrone* micronizing mill with isopropanol. The solution was then evaporated to dryness at 50 ºC over 48 h and the fine powder was subsequently analysed as a thin smear. Measurements were performed on a *Pananalytical X'Pert Pro*. XRD patterns and relative mineral abundances are given, respectively, in **Figures A.1** and **Table A.2** (Appendix). Samples were scanned over an angular range of between 2 – 76º (2θ) with a step size of 0.04° 2θ (for excluded 2θ regions see **Table A.2**). Copper Kα1 radiation was selected from the primary beam using a germanium 111 single–crystal monochromator and the unit–cell parameters were determined using *Louër`s DICVOL91* indexing routine of the *STOE WinXPOW* program package (Boultif and Louër, 1991). Quantitative mineralogical analyses were performed using *Siroquant v2.0* software (Taylor, 1991). A compilation of identified mineral phases by XRD, microprobe and optical analysis is given in **Fig. 3.10**. Relative mineral abundances are given in **Fig. 3.11**.

3.4.6 Electron probe micro–analysis (EPMA)

Polished thin sections (<25 µm thick) were made from selected samples and carbon coated. Microprobe analyses were performed on a *Cameca SX–100* electron microprobe with a wavelength dispersive system at operating conditions of 15 kV, a counting time of 10 – 50 s, and a beam current of 20 nA. The obtained data are typically accurate to within ±0.5 % and the precision of the results is better than ±0.1 %. Detection limits of element oxides concentrations range between 0.02 and 0.10 ppm. Analyses of key mineral phases from the range of measured samples are shown in **Table 3.4 – 3.10**.

3.5 Results

Chemical compositions of representative samples from the Ni laterite (host laterite), serpentinised dunite (bedrock) and clay–rich veins are given in **Table 3.1 – 3.3**.

3.5.1 Host laterite and bedrock

The Ni laterite is characterised by SiO_2 contents (**Fig. 3.5a**) that increase from the bedrock (39.0 – 41.5 wt%), through the saprock (36.0 – 54.5 wt%), and towards the saprolite (70.2 – 90.3 wt%). The silica cap consists of 87.2 wt% SiO_2. The MgO content shows the opposite trend (**Fig. 3.5b**) and there is a significant negative correlation between MgO content and SiO_2 content ($R^2 = 0.94$; p–value = $3.7 \cdot 10^{-9}$). MgO exhibits a general decrease from the bedrock (33.1 – 35.5 wt%), through the saprock (20.1 – 31.8 wt%), with a shift towards lower, but variable MgO concentrations in the saprolite (0.4 – 8.0 wt%) and the silica cap (1.0 wt%). The Mg–discontinuity is situated at the transition between the saprock and the coarse saprolite.

Concentrations of CaO, Na_2O, and K_2O are variable, but they are generally lower than 1.0 wt% throughout the profile. Fe_2O_3 concentrations (**Fig. 3.5c**) slightly increase from the bedrock (9.4 – 11.0 wt%) to the saprock (10.8 – 12.7 wt%), and vary between 5.8 and 18.2 wt% in the saprolite. The silica cap has 8.54 wt% Fe_2O_3. The Al_2O_3 content is low in the dunite parent rock (1.0 – 1.7 wt%) and remains relatively constant in the overlying laterite (0.7 –1.9 wt%). The TiO_2 content of bedrock is between 0.01 and 0.02 wt%, except for sample B3 (0.07 wt% TiO_2), and remains relatively constant throughout the laterite (0.01 – 0.03 wt%).

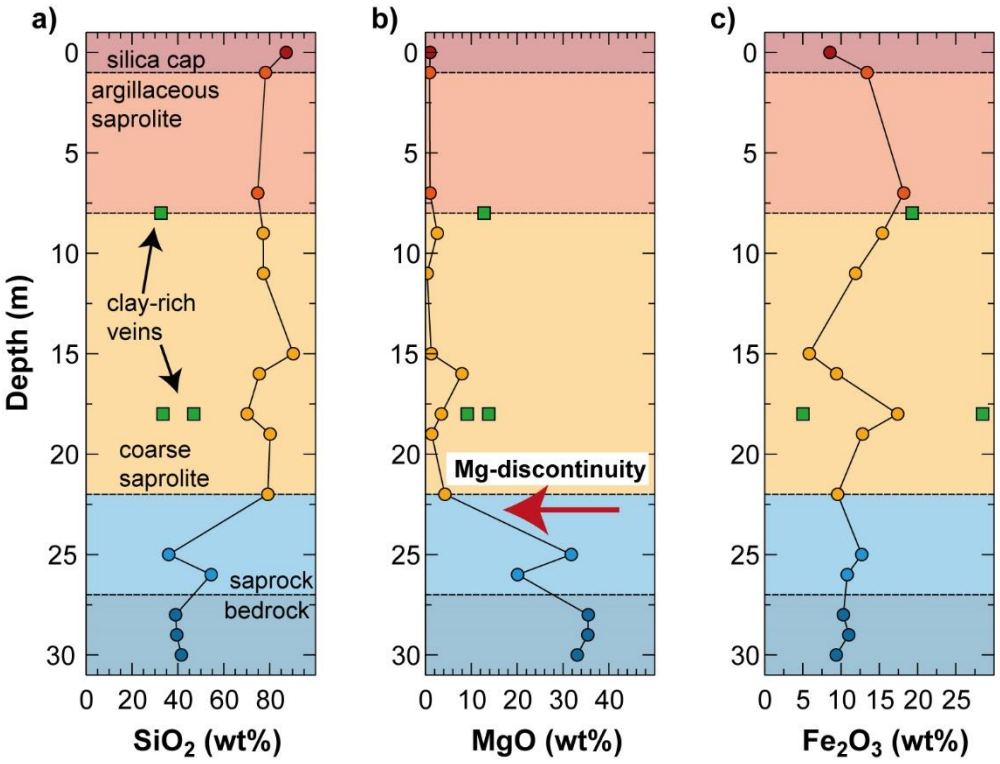

Fig. 3.5. Concentrations of **a)** SiO_2, **b)** MgO, and **c)** Fe_2O_3 in wt% in the São João do Piauí weathering profile. Circles represent host laterite and bedrock samples, whereas squares are from intercalated clay–rich vein samples. The horizontal dashed lines mark the transition between individual laterite horizons.

Concentrations of Ni, Co, Mn, and especially Cr are very variable (**Fig. 3.6**), in particular in the coarse saprolite. The Ni concentration of the bedrock is between 0.2 and 0.3 wt% and is highest in the overlying saprock (1.3 – 1.6 wt%). In the saprolite units, Ni concentrations vary between 0.1 and 1.0 wt% and show a preferred Ni accumulation in the lowest and in the central part of the coarse saprolite. The Co content increases from the bedrock (111 – 114 ppm) through the saprock (158 – 268 ppm) and the saprolite (84 – 241 ppm), with Co accumulation in the saprock and the lower coarse saprolite. Cr widely varies in the parent rock (0.4 – 1.0 wt%) and is also variable throughout the overlying laterite units (0.2 – 0.8 wt%). Mn contents range from 0.10 to 0.18 wt% MnO_2 in the bedrock and are slightly higher in the saprock and lower saprolite (0.12 – 0.20 wt%). The upper saprolite units show Mn contents of between 0.04 and 0.14 wt% MnO_2.

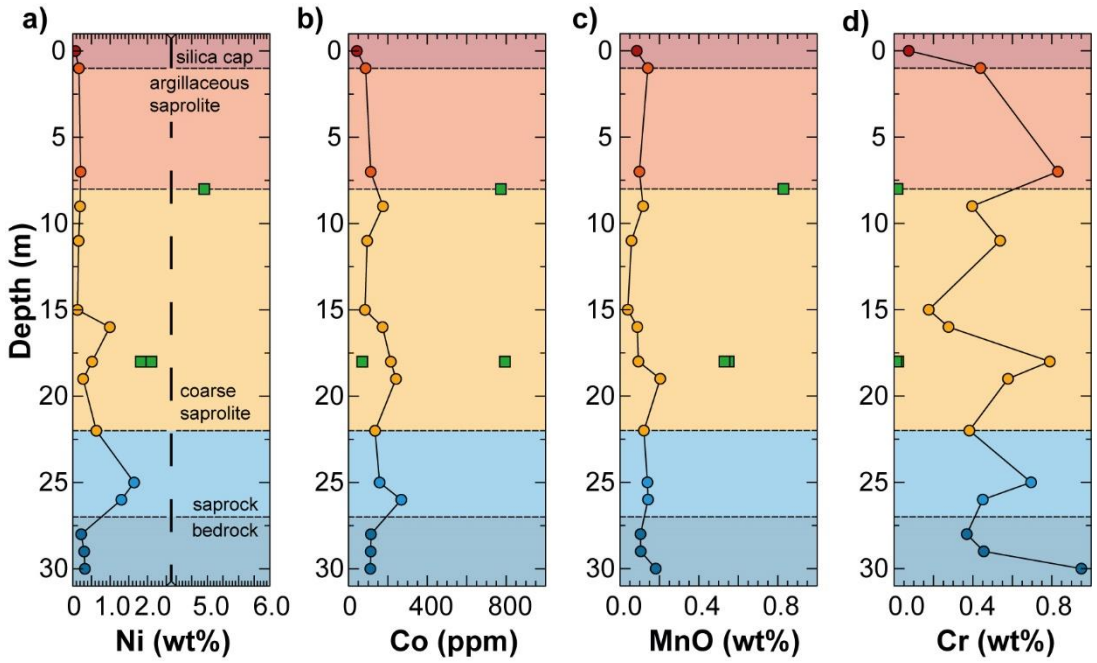

Fig. 3.6. Concentrations of **a)** Ni, **b)** Co, **c)** MnO, and **d)** Cr in the São João do Piauí weathering profile. Circles represent host laterite and bedrock samples, whereas squares are from intercalated clay–rich vein samples. The horizontal dashed lines mark the transition between individual laterite horizons.

Total REE concentrations are low in the unweathered bedrock (~0.2 ppm), very low in the saprock (~0.03 ppm), and slightly higher in the coarse (~0.8 ppm) and argillaceous saprolite (~0.9 ppm), although there are wide variations within the coarse saprolite that range between 0.1 and 3.1 ppm (**Fig. 3.8**). Mean total REE contents of the weathering products show moderate correlations (**Fig. 3.7**) with Rb (R^2 = 0.69; p–value = $5.7 \cdot 10^{-3}$) and with Cs (R^2 = 0.45; p–value = $4.5 \cdot 10^{-4}$).

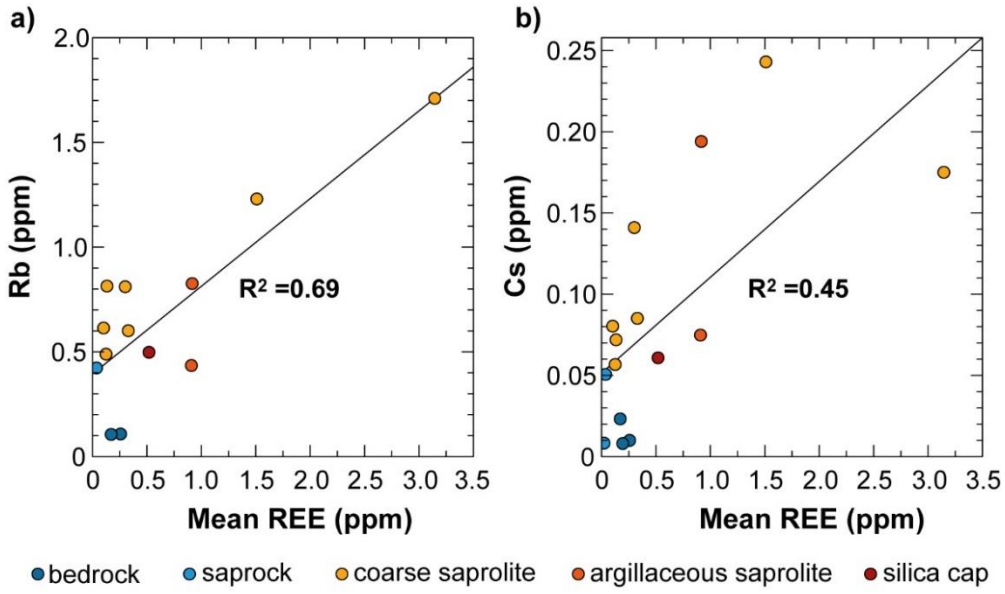

Fig. 3.7. **a)** Rb vs. average total REE concentration and **b)** Cs vs. average total REE concentration of host laterite samples of the 'open pit' weathering profile. The average total REE concentration and concentrations of Rb and Cs show moderate correlations, in particular in the coarse and argillaceous saprolite.

Chondrite normalised REE patterns of dunite parent rock samples are rather flat, with a negative Ce anomaly observed for B1 and B2 and a positive Eu anomaly in B3 (**Fig. 3.8**). The heavy REE (Tb – Lu) are slightly depleted compared to the light REE (La – Gd) in B1 and B2. The saprock is depleted in all REE, in particular in the light REE, compared to the bedrock. The REE patterns of coarse saprolite samples are more variable. Most samples (CS1, CS2, CS4, CS5, CS6) have REE contents slightly enriched or similar to the parent rock and show a pronounced negative Ce anomaly (**Fig. 3.8**). Samples CS1, CS2, CS5, and CS6 closely resemble the patterns of the bedrock samples B1 and B2. CS3 and CS7 are strongly enriched in the light REE compared to the bedrock and show a pronounced negative Ce anomaly. CS3 shows an enriched and flat pattern towards the heavy REE, whereas CS7 exhibits a rather steep slope towards the heavy REE and has Tm, Yb, and Lu concentrations similar to the parent rock. CS4 shows a small positive Eu anomaly and resembles the REE pattern of the parent rock sample B3. The argillaceous saprolite is enriched in the light REE compared to the parent rock and shows a flat pattern for the heavy REE with concentrations similar to the parent rock sample B3. Similarly, the silica cap is enriched in the light REE but has heavy REE concentrations rather similar to the parent rock. Overall, most of the laterite units show a limited REE fractionation relative to the parent rock, which in turn, has a relatively flat REE pattern. The saprock samples are depleted in all REE compared to the parent rock.

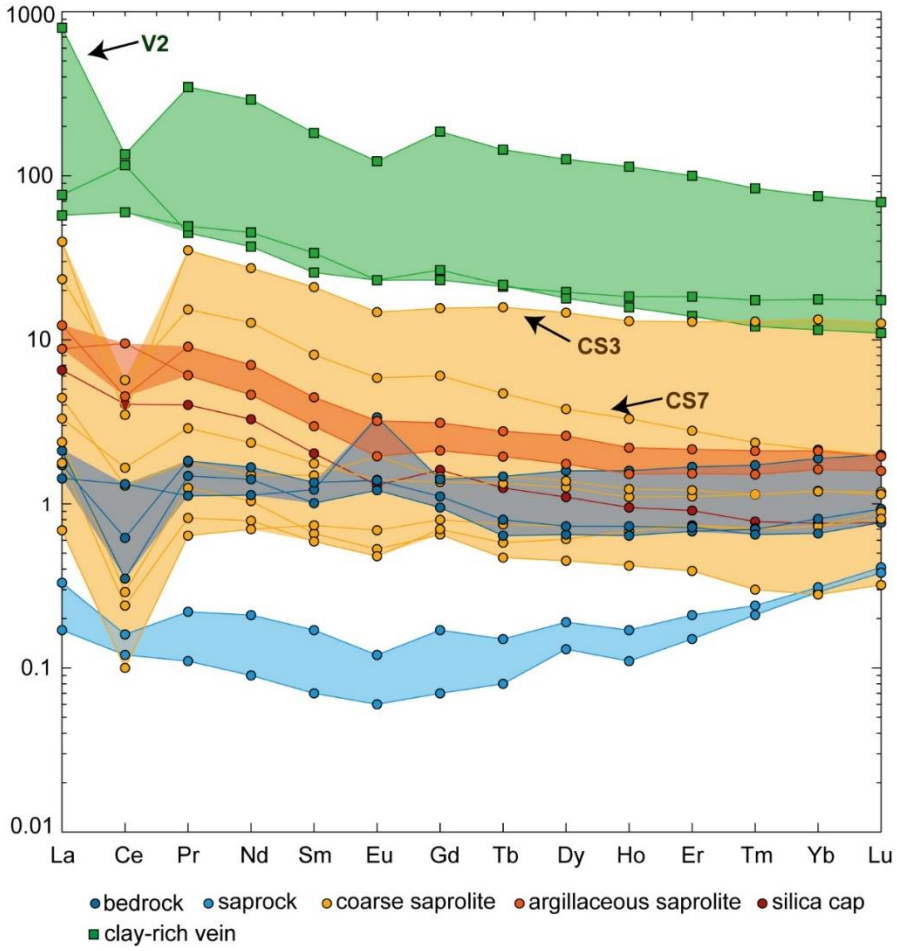

Fig. 3.8. Chondrite–normalised REE patterns of host laterite (circles) and vein samples (squares) from the São João do Piauí Ni deposit with highlighted fields for clay–rich veins (green), coarse saprolite (light orange), argillaceous saprolite (orange), saprock (light blue), and bedrock (blue). Most laterites show a flat REE pattern with a negative Ce–anomaly. Bedrock sample B3 shows a positive Eu–anomaly. The saprock is strongly depleted in the light REE, whereas veins are significantly enriched in the light REE. Chondrite values are from McDonough and Sun (1995).

3.5.2 Clay–rich veins

Clay–rich veins show SiO_2 contents of between 32.6 and 46.9 wt% and MgO contents of between 9.13 wt% and 13.8 wt% (**Fig. 3.5**). Unlike the host laterite units, SiO_2 concentrations do not increase towards the surface of the weathering profile, and the veins do not contain secondary precipitated silica. Al_2O_3 concentrations are between 10.5 and 19.8 wt%, which is 10 times higher than the concentrations in the dunite (~1.3 wt%) and the overlying laterite units (~1.0 wt%). The Fe_2O_3 content is more variable and ranges from 5.01 to 28.5 wt% (**Fig. 3.5**). The average concentration of the mobile elements CaO (0.14 wt%), Na_2O (0.80 wt%), and K_2O (0.16 wt%) is low, but higher than in the host laterite. TiO_2 contents are extremely variable and range between 0.18 and 3.81 wt%.

Ni, Co and Mn concentrations are significantly higher in the veins than in the dunite and the host laterite units. Ni is clearly enriched and shows concentrations of between 1.8 and 5.0 wt% with the highest Ni concentration in sample V2 in the upper part of the laterite. The Co content is low in V3 (70 ppm), but very high in V2 (773 ppm) and V4 (794 ppm). The MnO_2 concentration ranges between 0.5 and 0.8 wt%. Cr appears to be depleted in the veins compared to the surrounding host laterite units and has concentrations of between 119 and 212 ppm. Fluid mobile elements (Rb, Cs, Pb, Li, Zn; Aiuppa et al., 2000; Brusca et al., 2001) are consistently enriched in the veins compared to the host laterite units (**Table 3.2**). The average concentration of moderately mobile (e.g. Sc, V) and less mobile elements (e.g. Y, Nb, Th, Zr) is also considerably higher in the veins compared to the host laterite (**Table 3.2**). For example, Th concentrations (2 – 14 ppm) are about 150 times higher and Zr concentrations (22 – 69 ppm) are up to 60 times higher compared to the host laterite units and the dunite parent rock. Similarly, total REE concentrations are 20 to 40 times higher and reach several tens to hundreds of ppm (**Table 3.3**). The veins are strongly enriched in all REE with respect to chondrite and they show a moderate light REE enrichment compared to heavy REE (similar to CS7; **Fig. 3.8**). Sample V2 is highly enriched in the REE compared to chondrite, especially La (~1000 times chondrite).

Table 3.1. Major element content of laterite samples from the São João do Piauí weathering profile.

Depth (m)	Sample[a]	SiO_2 (wt%)	TiO_2 (wt%)	Al_2O_3 (wt%)	Fe_2O_3 (wt%)	MnO (wt%)	MgO (wt%)	CaO (wt%)	Na_2O (wt%)	K_2O (wt%)	TOC (wt%)	CO_2 (wt%)	H_2O (wt%)	LOI (wt%)	Total[b] (wt%)
LOD[c]			0.005								0.03	0.12	calc.	n.d.	–
Host Laterite (serpentinised dunite protolith)															
0	SC	87.2	0.022	0.772	8.54	0.085	1.01	0.063	0.642	0.025	0.16	b.d.	1.04	1.20	100.0
1	AS2	78.2	0.016	0.687	13.4	0.141	0.913	0.007	0.005	b.d.	0.03	b.d.	3.95	3.98	98.1
7	AS1	74.8	0.034	1.21	18.2	0.098	1.02	0.013	1.19	0.034	0.06	b.d.	3.83	3.89	101.7
9	CS7	77.2	0.010	0.841	15.4	0.117	2.59	0.022	0.576	0.039	0.15	b.d.	2.31	2.46	100.2
11	CS6	77.3	0.014	1.20	11.9	0.053	0.380	0.009	0.050	0.003	b.d.	b.d.	4.15	4.15	95.9
15	CS5	90.3	0.006	0.422	5.84	0.039	1.28	0.018	0.695	0.035	0.05	b.d.	2.20	2.25	101.3
16	CS4	75.5	0.014	1.06	9.41	0.088	7.97	0.015	0.966	0.032	b.d.	b.d.	6.53	6.53	103.0
18	CS3	70.2	0.022	1.86	17.4	0.093	3.48	0.039	0.118	0.007	b.d.	b.d.	3.51	3.51	98.2
19	CS2	80.2	0.017	1.24	12.8	0.204	1.37	0.012	1.40	0.040	0.03	b.d.	2.66	2.69	100.9
22	CS1	79.2	0.008	0.704	9.55	0.121	4.25	0.007	0.171	0.011	b.d.	b.d.	2.94	2.94	98.1
25	SR2	36.0	0.016	1.18	12.7	0.139	31.8	0.008	0.265	0.005	0.05	0.15	12.6	12.8	97.4
27	SR1	54.5	0.012	0.901	10.8	0.142	20.1	0.022	0.039	b.d.	0.04	0.13	9.07	9.24	97.6
28[d]	B3	39.0	0.074	1.33	10.3	0.104	35.5	0.065	0.185	b.d.	0.06	0.30	12.2	12.6	99.9
29[d]	B2	39.5	0.008	0.952	11.0	0.105	35.4	0.050	0.138	0.005	b.d.	0.12	13.0	13.1	101.1
30[d]	B1	41.5	0.017	1.67	9.37	0.181	33.1	0.044	0.290	0.017	0.07	0.15	11.2	11.4	99.0
Magnesite vein (product of serpentinised dunite weathering)															
21	V1	3.46	b.d.	0.052	0.473	0.015	44.9	0.207	0.258	b.d.	0.88	46.4	1.52	48.8	98.2
Clay–rich veins															
8	V2	32.6	3.81	10.5	19.3	0.829	12.8	0.082	1.36	0.189	0.03	0.15	10.7	10.9	97.8
18	V3	33.5	3.67	13.3	28.5	0.551	13.8	0.197	0.398	0.253	0.05	b.d.	5.00	5.05	101.6
18	V4	46.9	0.178	19.8	5.01	0.530	9.13	0.129	0.649	0.039	b.d.	b.d.	12.6	12.6	97.2

Note All data were obtained using X–ray fluorescence spectroscopy using fused sample discs (beads). Ti concentrations were obtained using pressed sample powder tablets. Host laterite refers to sample material that is representative for the particular location and depth within the weathering profile. Clay–rich veins refers to veins and layers that penetrate the host laterite. The detection limit (LOD) for all major elements is about 0.5 ppm.

b.d. Below detection limit

n.d. Not determined

calc Calculated; H_2O = LOI – TOC – CO_2

a Sample codifications: B=Bedrock, SR=Saprock, CS=coarse saprolite, AS=Argillaceous saprolite, SC=Silica cap, V=Magnesite vein or clay–rich vein

b Totals are calculated as the sum of all major elements, trace elements, and rare earth elements.

c Limit of Detection. The LOD is 0.5 ppm unless shown otherwise. LOD = Average concentration of blank + 3·(1SD)

d Virtual depth: the local bedrock was sampled next to weathering profile, as it does not outcrop in the excavated pit.

Table 3.2. Trace element content of laterite samples from the São João do Piauí weathering profile.

Depth (m)	Sample[a]	Ba (ppm)	Co (ppm)	Cs (ppm)	Cr (ppm)	Cu* (ppm)	Hf (ppm)	Li (ppm)	Nb (ppm)	Ni (ppm)	Rb (ppm)
LOD[b]		0.029	0.03	0.0003	0.0001	2	0.0003	0.01	0.0019	1	0.005
Host laterite (serpentinised dunite protolith)											
0	SC	30.4	42.6	0.061	745	39.4	0.061	5.53	0.212	695	0.498
1	AS2	67.3	87.1	0.075	4380	236	0.031	0.102	0.048	1670	0.435
7	AS1	29.4	113	0.194	8310	208	0.054	0.566	0.204	2130	0.826
9	CS7	20.1	175	0.175	3960	157	0.023	2.95	0.022	1970	1.71
11	CS6	18.8	95.1	0.085	5380	287	0.001	0.173	0.013	1590	0.601
15	CS5	65.9	83.8	0.072	1760	89.3	0.007	1.95	0.026	1280	0.814
16	CS4	61.5	173	0.141	2760	399	0.016	1.09	0.020	9910	0.811
18	CS3	68.3	215	0.243	7900	203	0.119	0.317	0.096	5180	1.23
19	CS2	61.2	241	0.057	5780	287	0.020	6.39	0.025	2790	0.489
24	CS1	53.8	135	0.080	3820	204	0.014	2.89	0.031	6320	0.614
25	SR2	36.0	158	0.008	6950	296	0.015	0.889	0.034	16400	b.d.
27	SR1	44.9	268	0.051	4500	177	0.019	0.987	0.047	13000	0.423
28[c]	B3	6.06	114	0.001	3690	17.9	0.140	0.698	0.266	2270	0.108
29[c]	B2	8.37	113	0.023	4550	147	0.028	0.322	0.072	3080	0.106
30[c]	B1	1.69	111	0.008	9500	8.20	0.027	0.403	0.056	3260	b.d.
Magnesite vein (product of serpentinised dunite weathering)											
21	V1	7.42	5.46	0.010	50.3	3.10	0.003	0.238	0.054	295	0.067
Clay–rich veins											
8	V2	108	773	7.59	171	612	2.74	29.9	39.6	49500	21.2
18	V3	194	70.1	14.1	212	819	0.772	52.2	10.4	21000	27.4
18	V4	422	794	1.56	119	1310	2.86	32.9	4.04	18200	3.16

Note	Data determined by ICP–MS unless otherwise stated. Host laterite refers to sample material that is representative for the particular location and depth within the weathering profile. Clay–rich veins refers to veins and layers that penetrate the host laterite weathering profile.
*****	Determined by XRF spectroscopy.
b.d.	Below detection limit
a	Sample codifications: B=Bedrock, SR=Saprock, CS=Coarse saprolite, AS=Argillaceous saprolite, SC=Silica cap, V=Magnesite vein or clay–rich vein
b	Limit of Detection. LOD = Average concentration of blank + 3·(1SD).
c	Virtual depth: the local bedrock was sampled next to the weathering profile, as it does not outcrop in the excavated pit.

Table 3.2. (Continued). Trace element content of laterite samples from the São João do Piauí weathering profile.

Depth (m)	Sample[a]	Pb (ppm)	Sc (ppm)	Sn (ppm)	Sr (ppm)	Th (ppm)	U (ppm)	V* (ppm)	Y (ppm)	Zn* (ppm)	Zr (ppm)
LOD[b]		0.005	0.022	0.012	0.018	0.0001	0.01	3	0.0015	2	0.022
Host Laterite (serpentinised dunite protolith)											
0	SC	5.09	3.26	0.088	1.90	0.57	0.195	23.7	1.77	31.3	1.75
1	AS2	5.28	7.34	0.033	0.882	0.097	0.155	43.1	2.34	52.6	1.24
7	AS1	1.20	9.32	0.090	1.52	0.17	0.265	50.7	3.02	117	1.76
9	CS7	0.967	5.07	0.043	0.993	0.016	0.259	26.7	15.2	141	0.595
11	CS6	0.423	6.29	0.030	1.15	0.009	0.283	41.5	1.55	91.1	0.320
15	CS5	0.193	2.58	0.045	0.757	0.098	0.073	14.9	1.14	43.7	0.185
16	CS4	0.889	6.02	0.057	1.13	0.010	0.061	34.9	2.00	207	0.610
18	CS3	6.17	7.38	0.078	5.07	0.054	0.056	49.2	5.59	149	4.00
19	CS2	0.537	6.29	0.047	0.800	0.026	0.044	39.6	1.77	78.3	0.743
24	CS1	0.294	4.38	0.239	0.970	0.017	0.062	29.2	1.38	63.6	0.457
25	SR2	0.352	1.44	0.052	0.932	0.010	0.017	43.8	0.196	87.7	0.524
27	SR1	0.311	5.04	0.045	1.34	0.014	0.121	36.4	0.325	113	0.632
28[c]	B3	0.361	5.68	0.080	1.31	0.053	0.142	35.5	2.61	68.9	4.71
29[c]	B2	1.15	5.72	0.158	1.51	0.039	0.198	32.7	1.42	86.7	1.01
30[c]	B1	0.226	0.800	0.074	0.687	0.015	0.340	46.3	1.61	122	0.938
Magnesite vein (product of serpentinised dunite weathering)											
21	V1	0.087	0.027	0.025	1.92	0.006	b.d.	b.d.	0.430	4.70	0.078
Clay–rich veins											
8	V2	3.94	52.3	3.93	7.16	3.2	2.30	164	238	570	69.0
18	V3	2.66	42.7	0.653	6.36	2.0	0.163	240	25.7	406	21.9
18	V4	14.3	8.15	0.635	13.0	14	0.906	19.7	32.8	426	60.9

Note	Data determined by ICP–MS unless otherwise stated. Host laterite refers to sample material that is representative for the particular location and depth within the weathering profile. Clay–rich veins refers to veins and layers that penetrate the host laterite weathering profile.
*****	Determined by XRF spectroscopy
b.d.	Below detection limit
a	Sample codifications: B=Bedrock, SR=Saprock, CS=Coarse saprolite, AS=Argillaceous saprolite, SC=Silica cap, V=Magnesite vein or clay–rich vein
b	Limit of Detection. LOD = Average concentration of blank + 3·(1SD)
c	Virtual depth: the local bedrock was sampled next to weathering profile, as it did not outcrop in the excavated pit.

Table 3.3. Rare earth element (REE) content of laterite samples from the São João do Piauí weathering profile.

Depth (m)	Sample[a]	La (ppm)	Ce (ppm)	Pr (ppm)	Nd (ppm)	Sm (ppm)	Eu (ppm)	Gd (ppm)	Tb (ppm)	Dy (ppm)	Ho (ppm)	Er (ppm)	Tm (ppm)	Yb (ppm)	Lu (ppm)
LOD[b]		0.01	0.005	0.0002	0.001	0.00015	0.00002	0.0002	0.00002	0.0001	0.00006	0.00008	0.00001	0.0003	0.00001
Host Laterite (serpentinised dunite protolith)															
0	SC	1.55	2.48	0.372	1.50	0.30	0.073	0.32	0.045	0.27	0.052	0.146	0.019	0.123	0.019
1	AS2	2.09	5.83	0.563	2.11	0.44	0.11	0.42	0.070	0.43	0.083	0.244	0.037	0.261	0.039
7	AS1	2.90	2.77	0.842	3.21	0.66	0.18	0.62	0.10	0.64	0.12	0.344	0.052	0.338	0.048
9	CS7	9.39	2.14	3.26	12.5	3.1	0.83	3.1	0.57	3.6	0.71	2.06	0.319	2.14	0.31
11	CS6	0.785	1.02	0.268	1.08	0.26	0.079	0.27	0.048	0.31	0.060	0.178	0.028	0.194	0.028
15	CS5	0.564	0.180	0.116	0.475	0.098	0.030	0.13	0.017	0.11	0.023	0.062	0.007	0.046	0.008
16	CS4	1.05	0.789	0.166	0.684	0.22	0.11	0.29	0.053	0.34	0.067	0.193	0.028	0.192	0.029
18	CS3	5.53	3.48	1.42	5.80	1.2	0.33	1.2	0.17	0.93	0.18	0.447	0.058	0.345	0.049
19	CS2	0.422	0.150	0.076	0.362	0.088	0.027	0.14	0.021	0.15	0.037	0.118	0.018	0.117	0.022
24	CS1	0.163	0.060	0.060	0.322	0.11	0.039	0.16	0.027	0.18	0.040	0.116	0.017	0.117	0.020
25	SR2	0.040	0.073	0.010	0.042	0.011	0.003	0.014	0.003	0.031	0.006	0.025	0.005	0.046	0.009
27	SR1	0.078	0.097	0.021	0.095	0.025	0.007	0.034	0.005	0.047	0.010	0.034	0.006	0.051	0.010
28[c]	B3	0.339	0.811	0.104	0.515	0.18	0.19	0.28	0.053	0.39	0.087	0.268	0.042	0.304	0.049
29[c]	B2	0.500	0.214	0.137	0.646	0.15	0.068	0.19	0.023	0.16	0.035	0.109	0.017	0.130	0.023
30[c]	B1	0.408	0.381	0.170	0.763	0.20	0.078	0.22	0.029	0.18	0.04	0.115	0.016	0.107	0.019
Magnesite vein (product of serpentinised dunite weathering)															
21	V1	0.142	0.159	0.053	0.244	0.08	0.013	0.096	0.015	0.097	0.018	0.047	0.006	0.040	0.006
Clay–rich veins (intercalated troctolite protolith)															
8	V2	189	82.8	32.2	133	27	6.9	37	5.2	31	6.2	16.0	2.07	12.1	1.7
18	V3	13.6	36.7	4.57	20.6	5.0	1.3	5.3	0.78	4.4	0.86	2.23	0.298	1.85	0.27
18	V4	18.1	71.0	4.16	16.9	3.8	1.3	4.6	0.76	4.8	1.0	2.93	0.431	2.84	0.43

Note	Data determined by ICP–MS unless otherwise stated. Host laterite refers to sample material that is representative for the particular location and depth within the weathering profile. Clay–rich veins refers to veins and layers that penetrate the host laterite weathering profile.
b.d.	Below detection limit
a	Sample codifications: B=Bedrock, SR=Saprock, CS=Coarse saprolite, AS=Argillaceous saprolite, SC=Silica cap, V=Magnesite vein or clay–rich vein
b	Limit of Detection. LOD = Average concentration of blank + 3·(1SD)
c	Virtual depth: local bedrock was sampled next to weathering profile, as it does not outcrop in the excavated pit

3.5.3 Degree of weathering

There are various geochemical indices that can be used to estimate the degree of weathering, including the chemical index of alteration (CIA ; Nesbitt and Young, 1982), the index of lateritisation (IOL; Schellmann, 1981), the Mg index (Maynard, 1992), and the ultramafic index of alteration (UMIA; Aiglsperger et al., 2016). In an attempt to quantify and visualise geochemical changes in the São João do Piauí weathering profile, the mafic index of alteration (MIA) was used (Babechuk et al., 2014). The MIA expresses weathering based on the loss of alkali– and alkali–earth–elements and relative gains of Al (and Fe). Unlike the CIA and IOL, it considers the redox–sensitivity of Fe and includes the Mg content of the sample, which is of particular importance during weathering of peridotites. SiO_2 is usually lost during weathering, in particular in well drained and humid climates (e.g. Gleeson et al., 2004; Butt and Cluzel, 2013). Thus, most weathering indices are conditioned to use the loss of SiO_2 to express progressive weathering. The MIA excludes the SiO_2 content (unlike the CIA or UMIA) and can therefore, be applied to Ni laterites that show silica enrichment due to arid weathering conditions. Weathering occurred near the paleo–surface at the São João do Piauí deposit, hence, Fe is considered to be present as Fe^{3+} and MIA values can be calculated as follows:

$$MIA(ox) = 100 \times \frac{Al_2O_3 + Fe_2O_3}{Al_2O_3 + Fe_2O_3 + MgO^* + CaO + Na_2O + K_2O} \quad (3.1)$$

The MIA is calculated using molar ratios of the major element oxides. MgO* is total MgO less Mg in carbonate, assuming that 1 mole MgO combines with 1 mole CO_2 to form 1 mole $MgCO_3$. MgO* is used instead of CaO* (Babechuk et al., 2014), as the predominant carbonate phase in the Ni laterite is Ca–poor magnesite (**Table 3.9**).

For dunites that weathered under oxidising conditions, MIA values basically monitor the Mg loss of primary silicates (e.g. olivine, serpentine, and chlorite) and the relative Fe gain due to the formation of secondary Fe–oxyhydroxides (goethite, hematite). Low MIA values indicate a high abundance of MgO, which is associated with the presence of primary Mg–silicates, and hence, represent unaltered rock. Increasing index values indicate progressively more altered rock material and a value of 100 signals a complete removal of MgO, CaO, Na_2O, and K_2O and their replacement with Fe–oxyhydroxides (*Equation 3.1*). The concentration of Al_2O3, CaO, Na_2O, and K_2O in dunites is generally low and does not significantly affect MIA values. However, fluid–induced rejuvenation of weathered rock material can lower MIA values.

MIA values of the weathering profile (**Fig. 3.9a**) generally increase upwards from the serpentinised bedrock (8), through the saprock horizon (10–13) and towards the lower coarse saprolite (39–62). The central coarse saprolite shows slightly lower MIA values of between 25 and 49, as MgO concentrations are rather higher (up to 7.97 wt%) than they are in the generally MgO–depleted coarse saprolite (0.31–4.14 wt%). The central coarse saprolite hosts abundant clay–veins and has the highest Ni concentration within the coarse saprolite (0.99 wt% Ni). MIA values further increase in the upper coarse saprolite (59 – 91) and in the argillaceous saprolite (74 – 81). Although Fe concentrations are very variable, the range of MIA values in the clay–rich veins is narrow (40 – 49), as the ratio between the sum of the mobile (Mg, Ca, Na, K) and immobile elements (Fe, Al) is similar.

A ternary AF–S–M (Al_2O_3 + Fe_2O_3 – SiO_2 – MgO) plot shows that the trend of increasing MIA values of the host laterite towards the top of the profile results from Mg loss rather than from residual Fe gain. Continuous weathering of Mg–silicates leads to the formation of microscopic voids. Si is gained, which ‘dilutes’ the primary rock material, and balances Mg losses. Fe remains constant, which results in a horizontal trend in the plot (**Fig. 3.9b**). The clay–rich veins show a rather typical, combined loss of Mg and Si that leads to a relative Fe enrichment and a vertical trend in the AF–S–M plot.

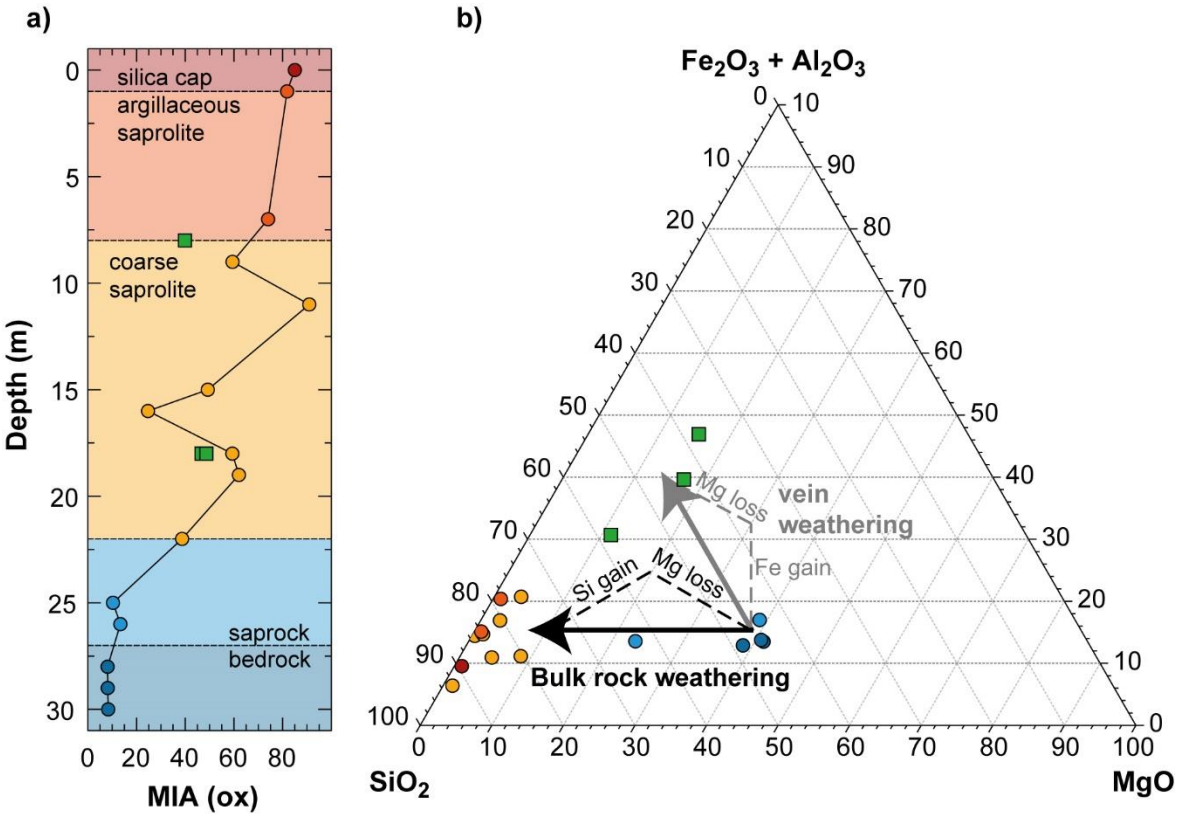

Fig. 3.9 a) The mafic index of alteration (MIA) trend of the São João do Piauí weathering profile. **b)** AF–S–M plot of laterite and clay–rich vein samples. Samples from the host laterite and clay–rich vein samples exhibit two different weathering trends. Weathering of the host laterite led to Mg loss and Si gain. The Fe content remains stable, which means that the amount of lost Mg equals the amount of gained Si (similar length of lines in plot). The vein samples show a loss of Mg, whereas Fe is gained during weathering and Si remained constant, assuming that the veins originate from weathering of rock material similar to the parent rock composition of the host laterite.

3.6 Profile mineralogy

Fig. 3.10 gives an overview of the mineralogy of the weathering profile, determined by XRD, optical microscopy and microprobe analysis, in a simplified stratigraphic profile derived from a combination of the geologic sections in **Fig. 3.4**. A summary of the relative abundances of identified major mineral groups is presented in **Fig. 3.11**.

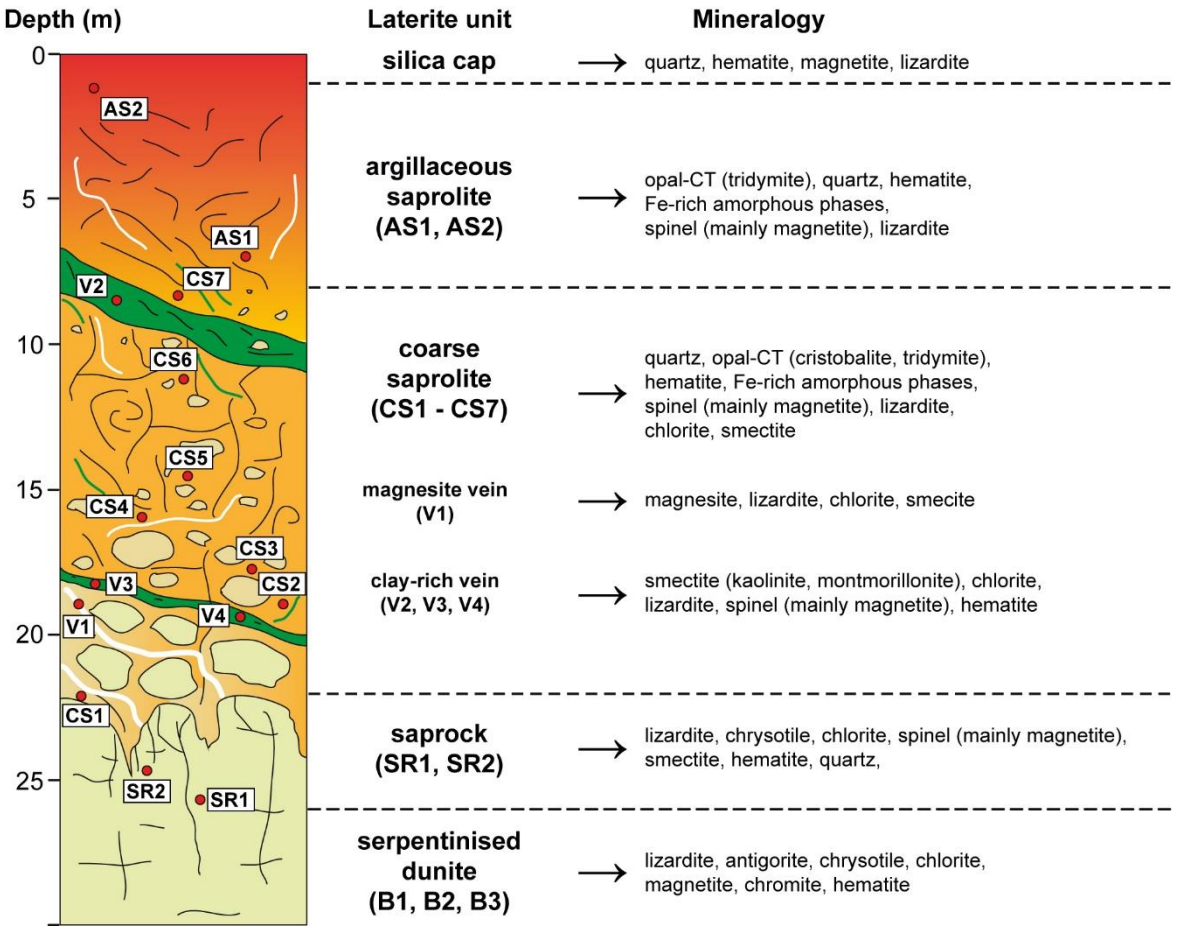

Fig. 3.10. Simplified stratigraphic profile of the São João do Piauí weathering profile divided into main units with the predominant mineralogy. Strongly serpentinised dunite (B samples) grades into a relatively narrow saprock zone (SR samples), which underlies a thick coarse saprolite horizon (CS samples). Argillaceous saprolite (AS samples) is present at shallower depths. The profile is capped by a siliceous horizon (SC sample). Clay–rich zones (V samples) occur throughout the entire profile, in particular in the coarse saprolite. In places, magnesite veins occur, in particular in the saprock and argillaceous saprolite.

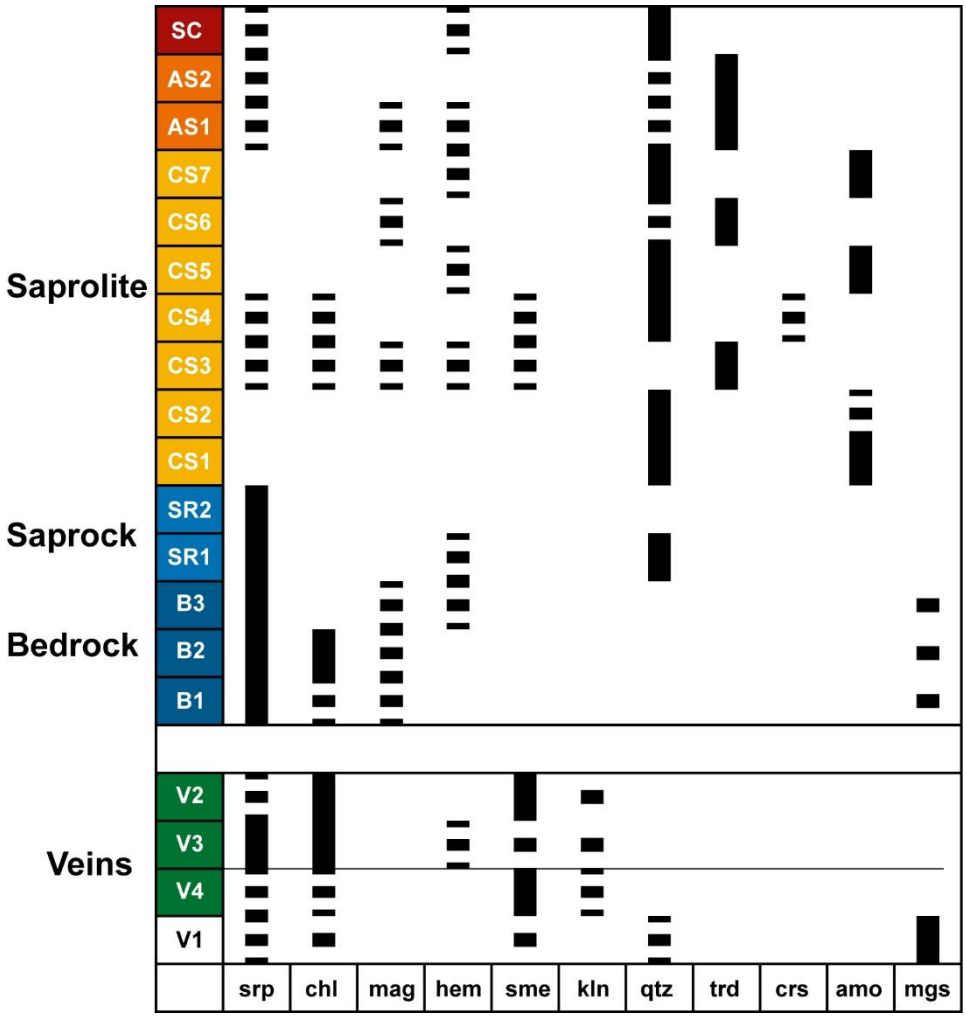

Fig. 3.11. Relative mineral abundances of host laterite and vein samples. Mineral abbreviations are from Siivola and Schmid (2007). Mag (magnetite) includes Fe–rich magnetite, Ti–rich magnetite, Cr–rich magnetite, and chromite. Amo = amorphous phase. Solid lines represent major mineral phases (>30%), dashed lines represent minor mineral phases (<30%), and single squares represent identified, but not quantified mineral phases that occur in trace amounts.

3.6.1 Bedrock (serpentinised dunite)

The bedrock (B1, B2, and B3) is a fine–grained serpentinised dunite with Mg–rich serpentine (srp) and chlorite (chl) as main minerals (**Table 3.4**). Cr–rich magnetite (mag) is the main accessory phase (**Table 3.5**). Unaltered bedrock has a bluish to greenish colour and shows poorly orientated brown veinlets, which are characteristic for serpentinised dunites (Aumento and Loubat, 1971). The bedrock is texturally heterogeneous with varying mineral abundances, in particular the relative amount of primary oxides fluctuates.

Lizardite is the main serpentine polymorph and has a tabular to prismatic habit. The lizardite pseudomorphically replaces the primary euhedral olivine in a typical hour glass structure (**Fig. 3.12c**). Incipient alteration of the bedrock may be identified by the presence of SiO_2–enriched serpentine crystals (**Fig. 3.13a**) and hematite (hem) in sample B3. Dissolution of serpentine progresses along trans–granular cracks and mineral edges (**Fig. 3.12a, b**). Chrysotile is present as finely disseminated mm–sized veins and in places, it forms veins of several cm. The chrysotile consists of fibrous filaments (asbestos) that are aligned normal to the vein walls (**Fig. 3.12e, f**). Chrysotile shows a high birefringence in altered parts, which indicates elevated Ni contents (Deer et al., 2013). The presence of antigorite indicates prograde orogenic serpentinisation of the dunite (Moody, 1976; Wicks and Whittaker, 1977). Chlorite occurs as interstitial mineral aggregates and along trans–granular cracks and fractures of serpentine. None of the parent rock samples contain quartz (qtz). Secondary Cr–poor magnetite forms between serpentine grains or as localised nests and is particularly abundant within chrysotile veins (**Table 3.6**). In places, altered bedrock contains small amounts of brucite, talc and magnesite (mgs) that were identified by their relatively high birefringence.

3.6.2 Saprock

The saprock (SR1, SR2) consists of fine–grained, solid rock material with a low density that shows a bright brown to ochre colour and a pronounced mesh and mosaic–like texture, due to progressive serpentine dissolution, which leads to an accentuation of Fe–oxides that then appear as shiny black to silver crystals. Altered primary serpentine is the dominant Ni host (**Fig. 3.13c** and **Table 3.4**). Quartz is present as inter–granular fillings between variably decomposed serpentine grains and secondary Cr–poor magnetite. Dark brown serpentine cores reflect oxidative dissolution and associated hematite formation (**Fig. 3.12c, d**). Deformed chrysotile with interstitially grown magnetite indicates brittle tectonic activity during weathering (**Fig. 3.12e, g**). The saprock samples show no significant carbonate or talc accumulations, however, in places, magnesite veins up to a few cm thickness (sample V1) are abundant and a few grade up into the saprolite. Fine–grained talc is usually present as fractures fillings and exhibits a bright white colour and a high purity.

Table 3.4. Representative compositions of variably altered serpentine from different horizons. Element oxides are given in wt%

Horizon	parent rock		saprock/ coarse saprolite			argillaceous saprolite			
serpentine	unaltered	SiO_2–enriched	Mg–depleted	Ni–enriched	SiO_2–enriched	high Fe	high – moderate Fe	moderate – low Fe	low Fe
	Fig. 3.13a	**Fig. 3.13a**	**Fig. 3.13b**	**Fig. 3.13c**		**Fig. 3.13d**			
Number of analyses	n = 13	n = 5	n = 8	n = 9	n = 6	n = 3	n = 18	n = 17	n = 30
SiO_2	44.2	89.9	39.2	34.2	91.4	43.3	67.2	76.5	84.1
Al_2O_3	0.22	0.13	0.88	0.03	0.08	0.40	0.25	0.18	0.13
MgO	38.3	2.07	31.3	25.8	4.42	0.79	0.49	0.17	0.11
CaO	0.06	<0.04	<0.04	<0.04	<0.04	<0.04	<0.04	<0.04	<0.04
TiO_2	<0.03	<0.03	<0.03	<0.03	<0.03	0.04	<0.03	<0.03	<0.03
MnO	<0.04	<0.04	0.28	0.14	<0.04	0.39	0.27	0.10	<0.04
FeO	1.63	0.18	2.81	3.49	3.36	43.0	19.8	9.15	1.94
CoO	<0.02	<0.02	0.03	<0.02	<0.02	0.14	0.03	<0.02	<0.02
NiO	0.49	0.05	0.16	2.62	0.51	1.43	0.37	0.20	0.05
Cr_2O_3	<0.03	<0.03	<0.03	<0.03	0.04	1.50	0.82	0.39	0.09
Total	85.1	92.4	74.9	66.6	100.0	91.4	89.4	86.9	86.6

Note: Totals are calculated from the full range of analysed elements, including Na, Si, Al, Mg, K, Cl, Ca, Ti, Mn, Fe, Co, Ni, Cr, S, Cu, Zn, Ba, Sc, V, and P. Mineral compositions reflect average chemical compositions of individual spot analyses of one or more crystal grains by electron probe micro–analyser (EPMA).

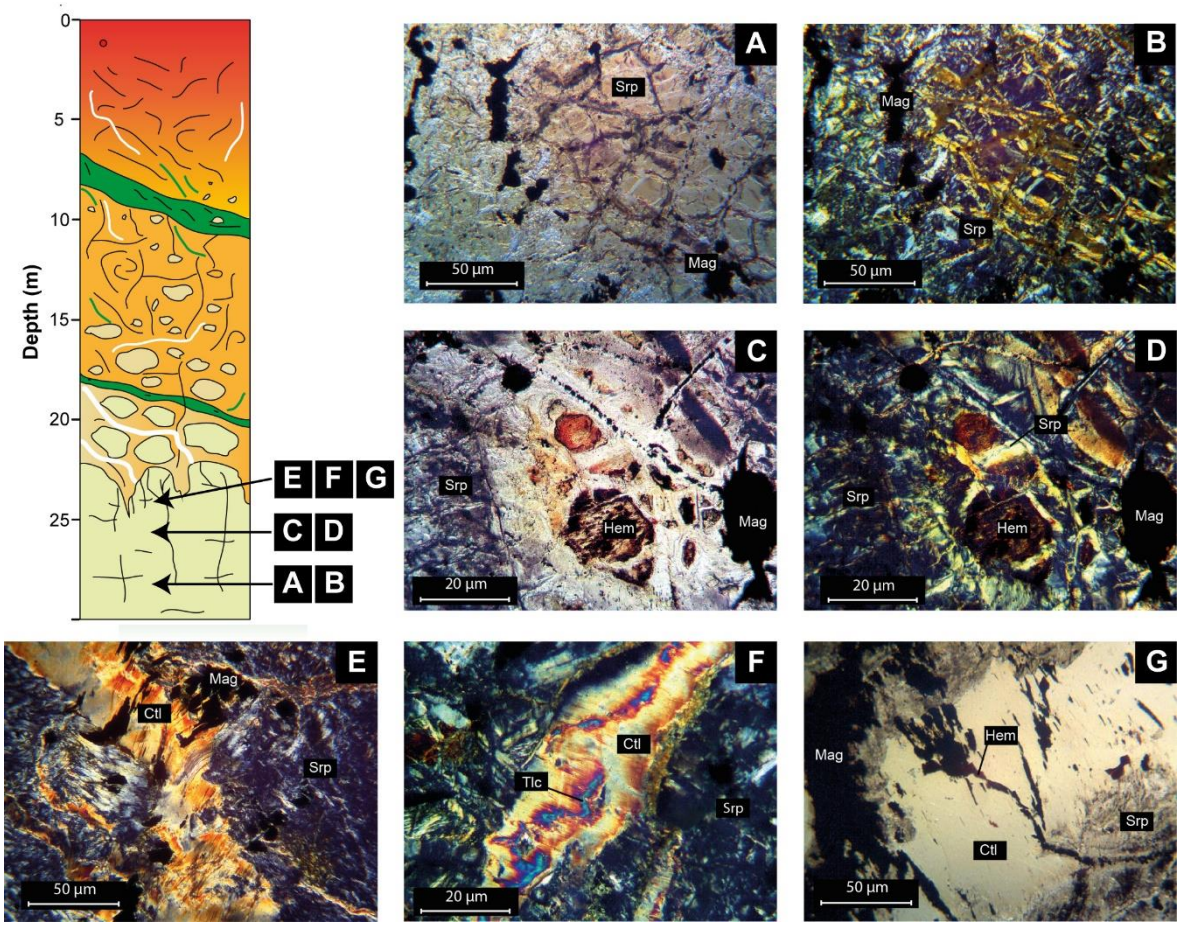

Fig. 3.12 Thin section photos of the mineral assemblages of the parent rock (A, B), and saprock (C, D, E, F, G). **a, b)** Strongly serpentinised olivine grains (srp) in a typical mesh–network texture with abundant primary and secondary magnetite (mag) under (A) plain–polarised light (PPL), and (B) crossed–polarised light (XPL), respectively. The yellow–brownish intergranular cracks are oxidised Fe–rich mineral veins that reflect incipient serpentine weathering. **c, d)** Pseudomorph replacement of hour–glass shaped serpentine by a mixture of magnetite (mag) and hematite (hem) under (C) plain–polarised light (PPL), and (D) under crossed–polarised light (XPL), respectively. **e, f, g)** Deformed, fibrous chrysotile with interstitially grown magnetite and talc (tlc) from serpentine dissolution indicates syn–tectonic activity during weathering.

Table 3.5. Representative compositions of primary Cr–rich magnetite and chromite. Element oxides are given in wt%.

Horizon (oxide)	bedrock (Cr–magnetite)	coarse saprolite (magnesio–chromite)		
		core	mantle	rim
	Fig. 3.13a	**Fig. 3.13e**		
Number of analyses	n = 9	n = 4	n = 4	n = 4
Al_2O_3	0.60	34.8	4.60	0.12
MgO	3.25	10.8	1.38	0.12
TiO_2	0.43	0.42	0.31	0.02
MnO	3.54	0.15	0.40	0.12
FeO	16.9	6.25	13.6	27.3
Fe_2O_3	41.8	15.5	33.7	67.4
NiO	0.15	0.16	0.22	<0.04
CoO	0.07	<0.02	<0.02	<0.02
Cr_2O_3	29.9	31.2	25.3	0.46
Total	98.1	99.8	89.4	96.5

Note: Totals are calculated from the full range of analysed elements, including Na, Si, Al, Mg, K, Cl, Ca, Ti, Mn, Fe, Co, Ni, Cr, S, Cu, Zn, Ba, Sc, V, and P. Mineral compositions reflect average chemical compositions of individual spot analyses of one or more crystal grains by electron probe micro–analyser (EPMA).

Table 3.6. Representative compositions of Cr–poor (secondary formed) magnetite. Element oxides are given in wt%.

Horizon	bedrock	coarse saprolite		argillaceous saprolite
		Fig. 3.13f		
Number of analyses	n = 13	n = 15	n = 15	n = 2
Al_2O_3	0.05	<0.04	<0.04	0.10
MgO	0.91	0.26	0.25	0.12
TiO_2	0.10	<0.03	<0.03	<0.03
MnO	0.36	0.42	0.37	0.18
FeO	27.0	28.4	27.9	26.5
Fe_2O_3	66.7	70.3	69.0	65.5
NiO	0.17	<0.04	<0.04	0.10
CoO	<0.02	<0.02	<0.02	<0.02
Cr_2O_3	2.65	0.04	0.30	0.50
Total	98.5	100.0	98.6	94.2

Note: Totals are calculated from the full range of analysed elements, including Na, Si, Al, Mg, K, Cl, Ca, Ti, Mn, Fe, Co, Ni, Cr, S, Cu, Zn, Ba, Sc, V, and P. Mineral compositions reflect average chemical compositions of individual spot analyses of one or more crystal grains by electron probe micro–analyser (EPMA).

3.6.3 Coarse saprolite

The coarse saprolite (samples CS1 – CS7) represents the major unit of the Ni laterite and shows a variable colour ranging from pale yellow to deep red, which reflects the relative amount of hematite. The adcumulate parent rock fabric is almost perfectly preserved by infiltration of secondary silica into the original serpentine mesh structure. Serpentine and chlorite show a high degree of decomposition and relicts are only preserved in the lowermost and central part of the coarse saprolite, where they occur together with small amounts of Ni–rich smectite. The Ni concentration in the coarse saprolite is very variable and broadly correlates with the presence of Ni–enriched serpentine (**Fig. 3.13c**). Hematite that likely originates from goethite dehydration shows low Ni concentrations (**Table 3.7**). Secondary magnetite occurs as large euhedral to subhedral crystals (**Fig. 3.13f**). Tridymite and cristobalite are present as micro–crystalline cement in the mineral assemblage. Amorphous phases can be abundant in the saprolite, consisting of secondary silica (chalcedony) and cryptocrystalline Fe–rich phases. In the lower part of the saprolite horizon, secondary magnetite has formed on primary chromite (**Fig. 3.13e**), whereas the relative amount of spinel decreases towards the uppermost surface of the coarse saprolite horizon and into the overlying argillaceous saprolite. Decreasing amounts of spinel are associated with continuous hydrolysis and the formation of Fe–rich hydroxides and Fe–oxides, with no visible crystals, and a yellow–brown streak; this assemblage is commonly referred as 'limonite' (**Fig. 3.14b, d**), although a classic limonite horizon in which the parental rock fabric has been lost is absent in the profile.

Table 3.7. Representative compositions of hematite from different laterite horizons. Element oxides are given in wt%.

Laterite horizon	Coarse saprolite		Argillaceous saprolite	Silica cap
Number of analyses	n = 6	n = 10	n = 3	n = 5
SiO_2	0.47	0.87	1.76	1.16
TiO_2	<0.03	0.05	0.04	0.04
MnO	0.39	0.28	0.24	0.43
Fe_2O_3	98.6	96.4	95.0	95.4
CoO	<0.02	<0.02	<0.02	<0.02
NiO	0.05	<0.04	0.10	<0.04
Cr_2O_3	0.06	1.93	0.47	1.94
Total	99.9	100.00	98.0	99.3

Note: Totals are calculated from the full range of analysed elements, including Na, Si, Al, Mg, K, Cl, Ca, Ti, Mn, Fe, Co, Ni, Cr, S, Cu, Zn, Ba, Sc, V, and P.

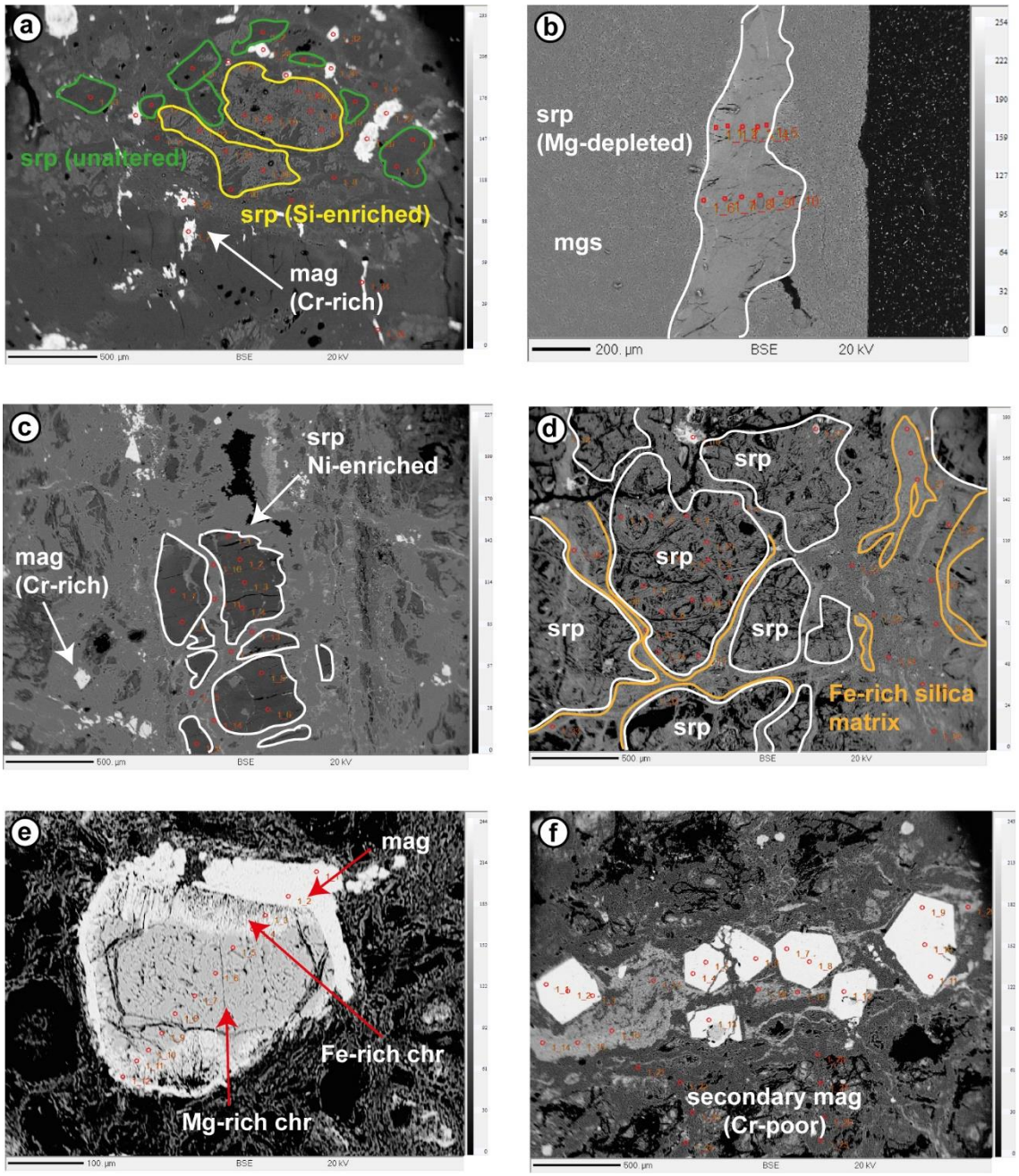

Fig. 3.13. BSE images of variably altered serpentine minerals from different laterite horizons (a, b, c, d), and primary (e) and secondary (f) oxides. **a)** Incipient weathering of serpentine in the parent rock is characterised by a loss of Mg and retention of SiO_2 (**Table 3.4**). **b)** Mg–depleted serpentine remnant (**Table 3.4**) in magnesite vein (**Table 3.9**) sampled nearby the saprock horizon. **c)** Ni–enriched serpentine (**Table 3.4.**) in a matrix of variably decomposed serpentine and secondary silica representative for saprock and the lower coarse saprolite. **d)** The presence of strongly altered Fe–rich serpentine remnants (**Table 3.4**) in a Fe–rich silica matrix is characteristic for the argillaceous saprolite. **(e)** Mg–rich primary chromite with a Fe–rich dissolution mantle and a secondary magnetite–rich rim (**Table 3.5**). **(f)** Secondary formed, subhedral magnetite within a coarse saprolite sample (**Table 3.6**).

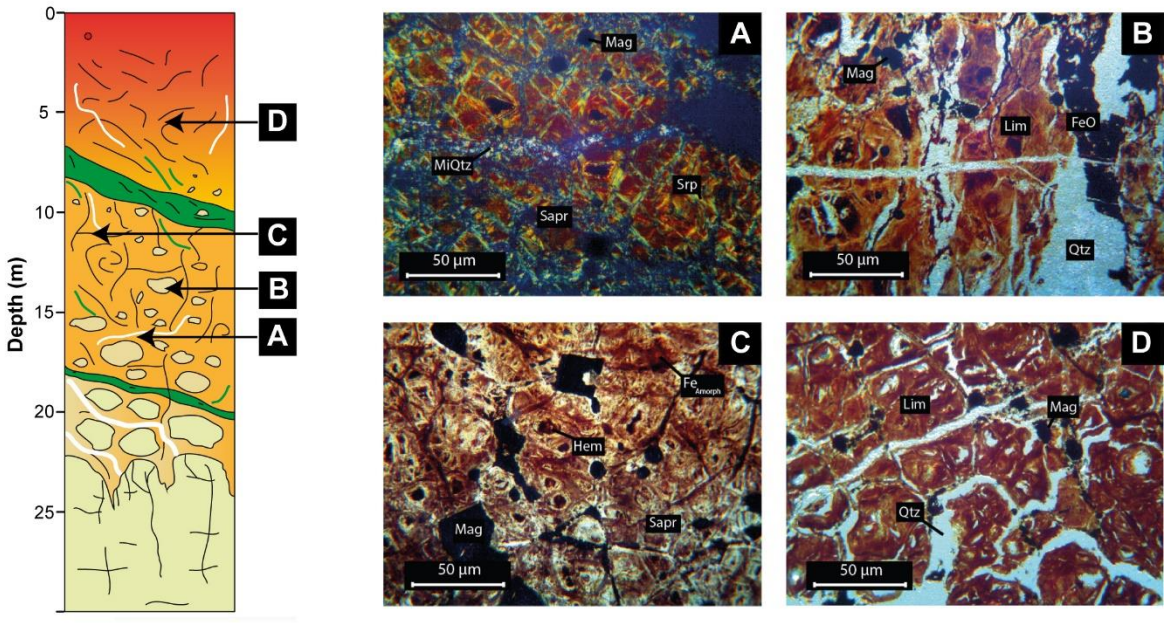

Fig. 3.14. Thin section photos of the main mineral assemblages in the coarse (a, b, c), and argillaceous saprolite (d). **a, xpl)** Relic texture of strongly hydrolysed serpentine (srp) in which the original minerals are replaced with an iron– and silica–rich amorphous mass or with finely disseminated hematite aggregations (sapr). Secondary silica infiltrated interstitial mineral spaces are precipitated as micro–crystalline quartz (miqtz). **b, ppl)** Typical rock texture in the upper part of the coarse saprolite, in which spherical weathering of individual serpentine relicts is dominant. The former presence of serpentine can only be inferred due to the stabilising anastomosing quartz network that preserves the primary rock texture. **c, ppl)** relatively silica–poor section of upper coarse saprolite with subhedral, secondary crystallised magnetite (mag). The primary rock texture is visible upon former grain boundaries that were replaced with magnetite aggregations. **d, ppl)** Dominating rock texture of the argillaceous saprolite, in which former serpentine grains are completely replaced by a microcrystalline aggregation of hematite and secondary silica in between a network of quartz and rounded magnetite that is slowly altered to hematite.

3.6.4 Argillaceous saprolite

The argillaceous saprolite (AS1, AS2) is less variable in colour and is more reddish brown compared to the underlying coarse saprolite. Original textural elements are only present as relicts and authigenic weathering products are rare. The argillaceous saprolite is dominated by secondary silica and hematite (**Table 3.7**) with small amounts of secondary magnetite (**Table 3.6**), and some remnants of strongly decomposed serpentine (**Table 3.4**). However, preserved serpentine minerals are rare and replaced by silica and amorphous Fe–rich phases. In places, the argillaceous saprolite is allochthonous and shows variable amounts of brecciated rock material in a silica–dominated matrix. Sample AS1 is an admixture of in–situ formed saprolite and high amounts of brecciated saprolite that stems from the top of the local plateau and was re–deposited at lower depths down on the flank of the hill as ferricrete (e.g. Widdowson, 2008). In this connection, the term ‘laterite’ refers to in–situ altered rock, whereas ‘ferricrete’ describes material with a large allochthonous input (e.g. Aleva, 1994).

3.6.5 Siliceous cap

A siliceous horizon is present at the top of the weathering profile, which protects the underlying regolith units from erosion. The siliceous cap has a bright to deep red colour and is dominated by mosaic coarse grained quartz with hematite, magnetite and identified relics of primary serpentine. The silica cap sample (SC) is considered to be the ultimate residual product of dunite weathering that may be expected under arid weathering conditions, as proposed by Butt (2014).

3.6.6 Magnesite veins

Magnesite veins (V1) of various size occur throughout the profile, in particular in the saprock and argillaceous saprolite (**Fig. 3.15a**). In the coarse saprolite, veins are either absent or relatively small and reach only a few mm thickness. They mainly consist of relatively pure magnesite (**Table 3.9**) with interstitially grown secondary silica and enclose Mg–depleted serpentine remnants (**Fig. 3.13b**).

3.6.7 Clay–rich veins and layers

The Ni laterite is characterised by the abundant presence of clay–rich veins and layers (V2, V3, V4) that pervade the entire profile. Their width varies between a few centimetres and ~3 m. Small veins have individual lengths between 0.5 and 1.5 m, whereas wide layers can be traced throughout the profile (**Fig. 3.4**). The veins and layers appear to be similar orientated within the laterite (**Fig. 3.3c**), which creates a 'network' of clay–rich zones. The layers often show a sharp contact between the surrounding host laterite, while the veins usually end in the form of small fingers within the host laterite. The veins and layers mainly consist of variable amounts of serpentine, chlorite and Ni–rich smectites (**Fig. 3.15b, c, d** and **Fig. 3.16**). Kaolinite was also identified. Ni–rich smectite is the main Ni host together with asbolane that additionally has a high Co content (up to 16.4 wt% NiO; **Table 3.8**). Al–bearing serpentine was identified as progenitor of Ni–rich smectite (**Table 3.10**). The presence of Mn–rich anastase (**Table 3.9**) in two vein samples (V2 and V3) is associated with high whole–rock Ti concentrations.

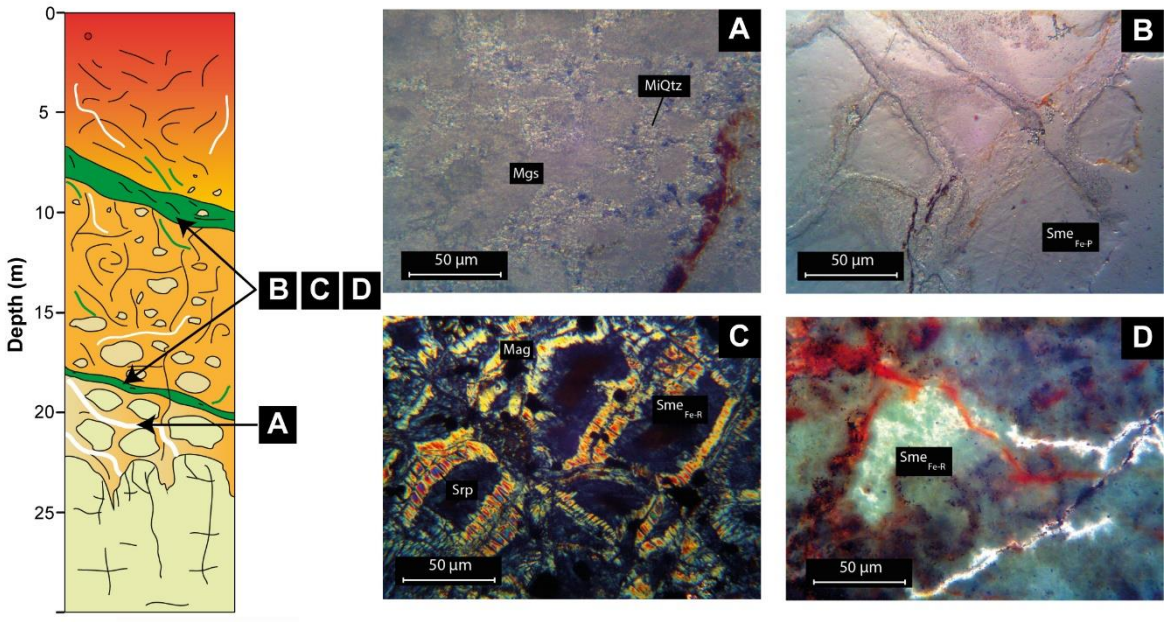

Fig. 3.15. Thin section photos of the main mineral assemblages in (A) magnesite veins and (B, C, D) clay–rich veins. **a, ppl)** Magnesite–rich (mgs) fracture fillings with interstitially grown micro–crystalline quartz (miqtz). **b, ppl)** Ni–bearing smectite with a low Fe content ($sme_{Fe\text{-}P}$) with a typical pale grey colour. **c, xpl)** Spheroidal weathering of serpentine and associated Fe–rich smectite ($sme_{Fe\text{-}R}$) formation within core remnants of old serpentine grains. **d, ppl)** Green to teal coloured Ni–rich smectite with small hematite (red) and talc (white) veins. This is the main type of smectite in vein samples and is responsible for its macroscopic appearance.

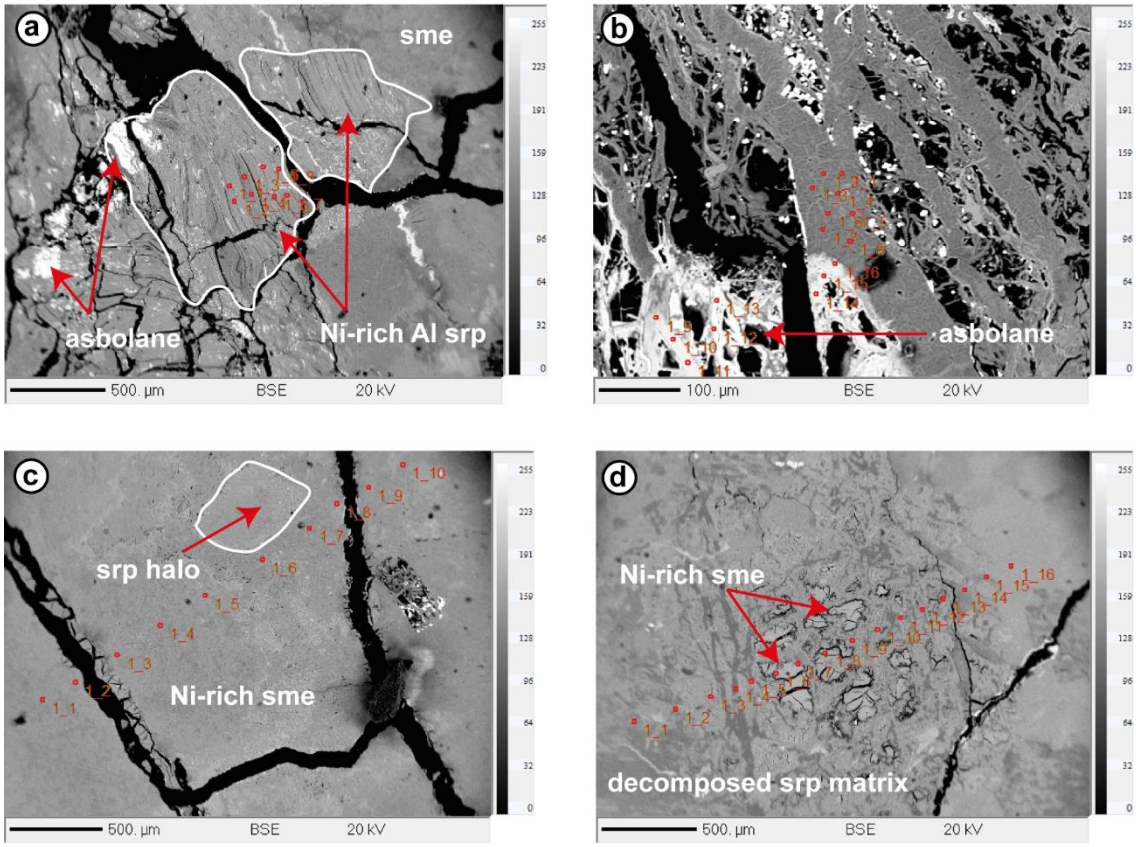

Fig. 3.16. BSE images of Ni minerals in clay–rich veins (**Table 3.8 and 3.10**). **(a)** Formation of Ni–rich smectite from Al–bearing serpentine (probably brindleyite) with additional formation of Ni– and Co–rich asbolane. **(b)** Asbolane formation within smectite–bearing veins. **(c)** Highly crystalline Ni–rich smectite forming between transgranular rock fissures. **(d)** Direct smectite formation from strongly decomposed Al–bearing serpentine (**Table 3.10**).

Table 3.8. Representative compositions of Ni and Co–bearing minerals in clay–rich veins. Element oxides are given in wt%.

Mineral	Ni–rich (Al) serpentine (brindleyite)	Mg–rich smectite (Ni–nontronite)	Fe–rich smectite (Ni–nontronite)	Ni and Co– rich oxyhydroxide (asbolane)
	Fig. 3.16a	**Fig. 3.16b**	**Fig. 3.16d**	**Fig.3.16a, b**
Number of analyses	n = 8	n =34	n =2	n =2
SiO_2	35.6	48.6	34.7	1.43
Al_2O_3	14.0	13.3	13.8	2.62
MgO	18.0	14.1	21.9	3.06
CaO	0.07	0.07	<0.04	<0.04
K_2O	0.32	<0.04	<0.04	0.04
Na_2O	0.09	0.12	<0.06	0.22
TiO_2	1.19	<0.03	<0.03	0.08
MnO	0.56	0.05	0.34	41.3
FeO	12.6	2.43	13.1	0.77
CoO	0.07	0.09	<0.02	5.82
NiO	6.83	11.5	3.18	16.4
Cr_2O_3	<0.03	0.11	0.05	<0.03
Total	89.5	90.8	87.4	73.8

Note: Totals are calculated from the full range of analysed elements, including Na, Si, Al, Mg, K, Cl, Ca, Ti, Mn, Fe, Co, Ni, Cr, S, Cu, Zn, Ba, Sc, V, and P.

Table 3.9. Representative compositions of magnesite and secondary Mn–rich anastase. Element oxides are given in wt%.

Mineral	magnesite	Mn–rich anastase
	Fig. 3.13b	
Number of analyses	n = 6	n = 5
SiO_2	<0.05	<0.05
Al_2O_3	<0.04	<0.04
MgO	49.2	0.14
CaO	0.49	<0.04
K_2O	<0.04	<0.04
Na_2O	<0.06	<0.06
TiO_2	<0.03	53.1
MnO	<0.04	5.96
FeO	0.24	40.4
CoO	<0.02	<0.02
NiO	0.09	0.05
Cr_2O_3	<0.03	<0.03
Total	50.4	99.9

Note: Totals are calculated from the full range of analysed elements, including Na, Si, Al, Mg, K, Cl, Ca, Ti, Mn, Fe, Co, Ni, Cr, S, Cu, Zn, Ba, Sc, V, and P.

Table 3.10. SEM analysis of Ni–rich smectite formation from an Al–rich decomposed serpentine matrix (**Fig. 3.16d**) in clay–rich veins. Element oxides are given in wt%.

Spot Number	1	2	3	4	5	6	7	8	9	10	11	12	13	14	15	16
SiO_2	33.1	41.5	34.9	35.4	40.4	48.9	49.3	50.6	35.4	35.2	34.3	29.8	40.0	45.6	34.0	42.9
Al_2O_3	21.3	13.1	16.7	13.8	14.0	8.77	9.75	8.87	15.2	13.2	14.5	9.52	12.7	12.2	14.9	12.0
MgO	25.7	23.4	21.0	16.9	18.8	3.81	7.39	4.00	21.9	21.5	22.3	11.9	13.3	15.8	16.3	19.5
TiO_2	<0.03	<0.03	<0.03	<0.03	<0.03	0.04	<0.03	<0.03	<0.03	<0.03	<0.03	<0.03	<0.03	<0.03	<0.03	<0.03
MnO	0.10	0.05	0.31	0.35	0.22	0.12	0.07	0.07	0.36	0.30	0.37	0.18	0.14	<0.04	0.20	0.05
FeO	2.39	2.23	9.84	9.88	11.6	12.1	9.68	12.5	12.3	12.4	13.9	9.00	9.17	3.83	6.98	1.92
CoO	0.07	0.10	<0.02	0.04	0.03	0.06	0.05	0.08	0.03	0.03	<0.02	0.03	0.04	0.10	0.09	0.11
NiO	6.00	12.2	5.05	5.62	7.19	10.9	10.3	11.8	3.93	3.98	2.39	5.65	8.40	13.2	11.9	13.3
Total	89.1	93.1	88.1	82.4	92.6	85.5	87.2	88.7	89.3	86.8	87.9	66.4	84.2	91.4	84.8	90.2

Note: Totals are calculated from the full range of analysed elements, including Na, Si, Al, Mg, K, Cl, Ca, Ti, Mn, Fe, Co, Ni, Cr, S, Cu, Zn, Ba, Sc, V, and P.

3.7 Discussion

3.7.1 Choice of a suitable immobile element

Ni laterites form during weathering of ultramafic rock material and are subject to intense and long–lasting chemical and mechanical processes (Golightly, 1981, 2010; Freyssinet et al., 2005). To properly understand element behaviour, and to differentiate between redistribution by chemical or physical (collapse/dilation) processes (e.g. Brimhall et al., 1991; Oh and Richter, 2005; Amundson, 2013), element concentrations need to be normalised to an 'immobile index element' that is retained in the rock during weathering. Choosing the 'right' immobile element is a challenging task. Most elements show a certain degree of mobility under specific conditions (e.g. Middelburg et al., 1988; Cornu et al., 1999) and/or are not uniformly distributed within the parent rock (e.g. Nesbitt, 1979). Elements that are favourably retained and commonly used for normalisation include Al, Ti, Zr, Hf, Nb, Ta, Th, and the REE (e.g. Nesbitt, 1979; Middelburg et al., 1988; Gouveia et al., 1993; van der Weijden and van der Weijden, 1995; Venturelli, 1997; Hill et al., 2000a; Som and Joshi, 2002; Brown et al., 2003; Oh and Richter, 2005; Amundson, 2013; Babechuk et al., 2013, 2017; Paulukat et al., 2015). These elements are hosted in (1) weathering resistant (primary and secondary) oxides (e.g. Ti, Zr, Nb in Cr–spinel, chromite, magnetite, hematite, baddeleyite, or titanite) or (2) in newly formed oxy–hydroxides that are stable in the weathering environment (e.g. Al, Th, Nb, Ta, REE in goethite or gibbsite).

Ti, Zr, Hf, Nb, Ta, and Th are high field strength elements (HFSE; Reagan and Meijer, 1984; Stebbins et al., 1984). They have an ionic potential of between 3 and 12 (e.g. Ti^{4+}, Zr^{4+}, Nb^{5+}) and easily hydrolyse in solution; however, their oxides and hydroxides are only sparingly soluble (Van Baalen, 1993). If two 'immobile' elements are perfectly conservative, their concentrations should be highly co–linear (Cann, 1970; Maynard, 1992; Rye and Holland, 1998). REE concentrations of the laterite samples are highly correlated (R^2 = 0.90 – 0.99). However, REE mobility is indicated by (1) high light REE contents in clay–rich veins and (2) moderate fractionation between the REE, in particular in vein and saprock samples, compared to the parent rock (**Fig. 3.8**).

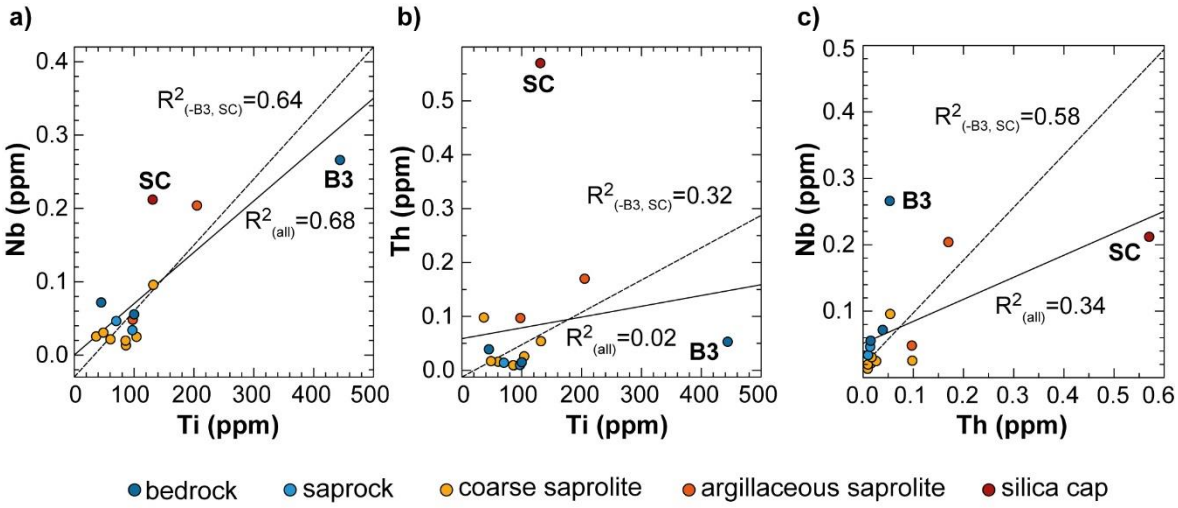

Fig. 3.17. Relationship between **a)** Ti and Nb, **b)** Ti and Th, and **c)** Th and Nb in the weathering profile. Linear regression trends for all samples from the profile are shown by the solid lines; linear regression trend for all samples except B3 and SC is shown by the dashed lines. The parent rock sample B3 shows a wide range of Ti and Nb concentrations, probably due to a pronounced cumulate structure in the parent dunite rock.

Apart from the REE, highest correlation coefficients occur between Ti, Nb, and Th (**Fig. 3.17**). Nevertheless, the dunite parent rock in the UZ shows a pronounced cumulate structure (Salgado et al., 2014; Verma and Oliveira, 2015), and Ti concentrations vary from 45 to 444 ppm and Nb concentrations vary from 0.06 and 0.27 ppm. The heterogeneous distribution of Ni and Tb complicates their use as an immobile element index. By contrast, Th is mostly concentrated in silicates, whose relative mineral abundance is less variable, such that Th concentrations have a narrower range, from 0.02 to 0.05 ppm. The São João do Piauí weathering profile is mainly composed of strongly silicified coarse saprolite; concentrations of Ti, Nb and Th are relatively similar within this unit (**Fig. 3.18**), which indicates that significant shrinkage has not occurred.

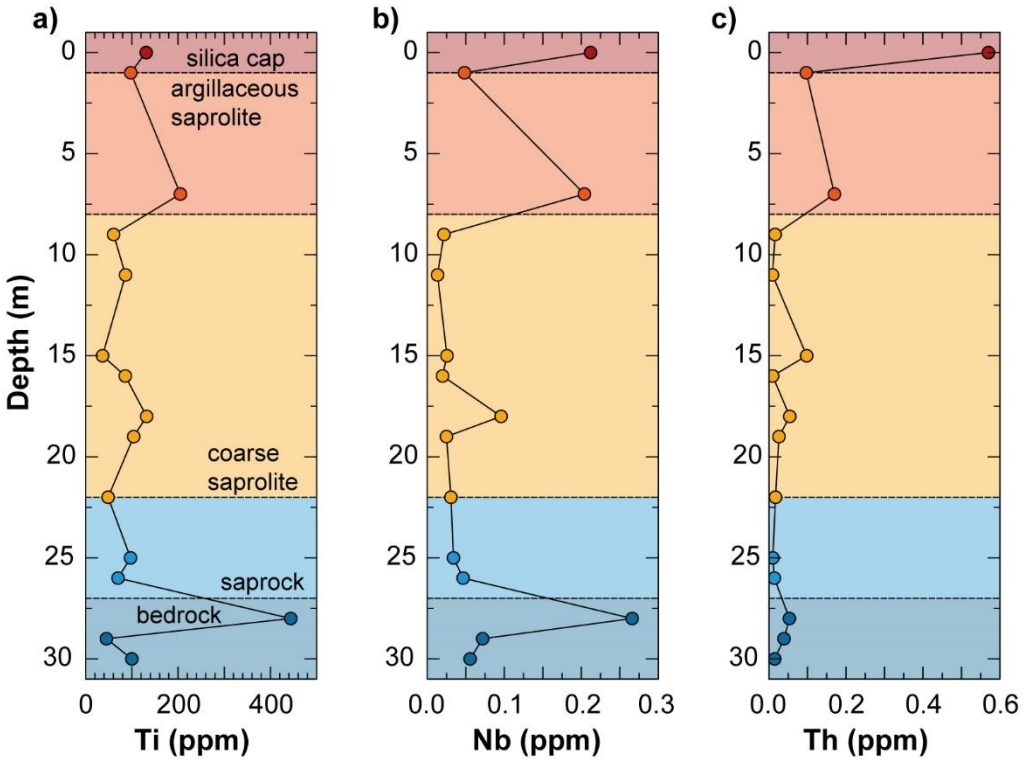

Fig. 3.18. Concentrations of **a)** Ti, **b)** Nb, and **c)** Th in the São João do Piauí weathering profile. The horizontal dashed lines mark the transition between individual laterite horizons.

Ti is considered to be the least mobile element in modern oxidative weathering environments and is only mobile on a profile scale in the presence of high amounts of dissolved organic matter (Cornu et al., 1999; Gong et al., 2011). As TOC concentrations in the laterite are very low (<0.2 wt%), Ti was selected as the 'primary immobile index element', with Nb and Th as 'trend controlling index elements', to allow a more resilient interpretation of the data. Relative element gains or losses are reported as fractions or so–called *tau values* (Amundson, 2013);

$$\tau_{x,(i)} = \frac{c_{x,l}/c_{i,l}}{c_{x,p}/c_{i,p}} - 1 \quad (3.2)$$

where c is the concentration of the element of interest (x) and an immobile element (i) in the laterite (l) or the parent rock (p). Average Ti (100 ppm), Nb (0.08 ppm), and Th (0.14 ppm) concentrations of parent rock samples are used as $c_{i,p}$. τ–values provide a representation of chemical processes occurring in the weathering profile, whereas sample/parent rock ratios (upgrade factor) also include physical (collapse/dilation) effects.

3.7.2 Physical evolution of the Ni laterite

The relationship between τ–value and upgrade factor of a certain element can be used to estimate whether the laterite formation experienced dilation or collapse during its evolution. If the upgrade factor of a sample is higher than its τ–value, collapse has occurred, whereas an upgrade factor that is lower than its τ –value indicates dilation.

A comparison between τ–values and upgrade factors (**Fig. 3.19**) of the most important major elements (i.e. Mg and Fe) and economic elements (i.e. Ni, Co, and REE) suggests that the saprock and coarse saprolite underwent dilation. Preserved serpentine halos in the coarse saprolite also support dilation, as collapse would have led to destruction of the residual mineral structure on a micro– and macroscopic scale. Dilation was likely caused by the combination of saprolite formation and secondary silica infiltration. Early stages of laterite formation (i.e. incipient saprolite formation) are commonly characterised by 'isovolumetric weathering' (e.g. Cleaves, 1974). Secondary minerals have lower densities than primary minerals, which compensate for the mass loss from Mg removal, thereby sustaining the original rock volume. The weathering profile shows a massive infiltration of secondary silica that replaced dissolved serpentine material. Hence, saprolite formation combined with re–silification may led to a relative volume increase of the saprock and coarse saprolite units.

The position of the argillaceous sample AS1 in **Fig. 3.19** is indicative of slight collapse and is probably associated with admixture of allochthonous material. On the other hand, the position of sample AS2 in **Fig. 3.19** is consistent with a general dilation of the entire weathering profile from the saprock up to the argillaceous saprolite.

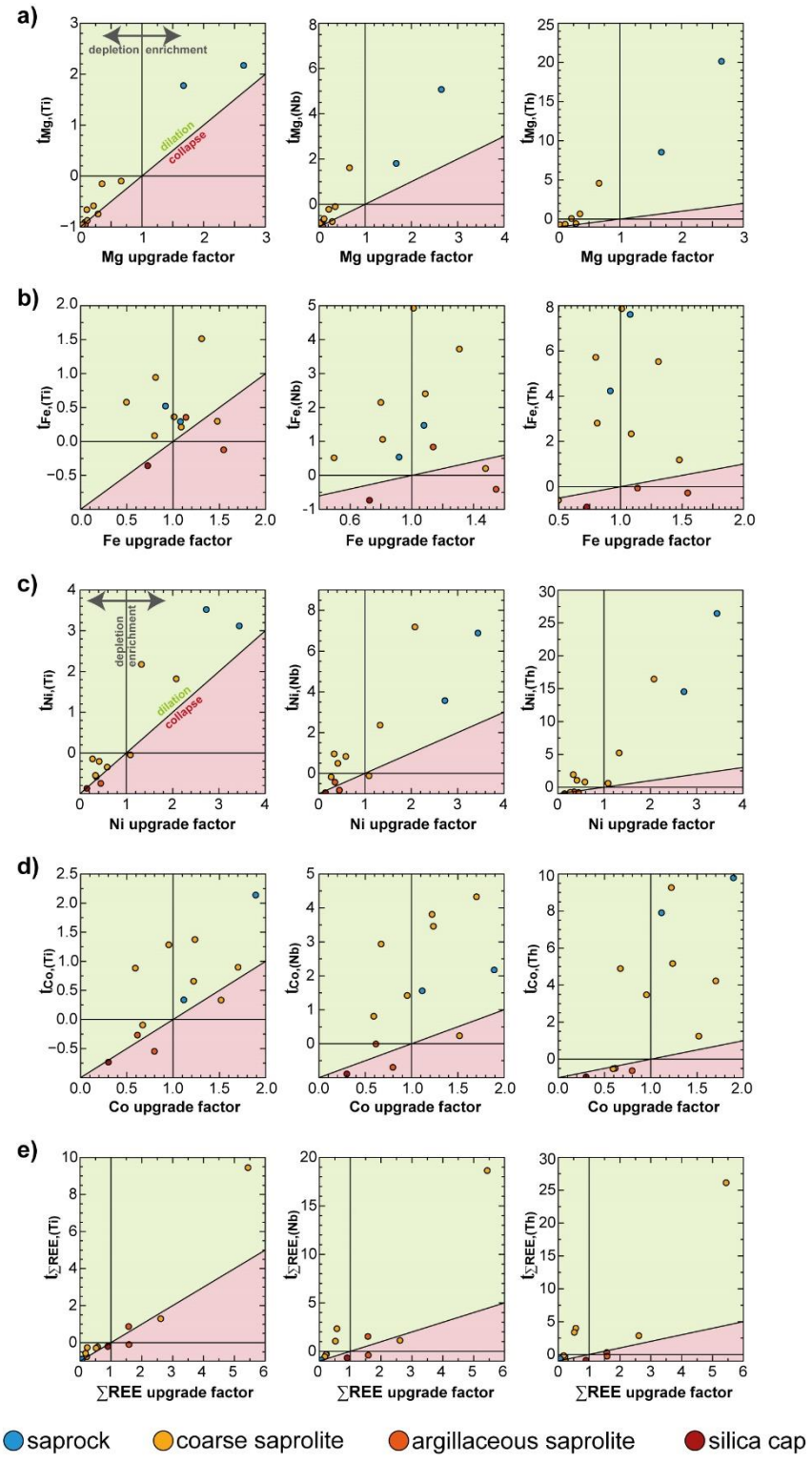

Fig. 3.19. τ–values vs. upgrade factor for **a)** Mg, **b)** Fe, **c)** Ni, **d)** Co, and **e)** ∑REE from laterite samples of the São João do Piauí Ni deposit. τ –values were calculated using Ti (left), Nb (centre), and Th (right) as the immobile element (see *equation 3.2*). The upgrade factor is calculated by normalising the concentration of the sample to the average concentration of the bedrock samples (B1 – B3).

τ–values using Th as immobile element are high compared to τ–values calculated using Ti and Nb (**Fig. 3.19**), which implies a very high degree of dilation that is unrealistic. This is likely because in dunites, Th is predominantly present in Mg–silicates, which are dissolved during the lateritisation process. Subsequent sorption of Th onto clays and oxyhydroxides means that Th is likely to be relatively mobile in supergene environments (Cromieres et al., 1998; Reiller et al., 2002; Hongxia et al., 2006; Seco et al., 2009). This idea is supported by high Th concentrations of between 2 and 14 ppm in clay–rich veins compared to an average Th concentration of 0.09 ppm and 0.04 ppm in the laterite and parent rock, respectively.

Clay–rich vein samples V2 and V3 are also rich in Ti, with concentrations of up to 3.81 wt%. This may also be due to sorption onto clays (e.g. Du et al., 2012), or residual Ti accumulation due to initial heterogeneities from magmatic cumulates (Salgado et al., 2016). The identification of anastase in veins (**Table 3.9**) reveals the former presence of sphene or ilmentite. Therefore, high Ti concentrations likely result from residual Ti accumulation, as Ti mobility that is associated with anastase formation, occurs only at the mineral scale (Anand and Paine, 2002; Schroeder et al., 2002). Hence, in this deposit, Ti is considered to be the least mobile element, whereas Nb and Th can be used to confirm general τ–trends, rather than represent individual immobile marker elements.

3.7.3 Chemical enrichment in the Ni laterite

Fig. 3.20 shows the pattern of loss or gain of Mg, Fe, and Si relative to the parent rock in the weathering profile. Using Ti as an immobile element index, positive τ_{Mg} values (>0) in the saprock indicate Mg enrichment by percolating fluids, whereas τ_{Mg} values as low as –0.95 (corresponding to a loss of 32.9 wt% in MgO) in the overlying saprolite and silica cap reflect drastic Mg loss, which results from dissolution of primary serpentine and chlorite. τ_{Mg} values close to zero that correspond with relatively high Ni concentrations (~1.0 wt%) and the presence of Ni–rich primary serpentine indicate fluid–derived Mg rejuvenation the central part of the coarse saprolite.

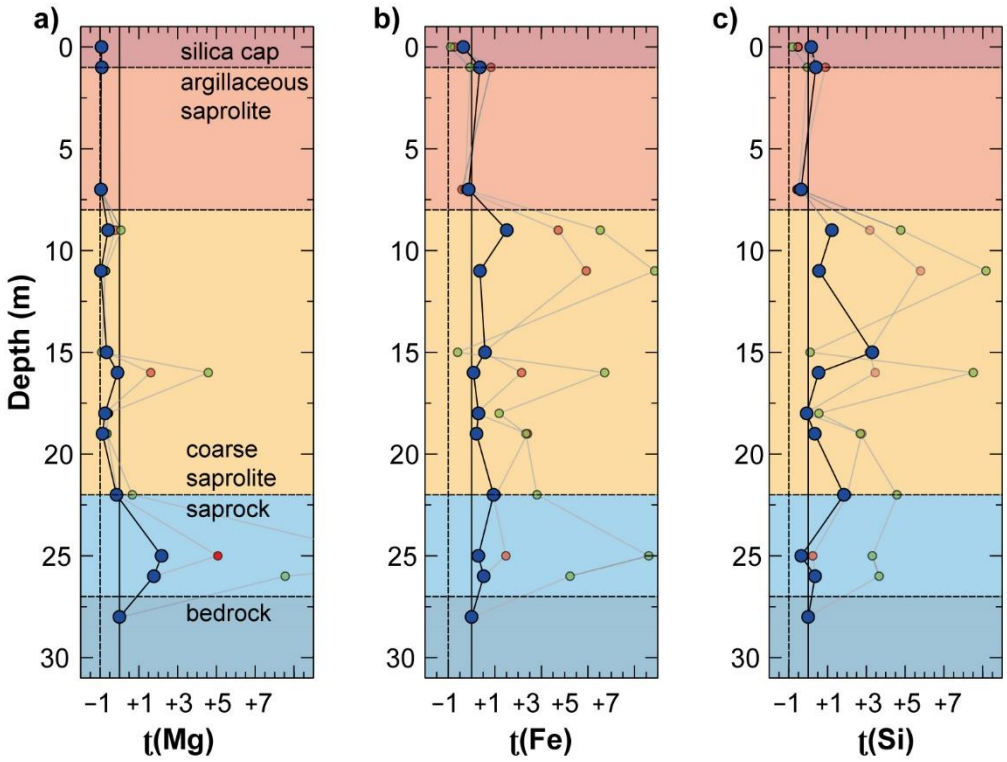

Fig. 3.20. Profiles of **a)** τ_{Mg}, **b)** τ_{Fe}, and **c)** τ_{Si} in the São João do Piauí weathering profile. τ–values are reported as fractions, where –1 on the x–axis (dashed vertical line) represents loss of all of the element with respect to the bedrock. Blue, green, and red circles represent τ–values using, respectively, Ti, Th, and Nb as the immobile element.

Iron is enriched throughout most of the profile, in particular in the coarse saprolite and saprock horizons, with τ_{Fe} values of 0.6 (+5.82 wt%) and 0.4 (+4.16 wt%), respectively. A τ_{Al} value of 0.4 in the coarse saprolite (+0.57 wt%) and in the saprock (+0.48 wt%) as well as strong correlation between τ_{Fe} and τ_{Al} (**Fig. 3.21a**) suggest a co–genetic Fe and Al enrichment (Schellmann, 1994). Potential sources for mobilised Fe and Al in the profile are indicated by negative τ_{Fe} and τ_{Al} values of samples AS1 and SC, which represent near–surface regolith units that experienced the highest degree of weathering in the profile. Losses of Fe and Al are usually associated with low pH weathering solutions (Grubb, 1963; Schorin and Puchelt, 1987; de Oliveira and Campos, 1991). Ultramafic rocks have a high natural pH buffering capacity that leads to a constant near–neutral pH in percolating weathering solutions during incipient and moderate stages of weathering (e.g. Robinson, 1997). When weathering is advanced, however, most of the Mg and other alkali–elements are removed from solution and pH falls (e.g. de Oliveira and Campos, 1991; Desai et al., 2018).

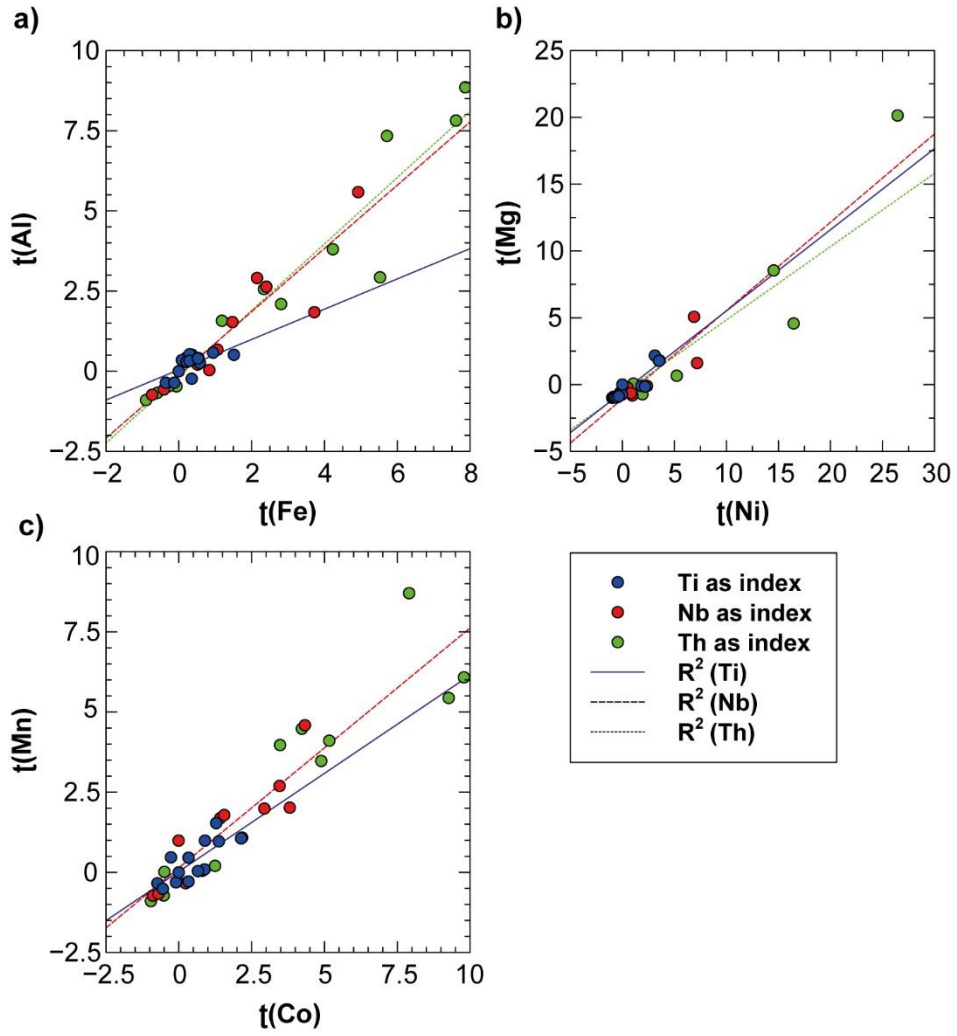

Fig. 3.21. Relationships between **a)** τ_{Fe} and τ_{Al}, **b)** τ_{Ni} and τ_{Mg}, and **c)** τ_{Co} and τ_{Mn}. **a)** The weathering profile experienced Fe and Al enrichment in lower laterite units due to relatively acidic conditions at the surface that led to migration and subsequent accumulation in less weathered horizons, where a neutral to alkaline pH predominates. Simultaneous Fe and Al mobilisation from shallow horizons implies an advanced to extreme degree of weathering. **b)** The co–linear Mg and Ni enrichment exemplifies the secondary character of serpentine as the main Ni ore in lower laterite units. Co–linear Mg and Ni depletions show that mobile Ni stems from the breakdown of altered serpentine minerals from shallower parts. **c)** The co–linear behaviour of Mn and Co shows that asbolane is the main Co ore in the weathering profile as indicated by its presence in clay–rich veins (**Table 3.8**).

The weathering profile is covered by a dense shrub vegetation, which can effectively lower the pH of infiltrating weathering solutions and further facilitate iron and aluminium mobilisation by complexation with organic acids (Freyssinet and Farah, 2000; Beukes et al., 2002). Negative τ–values are therefore interpreted to reflect fluid–induced Al and Fe mobilisation, which renders the pH of weathering solutions to lower than 4 (Peterson, 1971; Norton, 1973).

By contrast, samples with positive τ–values are interpreted to reflect fluid–derived Al and Fe retention under higher pH conditions in less weathered, deeper horizons. τ_{Si} values are variable in the profile, but generally agree with observations of large SiO_2 enrichments in the coarse saprolite with an average τ_{Si} value of 1.1 (corresponding to a gain of +44.0 wt% SiO_2). Silica mobilisation is indicated in samples AS1 and SC, similar to the behaviour of Fe and Al that were lost from the shallow horizons of the laterite. τ_{Fe}, τ_{Al} and τ_{Si} are co–linear when Nb and Th are used as index elements, which implies simultaneous migration of Fe, Al and Si. This means that as iron and aluminium become enriched in the coarse saprolite, low pH fluids also transport mobile silica deeper into the profile.

Fig. 3.22 shows gains or losses of Ni, Co, and REE in the Ni laterite relative to the underlying parent rock. Ni enrichment is highest in the saprock and the lower coarse saprolite with τ_{Ni} values of between 2.2 and 3.5, which corresponds to Ni concentrations of between 0.6 and 1.6 wt%. Ni is also enriched (τ_{Ni} = 1.8) in the central coarse saprolite with a Ni concentration of 1.0 wt%. The strong correlation between τ_{Mg} and τ_{Ni} (**Fig. 3.21b**) demonstrates the secondary character of the Ni ore and shows that Ni was likely mobilised from shallower depths, as indicated by negative τ_{Ni} values in the argillaceous saprolite and silica cap. Mobile Ni migrated downwards (*per descensum*) into deeper laterite horizons (τ_{Ni} values>0), where it re–combined with Mg to form Ni–rich serpentine (e.g. de Chetelat, 1947; Schellmann, 1994; Fu et al., 2019). Significant Co enrichments are situated in the upper saprock and the lower coarse saprolite, in particular at the transition between the two (τ_{Co} = 1.4 – 2.2). Strong correlations between τ_{Mn} and τ_{Co} (**Fig. 3.21c**; R^2 = 0.61 – 0.87) and the identification of asbolane (Mn–oxide) in veins also suggest the presence of asbolane as important Ni and Co bearing ore in the transition zone. However, Co concentrations are sub–economic (135 – 268 ppm). Negative τ_{Co} values for the argillaceous saprolite and the silica cap likewise indicate Co mobilisation from higher parts of the profile, similar to the behaviour Ni (e.g. Yongue-Fouateu et al., 2006).

The REE show a strong enrichment in the upper coarse saprolite ($\tau_{\sum REE}$ = 9.5) and a smaller enrichment in the central coarse saprolite ($\tau_{\sum REE}$ = 1.3). The upper coarse saprolite is highly enriched, particularly in light REE, and shows a ∑REE concentration of 44 ppm compared to 3 ppm in the parent rock. By contrast, the saprock is depleted in the light REE, with τ_{REE} values as low as –0.95 (–2.4 to –2.6 ppm) compared to the parent rock. The REE fractionation patterns indicate that the light REE are preferentially mobilised during the early stages of weathering (i.e. saprock formation), which is generally associated with loss of the most mobile elements (e.g. Mg, Ca, Rb) due to percolating weathering solutions (Sanematsu et al., 2011; Kynicky et al., 2012).

The strong depletion of the light REE in the saprock illustrates that even incipient weathering can mobilise significant amounts of the REE. The REE are generally either retained in secondary phosphates, such as gorceixite $(Ba)Al_3(PO_4)_2(OH)_5 \cdot H_2O$; Da Costa and Araújo, 1996), or adsorbed onto smectites (Price et al., 1991). τ–values for barium do not correlate with the REE and phosphorus concentrations are generally low in dunites; however $\tau_{Rb(Ti,Nb,Th)}$ show moderate correlations with τ_{REE} ($R^2 = 0.52 – 0.69$), which renders adsorption onto clays more likely (Nesbitt et al., 1980; Hill et al., 2000b). Since inputs of allochthonous material appear to be small, the likely source of REE enrichment is saprock material that formerly overlaid the weathering profile and has now been eroded. In this way, the REE are enriched in the very earliest phase of laterite profile development.

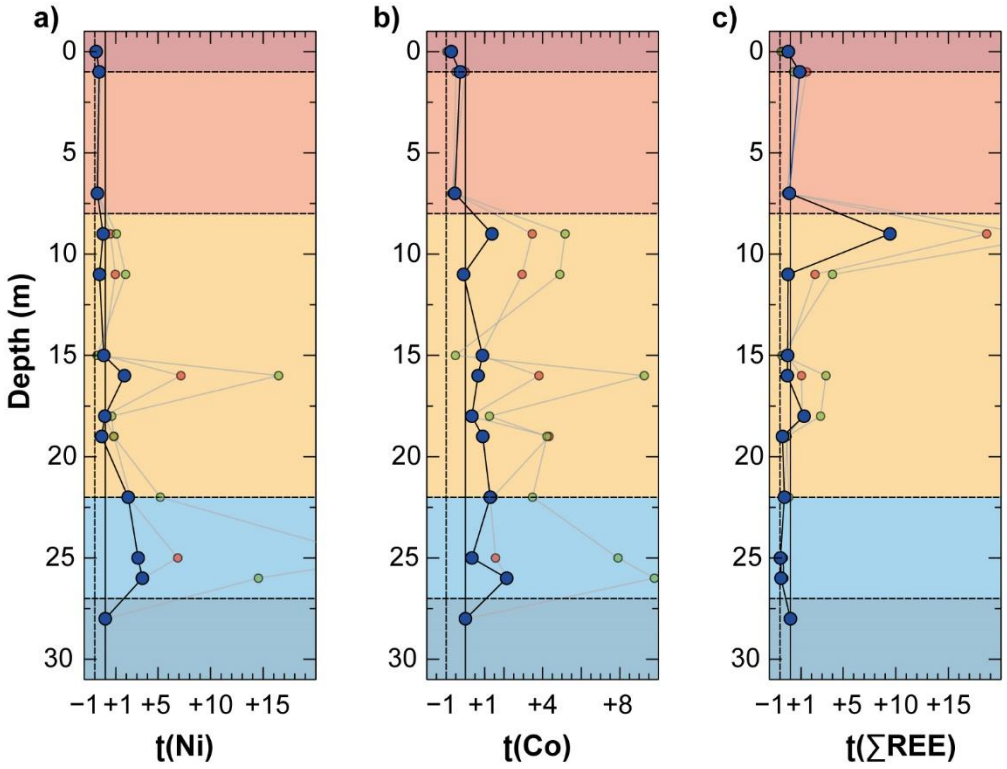

Fig. 3.22. Profiles of **a)** τ_{Ni}, **b)** τ_{Co}, and **c)** $\tau_{\sum REE}$ in the São João do Piauí weathering profile. τ–values are reported as fractions, where –1 on the x–axis (dashed vertical line) refers complete loss of the element with respect to the bedrock. Blue, green, and red circles represent τ–values calculated using, respectively, Ti, Th, and Nb as the immobile element.

3.7.4 Clay–rich veins

Intercalated clay–rich veins occur in abundance in the weathering profile and have the highest Ni, Co and REE contents. Ni–rich smectite and asbolane are the main ores (**Table 3.8**). However, τ–values calculated using the average composition of the dunite bedrock show strong depletions (as low as –0.95) in all major elements as well as Ni, Co and the REE, which is inconsistent with Ni concentrations of up to 5.0 wt% and Co concentrations of up to 794 ppm in the veins. This is because the index elements (Ti, Nb, and Th) also have extremely high concentrations in the clay–rich veins compared to the host laterite and the dunite parent rock (*see equation 3.2*). To the first order, high concentrations of relatively insoluble Ti, Nb, and Th imply that clay–rich veins represent a very small residual fraction of a progenitor that has lost large amounts of its original rock material, thus residually enriching the immobile element content. Mobilisation of Ti, Nb, and Th on a profile scale is unlikely, but cannot be ruled out in intensively weathered horizons (Du et al., 2012). Alternatively, high Ti, Nb, and Th concentrations could be explained by allochthonous inputs of clay material from other rocks. This would increase Si, Al, and Ti, and decrease Fe and Cr contents (Schellmann, 1989). However, the clayey material in this weathering profile has very low Ti concentrations (**Tables 3.8** and **3.10**) and high whole–rock Ti contents result from the presence of anastase as a secondary product of ilmenite weathering (**Table 3.9**). The fact that clay–rich zones can reach a thickness of several meters in the weathering profile (**Fig. 3.4**) renders allochthonous input of Ti, Nb, and Th unlikely and a residual origin is favoured. In general, clay–rich zones in Ni laterites that developed from a dunite precursor are dominated by Fe–rich nontronite with only small amounts of Al (Brand et al., 1998; Elias, 2002).

Clay–rich veins in this weathering profile, however, have relatively high Al concentrations of between 10.5 and 19.8 wt%, together with moderate Mg contents. Furthermore, the presence of kaolinite, which is a weathering product of feldspar, indicates that the progenitor was likely not the dunite parent rock from which the host laterite formed (e.g. Banfield, 1990; Wilson, 2004). A possible explanation for the presence of kaolinite is weathering of leucotroctolite that consists of high relative amounts of plagioclase and is documented to occur as intercalations in the dunite parent rock (Salgado et al., 2014, 2016). The intercalations can reach a thickness of several meters and occur abundantly in the UZ, particularly at lower depths (Salgado, 2014). Weathering of troctolite may explain the high Al contents in vein samples compared to low concentrations in the dunite parent rock and the overlying regolith units.

Unweathered troctolites have Al concentrations of 20±5 wt% (e.g. Berg, 1980; Xue and Morse, 1993; Amelin and Semenov, 1996; Cottin et al., 1998; Aiuppa et al., 2000; Barmina and Ariskin, 2002; Kaczmarek et al., 2008; Su et al., 2012; Salgado et al., 2014), which is higher than the Al content of the weathered samples and appears to rule against residual enrichment of Al. However, Al mobility has been observed in the host laterite and the veins are utilised as fluid flow pathways, so Al may have been mobilised by low pH fluids and was subsequently removed from the weathering profile.

Troctolites are also Ti–enriched compared to other peridotites (Arai and Matsukage, 1996), which may explain high Ti contents in the veins. Field observations show that the weathering profile experienced stress–induced faulting, particularly along the transitions between the host laterite and intercalated veins. As the host laterite is strongly silicified and experienced dilation during weathering, faulting may have occurred due to significant mass loss of troctolite material and subsequent shrinking, which likely led to brittle strike–slip movements and to dissection of the formation as observed in the field. Although mass balance calculations are clearly difficult to apply on the intercalated veins and layers because of their ambiguous origin, it seems likely that high Ni, Co, and REE concentrations resulted from scavenging from fluids enriched in mobile elements, as residually formed Ni–rich smectites usually have Ni concentrations as high as 2.0 wt% (Brand et al., 1998; Butt and Cluzel, 2013). Higher Ni concentrations are associated with a secondary fluid–derived enrichment processes, which agrees with field observations and show that the veins control the principal fluid migration within the profile. Mobilised nickel was likely transported from shallower depth through veins and scavenged by smectites, which is supported by high Ni concentrations in veins that are situated at shallow depth compared to veins with a lower Ni concentration that occur deeper in the profile.

3.7.5 Silicification of the Ni laterite

Silicified Ni laterites commonly form over dunites or their serpentinised equivalents. Important examples are located in Australia (Mt Keith, Cawse, Ravensthorpe, Marlborough), Tanzania (Haneti), Turkey (Çaldağ), India (Sukinda), and Brazil (Niquelandia, Barro Alto). All these Ni laterites show an intense silicification of at least one regolith unit that overlies the dunitic parent rocks (Al–poor) of komatiites, ophiolites and layered complexes (Butt, 2014). Some authors suggest the silica has a hydrothermal origin, but it is now generally accepted that it is derived from weathering of Mg–silicates in the parent rock (Butt and Zeegers, 1992; Eggleton, 2001).

The majority of the dunite parent rock consists of Mg–rich serpentine. Therefore, the principal chemical reaction that governs weathering and the formation of the Ni deposit is as follows (Park and Fan, 2004):

$$Mg_3Si_2O_5(OH)_4 + 3CO_2 + 2H_2O \rightarrow 3MgCO_3 + 2SiO_2 + 4H_2O \quad (3.3)$$

The presence of CO_2 in infiltrating meteoric fluids leads to dissolution of Mg–serpentine and formation of magnesite and silica. However, magnesite will only precipitate in poorly drained profiles and Mg is otherwise removed by percolating weathering solutions (*equation 3.4*).

$$MgCO_3 + H_2O \rightarrow Mg^{2+} + HCO_3^- + OH^- \quad (3.4)$$

This is reflected by increasing MIA values that monitor the loss of Mg (**Fig. 3.23a**). The predominant arid climate in the region leads to retention of mobilised silica and subsequent precipitation, which results in a massive silicification of the profile. However, the characteristics of the silicification process have rarely been discussed in detail (Freyssinet et al., 2005; Thorne et al., 2009; Butt, 2014). The 'open pit' profile shows silicification of all laterite units with an average SiO_2 content of 72 wt%. Silicification occurs down to the saprock above the permeability barrier, which is situated closely below the Mg–discontinuity. An indurated siliceous horizon covers the Ni laterite, which is usually considered to be strong evidence that climate changed to become more seasonally dry and arid at least during later stage of laterite formation (Stephens, 1971). In a humid climate mobile silica is usually evacuated, while a shift towards a dryer climate leads to oversaturation of Si–rich fluids and eventually to secondary silica precipitation (Lacinsky and Styles, 2013). Exceptions from this general trend are oxide–dominated Ni laterite deposits that formed in a tropical climate and have a very high water table in which Si–rich fluids reside in the profile and cannot be evacuated (i.e. Çaldağ).

The silica cap of the 'open pit' probably formed from underlying argillaceous saprolite material due to significant loss of Fe and Al from low pH weathering fluids that originate from interaction with overburden shrub vegetation. These weathering solutions evacuated Fe and Al from surficial regolith units and also partly mobilised silica. However, as the amounts of Fe and Al are significantly smaller than the amount of Si, this process resulted in silica enrichment and the formation of a virtually pure silica horizon.

The exact conditions that lead to silicification of lower laterite units are unclear, although it is commonly considered to be due to silica saturation of percolating weathering solutions (Butt, 2014). The strong correlation between Mg loss and Si gain (**Fig. 3.9b**) in the laterite as well as the concordant replacement of serpentine by silica (**Fig. 3.23b**) agree with a single step mechanism of Mg–silicate dissolution and immediate silica precipitation during humid periods as proposed by Lacinska and Styles (2013). Immediate silica precipitation may occur from a silica saturated fluid that had taken up silica from surficial laterite units and transported it deeper in the profile. The dissolution of Mg–silicates, then, leads to an oversaturation and immediate precipitation of silica. In the weathering profile, silica was identified to be present as quartz, tridymite and occasionally cristobalite. The identification of tridymite indicates the presence of opal–CT, a mature silica precipitate (Kastner et al., 1977). The solubility of tridymite is higher than that of quartz, hence, silica in solution first precipitates as tridymite. When the silica concentration in the fluid is lower than the equilibrium solubility of tridymite, quartz will precipitate (Mackenzie and Gees, 1971). Most silica in the argillaceous saprolite consists of tridymite, whereas the coarse saprolite is dominated by quartz, which implies different silica concentrations in weathering solutions and may reflect a change in the height of the water table. Tridymite can precipitate from a solution that has a high silica concentration, which suggests a high standing water table and poor drainage. By contrast, quartz indicates lower silica concentrations in the weathering fluid and hence a lower water table and better drainage. Therefore, the transition from tridymite in the argillaceous saprolite to quartz in the coarse saprolite may indicate improved local drainage conditions during the formation of the Ni laterite. Further evidence for variable element removal rates is given by the presence or absence of magnesite veins in the profile. The low abundance of magnesite veins in the coarse saprolite demonstrates rapid Mg removal due to a low water table. The argillaceous saprolite, however, shows abundant magnesite, consistent with a high standing water table.

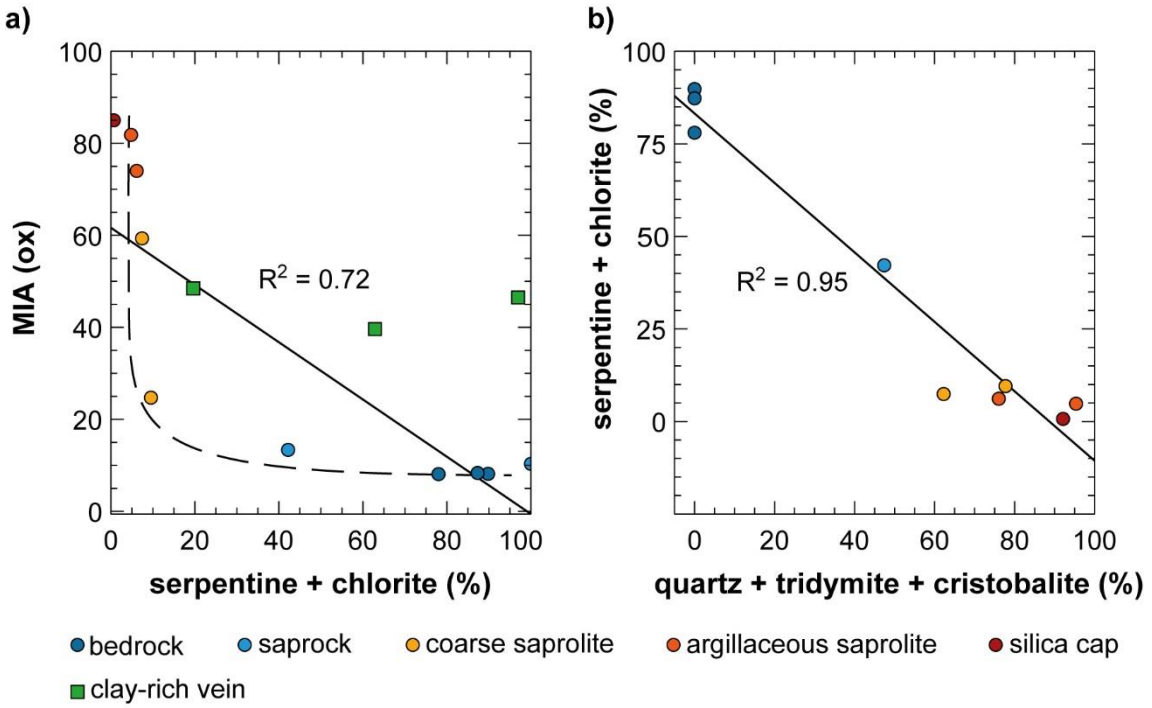

Fig. 3.23. **a)** MIA value vs. relative amount of serpentine and chlorite. The loss of Mg–rich primary minerals (i.e. serpentine, chlorite) from the parent rock leads to increased MIA values roughly following an exponential trend (dashed line). The relatively flat tail of the exponential trend is due to re–silicification of saprock material that only 'dilutes' the primary mineral content without significant loss of Mg. The steep slope at low primary mineral contents reflects the onset of Mg loss at the saprock/saprolite transition and the progressive relative Fe–enrichment in residual serpentine and chlorite. Clay–rich vein samples do not show a correlation, which means that secondary clay formation took place under a relatively constant Mg content. **b)** Relative amount of serpentine and chlorite vs. relative amount of secondary silica (i.e. quartz, tridymite, cristobalite). The linear trend of the samples demonstrates the in–situ replacement of primary minerals by secondary silica, which is balanced by the loss of solubilised material and preserves the integrity of the leached, residual rock material.

3.7.6 Classification of the São João do Piauí Ni deposit and implications for its formation

Ni laterites are typically classified according to their dominant Ni–ore type (Elias, 2002; Marsh and Anderson, 2011). Most Ni laterites have two ore types and thus, represent mixed deposits. Commonly, in the deeper parts of a laterite, Ni is present in hydrous Mg–silicates or in smectites. In shallower horizons Ni is found to be residually enriched in oxides (Brand et al., 1998; Berger et al., 2011). The laterite of the São João do Piauí Ni deposit consists of abundant secondary silica, authigenic weathering products of the parent rock (i.e. serpentine, chlorite), and hematite as the oxide component, which is typical for Ni laterites that are located in stable cratonic regions and developed from a serpentinised dunite parent rock (Brand et al., 1998; Elias, 2002; Butt and Cluzel, 2013). However, the hematite is Ni–poor, so the São João do Piauí laterite is not a classic oxide deposit. Ni is exclusively hosted in altered serpentine remnants and highest concentrations (up to 1.6 wt%) are found in Ni–enriched primary serpentine in the lower laterite units. Ni–rich smectite is present in intercalated veins and layers that have even higher Ni concentrations of up to 5.0 wt%. Co and REE are also highly enriched in the clay–rich zones, but their concentrations are generally lower than 0.5 wt% and ~100 ppm, respectively and thus, of sub–economic grade (Peek et al., 2009; Cocker, 2014). The clay–rich veins and layers originate from weathering of an Al–rich peridotite that occurs as a minor rock phase in the dunite. This is most likely leucotroctolite, which has been documented to occur in the UZ (Salgado et al., 2014) and is the only obvious source of large amounts of Al. Therefore, the São João do Piauí Ni deposit is primarily a secondary hydrous Mg deposit with a minor clay–silicate component that is nevertheless the principal source of Ni in the formation.

The ‘open pit’ weathering profile is situated on the gentle sloping flank of a hill, where drainage conditions are probably more favourable than they are on the central, relatively flat tabular top of the hill. It is expected that the highest Ni grades in the host laterite are found in the saprock horizon along flanks where the density of clay–rich intercalations is low, as smectites act as scavenger of mobile Ni that descends from the top of the profile, precluding Ni enrichment in the host laterite. However, the highest absolute Ni contents are expected to occur in areas with abundant intercalations at the southern border of the UZ, along the transition to the TMZ, where the dunite bedrock grades into troctolite, in particular at shallower depths.

The evolution of the São João do Piauí Ni deposit and the associated type of Ni–ore formation can be explained by weathering of Al–poor dunite and intercalated Al–rich troctolite in a two–step process that was determined by the geological evolution of NE Brazil. In the Early Eocene, the South American erosion cycle led to extensive pediplanation of the Brazilian shield area and the exposure of the ultramafic Brejo Seco Complex, which eventually resulted in a relatively flat topography with a low relief (King, 1956; Melfi et al., 1988; Bezerra et al., 2008). During the Eocene, all exposed units of the ultramafic BSC likely developed a lateritic cover, such as the small intrusions of the 'alpine serpentine belt' in Brazil (i.e. Serra das Marrecas, Andorinha; Schobbenhaus, 1976; Barros de Oliveira et al., 1992). In the case of the UZ, abundant secondary silica formed, which was predominantly retained due to low annual rainfall and the low Al–content of the dunite, which prevented significant clay formation. The low precipitation nevertheless permitted smectite formation from troctolite weathering products. The low relief impeded drainage and led to a high standing water table, so element removal rates in weathering solutions were low and dissolution of the original mineral assemblage was slow. This inhibited the development of a deep weathering profile (e.g. Wells and Butt, 2006) and Ni was retained in altered primary serpentine rather than incorporated into secondary Fe–oxyhydroxides, which is typical for strongly serpentinised dunites, in particular for ultramafic intrusions that underwent a long–lasting prograde orogenic metamorphism, such as the Brejo Seco Complex (Moody, 1976, Butt and Cluzel, 2013; Salgado et al., 2016). Retention of silica also diluted the Ni ore, which prevented substantial Ni enrichment in the dunite weathering products.

In the Middle to Late Cenozoic, a second phase of uplift initiated the Velhas erosion cycle. During this period, all units of the BSC were successively eroded. In the UZ, however, denudation of the upper most rock units likely resulted in the formation of a massive silica–rich horizon that strongly impeded continued erosion. As a result, the UZ emerges as a local hill in the otherwise low–lying pediplain area. This relief inversion with respect to the surrounding country rocks led to enhanced drainage conditions, in particular at the flanks of the hill, where the 'open pit' weathering profile is situated. As a result, the water table was lower in the short, but intense, rainy season, increasing the rate of removal of weathering solutions, in particular mobilising residually-hosted Ni in upper laterite horizon. The mobile Ni pool was transported down the profile and incorporated into slightly altered, Mg–depleted serpentine in the lower saprolite and saprock.

The presence of gem–quality chrysoprase (Ni–chalcedony) as well as positive τ_{Si}–values in the deeper parts of the profile indicates that the lowered water table also facilitated dissolution of secondary silica and translocation of the silica together with Ni into the deeper parts of the profile (e.g. Eggleton et al., 2011). The well–developed silica box–network in the coarse saprolite further suggests that this horizon started to form in the Velhas cycle, when uplift resulted in a lower water table. The argillaceous saprolite also has high silica concentrations, but secondary silica is more disseminated and the box–network that is characteristic for the coarse saprolite is absent. Thus, the argillaceous saprolite likely formed prior to uplift in a low relief setting with a high standing water table.

Ni laterites that are found in arid regions outside the humid tropics (e.g. NW Australia, USA, the Balkans, Turkey, Ural) are usually considered to indicate a change of climate or continental drift, especially those deposits that host Ni in Mg–silicates (Bourman, 1993; Brand et al., 1998; Elias, 2002; Butt and Cluzel, 2013). However, the São João do Piauí Ni deposit formed in a stable cratonic region under predominantly arid conditions, and precipitation is much lower than the minimum threshold for Ni laterite formation (~1000 mm/yr; Thorne et al., 2012). A determining key factor may be the strong seasonality and the El Niño controlled high magnitude rainfall events that have been variable in the geologic past, but have prevailed since the Cenozoic (Peterson and Haug, 2006). Although the region has usually never received more than 800 mm/yr of rain since the Late Cretaceous (Ramos, 1975), it only falls for 3 to 4 months of the year, which is apparently sufficient to allow the formation of economic Ni grades. The complete absence of precipitation in the dry season means that Ni laterite formation only progresses during the rainy season.

Since the exposure of the parent units in the Early Cenozoic the climate has remained constantly arid, so the rate of Ni laterite formation can be estimated. The regolith is between 8 m (plateau) and 30 m (flank) thick and was exposed during the South American erosion cycle (56 – 36 Ma), which results in average formation rates of between 0.1 to 0.2 m/Myr for the plateau and 0.5 to 0.8 m/Myr for the flanks, although the progression of the weathering front was likely slightly faster after the uplift during the Velhas cycle. These rates are very slow compared to other large lateritic regoliths that form with rates of between 3 and 60 m/Myr (e.g. Nahon, 1986; Freyssinet and Farah, 2000; Retallack, 2010). Nevertheless, the São João do Piauí Ni deposit indicates that arid regions with a short but intense rainy season can also be conducive to Ni laterite formation, as the parent rock mineralogy allows the formation of a siliceous cover that protects the underlying laterite from erosion in dry periods.

3.8 Conclusion

Mineralogical and geochemical data show that the São João do Piauí Ni deposit is a mixed Ni laterite with a dominant hydrous Mg–silicate component and a minor clay–silicate component. The mixed Ni–ore mineralogy results from weathering of an Al–poor dunite host rock with intercalated Al–rich troctolite layers. The weathering products of the dunite mainly consist of secondary silica, hematite, and variably altered primary serpentine. Ni–serpentine is the main Ni ore in the saprock and lower saprolite horizon, whereas Ni–smectite predominates in weathering products of troctolite veins and layers. Ni concentrations of up to 1.6 wt% in the saprock and lower saprolite result from replenishment by weathering fluids that leached residually accumulated Ni from upper regolith units and transported it downwards through the intercalated clay–rich layers that serve as pathways for meteoric water. Mobile Ni was taken up into clays during its passage through the profile, which led to high Ni concentrations of up to 5.0 wt%, in particular at shallower depths. The presence and relative abundance of Ni–rich veins and layers largely determines the Ni content of the bulk rock; where the vein abundance in the saprock and saprolite is low, Ni concentrations are high. Highest Ni grades are likely to be found in lower landscape positions on the flanks of the local plateau.

Uplift in the Early Cenozoic led to the exposure of the BSC including the UZ (dunite parent rock) and incipient laterite formation. Lateritisation progressed slowly in a low relief setting in its initial stages, and Ni was residually accumulated due to a relatively high water table. Because of the predominantly arid climate, however, silica was retained in the weathering profile so Ni was only slightly enriched relative to the parent rock. Orogenic–derived serpentinisation of olivine in the dunite meant that the serpentine minerals have a rather low weathering susceptibility, which led to accumulation of Ni in primary serpentine rather than in oxides. A subsequent uplift event in the Middle to Late Cenozoic triggered an erosional phase, which removed regolith material from all units of the BSC. However, the laterite material overlying the dunite of the UZ likely experienced lower rates of erosion, as it was protected by a more silica–rich cap compared to adjacent units. The resulting relief inversion enhanced the drainage rate and lowered the water table and thus, enhanced the rate of chemical weathering. This led to: (1) massive leaching of the uppermost regolith units and the formation of a virtually pure, silica cap, which in turn had a positive feedback on the relief as it protected the hill from erosion in the dry season compared to adjacent rock units; (2) accumulation of Ni, Co, REE, Li, Rb, Pb, and Zn in clay–rich veins and layers that scavenged mobile elements from the percolating weathering solution in the wet season, and (3) uptake of Ni and Co remaining in the fluid in the lower laterite, which led to economic enrichment of these elements in the saprock and lower coarse saprolite.

The formation of the siliceous top horizon was driven by mobilisation of Fe and Al under low pH conditions, which relatively concentrated silica and transported Fe and Al deeper into the profile. A dense shrub vegetation likely favoured low pH conditions at the surface and supported mobilisation of Fe and Al. Silica was also partially mobilised by percolating weathering solutions. The downwards migration of dissolved silica and its subsequent precipitation from a silica over–saturated fluid formed a massive silica box–network in the coarse saprolite, which impeded collapse of the host laterite. Weathering of intercalated troctolite material was probably associated with a large mass loss due to feldspar dissolution and triggered dissection of the surrounding rather brittle laterite.

Laterite formation and the progression of the weathering front principally proceeded only in the short but intense wet season as high magnitude rainfall events strongly leached the upper regolith units and transported mobile elements downwards. During the long dry season evaporation dominated, which led to hematite formation and silica retention. Laterite formation however largely ceased during the dry season and mechanical erosion was rather low because of the protective siliceous cap. These strong seasonal differences drove the formation and persistence of the siliceous cap, which would likely not have developed in a tropical climate and would therefore, have prevented the formation of the underlying Ni deposit. As the climatic conditions under which the Ni laterite formed in the past are similar to those of the present day, the formation is interpreted to continue to actively form.

The São João do Piauí Ni deposit is an example of a Ni laterite that evolved in a predominantly hot and arid climate in which precipitation during the entire course of lateritisation likely never exceeded 1000 mm/yr, which is generally considered to be the minimum amount required to form an economically valuable Ni laterite. Although estimated formation rates are about 10 to 100 times lower than other Ni laterite deposits, the 2 – 3 month long and very intense rainy season combined with a low water table is sufficient to produce a regolith that is characterised by a high degree of weathering and high, ‘mineable’ Ni concentrations. Thus, the widely accepted paradigm that Ni laterite formation only occurs under tropical climatic conditions needs to be extended to include semi–arid regions that have short but intense wet seasons.

Chapter 4 Behaviour of chromium and nickel isotopes during the formation of the São João do Piauí Ni laterite deposit

4.1 Abstract

The São João do Piauí Ni deposit is an actively forming Ni laterite that has developed over the past 50 Myrs in a predominantly arid climate from a strongly serpentinised dunite parent rock. This study investigates the behaviour of Cr and Ni during Ni laterite formation as well as the evolution of their isotopic compositions during the different stages of weathering, in particular focused on the breakdown of the primary Mg–rich mineral assemblage and the supergene Ni enrichment. The chromium isotopic composition of the laterite is highly variable, ranging from $\delta^{53}Cr$ = –1.70 ‰ to $\delta^{53}Cr$ = –0.12 ‰. The $\delta^{53}Cr$ value of the bedrock ($\delta^{53}Cr$ = –0.18 ‰) is within the range of the igneous Cr isotope inventory. Loss of Cr under high pH conditions in the laterite profile results in preferential enrichment of light Cr isotopes in weathering products and, in support of this, soil pore water and a water sample from a nearby river are strongly enriched in heavy Cr isotopes relative to the bedrock, with $\delta^{53}Cr$ values of, respectively, 4.31 ‰ and 0.76 ‰. The evolution of the Cr isotopic composition in the laterite is principally controlled by the mineralogical properties of the ultramafic parent rock and changes in $\delta^{53}Cr$ can mainly be attributed to loss of isotopically heavy Cr from silicate minerals (serpentine, chlorite); by contrast, Cr–bearing oxide minerals (magnetite, chromite) are largely unaffected by weathering and loss of Cr from oxides only occurs in the later stages of profile development. A simple Rayleigh fractionation model shows that changes in the Cr isotopic composition with depth in the laterite are consistent with the loss of the primary Mg–silicate assemblage, which is accompanied by isotope fractionation, and retention of Cr in oxides. Moreover, the Ni isotopic composition of the laterite profile is also widely variable, ranging from $\delta^{60}Ni$ = –0.91 ‰ to $\delta^{60}Ni$ = 0.05 ‰. This variation can mainly be attributed to a preferential retention of light Ni isotopes in Ni–enriched secondary minerals. The degree of nickel enrichment correlates with low $\delta^{60}Ni$ values and smectite–rich Ni–ore samples in the laterite have $\delta^{60}Ni$ values as low as –0.91 ‰ that is the lowest $\delta^{60}Ni$ value for a natural sample recorded to date. The new data further show that light Ni isotope enrichment is not restricted to Fe–oxyhydroxide and smectite minerals but can also be found in silicate weathering products that form from Mg–rich silicates, such as Ni–rich serpentine, in the saprock horizon of the laterite profile.

4.2 Introduction

Lateritic weathering is one of the major processes that alters the geomorphology of the Earth and drives the geochemical cycling of elements on the continental surface, which has a strong influence on chemical and isotopic fingerprints that are transferred into hydrological reservoirs (Marker et al., 1991; Compton et al., 2003; Traoré et al., 2008; Rauch and Pacyna, 2009). Nickel laterites form by surficial (oxidative) weathering of ultramafic rocks and represent the main continental reservoirs of Cr and Ni (Nriagu and Nieboer, 1988; Roberts and Proctor, 1992; Guillot and Hattori, 2013; McClain and Maher, 2016). Ultramafic provinces cover only a small area on a global scale (~0.2%), however, their mineralogy makes them prone to weathering and lateritic weathering products have a significant contribution to the Cr and Ni budget of the hydrosphere (Cameron and Vance, 2014; McClain and Maher, 2016; Ratié et al., 2018).

Nickel laterites are therefore key to assessing the behaviour of Cr and Ni during the transformation of rock to soil in the Critical Zone, and for constraining the processes that govern Cr and Ni isotope fractionation in ultramafic rock–regolith systems. Ni laterite formation principally constitutes evacuation of mobile elements (Mg, Ca, ± Si) and retention of immobile elements (Fe, Al, ± Si). Primary Mg–silicates are dissolved and replaced by secondary Fe–rich minerals, which is accompanied by a variable mobilisation of Cr and Ni. Ni either accumulates in–situ or migrates deeper into the profile to form economically viable Ni–rich horizons (Brand et al., 1998; Elias, 2002; Butt and Cluzel, 2013). The fate of Cr and Ni during weathering depends on several factors, such as parent rock mineralogy, drainage, tectonic relief, collapse of the regolith profile, pH–E_h conditions, and the availability of oxidants, reductants, or sorbents (e.g. Harter, 1983; Uren, 1992; Fendorf, 1995; Oze, 2004; Oze et al., 2004; Kierczak et al., 2016). Rock weathering, and in particular laterite formation, is a continuous process over several million years, but it is important to note that the aforementioned factors will likely change over the course of lateritisation, which will also affect Cr and Ni cycling. Laterites and paleosols generally tend to be depleted in heavy Cr and Ni isotopes compared to their underlying ultramafic progenitors (Crowe et al., 2013; Berger and Frei, 2014; Paulukat et al., 2015; Ratié et al., 2015, 2018; Novak et al., 2017; Gueguen et al., 2018; Spivak-Birndorf et al., 2018; Wille et al., 2018), whereas waters from ultramafic catchments, rivers, and seawater are generally enriched in heavy isotopes (Bonnand et al., 2013; Farkaš et al., 2013; Cameron and Vance, 2014; Scheiderich et al., 2015; D'Arcy et al., 2016; Goring-Harford et al., 2018).

However, secondary processes can lead to retention of previously mobilised Cr and Ni deeper in laterite profiles, which can lead to an enrichment of heavy isotopes in distinct horizons compared to the underlying protolith (e.g. Paulukat et al., 2015; Ratié et al., 2018).

The major processes that drive Cr isotope fractionation during weathering are redox–controlled reactions (kinetic isotope fractionation) and isotope exchange reactions (equilibrium isotope fractionation) between Cr^{3+} and Cr^{6+}. The impact of the latter may, however, be limited in laterite systems, because isotope exchange under optimal conditions (low Cr^{6+} concentration, high Cr^{3+}concentration) is slow (>20 years; Wang et al., 2015), and co–existing Cr^{3+} and Cr^{6+} need to be in direct contact for much longer than the period for which weathering solutions typically reside in the regolith profile (e.g. Thorne et al., 2012). The loss of heavy Cr isotopes that is observed in modern and ancient regolith profiles is interpreted to be mainly driven by the oxidation of Cr^{3+} to Cr^{6+} by Mn–oxides, which were in turn oxidised by molecular O_2 (e.g. Eary and Rai, 1987; Zasoski and Fendorf, 1992; Economou-Eliopoulos et al., 2014). The interdependency between loss of heavy Cr isotopes from rocks and the presence of O_2 has been widely employed to trace past oxygenation events and to investigate the evolution of the Earth's early atmosphere (e.g. Crowe et al., 2013; Paulukat et al., 2015; Gilleaudeau et al., 2016; Frei et al., 2017). However, the exact mechanisms of Cr isotope fractionation during oxidation are poorly understood, and experimental studies have yielded very variable Cr isotope fractionations of between –2.5 and +1.1 ‰ in the Cr^{6+} product relative to the Cr^{3+} reactant (Bain and Bullen, 2005; Ellis et al., 2008; Zink et al., 2010; Wang et al., 2010; Joshi et al., 2011). This variability likely originates from the complex nature of Cr oxidation, which includes multiple reaction steps, parallel oxidation pathways, and disproportionation of different Cr–species (Knoblowitz and Morrow, 1976; Silvester et al., 1995; Banerjee and Nesbitt, 1999).

By contrast, Ni isotope fractionation is redox–independent on the Earth's surface and theoretical calculations show that fractionation is driven by differences in bonding environment between aqueous and solid Ni^{2+} species (Fujii et al., 2011, 2014). Sorption of aqueous Ni onto secondary mineral surfaces (e.g. Fe–oxyhydroxides, sepiolite), and later diffusion into the crystal lattice that plays a dominant role during surficial Ni cycling and supergene enrichment (Peacock and Sherman, 2007), have been shown to preferentially incorporate light Ni isotopes into the mineral, thus enriching the Ni that remains in the fluid in heavy Ni isotopes (Gall et al., 2013; Estrade et al., 2015; Ratié et al., 2015, 2018; Wasylenki et al., 2015; Gueguen et al., 2018). Primary mineral dissolution appears to lead to no significant Ni isotope fractionation (Ratié et al., 2018), so Ni isotope variations in weathering profiles may mainly trace fluid–derived enrichment and depletion processes during secondary mineral formation (e.g. Estrade et al., 2015).

Here, we present Cr and Ni isotope data from the São João do Piauí Ni laterite in Brazil. The data allow us to describe the behaviour of Cr and Ni isotopes during the evolution of the laterite and the development of supergene enriched Ni–horizons. We show that $\delta^{53}Cr$ values principally reflect loss of Cr from the silicate fraction of the parent bedrock, while Cr residing in the oxide fraction of the rock is only affected by weathering processes in later stages of laterite formation, and that very low $\delta^{60}Ni$ values are associated with Ni–enriched horizons. The implications of these data for understanding ore formation processes are also discussed.

4.3 Geology and characterisation of the Ni laterite

The São João do Piauí Ni deposit is a small laterite body in Northeast Brazil that has 72 million tons of ore with mean grades of 1.0 wt% Ni and 0.05 wt% Co (Brazilian Nickel Limited, 2017). The Ni laterite formed by weathering of serpentinised dunite of the Brejo Seco Complex (BSC; **Fig. 4.1**), which is a layered igneous intrusion of Precambrian age (Barros de Oliveira et al., 1992; Salgado et al., 2016). Exposure of the BSC occurred in the Early Cenozoic during the South American erosion cycle (56 – 36 Ma) and laterite formation commenced in a predominantly hot and arid climate that is characterised by a strong seasonality (King, 1956; Mabesoone and Castro, 1975; Trescases et al., 1981; Bezerra et al., 2008; Japsen et al., 2012). In the Late Cenozoic, a phase of uplift triggered an extensive pediplansiation in the Brazilian shield area (called the Velhas erosion cycle) that eroded all of the ultramafic rock units of the BSC and their overlying lateritic weathering products. However, the serpentinised dunite and its overlying regolith prevailed, because the upper part of the regolith formed an indurated silica cap that minimises mechanical erosion. As a result, the serpentinised dunite and its overlying Ni–rich regolith mantle now emerge as a local hill in the otherwise pediplain shield area. Since the exposure of the hill, the climate in Northeast Brazil has been constantly hot and dry with a short, intense rainy season. Conditions in the Early Cenozoic were more humid, however, precipitation likely never exceeded 1000 mm/yr during the entire course of lateritisation due to the presence of variably strong El Niño events that control the regional climate of Northeast Brazil (Ramos, 1975; Louise Jeffery et al., 2012; Gurgel et al., 2013). The Ni laterite is actively forming, however, due to low amounts of rain and a long dry season, lateritisation only progresses during the wet season, so thickening rates are very low, and were calculated to be lower than 1 m/Myr (**Chapter 3**).

Behaviour of chromium and nickel isotopes during the formation of the São João do Piauí Ni laterite deposit

The Ni laterite of the São João do Piauí Ni deposit is between 8 and 30 m thick and the formation mainly consists of variably weathered, strongly silicified saprolite material (up to 90 wt% SiO_2) with abundant clay–rich veins and layers that are embedded in the profile and likely stem from weathering of troctolite material that was intercalated in the serpentinite during the genesis of the BSC (Verma and Oliveira, 2015; Salgado et al., 2016). The strong silicification is a result of the arid climate that retained silica in the dry season and transported mobilised silica via weathering solutions deeper in the profile in the wet season (Lacinska and Styles, 2013; Butt, 2014). Extensive leaching of iron and aluminium from the uppermost regolith units, which are characterised by low pH conditions due to a dense overburden vegetation, led to the formation of an indurated siliceous cover. The low initial Al content of the dunite hampered the formation of siliceous clays; rather, weathering led to the formation of an oxide dominated deposit with hematite as the main Fe–oxide, which is typical for serpentinised dunites in stable cratonic regions (Butt and Cluzel, 2013). However, Ni is predominantly retained in primary serpentine, and is not widely incorporated into secondary formed Fe–oxides, due to a strong orogenic serpentinisation of the dunite that increased the weathering resistivity of serpentine (Wicks and Whittaker, 1977; Salgado, 2014). In support of this, relic serpentine halos are present even in the silica cap. The later relief inversion during the Velhas erosion cycle lowered the water table and increased uptake of elements by percolating weathering solutions, triggering the formation of a hydrous Mg–silicate component with Ni–rich serpentine as the main ore. Weathering solutions were preferentially channelled through clay–rich veins and layers of former troctolite intercalations, which induced significant scavenging of fluid–derived Ni by smectites and led to the formation of a minor, however, highly Ni–enriched clay–silicate component in the deposit that largely determines the Ni content of the deposit on a profile scale. Any Ni that remained in the percolating solutions was eventually accumulated in the lowermost laterite horizon close to the Mg–discontinuity and the permeability barrier of the profile in slightly altered, primary serpentine minerals in the saprock horizon. Concentrations of Ni in Ni–enriched horizons range between 1.0 and 1.6 wt% in the host laterite, whereas clay–rich veins show Ni contents of up to 5.0 wt%, in particular in shallow horizons.

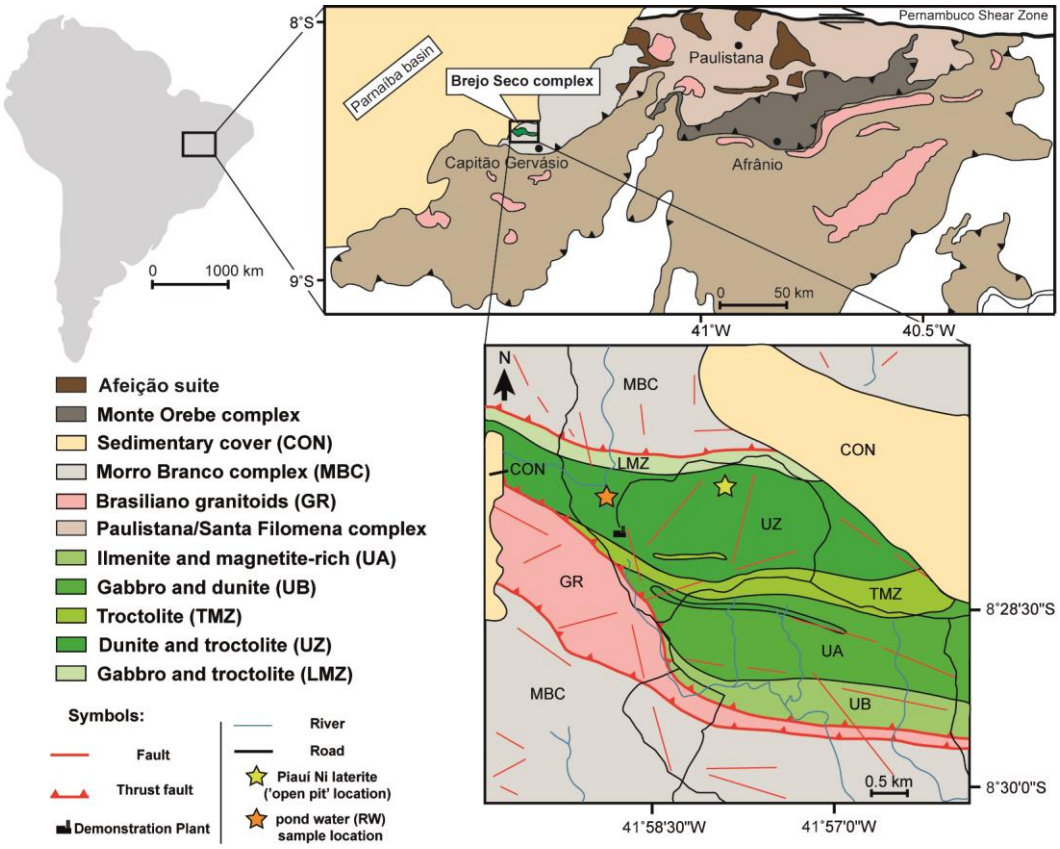

Fig. 4.1. Regional geological map of the Riacho do Pontal orogen and local geological map of the Brejo Seco complex (BSC) and its adjacent tectonic units modified after Caxito et al. (2014) and Salgado et al. (2016). The Brejo Seco complex (BSC) intruded into the south–western edge of the Precambrian Morro Branco complex and is located at the south–eastern border of the Parnaíba basin. The layered magmatic body was inverted during the Brazilian Orogeny and was later amalgamated on units of the Morro Branco massif and the Rajada granite in a thrust–fold belt tectonic setting. The yellow star marks the position of the studied laterite weathering profile, which is situated on the lower lands of the tabular hill that emerges as an erosion remnant in the otherwise flat area. The orange star marks the position of river water sample collected from the UZ (Ultramafic Zone).

4.4 Sample material and analytical methods

Rock samples and water samples were collected from the ‘open pit’ weathering profile of the São João do Piauí Ni laterite, which is situated on the N–facing gentle slope of a small hill in the central area of the Northern part of the Ultramafic Zone (UZ; **Fig. 4.1**). The profile comprises 16 regolith samples from the laterite formation, three dunite parent rock samples, one magnesite vein, and three clay–rich vein samples that stem from weathering of intercalated troctolite material. A pore water sample (PW) was taken at the bottom of the ‘open pit’ in the saprock horizon, close to the permeability barrier of the regolith units and the underlying parent rock. The river water (RW) sample was taken nearby from a small stream, whose catchment area includes the lateritic regolith cover of the local hill of the UZ.

The parent rock (B1 – B3) is a fine–grained serpentinised dunite that consists of abundant (85 to 95 vol%) Mg–rich silicates (i.e. serpentine, chlorite) and accessory Cr–rich magnetite and chromite. The overlying lateritic regolith profile consists of a saprock horizon (SR1, SR2) that is characterised by Ni–enriched, partly dissolved serpentine minerals and the abundant presence of intercalated magnesite veins (V1), followed by a thick coarse saprolite (CS1 – CS7) and an argillaceous saprolite (AS1, AS2), which both consist of high amounts of secondary silica (quartz, tridymite, and cristobalite) and minor amounts of hematite and other oxides. The saprolite material often shows a near complete loss of the original Mg–silicate assemblage and partly preserved serpentine is rarely found in the coarse saprolite, whereas the overlying argillaceous saprolite generally shows a higher abundance of relict serpentine. The uppermost unit, the silica cap (SC), consists almost entirely of secondary silica with minor oxides and traces of remnant serpentine. Smectites are present in some saprolite samples, in particular in the central part of the coarse saprolite and correlate with economic Ni enrichments. Clay–rich vein samples (V2 – V4) principally consist of a variable mixture of smectites, serpentine, chlorite, and kaolinite. A schematic illustration of the weathering profile and the predominant mineralogy of individual laterite horizons is given in **Fig. 4.2**.

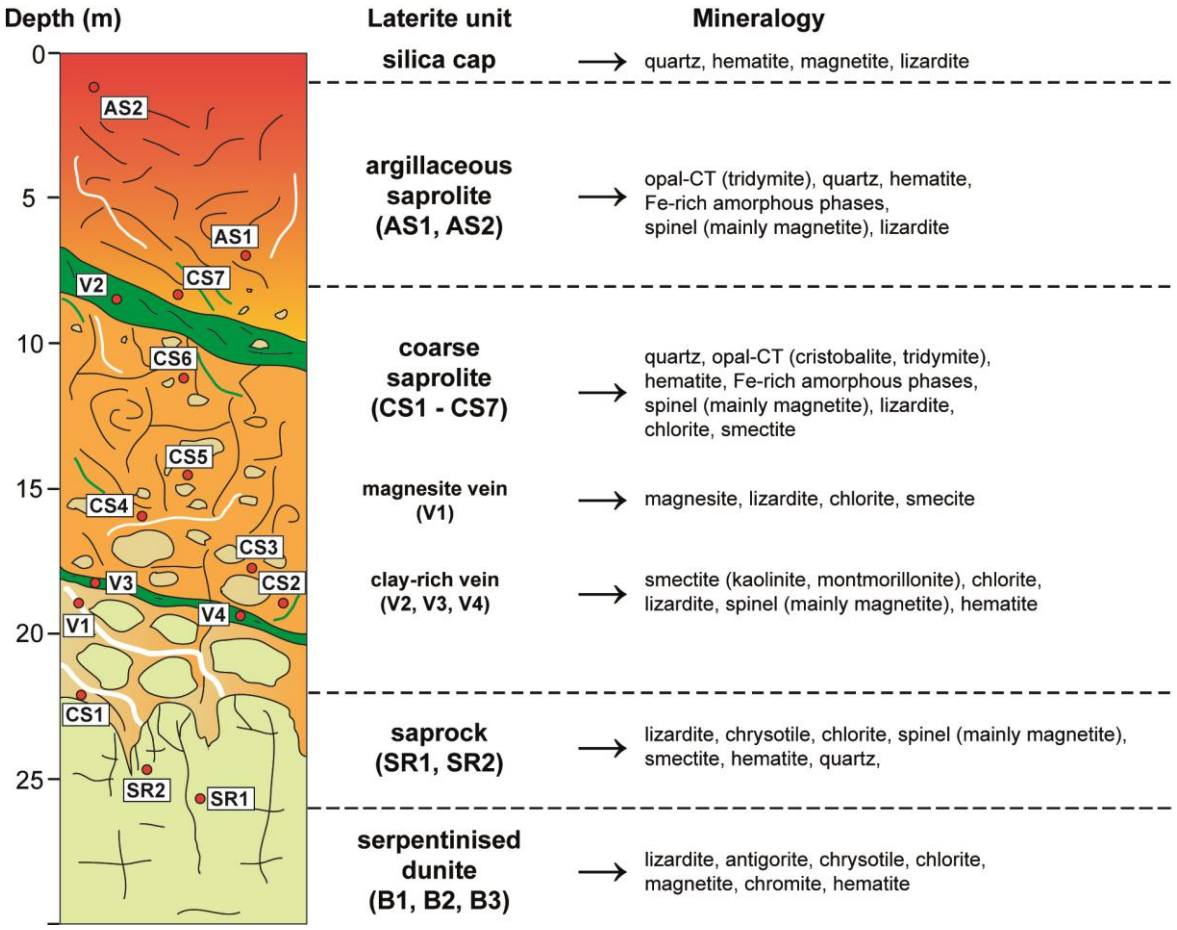

Fig. 4.2. Simplified stratigraphic profile of the 'open pit' weathering profile from the São João do Piauí Ni deposit divided into main laterite units with the predominant mineralogy. Strongly serpentinised dunite (B samples) grades into a relatively narrow saprock zone (SR samples), which underlies a thick coarse saprolite horizon (CS samples). Argillaceous saprolite (AS samples) is present at lower depths. The profile is capped by a siliceous top horizon (SC sample). Clay–rich zones (V samples) occur throughout the entire profile, in particular in the coarse saprolite. In places, magnesite veins are present, in particular in the saprock and argillaceous saprolite.

4.4.1 Rock sample preparation

Rock samples were broken into chips using a hand–operated splitter and dried at 105°C for 24 h. Subsamples of rock chips were taken for separation of the clay–sized fraction. Remaining material was then ground in an agate mortar for about 3 min to reduce the grain size to <100 µm and homogenise the sample. The sample powders were then dried at 105°C for 24 h and were subsequently used for the whole–rock element and isotope analysis. All acid reagents that were used for chemical analyses were sub–boiled, except HF and $HCLO_4$ that were *Romil UpA* grade.

All lab work and measurements were undertaken at the *University of Southampton*, except the Ni isotope analysis that was performed at the *Institut de recherche en astrophysique et planétologie (IRAP)*, Toulouse.

The separation of the clay–sized particle fraction from chipped whole–rock material was done using gravitational particle segregation after Salemi et al. (2010). The chipped material was gently crushed (not ground) using an agate mortar and a pestle to avoid any physical alteration of the particles. After crushing, samples were dispersed in *Milli–Q* grade water and the solution was transferred into a borosilicate glass cylinder. About 60 g/l of 10 w/v% $(NaPO_3)_6$ was added and the solution was stirred for 1h. Then, 7 ml $MgCl_2$ was added to accelerate particle sedimentation and the solution was allowed to settle particles larger than 4 µm, which distinguishes the silt and clay fractions (Wentworth, 1922). The settling time (~3 h) was calculated by Stokes` law considering the dimensions of the cylinder and the density of the particles that was estimated based on their mineralogy. The supernatant solution containing particles smaller than 4 µm was decanted and centrifuged. The procedure was repeated until the supernatant solution was clear (usually two times) to account for clay particles that were close to the bottom of the cylinder at the start of settling process. The clay separate samples were then dried at room temperature.

4.4.2 Dissolution procedure for whole–rock Ni concentration measurements and clay–separate Cr concentration measurements

Whole–rock samples and clay–separate samples were digested using a method adopted from Babechuk et al. (2010). About 100 mg of sample powder was weighed and dissolved in 3.5 ml HF and 1 ml concentrated HNO_3 at 130ºC for at least 60 h and then brought to incipient dryness. The dried samples were repeatedly re–dissolved in 3 ml concentrated HNO_3 and dried down. Then, samples were re–dissolved in 3 ml 3N HNO_3 and refluxed on a hotplate at 130ºC for 24 h. Sample solutions were transferred into centrifuge tubes and sample pots were washed with another 3 ml 3N HNO_3. The 6 ml solutions were centrifuged for 15 min at 3000 rpm, checked for residues, and clear solutions were transferred into sample vials. The process was repeated for samples with residues. Vials were filled up with 3N HNO_3 to reach a sufficient stock solution volume for subsequent dilutions. Whole–rock stock solutions and clay–separate solutions were diluted 2,000 and 20,000 times, respectively, for elemental analysis.

4.4.3 Dissolution procedure for whole–rock Cr concentration measurements

In order to accurately determine the whole–rock Cr concentration, a separate, relatively long dissolution method was applied to ensure a complete Cr recovery of sample material due to the presence of Cr–bearing oxides that are difficult to dissolve. About 100 mg sample powder was dissolved using a multiple–step acid dissolution method modified from Jain et al. (2000) that consists of: (1) aqua regia (mixture of HCl and HNO_3 in a 3:1 ratio) digestion at 160°C for 24 h, followed by (2) HF/HNO_3/$HClO_4$ digestion at 175°C for at least 7 days (14 days for oxide–rich samples), and (3) $HClO_4$ digestion at 180°C for 2 – 4 days. Fusion techniques were not employed because these do not guarantee complete Cr–oxide dissolution (Jain et al., 2000, and references therein). Sample solutions were evaporated to incipient dryness after each individual digestion step. After acid dissolution, sample material was re–dissolved in HCl and heated at 130°C for 48 h to dissolve fluorides that may have formed during the second dissolution step. The long digestion in HF/HNO_3/$HClO_4$ ensures full dissolution of Cr–oxides and warrants complete Cr–recovery, which is verified by the simultaneous processing of the DTS-2b rock standard that also has similar amounts of chromite compared to the analysed laterite samples. Sample solutions were then centrifuged for 15 min at 3000 rpm. All sample solutions that showed no evidence of residues after centrifuging were inspected under the microscope (10 times magnification) for small undissolved mineral grains. Samples that showed no evidence of residues under the microscope were considered to have been totally dissolved. These samples were then evaporated to incipient dryness and taken up in 7M HCl to create stock solutions. Whole–rock stock solutions were diluted between 10,000 and 1,000,000 times for the Cr concentration analysis.

4.4.4 Ni concentration analysis of whole–rock samples

Ni concentrations were determined on a *Thermo Fisher Scientific X–SERIES 2* inductively coupled plasma mass spectrometer (ICP–MS) together with all other trace element and rare earth element (REE) concentrations, except Cr, which was measured on a *Thermo Scientific ELEMENT 2* ICP–MS using whole–rock sample solutions that underwent a multiple–step acid dissolution (see above). The instrument was calibrated using the certified standard reference materials JB-1a, JB-3, JGb-1, BIR-1, BHVO-2, and the reference materials DTS-2B, JP-1 and JA-2 were measured as unknowns to determine the accuracy of the analyses. In and Re were added to sample solutions as internal standards to correct for matrix effects. Obtained concentrations of reference materials were accurate to better than 20% (1SD) for all trace elements and REE (better than 7% for Ni) of certified values (Imai et al., 1995; Babechuk et al., 2010; Day et al., 2015). The precision of repeated measurements was usually better than 10% (1SD). Detection limits vary between 0.01 ppb and 1 ppm for individual elements and are given with the results of the analyses of selected trace element and REE concentrations in **Tables 3.2**, **3.3**, and **3.4** in Chapter 3. Ni concentrations are given in **Table 4.6**.

4.4.5 Cr concentration analysis of whole–rock samples and clay separate samples

Cr concentration measurements of whole–rock (WR) samples and clay–separate (CLS) samples were performed on a *Thermo Scientific ELEMENT 2* ICP–MS and on a *Thermo Scientific Neptune* multi–collector inductively coupled plasma mass spectrometer (MC–ICP–MS) via isotope dilution. For the ICP–MS analysis, calibration standards were prepared from an internal laboratory Cr standard in a 3% HNO_3 matrix with Rh and In to correct for possible matrix effects. Samples were analysed in the same 3% HNO_3 matrix. Certified reference materials DTS-2b and JP-1 that both contain chromite were used as external standards. The reference material underwent the same dissolution procedure as the sample material. The average Cr concentration of the DTS-2b standard was accurate to better than 6% (Mukherjee et al., 2012; Robin-Popieul et al., 2012; Day et al., 2015) and the external precision of repeated measurements was better than 10% (1SD).

For the MC–ICP–MS analysis, aliquots containing 2 µg of Cr were taken from stock solutions and an appropriate amount of a $^{50}Cr/^{54}Cr$ enriched double spike was added and then processed as described in **Chapter 4.4.7**. The Cr ID concentrations were determined alongside with the Cr isotope analysis. The external precision of repeated measurements of DTS-2b is better than 10% (1SD)

4.4.6 Analysis of water samples

The Cr concentration of the water samples was determined using a single spike isotope dilution (ID) method after Bedson (2007) to ensure that the correct quantity of double spike Cr was added for subsequent Cr isotope measurements. A small aliquot was taken and a ^{53}Cr single spike was added. Measurements were performed on a *Thermo Scientific ELEMENT 2* ICP–MS and Cr concentrations were then determined from the $^{52}Cr/^{53}Cr$ ratio of the sample/spike mixture. However, reported Cr concentrations in **Table 4.5** were derived from double–spiked samples that were used for Cr isotope analysis, as the precision of this method is superior compared to the single spike method and is usually better than 0.05 % (1SD; Goring-Harford et al., 2018).

An appropriate amount of $^{50}Cr/^{54}Cr$ enriched double spike was added to the water samples based on individual sample weights and previously determined Cr concentrations. Due to the low Cr concentration in natural waters and the large sample volume (~1000 ml), it was necessary to pre–concentrate Cr in the river water sample by co–precipitation with Fe using a method from Goring-Harford et al. (2018). The river water sample was acidified (pH~2), and then left to equilibrate for 24 h. Later, the mixture was adjusted to pH between 8 and 9 to promote precipitation of Cr^{3+}. Finally, Fe^{2+}–hydroxide (10 ml) was added to quantitatively reduce any remaining Cr^{6+} by oxidation of Fe^{2+} to Fe^{3+}. Cr was quantitatively adsorbed on the precipitated Fe^{3+}–solid (Crawford et al., 1993; Fendorf and Li, 1996). The Cr–bearing solid was separated from the sample by vacuum filtration through pre–cleaned *Millipore Omnipore* filters (1 µm). The precipitate was then removed by soaking and washing the filter in 6M HCl and finally, the solution was dried down for 24 h at 95°C. As the volume of the sampled pore water was low (~40 ml), Cr was not co–precipitated with Fe and this sample was instead simply dried down at 95°C. The dried water samples were taken up in 6 ml of 7N HCl to create stock solutions.

4.4.7 Cr isotope analysis

Sample aliquots of dissolved WR samples and CLS samples containing 2 µg of Cr were taken from stock solutions and an appropriate amount of a $^{50}Cr/^{54}Cr$ enriched double spike was added. Sample–spike solutions were then evaporated to incipient dryness and were re–dissolved in 9N HCl. The chemical separation of Cr is based on the method of Bonnand et al. (2011) using a two–step chromatographic separation. In a first step, Fe was removed using *Bio–Rad AG1–X8* and 9N HCl, followed by a second step in which Ti and V were removed with *Bio–Rad AG50W–X12* and 6N HCl. Purified Cr samples were taken up in 3% HNO_3.

The Cr isotopic compositions of the samples and the Cr standard material SRM979 (Shields et al., 1966) were determined on a *Thermo Scientific Neptune* multi–collector inductively coupled plasma mass spectrometer (MC–ICP–MS) operated in medium resolution and sample solutions were injected using an *Aridus* desolvating nebuliser system. Sample solutions (1 ppm Cr) were diluted 8 times (125 ppb Cr) to give a 10–15 V signal on ^{52}Cr. The procedural Cr blank was lower than 10 ng and is negligible compared to the Cr content of each sample (2000 ng). Individual sample analyses consisted of 100 isotope ratio measurements with an integration time of 8 s. The background signal was measured using the same 3% HNO_3 solution that was used for the all sample solutions and was subtracted during deconvolution of the data from the sample signal. The injector wash time between individual runs was 12 min to avoid cross contamination and to ensure low background signals. Replicate measurements of the standard recovered by the double–spike technique were within an error of 0 ‰; $\delta^{53}Cr = 0.02 \pm 0.06$ ‰ (2SD, N = 71). The deconvoluted $^{53}Cr/^{52}Cr$ sample ratios were normalised to the mean ratio measured for the SRM979 standard and are reported in delta (δ) notation: $\delta^{53/52}Cr = [(^{53}Cr/^{52}Cr_{sample})/(^{53}Cr/^{52}Cr_{SRM979}) - 1] \times 1000$. The results of the Cr isotope analysis are shown in **Table 4.5**.

4.4.8 Ni isotope analysis

The chemical separation of Ni follows the method of Quitté and Oberli (2006) and comprises a five–step chromatographic procedure (**Table 4.1**). Aliquots of dissolved whole–rock samples containing 2 µg of Ni were taken from stock solutions, evaporated, and Ni was purified using *Bio–Rad AG1–X8* and 9N HCl to remove Fe in a first step, followed by a second step using AG1–X8 and 2N HCl to remove Zn. In the third step, a Ni–specific resin was used that contains dimethylglyoxime (DMG), which exclusively retains Ni on the resin at pH of between 8 and 9. Ni was eluted with 3N HNO_3 and the solution was further purified using a small volume of *Bio–Rad AGW50–X8* with 0.2N HCl to remove any remaining matrix elements, followed by 3N HCl to recover Ni from the column. In a last step, any remaining Fe and Zn was removed by repeating the first separation step with 6N HCl. Purified Ni samples were taken up in 0.1 N HCl. The Ni isotope compositions of the samples and the Ni standard material SRM986 (Gramlich et al., 1989) were determined on a *Thermo Scientific Neptune* MC–ICP–MS operated in medium resolution and sample solutions were injected using an Apex desolvating introduction system. Rock sample solutions and standard solutions (1 ppm Ni) were diluted 2.5 times (400 ppb Ni) to give a 15 – 20 V signal on ^{58}Ni. The procedural Ni blank was lower than 10 ng and is negligible compared to the Ni content of each sample (2000 ng). Individual sample analyses consisted of 100 isotope ratio measurements. The injector wash time between individual runs was 10 min to avoid cross contamination and to ensure low background signals. Replicate measurements of the standard yielded in an average $\delta^{60/58}Ni$ value of 0.00±0.09 ‰ (2SD, N = 47). The measured ratios of the samples were normalised to the mean ratio of the bracketing standards and reported in delta (δ) notation: $\delta^{60/58}Ni = [(^{60}Ni/^{58}Ni_{sample})/(^{60}Ni/^{58}Ni_{SRM986}) - 1] \times 1000$. Most samples show a mass–dependent isotope fractionation (**Fig. 4.3**). The results of the Ni isotope analysis are shown in **Table 4.6**.

Table 4.1. Five–step chromatographic Ni separation and purification scheme.

	1. Step Removing Fe	**2. Step** Removing Zn	**3. Step** Complexation of Ni (separation of Ni from matrix elements)	**4. Step** Removing remaining matrix elements	**5. Step** Purifying sample (removing any remaining Fe and Zn)
Column	10 ml poly-prep column	10 ml poly-prep column	10 ml poly-prep column	1 ml small-sized column	10 ml poly-prep column
Resin	2 ml pre-cleaned Bio-Rad AG1-X8 resin (200-400 mesh)	2 ml pre-cleaned Bio-Rad AG1-X8 resin (200-400 mesh)	2 ml pre-cleaned *TrisKem* NI-B50-A resin (100-150 mesh)	50 µl pre-cleaned Bio-Rad AG50W-X8 (200-400 mesh)	2 ml pre-cleaned Bio-Rad AG1-X8 resin (200-400 mesh)
Cleaning	10 ml MQ–water 10 ml 9N HCl	10 ml MQ–water 10 ml 2N HCl	10 ml MQ–water 10 ml 0.2 N $(NH_4)_3C_6H_5O_7$	1 ml MQ–water 1 ml 6N HCl (repeated 2–3 times)	10 ml MQ–water 10 ml 6N HCl
Equilibration	10 ml 9N HCl	10 ml 2N HCl	5 ml 0.2 N $(NH_4)_3C_6H_5O_7$ (pH = 8–9)	1 ml MQ water	10 ml 6N HCl
Introduction of sample	2 ml 9N HCl (immediate collection)	2 ml 2N HCl (immediate collection)	Ni–containing solution: 5 ml 1N HCl + 1 ml 1N $(NH_4)_3C_6H_5O_7$ + ~0.6 ml conc. NH_3 (for pH = 8–9)	0.2 ml MQ	2 ml 6N HCl (immediate collection)
Washing	2x2 ml 9N HCl	2x2 ml 2N HCl	20 ml 0.2 N $(NH_4)_3C_6H_5O_7$	2.5 ml 0.2 N HCl	2x2 ml 6N HCl
Elution	----------	----------	12 ml 3N HNO_3	0.5 ml 3N HCl	
Result	Sample in 6 ml 9N HCl	Sample in 6 ml 2N HCl	Sample in 12 ml 3N HNO_3	Sample in 0.5 ml 3N HCl	Sample in 6 ml 6N HCl

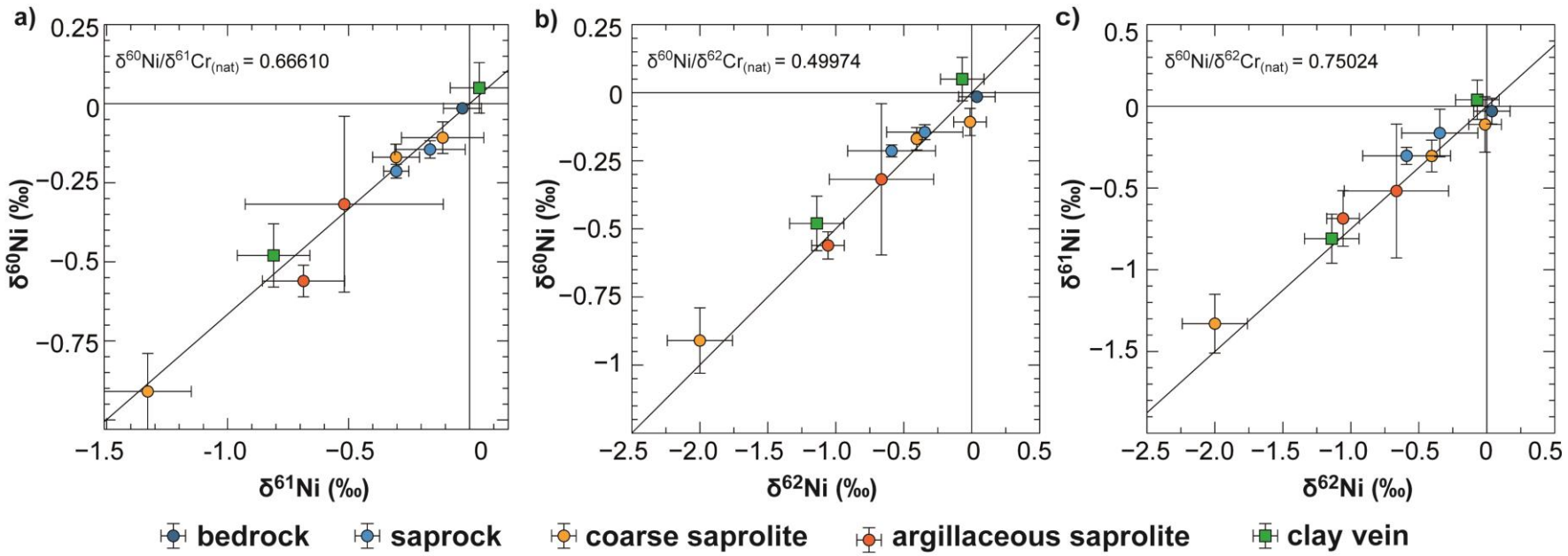

Fig. 4.3 Mass–dependent Ni isotope fractionation plots showing (a) $\delta^{60}Ni$ vs. $\delta^{61}Ni$, (b) $\delta^{60}Ni$ vs. $\delta^{62}Ni$, (c) $\delta^{61}Ni$ vs. $\delta^{62}Ni$. All samples plot within their errors on the mass–dependent fractionation line.

4.5 Results

4.5.1 Chromium

The chromium concentrations of the WR–, CLS–, and water–samples as well as their $\delta^{53}Cr$ values are given in **Tables 4.3**, **4.4**, and **4.5**. Whole–rock Cr concentrations range between 1760 and 9500 ppm (**Fig. 4.4a**), within the typical range observed in serpentinites and their weathering products (e.g. Morrey et al., 1992; Oze, 2003; Oze et al., 2004). Bedrock (B) Cr concentrations vary widely between 3690 and 9500 ppm, which can be attributed to (1) the adcumulate nature of the dunite that leads to varying relative abundances of oxides (Salgado et al., 2016), and to (2) slight variations of the degree of alteration of individual bedrock samples.

Cr in ultramafic rocks shows a bimodal distribution between silicate and oxide minerals with the latter generally hosting the majority of Cr (Becquer et al., 2003; Oze, 2004; Oze et al., 2004, 2007; Garnier et al., 2008). In the parent rock, Cr is hosted in serpentine (~0.03 wt% Cr_2O_3), chlorite (~2.59 wt% Cr_2O_3), Cr–bearing magnetite (~2.65 wt% Cr_2O_3) and in particular in chromite (~37.6 wt% Cr_2O_3). However, there is considerable variation in the Cr content of individual crystals that were measured and thus, the concentrations above are only estimates of average Cr contents (**Table 4.2**).

Whole–rock Cr concentrations in the overlying Ni–rich regolith units range from 745 to 8310 ppm and are consistently lower than that of bedrock sample B1, which is considered to best represent the mineralogy of the parent rock (*see discussion*). Cr concentrations in the saprock (SR) are between 4500 and 6950 ppm and the overlying coarse saprolite (CS) has Cr concentrations ranging from 1760 to 7900 ppm. The argillaceous saprolite (AS) has Cr concentrations of between 4380 and 8310 ppm and the silica cap (SC) has 745 ppm Cr.

Residual Cr enrichments are common among weathering products of ultramafic rocks due to the weathering stability of Cr–bearing oxides, and the massive Mg loss, which often leads to shrinking of the regolith, thereby, relatively enriching the Cr content (e.g. Schellmann, 1986; Bardossy and Aleva, 1990; Hill et al., 2000b). However, the laterite shows a massive retention of secondary silica, which infiltrated solution voids and precipitated as quartz, tridymite, and cristobalite and thus, hampered significant collapse of the regolith column, in particular in the coarse saprolite.

Therefore, residual (physical) Cr enrichment is minimal, in particular in the lower laterite units and low Cr concentrations are mainly attributed to oxidative Cr loss from the silicate fraction (e.g. McAlister and Smith, 1997), which is supported by very low Cr concentrations (<0.03 wt% Cr_2O_3) in serpentine grains in the saprock and lowermost saprolite. Cr concentrations in relic serpentine in the coarse and argillaceous saprolite indicate Cr enrichments in individual minerals of up to 0.61 wt% Cr_2O_3 (**Table 4.2**); however Cr is not generally enriched during weathering of the silicate fraction within these horizons, because the majority of serpentine minerals are decomposed and replaced by microcrystalline Fe–rich silicate aggregates with very low Cr. Thus, overall, the Cr concentration in the silicate fraction is lower than it is in the underlying saprock and parent rock units.

Analysed chromite grains from shallower horizons tend to be slightly Cr–depleted (31.2 – 34.3 wt% Cr_2O_3) compared to chromite in the parent rock (37.6 wt%). The quantification of Cr contents in hematite and magnetite, especially in upper portions of the profile, is ambiguous, because magnetite shows redox–induced pseudomorphic replacements towards hematite, so–called 'martitization', that hampers a direct comparison of Cr contents between the lower and upper horizons of the laterite profile, as magnetite slowly 'ages' to hematite. It is likely that a large part of Cr in hematite is initially derived from magnetite and does not stem from sorption of Cr mobilised during weathering of silicates (Mücke and Raphael Cabral, 2005). However, Cr^{6+} sorption onto hematite increases at low pH and maximum adsorption occurs at pH between 2 and 5, which could account for some Cr in hematite at shallow depth (Ajouyed et al., 2010).

Clay–rich veins (V2, V3, V4) have low Cr concentrations of between 119 and 212 ppm compared to weathering products of the serpentinised dunite (the host laterite), which is attributed to very low amounts of Cr–bearing oxides in the mineral assemblage. Unweathered troctolite intercalations apparently had very low initial Cr compared to the dunite parent rock, which is consistent with an average Cr content of 622 ppm and less than 2 vol% chromite in troctolite from several locations within the BSC described by Salgado (2014). The magnesite vein (V1) that was sampled in lower portions of the coarse saprolite shows a Cr concentration of 50.3 ppm. However, Cr is exclusively hosted in enclosed remnants of weathered serpentinite and surrounding magnesite has Cr concentrations of <0.03 wt%. Therefore, in subsequent discussions, Cr contents are normalised to the relative abundance of enclosed serpentinite (~2.4 vol%), which is considered to have a Cr content of 2095 ppm. This correction is applied to assess the impact of high pH (i.e. the presence of magnesite) on the Cr isotopic composition as a function of the Cr content of the sample.

Cr concentrations in the clay separates (CLS; **Fig. 4.4b**) generally increase from the saprock (102 – 230 ppm), through the coarse saprolite (795 – 6170 ppm) and the argillaceous saprolite (5220 – 18900 ppm) towards the silica cap (3120 ppm). The mineralogy of clay–separates has not intensively been investigated by XRD, however, they largely appear to consist of clay–sized particles of serpentine and chlorite at the bottom of the profile with an increasing amount of hematite and a little smectite towards the top. The trend of increasing Cr concentration in the clay fraction towards the surface is likely due to decreasing concentrations of other elements, such as Mg and Si, rather than accumulation of Cr.

The pore water (PW) sample that was taken in close contact with the saprock horizon has a relatively high Cr concentration of 22.9 ppm, which suggests that Cr is efficiently mobilised because the residence time of the fluid is short as the maximum time for fluid–rock interaction is only 2–3 months (i.e. the length of rainy season). The river water sample (RW) had a much lower Cr concentration (0.75 ppm). The low Cr concentration may be due to: (1) dilution with stream waters from adjacent non–ultramafic rock units of the Morro Bronco Complex to the North (**Fig. 4.1**); or (2) large amounts of rain within a short time period (dilution effect). Dilution with Cr from stream waters of adjacent units is rendered unlikely, as the water sample was taken at the source of a small river in the UZ (**Fig 4.1**). Areas, where Ni laterites occur, commonly receive between 1000 and 2500 mm/yr (Thorne et al., 2012). However, as most laterites develop in tropical climates, rainfall is more homogenously distributed over the year, which yields in about 80 to 210 mm/month. For comparison, the short but intense rainy seasons at the São João do Piauí Ni laterite translates to about 270 to 330 mm/month (Ramos, 1975), thus the relatively low Cr concentration is interpreted to be due to dilution by intense rainfall.

Table 4.2. Average Cr and Ni contents of major silicates and oxides in the Ni laterite profile.

Laterite horzion	bedrock		saprock		saprolite (Ni–depleted)		saprolite (Ni–enriched)		clay–rich veins	
	Cr_2O_3 (wt%)	NiO (wt%)	Cr_2O_3 (wt%)	NiO (wt%)	Cr_2O_3 (wt%)	NiO (wt%)	Cr_2O_3 (wt%)	NiO (wt%)	Cr_2O_3 (wt%)	NiO (wt%)
serpentine	0.03	0.49	<0.03	2.90	0.42	0.23	0.61	0.79	<0.03	6.83
chlorite	2.59	0.11	<0.03	2.28	n.p.		n.p.		n.d.	
magnetite	2.65	0.17	0.04	<0.04	0.50	0.10	0.30	<0.04	n.p.	
chromite	37.6	0.15	35.6	0.05	34.3	0.06	31.2	0.17	n.p.	
hematite	n.p.		n.d.		0.47	0.10	1.93	0.04	n.p.	
smectite	n.p.		n.p.						<0.03	10.5

n.d. Not determined.
n.p. Not present
Note The presented values represent estimated average Cr and Ni concentrations in respective laterite horizons, as the mineralogical composition of the samples is variable.

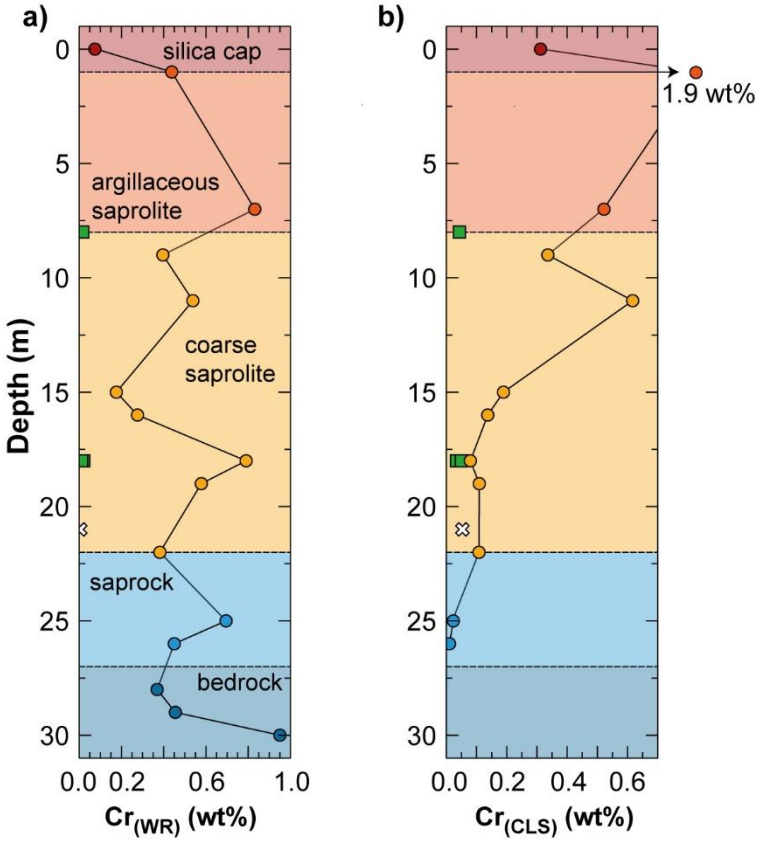

Fig. 4.4 a) The change of the whole–rock Cr concentration in the Ni laterite with depth. **b)** The change of the Cr concentration of clay–separates with depth. Circles represent samples from the host laterite that formed from weathering of dunite, whereas squares represent clay–rich vein samples that originate from weathering of intercalated Al–rich troctolite.

The change in the Cr isotopic composition with depth in whole–rock samples is shown in **Fig. 4.5a**. δ^{53}Cr values range from –0.12 to –1.70 ‰. However, most samples from the host laterite have a relatively narrow range of δ^{53}Cr values, between –0.12 and –0.43 ‰, except the argillaceous saprolite sample AS2 that has a very low δ^{53}Cr value of –1.40 ‰. The bedrock samples have δ^{53}Cr values of between –0.18 and –0.35 ‰, similar to the Cr isotopic composition of igneous rocks (δ^{53}Cr = –0.12±0.10 ‰; Schoenberg et al., 2008, 2016). Bedrock sample B2 (δ^{53}Cr = –0.35 ‰) is not entirely 'fresh' and shows incipient mineral transformation due to hydrolysis of serpentine, which indicates Cr loss and agrees with a negatively fractionated Cr isotopic composition compared to the igneous inventory. The saprock horizon shows δ^{53}Cr values ranging from –0.23 to –0.43 ‰, followed by the coarse saprolite that exhibits δ^{53}Cr values between –0.12 and –0.42 ‰, whereas the overlying argillaceous saprolite shows δ^{53}Cr values that range from –0.27 to –1.40 ‰. The silica cap has a δ^{53}Cr value of –0.23 ‰. Clay–rich veins show δ^{53}Cr values between –0.49 and –1.57 ‰ and the magnesite vein has a δ^{53}Cr value of –1.70 ‰, which represents the most ^{53}Cr–depleted sample in the profile. δ^{53}Cr values of the clay–sized fraction are generally lower than the corresponding whole–rock Cr isotopic composition. Clay separates from the saprock show δ^{53}Cr values of between –0.10 and –0.39 ‰, followed by the overlying coarse saprolite that has δ^{53}Cr values ranging from –0.49 to –1.68 ‰. The argillaceous saprolite shows δ^{53}Cr values of between –1.04 and –1.87 ‰. The pore water sample has a very high δ^{53}Cr value of 4.31±0.08 ‰, whereas the river water sample has a δ^{53}Cr value of 0.76±0.09 ‰.

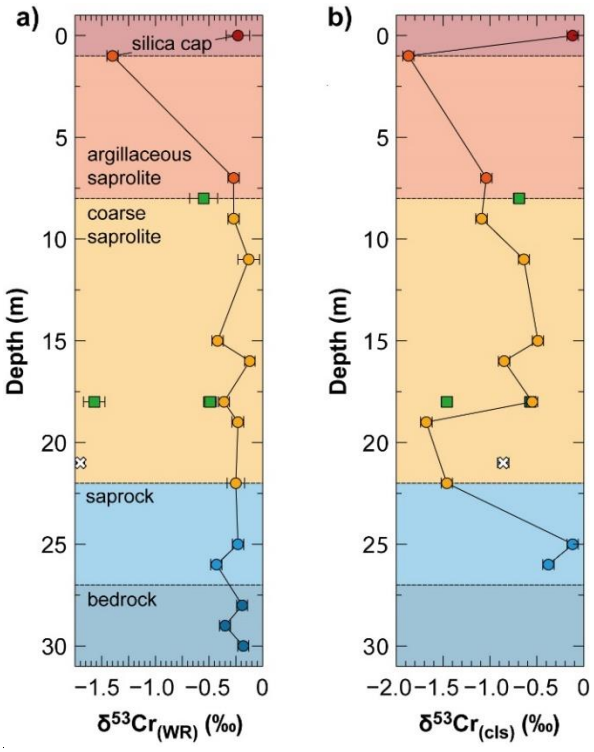

Fig. 4.5 a) Cr isotopic composition of whole–rock samples. **b)** Cr isotopic composition of clay separates. Circles represent samples from the host laterite that formed from weathering of dunite, whereas squares represent clay–rich vein samples that originate from weathering of intercalated Al–rich troctolite. The white cross represents the magnesite vein sample.

Table 4.3. Cr isotopic compositions and Cr concentrations of laterite whole–rock (WR) samples from the São João do Piauí Ni laterite.

		MC–ICP–MS							ICP–MS	MC–ICP–MS			
Depth	Sample	$\delta^{50}Cr$	$2\sigma_($	**$\delta^{53}Cr$**	**$2\sigma_{(m)}$**	$\delta^{54}Cr$	$2\sigma_{(m)}$	$^{56}Fe/^{54}Cr$	Cr^{a}	Cr^{b}	1SD[c]	No. of replicates	No. of digests
m		‰		‰		‰			ppm	ppm			
Host laterite (serpentinised dunite protolith)													
0	SC	0.47	0.23	**-0.23**	**0.11**	-0.46	0.22	0.18	745	827	180	3	2
1	AS2	2.89	0.07	**-1.40**	**0.06**	-2.77	0.07	0.11	4380	4390	90	3	2
7	AS1	0.55	0.07	**-0.27**	**0.06**	-0.53	0.07	0.05	8310	8920	<10	2	1
9	CS7	0.55	0.02	**-0.27**	**0.06**	-0.53	0.02	0.09	3960	4150	<10	2	1
11	CS6	0.26	0.20	**-0.13**	**0.10**	-0.25	0.19	0.07	5380	5670	1390	2	2
15	CS5	0.87	0.05	**-0.42**	**0.06**	-0.84	0.05	0.05	1760	1550	<10	2	1
16	CS4	0.24	0.10	**-0.12**	**0.06**	-0.23	0.09	0.17	2760	2650	200	3	2
18	CS3	0.74	0.09	**-0.36**	**0.06**	-0.71	0.09	0.02	7900	7360	240	4	2
19	CS2	0.47	0.02	**-0.23**	**0.06**	-0.45	0.02	0.06	5780	5420	<10	2	1
22	CS1	0.51	0.17	**-0.25**	**0.08**	-0.49	0.16	0.03	3820	4150	250	3	2
25	SR2	0.48	0.06	**-0.23**	**0.06**	-0.46	0.06	0.03	6950	6670	20	2	1
26	SR1	0.89	0.08	**-0.43**	**0.06**	-0.85	0.07	0.03	4500	4450	220	3	2
28	B3	0.39	0.06	**-0.19**	**0.06**	-0.37	0.05	0.04	3690	3910	10	2	1
29	B2	0.73	0.01	**-0.35**	**0.06**	-0.70	0.01	0.06	4550	4330	80	2	1
30	B1	0.36	0.02	**-0.18**	**0.06**	-0.35	0.02	0.06	9500	9050	180	2	1
Magnesite vein (product of serpentinised dunite weathering)													
21	V1	3.50	0.08	**-1.70**	**0.06**	-3.40	0.08	0.04	50.3	52.6	<10	2	1
Clay–rich veins* (product of troctolite weathering)													
8	V2	1.12	0.27	**-0.55**	**0.13**	-1.08	0.26	0.02	171	169	<10	3	2
18	V3	3.23	0.20	**-1.57**	**0.10**	-3.10	0.20	0.11	212	199	20	3	2
18	V4	1.00	0.12	**-0.49**	**0.06**	-0.97	0.11	0.03	119	108	20	3	2

* Vein sample within the whole–rock laterite unit.

a Cr concentration determined by single collector ICP–MS (from Chapter 3). Given concentrations are average values that were obtained from multiple individual measurements.

b Cr concentration determined by multicollector (MC) ICP–MS by isotope dilution. Given concentrations are average values from multiple individual measurements. The quantity of measurements is given as No. of measurements.

c 1SD refers to the standard deviation of replicate measurements of the samples and the given number describes the deviation of the last digits of the corresponding concentration. The standard deviation (SD) is given as rounded values, so that it only affects the first three significant figures (SF) of corresponding concentrations, deduced from the reproducibility of processed reference materials (i.e. DTS-2b).

Note $2\sigma(m)$ is the sample standard error of the mean (SEM) of two individual analyses, where $2\sigma(m)= 2SD/(N)0.5$ (N = number of measurements). The standard deviation of a single analysis is smaller than $2\sigma(m)$ and ranges between 0.01 and 0.03‰. The long–term reproducibility of the SRM 979 standard was chosen for samples that have a $2\sigma_{(m)}$ that is lower than 0.06.

Table 4.4. Cr isotopic compositions and Cr concentrations of clay separates (cls) from laterite samples from the São João do Piauí Ni laterite.

		MC–ICP–MS							ICP–MS	MC–ICP–MS
Depth	Sample	$\delta^{50}Cr$	2SD	**$\delta^{53}Cr$**	**2SD**	$\delta^{54}Cr$	2SD	$^{56}Fe/^{54}Cr$	Cr[a]	Cr[b]
m		‰		‰		‰			ppm	ppm
0	SC (cls)	0.24	0.12	**-0.12**	**0.06**	-0.23	0.12	0.08	3120	3330
1	AS2 (cls)	3.86	0.12	**-1.87**	**0.06**	-3.71	0.12	0.03	18900	19700
7	AS1 (cls)	2.15	0.12	**-1.04**	**0.06**	-2.07	0.12	0.01	5220	4910
9	CS7 (cls)	2.23	0.12	**-1.09**	**0.06**	-2.15	0.12	0.08	3360	3130
11	CS6 (cls)	1.32	0.12	**-0.64**	**0.06**	-1.27	0.12	0.05	6170	5930
15	CS5 (cls)	1.00	0.12	**-0.49**	**0.06**	-0.96	0.12	0.08	1890	1880
16	CS4 (cls)	1.76	0.12	**-0.85**	**0.06**	-1.69	0.12	0.09	1370	1270
18	CS3 (cls)	1.13	0.12	**-0.55**	**0.06**	-1.09	0.12	0.02	795	728
19	CS2 (cls)	3.45	0.12	**-1.68**	**0.06**	-3.31	0.12	0.07	1090	1120
22	CS1 (cls)	3.00	0.12	**-1.46**	**0.06**	-2.28	0.12	0.06	1080	1090
25	SR2 (cls)	0.21	0.12	**-0.10**	**0.06**	-0.21	0.12	0.12	230	241
26	SR1 (cls)	0.79	0.12	**-0.39**	**0.06**	-0.77	0.12	0.03	102	102
21	V1 (cls)	1.77	0.12	**-0.86**	**0.06**	-1.70	0.12	0.02	530	493
8	V2 (cls)	1.43	0.12	**-0.69**	**0.06**	-1.37	0.12	0.01	430	405
18	V3 (cls)	3.00	0.12	**-1.46**	**0.06**	-2.89	0.12	0.08	337	308
18	V4 (cls)	1.18	0.12	**-0.57**	**0.06**	-1.13	0.12	0.10	495	472

* Vein sample within the whole–rock laterite unit.

Note CLS samples have been digested and measured only once. 2SD of the isotope measurements refers to the long–term reproducibility of the SRM979 standard (i.e. 2SD($\delta^{53}Cr$) = 0.06).

a Cr concentration determined by single collector ICP–MS.

b Cr concentration determined by multicollector (MC) ICP–MS by isotope dilution. The standard deviation (SD) of individual measurements is not given and the reproducibility of the samples is deduced from the relative standard deviation of the processed DTS2b rock standard material (RSD = <10%).

Table 4.5. Cr isotopic compositions and Cr concentrations of water samples from the São João do Piauí Ni laterite.

Location	Sample	$\delta^{50}Cr$	$2\sigma_{(m)}$	$\delta^{53}Cr$	**$\delta^{53}Cr_{corr}$**	**$2\sigma_{(m)}$**	$\delta^{54}Cr$	$2\sigma_{(m)}$	$^{56}Fe/^{54}Cr$	Cr
		‰		‰			‰			ppb
bottom of pit (SR–interface)	pore water (PW)	-8.80	0.17	4.31	**4.31**	**0.08**	8.56	0.17	0.22	22900
local catchment	river water (RW)	-1.69	0.18	0.82	**0.76**	**0.09**	1.63	0.17	0.07	752

Note: $2\sigma_{(m)}$ is the sample standard error of the mean (SEM) of two individual analyses, where $2\sigma_{(m)}= 2SD/(N)^{0.5}$ (N = number of measurements). The standard deviation of a single analysis is smaller than $2\sigma_{(m)}$ and ranges between 0.01 and 0.03‰. $\delta^{53}Cr_{corr}$ refers to the $\delta^{53}Cr$ value of the sample corrected by the Cr isotopic composition of remaining Cr in the corresponding Fe^{2+} solution from the co–precipitation step. As the pore water did not undergo precipitation of Cr with Fe and Cr was instead recovered by drying of the sample, $\delta^{53}Cr_{corr} = \delta$. Cr concentration were determined by multicollector (MC) ICP–MS by isotope dilution.

4.5.2 Nickel

Nickel concentrations and Ni isotope compositions of analysed samples are given in **Table 4.6**. The Ni content of the laterite samples varies from 0.03 and 4.95 wt% Ni (**Fig. 4.6a**), which spans the full range of Ni contents that have been observed in weathering products of ultramafic rocks and locally even exceeds Ni concentrations of some of the most valuable Ni deposits, such as in New Caledonia (Brand et al., 1998; Elias, 2002; Butt and Cluzel, 2013). However, the occurrence of highly Ni enriched zones in the São João do Piauí Ni laterite is related to the presence of clay–rich veins and layers that only account for a minor amount of the total Ni compared to the host laterite.

The bedrock has whole–rock Ni concentrations of 0.28±0.05 wt%, with serpentine and chlorite as the main primary Ni minerals that have average Ni concentrations of 0.49 wt% and 0.11 wt%, respectively. In the overlying Ni laterite, saprock samples have high Ni concentrations (1.30 to 1.64 wt%) and Ni is significantly enriched in primary Mg–depleted serpentine minerals that have a Ni concentration of 2.62 wt% due to scavenging of mobile Ni leached from shallower parts of the laterite profile. The overlying saprolite horizons are characterised by large Ni variations ranging from 0.20 to 0.99 wt% with local Ni enrichments in the lower and central part of the coarse saprolite due to the presence of Ni–enriched primary serpentine and Ni–rich smectites, respectively. However, most saprolite samples show a pronounced loss of the primary mineral assemblage, which was in turn accompanied by significant loss of Ni. Residual serpentine is rare, in particular in the coarse saprolite, and relic serpentine minerals have Ni concentrations as low as 0.05 wt%. The predominant absence of relic serpentine in the coarse saprolite compared to the overlying argillaceous saprolite is interpreted to reflect weathering under a lowered water table that enabled an increased uptake of elements in percolating weathering solution and thus, a more efficient dissolution of the primary mineral assemblage. The silica cap and the magnesite–rich vein sample have very low Ni concentrations of 0.07 and 0.03 wt%, respectively. Clay–rich vein samples, which represent troctolite weathering products, have very high Ni concentrations, ranging from 1.82 to 4.95 wt%. Field observations revealed that these veins preferably transport percolating weathering solutions, therefore, high Ni concentrations likely reflect significant Ni scavenging by smectites and simultaneous formation of asbolane, which have Ni concentrations of 11.5 wt% and 16.4 wt%, respectively.

The change in the whole–rock Ni isotope composition with depth in the weathering profiles is shown in **Fig. 4.6b**. Laterite samples have δ^{60}Ni values ranging from 0.05 to –0.91 ‰. The least weathered bedrock sample (B1) has a δ^{60}Ni value of –0.01±0.09 ‰, within the range of igneous rocks (0.15±0.24 ‰; Elliot and Steele, 2017). However, the δ^{60}Ni value of B1 is relatively low, lying in the lower half of the δ^{60}Ni range reported for ultramafic rocks (–0.1 to 0.3 ‰; Cameron et al., 2009; Gall et al., 2013; Ratié et al., 2015; Spivak-Birndorf et al., 2018). Samples from the overlying laterite horizons are consistently depleted in heavy Ni isotopes compared to the serpentinised dunite parent rock, except one vein sample (V3) that shows a slightly higher δ^{60}Ni value of 0.05±0.09 ‰.

Ni–enriched samples with serpentine as the main ore in the saprock (SR1, SR2) have δ^{60}Ni values of between –0.14±0.09 ‰ and –0.21±0.09 ‰, whereas the Ni–enriched sample (CS4) from the central part of the coarse saprolite with smectite (~12 vol%) as the main ore has a lower δ^{60}Ni value of –0.91±0.12 ‰, which is the lowest δ^{60}Ni value yet reported for Ni–enriched saprolite material. Ni–depleted saprolite samples (CS5, CS6, AS1, AS2) have δ^{60}Ni values of between –0.11 and –0.56‰; samples from the argillaceous saprolite tend to be more depleted in heavy Ni isotopes. Vein sample V2, which consists of about 40 vol% smectite, has the highest Ni concentration (4.95 wt%) and has a δ^{60}Ni value of –0.48±0.10 ‰.

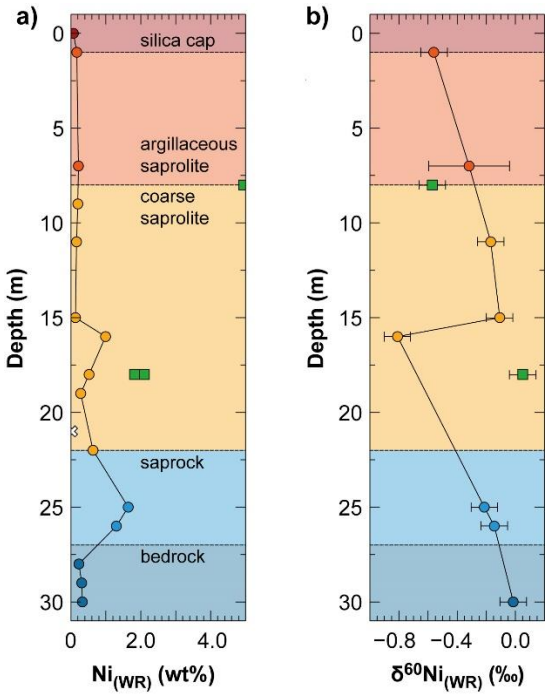

Fig. 4.6. **a)** Whole–rock Ni concentrations and **b)** Ni isotope composition of the laterite profile. Circles represent samples from the host laterite that formed from weathering of dunite, whereas squares represent clay–rich vein samples that originate from weathering of intercalated Al–rich troctolite.

Table 4.6. Ni isotope compositions of whole–rock (WR) samples from the São João do Piauí Ni laterite.

Depth	Sample	**δ^{60}Ni**	**$2\sigma_{(m)}$**	δ^{61}Ni	$2\sigma_{(m)}$	δ^{62}Ni	$2\sigma_{(m)}$	No. of replicates	Ni
m		‰		‰		‰			ppm
Host laterite (serpentinised dunite protolith)									
1	AS2	**-0.56**	**0.09**	-0.69	0.17	-1.06	0.12	1	1670
7	AS1	**-0.32**	**0.28**	-0.52	0.41	-0.66	0.38	1	2130
11	CS6	**-0.17**	**0.09**	-0.30	0.10	-0.40	0.12	3	1590
15	CS5	**-0.11**	**0.09**	-0.11	0.17	-0.01	0.12	1	1280
16	CS4	**-0.91**	**0.12**	-1.33	0.18	-2.00	0.24	6	9910
25	SR2	**-0.21**	**0.09**	-0.30	0.09	-0.59	0.32	2	16400
26	SR1	**-0.14**	**0.09**	-0.16	0.15	-0.35	0.28	2	13000
30	B1	**-0.01**	**0.09**	-0.03	0.08	0.04	0.13	2	3260
Clay–rich veins* (product of troctolite weathering)									
8	V2	**-0.48**	**0.10**	-0.81	0.15	-1.14	0.20	6	49500
18	V3	**0.05**	**0.08**	0.04	0.12	-0.07	0.16	3	21000

* Vein sample within the whole–rock laterite unit.

Note

$2\sigma_{(m)}$ is the sample standard error of the mean (SEM) of at least two individual analyses, where $2\sigma_{(m)}= 2SD/(N)^{0.5}$ (N = number of measurements). The standard deviation of a single analysis is smaller than $2\sigma_{(m)}$ and ranges between 0.01 and 0.03‰. For samples that have been measured only once, the 2SD value of the long–term reproducibility of the SRM986 standard is given (i.e. $2SD(\delta^{60}Ni) = 0.09$). The long–term reproducibility of the SRM 986 standard was chosen for samples that have a $2\sigma_{(m)}$ that is lower than 0.09.

Table 4.7. Selected major and minor element concentrations of laterite samples from the São João do Piauí Ni laterite.

Depth	Sample	MgO	SiO_2	Fe_2O_3	MnO	V	Ti	Nb	Th	MIA[a]
(m)		(wt%)	(wt%)	(wt%)	(wt%)	(ppm)	(ppm)	(ppm)	(ppm)	
	Host Laterite (serpentinised dunite protolith)									
0	SC	1.01	87.2	8.54	0.085	23.7	0.022	0.212	0.57	85.0
1	AS2	0.913	78.2	13.4	0.141	43.1	0.016	0.048	0.097	81.8
7	AS1	1.02	74.8	18.2	0.098	50.7	0.034	0.204	0.17	74.0
9	CS7	2.59	77.2	15.4	0.117	26.7	0.010	0.022	0.016	59.4
11	CS6	0.380	77.3	11.9	0.053	41.5	0.014	0.013	0.009	90.9
15	CS5	1.28	90.3	5.84	0.039	14.9	0.006	0.026	0.098	49.3
16	CS4	7.97	75.5	9.41	0.088	34.9	0.014	0.020	0.010	24.7
18	CS3	3.48	70.2	17.4	0.093	49.2	0.022	0.096	0.054	59.3
19	CS2	1.37	80.2	12.8	0.204	39.6	0.017	0.025	0.026	62.0
22	CS1	4.25	79.2	9.55	0.121	29.2	0.008	0.031	0.017	38.7
25	SR2	31.8	36.0	12.7	0.139	43.8	0.016	0.034	0.010	10.3
26	SR1	20.1	54.5	10.8	0.142	36.4	0.012	0.047	0.014	13.4
28	B3	35.5	39.0	10.3	0.104	35.5	0.074	0.266	0.053	8.1
29	B2	35.4	39.5	11.0	0.105	32.7	0.008	0.072	0.039	8.2
30	B1	33.1	41.5	9.37	0.181	46.3	0.017	0.056	0.015	8.4
	Magnesite vein (product of serpentinised dunite weathering)									
21	V1	44.9	3.46	0.473	0.0154	b.d.	b.d.	0.054	0.006	30.7
	Clay–rich veins* (product of troctolite weathering)									
8	V2	12.8	32.6	19.3	0.829	164	3.81	39.6	3.2	39.8
18	V3	13.8	33.5	28.5	0.551	240	3.67	10.4	2.0	46.7
18	V4	9.13	46.9	5.01	0.530	19.7	0.178	4.04	14	48.7

* Vein sample within the host laterite unit.

a Mafic index of alteration (MIA; Babechuk et al., 2014). The MIA(ox) is calculated as: MIA(ox) = 100 x $[(Al_2O_3 + Fe_2O_3)/(Al_2O_3 + Fe_2O_3 + MgO + CaO + Na_2O + K_2O)$.
Element concentrations that are used in the text, but are not listed in this table are given in **Table 3.2**, **3.3**, and, **3.4** in **Chapter 3**.

4.6 Discussion

4.6.1 Major element behaviour and degree of weathering

The Ni laterite is characterised by a rapid loss of Mg from the profile (**Fig. 4.7a**) and MgO concentrations decrease from 33.1 – 35.5 wt% in the parent rock, to 20.1 – 31.8 wt% in the saprock, and to 0.38 – 7.97 wt% in the overlying saprolite horizons and the silica cap (1.01 wt%). The loss of mobile elements, in particular Mg, results from the oxidative dissolution of serpentine, which is the dominant chemical process that exports mobile elements from the profile and thus determines the evolution of the laterite. On the other hand, Fe_2O_3 concentrations generally increase from the bedrock (9.37 – 11.0 wt%) to the saprock (10.8 – 12.7 wt%), and vary between 5.84 and 18.2 wt% in the saprolite (**Fig. 4.7a**). Concentrations of Fe_2O_3 correlate with the relative abundance of hematite in the samples. The silica cap has 8.54 wt% Fe_2O_3. The very low Fe content of the profile, in particular at shallower depth, is a result of high SiO_2 concentrations (**Fig. 4.7a**) that originate from retention of silica mobilised during the hydrolysis of serpentine, which serves to dilute the abundance of residual Fe. This is demonstrated by the general increase of SiO_2 concentrations in the profile from the bedrock (39.0 – 41.5 wt%), through the saprock (36.0 – 54.5 wt%), towards the saprolite (70.2 – 90.3 wt%) and the silica cap (87.2 wt%).

The geochemical changes that are associated with the breakdown of the primary silicate assemblage and the formation of secondary oxides under SiO_2 retention can be visualised by the mafic index of alteration (MIA; Babechuk et al., 2014). The MIA describes the weathering trend based on the loss of alkali– and alkali–earth–elements and relative gains of Al (and Fe), with low values corresponding to 'fresh' (unaltered) rock material and vice versa. MIA values in the profile (**Fig. 4.7b**) generally increase upwards from the parent rock (8), through the saprock horizon (10 – 13) and towards the lower coarse saprolite (39 – 62). The central coarse saprolite shows slightly lower MIA values of between 25 and 49 due to the presence of Mg–bearing smectite. MIA values further increase in the upper coarse saprolite (59 – 91) and in the argillaceous saprolite (74 – 81).

Embedded clay–rich veins show moderate MgO (9.13 – 13.8 wt%) and SiO_2 (32.6 – 46.9 wt%) contents compared to the host laterite. There is no secondary silica present in the veins, most likely due to high Al contents (10.5 – 19.8 wt%) that allowed formation of abundant clays, in particular at shallow depths. Fe concentrations in the veins vary widely (5.01 – 28.5 wt%), however, their MIA values span a narrow range (40 – 49), as the ratio of the sum of mobile (Mg, Ca, Na, K) and immobile elements (Fe, Al) is similar.

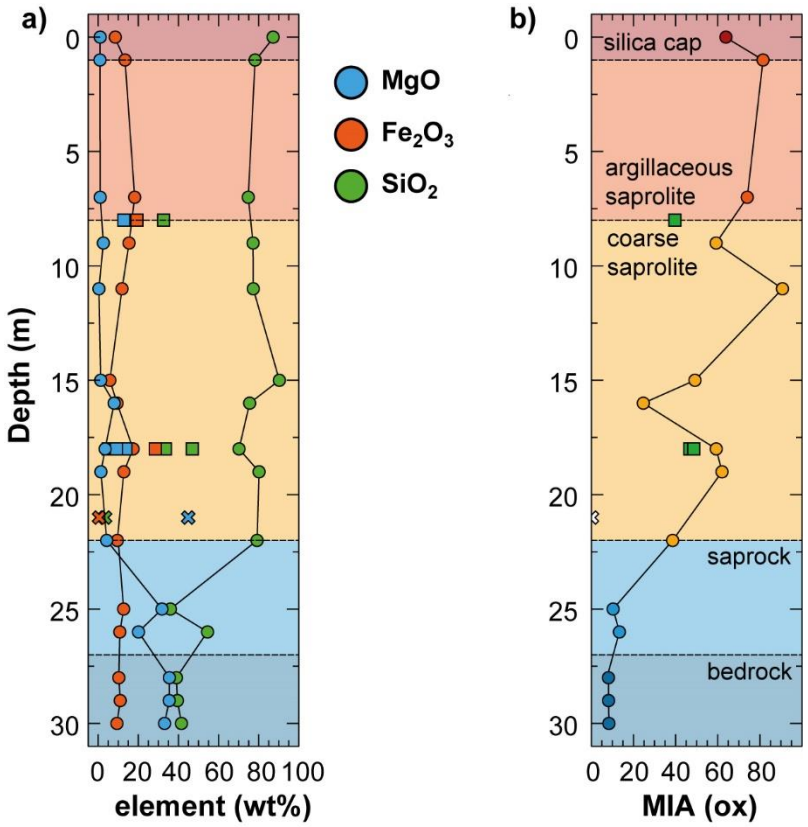

Fig. 4.7. The change of **a)** the concentration of major elements (i.e. Mg, Fe, Si) and **b)** the degree of weathering, expressed as the MIA (mafic index of alteration), with depth in the São João do Piauí Ni laterite.

4.6.2 Behaviour of chromium in the weathering profile

The serpentinised dunite on which the Ni laterite has developed is situated in the Ultramafic Zone (UZ) of the Brejo Seco Complex (BSC), which is a layered igneous body that intruded into a series of volcano–sedimentary rocks in the Precambrian. Unlike most parent rocks that underlie modern Ni laterites (Elias, 2002), the BSC does not have an ophiolitic origin; rather, it represents a former magma chamber in which the magmatic layers (e.g. Ultramafic Zone) were predominantly formed by fractional crystallisation from a differentiating magma, where mineral segregation processes played an important role (Verma and Oliveira, 2015; Salgado et al., 2016). Therefore, cumulate textures are likely responsible for variable contents of Cr, Ti, Nb, V (**Table 4.7**), and other elements that are mainly incorporated into oxide phases. Parent rock samples B1 and B2 show similar relative mineral abundances, in particular in the oxide fraction. However, B2 shows incipient alteration features under the microscope (presence of oxidised mineral veins) that probably led to a loss of Cr in a very early stage of alteration, which is supported by a low $\delta^{53}Cr$ value of –0.35±0.06 ‰.

Parent rock sample B3 shows the presence of abundant chrysotile, which likely formed at a late stage prior to exposure and is rather Cr–poor (e.g. Ningthoujam et al., 2012). Sample B3 has a relatively low Cr content, however, it also has a significantly higher Ti content compared to samples B1 and B2 as well as a higher relative abundance of oxides, which indicates the presence of ilmenite ($FeTiO_3$). Abundant ilmenite and chrysotile are likely responsible for the low whole–rock Cr content of parent rock sample B3. Salgado et al. (2014) intensively studied the progenitor units of the São João do Piauí Ni laterite and determined an average mineralogical composition of unweathered serpentinised dunite cumulate rock that consists of about 90 vol% of variably serpentinised olivine and less than 7 vol% Cr–bearing oxides (mainly Cr–magnetite and chromite). The remainder of the rock consists of varying amounts of inter–cumulates, such as plagioclase, pyroxene, pentlandite, and rarely phlogopite. The mineral content of bedrock sample B1 is similar to the average mineral composition of the serpentinised dunite from which the overlying Ni laterite developed and shows the least altered mineral assemblage. Therefore, its Cr concentration is used as the best estimate for the parent rock in following discussions of the evolution of the Cr isotopic composition in the laterite profile.

Bedrock normalised Cr concentrations (Cr_{bed}) as well as Cr concentrations normalised to Ti (Cr_{Ti}), Nb (Cr_{Nb}), and Th (Cr_{Th}), which are considered to be least mobile during weathering (e.g. Cornu et al., 1999; Gong et al., 2011), generally indicate a pattern of variable but significant loss of Cr from the laterite that increases from the bottom to the top of the profile (**Fig. 4.8**). As all of the regolith units in the laterite profile have undergone massive re–silification, significant shrinking of the laterite is unlikely to have occurred, which is reflected by similar trends in Cr_{bed} and (Cr_{Ti}), (Cr_{Nb}), and (Cr_{Th}). Therefore, apparent enrichment in Cr in some samples (e.g. high Cr_{Nb} values in the coarse saprolite), are rather interpreted to reflect an initially heterogeneous Nb content due to varying mineral abundances in the progenitor unit. In the following discussion, Cr_{bed} values are primarily used to discuss the behaviour of Cr and the evolution of the Cr isotopic composition in the laterite profile.

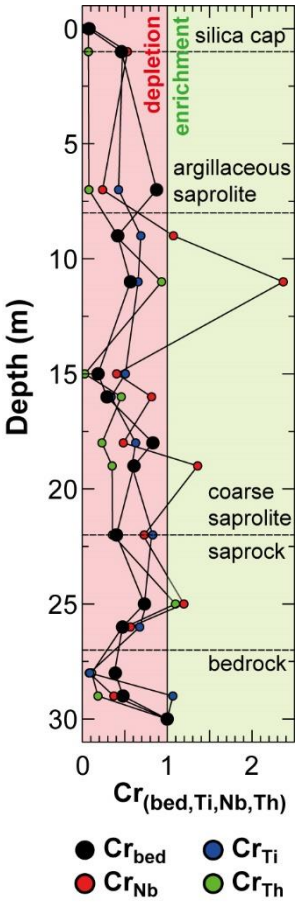

Fig. 4.8. Comparison of bedrock normalised Cr contents and bedrock normalised Cr contents that have been additionally corrected based on an immobile element to remove physical effects, such as collapse or dilation. The close correlation between the graphs demonstrates only small physical effects during laterite profile development and confirm its relative stability during weathering. Cr_{bed} is calculated according to $Cr_{sample}(wt\%)/Cr_{B1}(wt\%)$ and Cr_X is calculated as: $[Cr_{sample}(wt\%)/X_{sample}(wt\%)]/[Cr_{B1}(wt\%)/X_{B1}(wt\%)]$ with X = Ti (wt%), Nb (wt%), or Th (wt%). $Cr_{Ti,Nb,Th}$ are not given in traditional tau–values after Amundson (2013), as for the discussion of the Cr isotope evolution, it is necessary to relate the Cr content of the unaltered bedrock as fraction, defined as fCr(bed) = 1.

Cr in ultramafic rocks and in particular in dunites has a pronounced bimodal mineralogical distribution between silicates and oxides (Oze, 2003). In this laterite profile, chromite and in particular Cr–bearing magnetite are the most prevalent sources of Cr. The high relative abundance of Cr in the oxide fraction is reflected by high correlations with V (R^2 = 0.76; **Fig. 4.9a**), which is predominantly hosted in magnetite and chromite (e.g. Leblanc, 1986; Cawthorn et al., 2005). Cr contents are also positively correlated with Fe (R^2 = 0.50) and Al (R^2 = 0.68) (**Fig. 4.9b** and **c**), as chromite and magnetite also host the majority of Fe in the rock and mobilised Cr^{3+} that has not been oxidised will favourably be incorporated into secondary Al– and Fe–oxides (Oze, 2003 and references therein). On the other hand, Cr contents are considerably lower in the silicate fraction. Thus, although the silicate fraction (~95 %) dominates the mineralogy of the serpentinised dunite parent rock, the oxide fraction hosts most of the Cr.

Cr–bearing oxides have a very low weathering susceptibility and altered Cr–rich spinels are characterised by loss of Mg and Al, whereas Cr is relatively unaffected and is thus residually enriched in the mineral during alteration (Banerjee et al., 2015). Thus, Cr removal during weathering and is expected to mainly result from the hydrolysis of Cr–bearing silicates, in particular during the early stages of weathering.

Cr losses of > ~25% of the total Cr content in the saprolite and in the silica cap, as indicated by most Cr_{bed} values in the saprolite, may be inherited from heterogeneous Cr contents in the progenitor units of the laterite, as indicated by highly variable Cr concentrations in the parent rock samples. However, in later stages of weathering at low pH, weathering of Cr–bearing oxides can yield in high Cr mobilisation rates in the presence of Mn–oxides (Oze et al., 2007). Thus, the upper parts of the profile (i.e. saprolite, silica cap) may have experienced Cr loss from magnetite and chromite dissolution under low pH conditions (Garnier et al., 2008). Lower parts of the profile, in particular the saprock horizon, were likely unaffected by Cr loss from oxides, due to the dominating presence of Mg–silicates that have a high pH buffer capacity, which leads to alkaline conditions in percolating weathering solutions in which Cr mobilisation from oxides, in particular from chromite, is negligible (Oze et al., 2007).

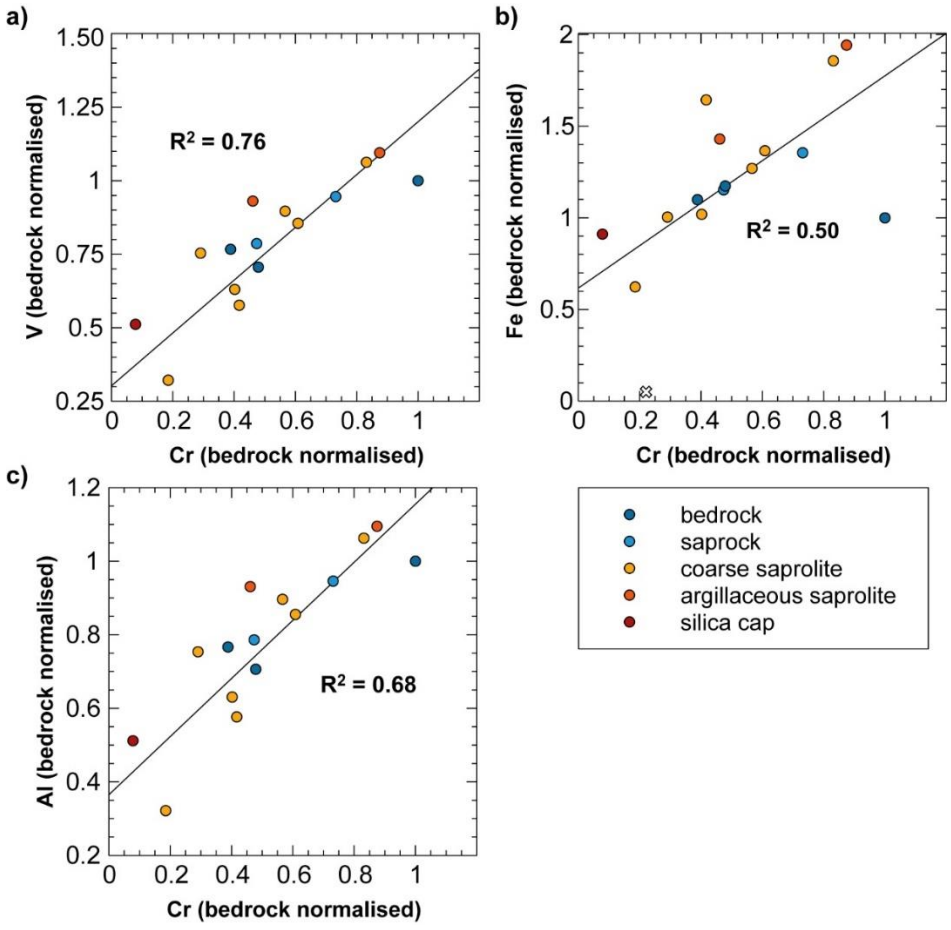

Fig. 4.9 a) Bedrock normalised V content vs. bedrock normalised Cr content revealing a correlation of R^2 = 0.76 between bedrock and host laterite samples. **b)** Bedrock normalised Fe content vs. bedrock normalised Cr content revealing a correlation of R^2 = 0.50 between bedrock and host laterite samples. **c)** Bedrock normalised Al content vs. bedrock normalised Cr content revealing a correlation of R^2 = 0.68 between bedrock and host laterite samples. All correlations are related to the mineralogical abundances of Cr in oxide minerals (chromite, Cr–bearing magnetite).

4.6.3 Cr isotopic composition of rock samples

Most laterite samples have $\delta^{53}Cr$ values that are lower than that of the underlying parent rock and have corresponding bedrock normalised Cr concentrations that indicate a Cr loss during weathering, which agrees with several studies of ancient and modern laterite profiles (e.g. Crowe et al., 2013; Frei and Polat, 2013; Berger and Frei, 2014; Frei et al., 2016).

The overall Cr isotopic range in the profile is 1.58 ‰ (–0.12 to –1.70 ‰), which is far higher than the range previously reported for modern (Phanerozoic) weathering profiles (0.2 to 0.6 ‰ ;Frei and Polat, 2013; Berger and Frei, 2014; Frei et al., 2014; Novak et al., 2017). The large range results from the extremely low $\delta^{53}Cr$ values of samples AS2 (–1.40±0.04 ‰), V3 (–1.57±0.10 ‰), and V1 (–1.70±0.04 ‰), which are close to the lower limit of reported $\delta^{53}Cr$ values in both ancient and modern weathering systems (Qin and Wang, 2017 and references therein). The magnesite vein sample V1 shows the isotopically lightest Cr composition with a $\delta^{53}Cr$ value of –1.70 ‰. Magnesite in this sample is Cr–free and thus, all Cr stems from small serpentinite remnants with a very low abundance (<1 vol%) of oxides that are enclosed in the secondary magnesite precipitate. This evidences that Cr removal from the silicates occurred under high pH conditions. Furthermore, sample AS2, which was taken close to a magnesite vein in the profile, is also strongly depleted in heavy Cr isotopes, indicating that Cr removal under alkaline conditions favours removal of heavy Cr isotopes, consistent with experimental findings of Berger and Frei (2014). Possible explanations for this interdependent relationship include a lowered ΔE_h–threshold at alkaline pH that promotes oxidation of Cr^{3+} to Cr^{6+} (Beverskog and Puigdomenech, 1997), as well as different Cr oxidation pathways under high pH compared to Cr oxidation under acid conditions (Silvester et al., 1995).

Clay separates (CLS) show $\delta^{53}Cr$ values of between –0.10 and –1.87 ‰ and the saprolite samples (CS + AS) are generally more depleted in heavy Cr than their corresponding whole–rock samples. The clay separates comprise predominantly of small disintegrated, partly dissolved primary minerals and newly formed secondary minerals that will likely have a low $\delta^{53}Cr$ due to oxidative Cr loss, whereas the whole–rock is a mixture of weathered (disintegrated) and unweathered (integrated) rock material, thus, it is expected that the whole–rock Cr isotopic composition generally has a higher $\delta^{53}Cr$ value. However, clay separates from the saprock (SR1, SR2) and from two veins (V1, V3) close to the bedrock have higher $\delta^{53}Cr$ values compared to their corresponding whole–rock samples. The through–flow of percolating weathering solutions in deeper parts of the laterite profile is limited due to the close proximity of the permeability barrier of the underlying parent rock.

Therefore, weathering solutions have a longer residence time in the deeper parts of the laterite profile than they do in the shallower parts of the profile, where solutions pass quickly through the rock. The longer residence time may allow a fraction of mobilised Cr^{6+} with a relatively high $\delta^{53}Cr$ value to be adsorbed on clay particles. Uptake of Cr^{6+} on secondary Fe–oxides, such as hematite, is unlikely, as hematite has a low Cr sorption capacity at high pH (Ajouyed et al., 2010).

4.6.4 Cr isotopic composition of water samples

The pore water that was sampled at the bottom of the pit at the transition zone between saprock and bedrock shows a highly fractionated Cr isotopic composition with a $\delta^{53}Cr$ value of 4.31 ‰ and a Cr concentration of 22.9 ppm, which is in excellent agreement with stream waters draining serpentinites that show $\delta^{53}Cr$ values of up to 3.96 ‰ and Cr concentrations ≤23 ppm (Farkaš et al., 2013). The difference between the Cr isotopic composition of the pore water and whole–rock samples from the lower saprock horizon is 4.74 ‰, which indicates that Cr isotopes are highly fractionated during hydrolysis of Cr–bearing silicates. Furthermore, it suggest that oxidative Cr loss during incipient weathering, which is characterised by high pH conditions, is accompanied by preferential loss of heavy Cr isotopes from the silicate fraction (i.e. serpentine, chlorite).

The river water sample also has a relatively high $\delta^{53}Cr$ value (0.76±0.09 ‰) compared to the bedrock; this value is within the range of $\delta^{53}Cr$ values for other river waters that are between –0.17 and 4.00 ‰ (Qin and Wang, 2017 and references therein). The $\delta^{53}Cr$ value of the river water reflects the sum of the abundance–weighted isotope compositions of Cr that was mobilised from different laterite units under variable pH conditions. Early stages of weathering are usually characterised by high pH conditions due to the dissolution of Mg–silicates, whereas later stages of weathering, when all Mg is removed, progress under low pH conditions (e.g. April et al., 1986; Marker et al., 1991; Schellmann, 1994; Butt and Cluzel, 2013). As the pore water has a far higher $\delta^{53}Cr$ value than the river water, this may indicate that Cr removal during the later stages of weathering (i.e. from shallower laterite units), is accompanied by lower, or no, Cr isotope fractionation. Secondary processes that could have altered the Cr isotopic composition of the river water, such as reduction of Cr^{6+} by organic matter or Fe^{2+}, have not been investigated. However, reduction of riverine Cr would have shifted the Cr composition of the remaining aqueous Cr^{6+} pool towards higher $\delta^{53}Cr$ values (e.g. Ellis et al., 2002, 2004; Frei et al., 2014; D'Arcy et al., 2016).

Therefore, the initial $\delta^{53}Cr$ value of the river water may have been even lower than 0.76 ‰, which supports the idea that the later stages of lateritic weathering progresses with no or low Cr isotope fractionation. Input of Cr from adjacent, granitic rocks in the catchment is likely to be low, because the Cr concentrations of these rocks are ~10 to 100 times lower than in ultramafic rocks, ranging between 50 and 200 ppm (e.g. Cullers, 1988).

4.6.5 Potential mechanisms of Cr isotope fractionation

The loss of isotopically heavy Cr into the fluid phase during weathering of ultramafic rocks is thought to be due to oxidation of Cr^{3+} by MnO_2 in a complex multi–stage reaction that results in preferential enrichment of heavy Cr isotopes in Cr^{6+}, which is far more soluble than Cr^{3+} and goes into the fluid phase (Eary and Rai, 1987; Zasoski and Fendorf, 1992; Silvester et al., 1995; Oze et al., 2007; Economou-Eliopoulos et al., 2014). The loss of isotopically heavy Cr into percolating weathering solutions is confirmed by the high $\delta^{53}Cr$ values of the pore water and river water samples and is consistent with numerous studies of waters from local outlet systems of ultramafic rock provinces, rivers, and the oceans, all of which have higher $\delta^{53}Cr$ than the rocks from which the Cr was lost (Bonnand et al., 2013; Farkaš et al., 2013; Paulukat et al., 2015; Scheiderich et al., 2015; D'Arcy et al., 2016; Novak et al., 2017; Goring-Harford et al., 2018).

Cr^{3+} is oxidised by the reduction of insoluble Mn^{4+}, which is present as MnO_2 in the rock, to soluble Mn^{2+} (Zasoski and Fendorf, 1992). **Fig. 4.10a** shows the Cr isotopic composition of whole–rocks as a function of the bedrock normalised Mn content. All regolith samples are slightly depleted in Mn compared to the bedrock, however, there is no apparent relationship between Mn and $\delta^{53}Cr$ (R^2 = 0.02; p–value = 0.65), which implies that fractionation of Cr isotopes is not directly related to the Mn content of individual laterite samples. Oxidation of Cr^{3+} is triggered by the reduction of insoluble Mn^{4+} to soluble Mn^{2+}, which could theoretically be readily extracted by percolating weathering solutions. However, weathering solutions are usually O_2–rich (e.g. Zasoski and Fendorf, 1992), as they infiltrate as meteoric water into the regolith profile. Therefore, the lack of correlation between Mn and $\delta^{53}Cr$ may indicate that reduced Mn^{2+} was 'back–oxidised' to insoluble Mn^{4+} by O_2 from meteoric waters producing a 'positive recycling feedback'.

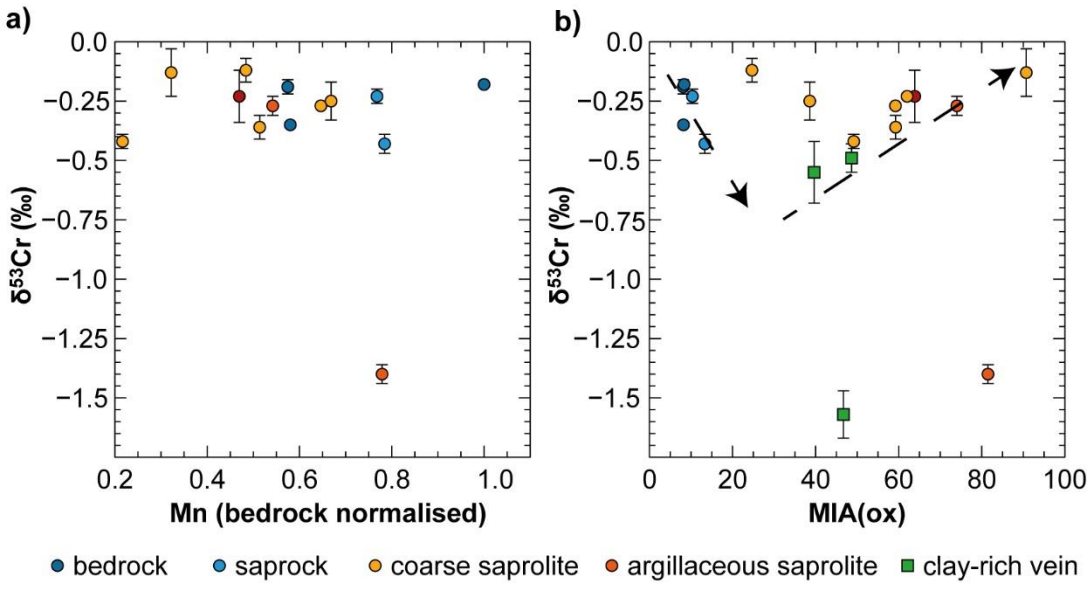

Fig. 4.10. **a)** $\delta^{53}Cr$ vs. bedrock normalised Mn content. **b)** $\delta^{53}Cr$ vs. MIA(ox) values. Note that $\delta^{53}Cr$ values tend to decrease as MIA values shift from 0 to 20, and increase between MIA = 40 – 100.

Furthermore, the loss of heavy Cr isotopes from the profile does not correlate with the degree of weathering predicted by MIA values (**Fig. 4.10b**). Rather, during incipient weathering stages (MIA: 0 – 20), $\delta^{53}Cr$ values strongly decrease and then increase again during moderate to late stages of weathering (MIA values >40), thereby forming a 'u–shaped' trend. This means, for instance, that most samples from the saprolite horizon have higher $\delta^{53}Cr$ values than samples from the underlying saprock, although they have been exposed to oxidative weathering processes for much longer and have lost a higher amount of Cr from the mineral assemblage. Uptake of Cr with a high $\delta^{53}Cr$ value from percolating weathering solutions is unlikely because Cr losses are much higher in the shallower horizons than they are in the deeper parts of the profile. Late stages of lateritic weathering are generally characterised by a low pH in the weathering solution due to the lack of Mg in the rock. The sorption capacity of hematite increases with decreasing pH (Ajouyed et al., 2010), which would allow oxidised Cr^{6+} to be taken up into secondary Fe–oxides. However, even if Cr isotope fractionation occurs at low pH, the whole–rock Cr isotopic composition would not reflect this, as oxidised Cr with a positively fractionated $\delta^{53}Cr$ value would not be removed by fluids and would remain in the rock. Thus, uptake of Cr^{6+} onto hematite that was released from the primary mineral assemblage would not change the $\delta^{53}Cr$ value of the–whole rock and cannot explain increasing $\delta^{53}Cr$ values at high degrees of weathering.

Therefore, the trend of decreasing $\delta^{53}Cr$ values during the early stages of weathering and the shift back towards higher $\delta^{53}Cr$ values in the later stages of weathering, both accompanied by loss of Cr, is considered to be a primary weathering signal that reflects oxidative Cr loss together with a strong mineralogical control. During oxidation, Cr^{3+} is thought to be first oxidised to Cr^{5+}, which has been recognised as the rate–limiting step, followed by disproportionation to Cr^{3+} and Cr^{6+} (Impert et al., 2008). Experimental results reveal that oxidative Cr removal and the change of the Cr isotopic composition progress with a fractionation on the $^{53}Cr/^{52}Cr$ ratio of $10^3 \cdot \ln\alpha$ (i.e. $\Delta^{53}/^{52}Cr_{(Cr^{6+}-Cr^{3+})}$) of 0.6‰ and that the Cr isotopic composition of the residual Cr^{3+} fraction can be described by a Rayleigh fractionation trend (Zink et al., 2010). On time scales of a few months, roughly the maximum contact time between the weathering solution and the laterite rocks, Cr isotope exchange has no effect on the Cr isotopic composition (Zink et al., 2010), thus Cr isotope fractionation during oxidative weathering can mathematically be approximated as a 'kinetic process' that occurs in a closed system, as the reactant (Cr^{3+} in minerals) is in limited supply and consumed by the reaction (oxidation to Cr^{6+}). As the product (Cr^{6+}) is continuously removed by percolating weathering solutions, back–reactions are considered to be not significant, especially during the early stages of weathering due to the high pH buffer capacity of ultramafic rocks that likely hampers secondary processes, which could potentially alter the Cr isotopic composition, such as Cr adsorption or Cr back–reduction.

The loss of Cr from the bedrock sample B1 can be recast as the fraction of Cr^{3+}(fCr^{3+}) that remains in the weathered rock. A simple fractionation model of aqueous Cr^{6+} loss due to Cr^{3+} oxidation starting from the parent rock Cr isotopic composition of $\delta^{53}Cr$ = –0.18 ‰ and extending to levels of Cr depletion observed in the laterite samples yields Cr isotope fractionation factors ($10^3 \cdot \ln\alpha \approx \varepsilon = \Delta^{53/52}Cr_{(Cr^{6+}-Cr^{3+})}$) that range between 0.01 and 1.90 ‰ (**Fig. 4.11**). Thus, some samples show significant Cr loss without significant Cr isotope fractionation, whereas other samples show a strong Cr isotope fractionation during Cr removal. If weathering proceeds sequentially, then it is expected that the $\delta^{53}Cr$ value of a sample that is situated higher in the profile is equal to or lower than the $\delta^{53}Cr$ value of its underlying progenitor, because it has been exposed to oxidative weathering conditions for longer and has therefore lost more Cr than the underlying less weathered rock horzion. However, except for sample AS2, the $\delta^{53}Cr$ values slightly increase from the saprock towards the saprolite and the silica cap (**Fig. 4.5a**). Especially, the silica cap (SC), which is the ultimate leftover of lateritisation (Lacinska and Styles, 2013; Butt, 2014) and has lost about 92 % of its initial Cr content under oxidative weathering conditions, has a Cr isotopic composition that is equal within the error to the $\delta^{53}Cr$ value of the unweathered parent rock sample B1.

The reason for the wide range of apparent Cr isotope fractionation factors is that Cr is found in association with two mineral groups, silicates and oxides, which have very different weathering susceptibilities. Most Cr is present in oxides, such as magnetite or chromite, whereas a smaller amount of Cr is present in the silicate fraction (principally serpentine and chlorite). When weathering starts to attack the mineral assemblage, silicates are more prone to weathering and silicate–bound Cr will be preferentially hydrolysed and lost to the fluid phase. By contrast, oxide–bound Cr remains virtually unaffected during oxidative weathering due to its extraordinary low weathering susceptibility (Velbel, 1993, 1999; Garnier et al., 2008).

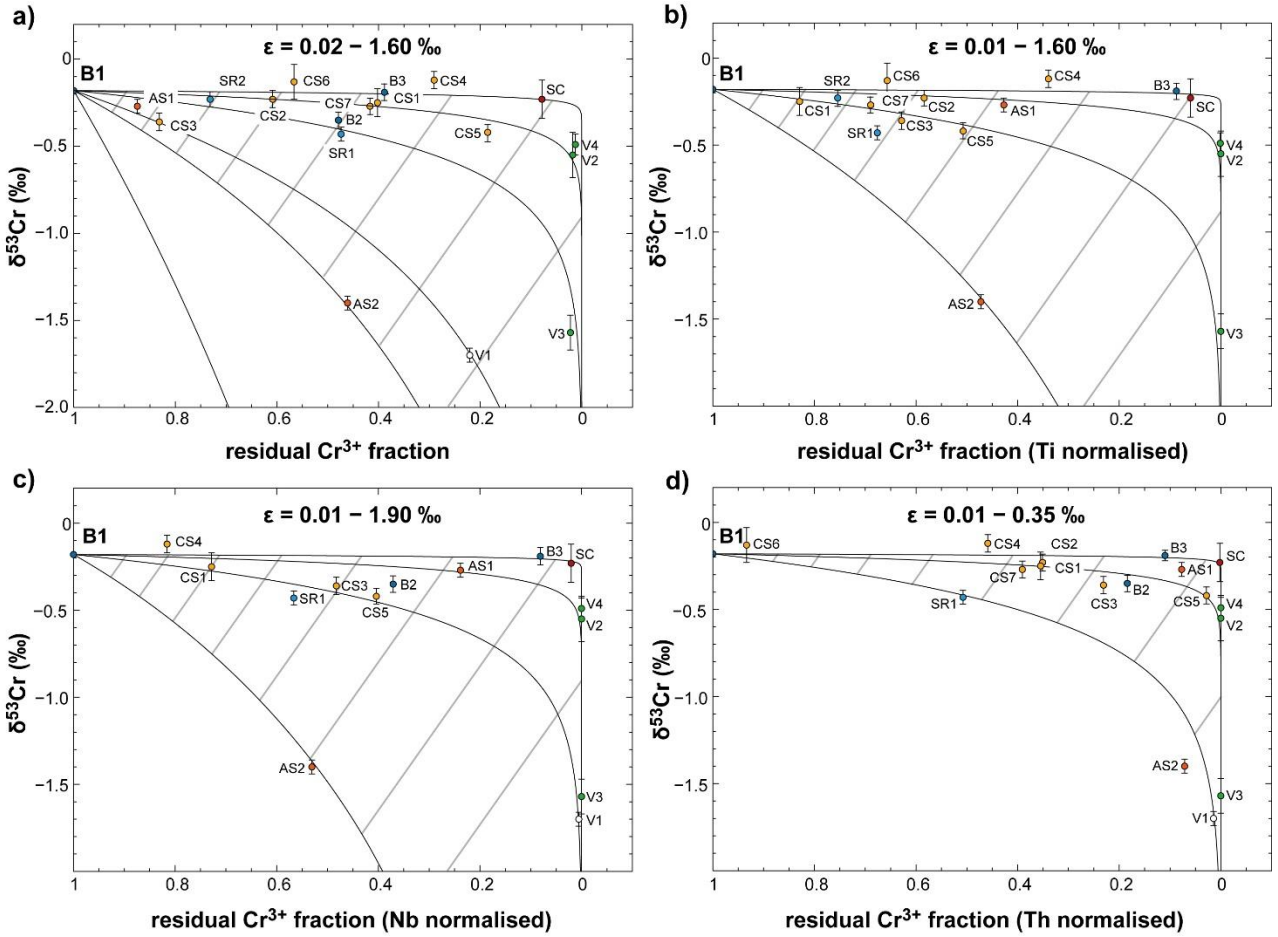

Fig. 4.11. Rayleigh distillation model of Cr isotope fractionation during Cr oxidation. **a)** $\delta^{53}Cr$ vs. fraction of Cr remaining in the bedrock , **b)** $\delta^{53}Cr$ vs. Ti normalised fraction of Cr remaining in the bedrock, **c)** $\delta^{53}Cr$ vs. Nb normalised fraction of Cr remaining in the bedrock , and **d)** $\delta^{53}Cr$ vs. Th normalised Cr fraction of Cr remaining in the bedrock. The Cr isotope fractionation factor between the bedrock and the laterite samples ranges between 0.01 and 1.90 ‰ (ε_{nat}). Normalised Cr contents are calculated as follows: $[Cr_{sample}(wt\%)/X_{sample}(wt\%)]/[Cr_{B1}(wt\%)/X_{B1}(wt\%)]$ with X = Ti (wt%), Nb (wt%), or Th (wt%). All fractionation factors are expressed as ε values (equivalent to $\Delta^{53}Cr$), defined as $\delta^{53}Cr^{6+}_{(aqueous)} - \delta^{53}Cr^{3+}_{(solid)}$, and are related to α by $\varepsilon \approx 1000 \cdot \ln\alpha$.

4.6.6 Modelling Cr isotope behaviour in the laterite profile

Oxidative weathering of ultramafic rocks leads to an incongruent mineral dissolution in which Cr–bearing silicates dissolve significantly faster than Cr–bearing oxides (Velbel, 1993, 1999; Garnier et al., 2008), which in turn is responsible for an incongruent Cr loss from the two mineralogical reservoirs. This can be described by a simple isotope mass balance equation (1):

$$\delta^{53}Cr(WR) = p(sil) \cdot \delta^{53}Cr(sil) + p(ox) \cdot \delta^{53}Cr(ox) \qquad (4.1)$$

with:

$\delta^{53}Cr(WR) = Cr\ isotope\ composition\ of\ the\ whole\text{–}rock\ (WR)$

$\delta^{53}Cr(sil) = Cr\ isotope\ composition\ of\ the\ silicate\ fraction$

$\delta^{53}Cr(ox) = Cr\ isotope\ composition\ of\ the\ oxide\ fraction$

$p(sil) = proportion\ of\ Cr\ in\ silicates$

$p(ox) = proportion\ of\ Cr\ in\ oxides$

and:

$$p(sil) + p(ox) = 1$$

Thus:

$$\delta^{53}Cr(WR) = p(sil) \cdot \delta^{53}Cr(sil) + [1 - p(sil)] \cdot \delta^{53}Cr(ox) \qquad (4.2)$$

As weathering proceeds, Cr–bearing silicates start to dissolve, a process that is accompanied by fractionation of Cr isotopes. The magnitude of Cr isotope fractionation during silicate weathering, ε, can be estimated from the difference between the Cr isotopic composition of the saprock and the Cr isotopic composition of the interstitial pore water sample: $\varepsilon = \delta^{53}Cr_{(SR1)} - \delta^{53}Cr_{(PW)} = 4.74$ ‰. Assuming that the $\delta^{53}Cr$ value of the pore water represents the cumulative Cr isotopic composition of total dissolved Cr over the pore water residence time of 2 to 3 months, the initial Cr isotope fractionation factor is likely to be slightly higher, and is here estimated to be $\varepsilon = 5.0$ ‰.

Due to the weathering resistivity of the oxide fraction it can be assumed that no Cr is lost from oxides so the Cr isotopic composition of the oxide fraction, $\delta^{53}Cr(ox)$, remains constant. The Rayleigh distillation equation that describes the evolution of the Cr isotopic composition of the residual silicate fraction, $\delta^{53}Cr(sil)$, as a function of the silicate Cr fraction, f(sil), given a constant fractionation factor α (recall that $\varepsilon \approx 1000 \cdot \ln\alpha$) in a closed system, is:

$$\delta^{53}Cr(sil) = [1000 + \delta^{53}Cr_0(sil)] \cdot \left[f(sil)^{[\alpha(sil)-1]}\right] - 1000 \qquad (4.3)$$

$\delta^{53}Cr_0(sil) = initial\ Cr\ isotope\ composition\ of\ the\ silicate\ fraction$

$\mathrm{f}(sil) = fraction\ of\ silicate\ fraction\ that\ remains\ in\ the\ rock$

The evolution of the whole–rock Cr isotopic composition can therefore be modelled by combining *equations 4.2* and *4.3*. For simplicity, Cr concentrations are normalised to the bedrock Cr concentration, although Cr concentrations can also be normalised to an immobile element, similar to **Fig. 4.11b**, **c**, and **d**.

Inserting equation (3) into equation (2) yields:

$$\delta^{53}Cr(WR) = p(sil) \cdot \left[[1000 + \delta^{53}Cr_0(sil)] \cdot \left[f(sil)^{[\alpha-1]}\right] - 1000\right] +$$

$$[1 - p(sil)] \cdot \delta^{53}Cr(ox) \qquad (4.4)$$

Equation (4) describes the Cr isotopic composition of the whole–rock as a function of the proportion of Cr in the silicate fraction that remains in the silicate fraction. As *p(sil)* describes the 'abundance–weighted' Cr content of the silicates, it follows:

$$p(sil) = [f(sil) \cdot c_0(sil)] \qquad (4.5)$$

$$where\ c_0(sil) = proportion\ of\ Cr\ residing\ in\ silicates\ in\ the\ unaltered\ bedrock$$

I.e:

$$c_0(sil) = \frac{rel\%(sil) \cdot wt\%(sil)}{rel\%(sil) \cdot wt\%(sil) + rel\%(ox) \cdot wt\%(ox)} \qquad (4.6)$$

$rel\%(sil) = relative\ silicate\ abundance\ in\ unaltered\ bedrock$

$rel\%(ox) = relative\ oxide\ abundance\ in\ unaltered\ bedrock$

$\text{wt}\%(sil) = Cr\ concentration\ in\ silicates\ in\ unaltered\ bedrock$

$wt\%(ox) = Cr\ concentration\ in\ oxides\ in\ unaltered\ bedrock$

Inserting *equation 4.5* into *equation 4.4* leads to:

$$\delta^{53}Cr(WR) = [f(sil) \cdot c_0(sil)] \cdot \Big[[1000 + \delta^{53}Cr_0(sil)] \cdot \big[f(sil)^{[\alpha-1]}\big] - 1000\Big] + \Big[1 - [f(sil) \cdot c_0(sil)]\Big] \cdot \delta^{53}Cr(ox) \qquad (4.7)$$

$\delta^{53}Cr_0(sil)$ is given by:

$$\delta^{53}Cr_0(sil) = \frac{[\delta^{53}Cr_0(WR) - [c_0(ox) \cdot \delta^{53}Cr(ox)]]}{c_0(sil)} \qquad (4.8)$$

$where\ \delta^{53}Cr_0(WR) =\ whole\text{–}rock\ Cr\ isotope\ composition\ of\ the\ unaltered\ bedrock$

and:

$$c_0(ox) = \frac{rel\%(ox) \cdot wt\%(ox)}{rel\%(sil) \cdot wt\%(sil) + rel\%(ox) \cdot wt\%(ox)} \qquad (4.9)$$

Instead of plotting $\delta^{53}Cr(WR)$ as function of $f(sil)$, it can be plotted as a function of the whole–rock Cr fraction $p(WR)$, that remains in the rock. It generally applies that:

$$p(WR) = p(sil) + p(ox)$$

At the beginning (suffix = 0), when no Cr has been lost from the rock, it follows that:

$$p(WR)_0 = p(sil)_0 + p(ox)_0 = 1$$

$$p(sil)_0 + p(ox)_0 = 1 \qquad (4.10)$$

$$[f(sil)_0 \cdot c_0(sil)] + p(ox)_0 = 1 \qquad (4.11)$$

At the beginning it further applies that:

$$f(sil)_0 = 1$$

Thus, it follows:

$$c_0(sil) + p(ox)_0 = 1$$

$$p(ox)_0 = 1 - c_0(sil) \qquad (4.12)$$

Cr in the oxide fraction is assumed to be completely retained during silicate breakdown. Therefore, *p(ox)* is constant and it follows that:

$$p(ox)_0 = p(ox)$$

Which yields:

$$p(ox) = 1 - c_0(sil) \qquad (4.13)$$

Thus it follows that:

$$p(WR) = [f(sil) \cdot c_0(sil)] + [1 - c_0(sil)] \qquad (4.14)$$

Rearranging *equation 4.14* in terms of *f(sil)* gives:

$$f(sil) = \frac{p(WR) + c_0(sil) - 1}{c_0(sil)} \qquad (4.15)$$

Inserting *equation 4.15* into *4.7* yields in:

$$\delta^{53}Cr(WR) = [[\frac{p(WR) + c_0(sil) - 1}{c_0(sil)}] \cdot c_0(sil)] \cdot \left[[1000 + \delta^{53}Cr_0(sil)] \cdot \left[[\frac{p(WR) + c_0(sil) - 1}{c_0(sil)}]^{[\alpha(sil)-1]}\right] - 1000\right] + \left[1 - [[\frac{p(WR) + c_0(sil) - 1}{c_0(sil)}] \cdot c_0(sil)]\right] \cdot \delta^{53}Cr(ox) \qquad (4.16)$$

Equation 4.16 describes the formula to calculate the Cr isotopic composition of the whole–rock as a function of the proportion of Cr that remains in the rock during oxidative weathering. *Equation 4.16* is valid from p(ox) ≤ *p(WR)* ≤ 1, and from 0 ≤ *p(WR)* ≤ p(ox) it is assumed that δ^{53}Cr(WR) = δ^{53}Cr(ox), as the oxide fraction is not considered to lose any Cr during the early stages of weathering, which are dominated by loss of Cr from silicates.

Model parameters can be obtained as follows:

1. $\mathrm{rel\%(sil)}$ quantification of mineral assemblage
2. $\mathrm{rel\%(ox)}$ quantification of mineral assemblage
3. $\mathrm{wt\%(sil)}$ mineral chemistry
4. $\mathrm{wt\%(ox)}$ mineral chemistry
5. α(sil) estimated from Cr isotopic composition of pore water sample
6. $\delta^{53}\mathrm{Cr}_0(\mathrm{WR})$ Cr isotopic composition of bedrock sample
7. $\delta^{53}\mathrm{Cr(ox)}$ Cr isotopic composition of separated oxide fraction, or literature value

Additionally:

$$rel\%(sil) \cdot wt\%(sil) + rel\%(ox) \cdot wt\%(ox) = wt\%(WR) \qquad (4.17)$$

because the mineralogy–weighted Cr content of the bedrock, which is used as the starting point for the model calculation, has to match the whole–rock Cr concentration of the bedrock. Bedrock sample B1 consists of about 5 % oxides (*rel%(ox)=0.05)* with an average Cr concentration of 14.9 wt% (*wt%(ox)*) and of about 95 % silicates (*rel%(sil) = 0.95)* with an average Cr concentration of 0.24 wt% (*wt%(sil)*), which yields a whole–rock Cr concentration of 0.95 wt% (*wt%(WR)*) that conforms to the measured whole–rock Cr concentration (**Table 4.3**). For the model calculation, a fractionation factor between aqueous Cr^{6+} and solid Cr^{3+} of α = 1.005 (ε = 5.0 ‰) is used. The Cr isotopic composition of unaltered bedrock is assumed to be equal to that of sample B1 (δ^{53}Cr = –0.18 ‰). Schoenberg et al. (2008) reported Cr isotopic compositions of chromitites, which are rocks that virtually only consists of chromite, and determined a δ^{53}Cr value of –0.08±0.06 ‰. Here, we assume that the δ^{53}Cr value of the oxide fraction is –0.10 ‰.

Fig. 4.12 and **4.13** show modelled pathways of the evolution of the whole–rock Cr isotopic composition of the bedrock as a function of the proportion of Cr that remains in the whole– rock. The black lines show the evolution of the Cr isotopic composition based on estimations of relative mineral abundances and mineral compositions from bedrock sample B1. In general, δ^{53}Cr(WR) shows a parabolic or u–shaped trend, similar to the trend observed between MIA–values and δ^{53}Cr(WR) in **Fig. 4.10b**. The graph reveals that the whole–rock Cr isotopic composition initially decreases due to preferential loss of heavy Cr isotopes from oxidative weathering of silicates, and retention of light Cr isotopes in the residual silicate fraction.

However, continued loss of Cr from the silicate fraction reduces the relative amount of Cr residing in the silicate fraction compared to the amount of Cr in the oxide fraction until a point, where the δ^{53}Cr value of the whole–rock starts to increase. When all silicate–bound Cr has been lost, the whole–rock Cr isotopic composition equals the Cr isotopic composition of the oxide fraction.

The violet lines in **Fig. 4.12** show pathways with slightly different relative mineral abundances but the same whole–rock Cr concentration of the bedrock. Slight changes in the abundance of silicates vs. oxides abundance can have a significant impact on the whole–rock Cr isotopic composition, and mineral assemblages with more silicates produce lower δ^{53}Cr values, and a broader range of δ^{53}Cr(WR). **Fig. 4.13** shows modelled whole–rock Cr isotope pathways with a constant Cr content in the mineral fractions, thus allowing the whole–rock Cr concentration to be variable. The pathways are similar to those shown in **Fig. 4.12**, however, the minimum whole–rock δ^{53}Cr value is considerably higher because the Cr concentration of the silicate fraction is lower.

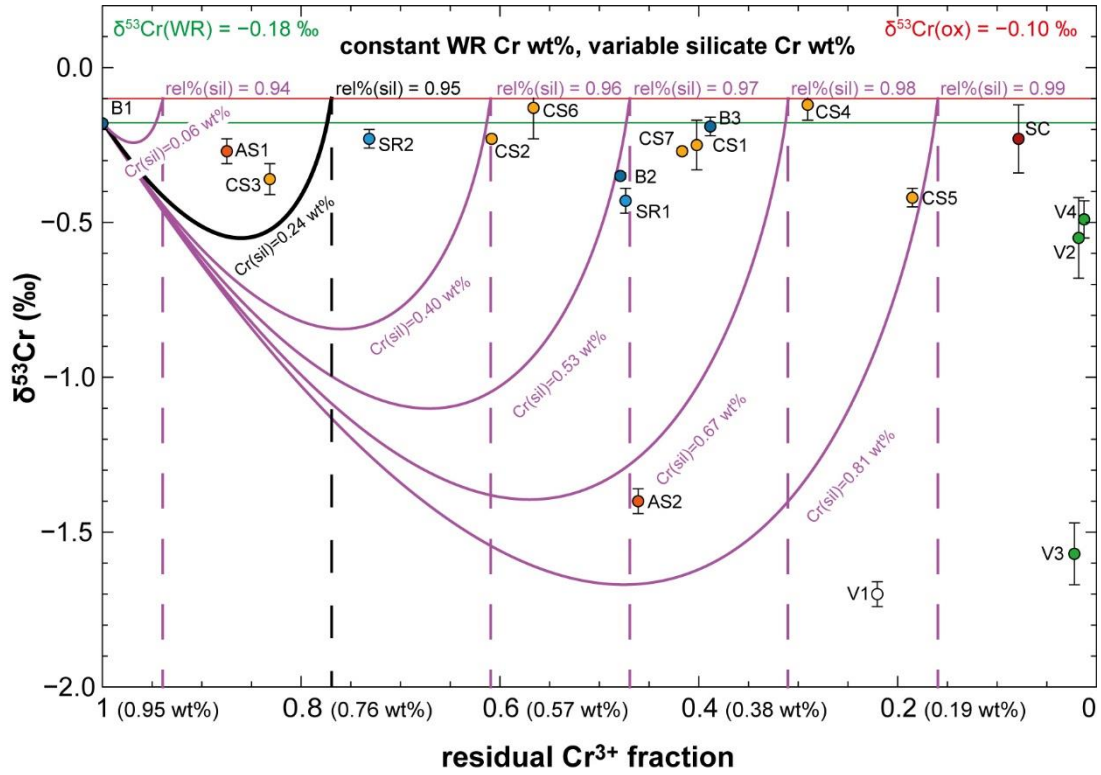

Fig. 4.12. Calculated Cr isotope fractionation pathways (black and violet) assuming incongruent mineral dissolution associated with Cr isotope fractionation from silicate–derived Cr only (ε = 5.0 ‰), whereas Cr in the oxide fraction is unaffected and has a constant δ^{53}Cr(ox) of –0.10 ‰. The black pathway uses the mineralogical properties of the bedrock sample B1 with 95 vol% relative mineral abundance and a Cr concentration of 0.24 wt% in the silicate fraction. Violet lines demonstrate the impact on the WR Cr isotopic composition assuming slight differences in the mineral chemistry (i.e. lower or higher relative mineral abundances and a corresponding lower or higher Cr concentration in the silicate fraction to achieve a constant WR Cr concentration). WR δ^{53}Cr values decrease due to preferential loss of heavy Cr isotopes from the silicate fraction up to a threshold, where WR δ^{53}Cr values start to increase, because the amount of Cr remaining in silicates has become so small that it has only a minimal effect on the total Cr budget (silicate + oxides) and the abundance–weighted Cr isotopic composition of the oxide fraction 'pulls' the WR δ^{53}Cr value towards δ^{53}Cr(ox) of –0.10 ‰, which is reached, when all silicate–derived Cr has been lost (dashed vertical lines).

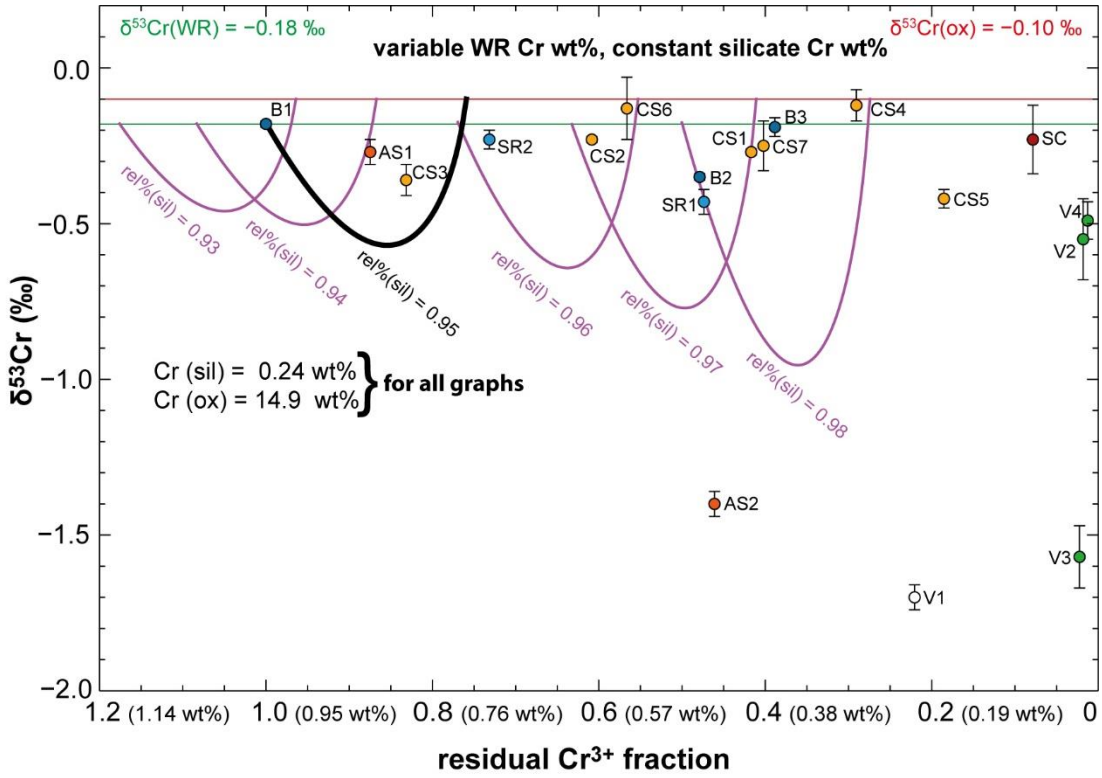

Fig. 4.13. Calculated Cr isotope fractionation pathways (black and violet) assuming incongruent mineral dissolution associated with Cr isotope fractionation from silicate–derived Cr only (ε = 5.0 ‰), whereas Cr in the oxide fraction remains unaffected and has a constant δ^{53}Cr(ox) of –0.10 ‰. All pathways use the mineralogical properties of the bedrock sample B1 with 95 vol% relative mineral abundance and a Cr concentration of 0.24 wt% in the silicate fraction. The black pathways assumes a WR Cr concentration of 0.95 wt% deduced from the parent rock sample B1. Violet lines demonstrate the impact on the WR Cr isotopic composition assuming a variable WR Cr concentration and constant Cr concentrations of silicates and oxides, Cr(sil) and Cr(ox), respectively. The trend of the graphs is similar to **Fig. 4.12**, although the minimum WR δ^{53}Cr value that can theoretically be achieved is much higher due to the relatively low Cr concentration in the silicate fraction.

The fractionation model shows that incongruent mineral dissolution of ultramafic rocks that have slight heterogeneities in their mineralogy can produce a wide variety of whole–rock Cr isotopic compositions, which can account for the observed Cr isotopic compositions in the laterite profile. Furthermore, the model demonstrates that the whole–rock Cr isotopic composition of strongly altered dunites or ultramafic weathering products more generally can be similar to or even higher than the Cr isotopic composition of their unaltered progenitors. However, the model cannot explain the δ^{53}Cr value of the silica cap that has a very low Cr content (**Fig. 4.12** and **4.13**). As the silica cap evolved from the same material as the underlying regolith units, it can be assumed that a similar amount of oxides was initially incorporated.

The extremely low Cr content of the silica cap compared to the bedrock, renders it likely that Cr loss can also occur without significant Cr isotope fractionation, probably in the later stages of weathering, which is consistent with an enhanced weathering rate of chromite under low pH conditions (Oze et al., 2007).

Overall, the model supports the idea that the Cr isotopic composition of the laterite profile has a strong mineralogical control. The model can also account for the very low $\delta^{53}Cr$ values measured in samples AS2 and V1 without the need for additional Cr sources. This incongruent mineral dissolution model can theoretically be extended to allow for Cr loss from two or more mineral phases, if good estimations of isotope fractionation factors between interstitial waters and individual mineral phases are available, because assuming a constant $\delta^{53}Cr$ of the oxide fraction, in particular chromite, may not be valid over the entire course of laterite formation (Garnier et al., 2008).

4.6.7 Behaviour of nickel in the weathering profile

The mineralogical distribution of Ni in the laterite profile is largely controlled by the weathering susceptibility of the silicate mineral assemblage, which hosts the majority of Ni and is the primary source of Ni during weathering. Small amounts of Ni were also found in Cr–bearing magnetite, however, its abundance–weighted Ni content is low and thus, oxide–bound Ni only accounts for a small portion of the residually accumulated Ni due to the high weathering stability of the oxide phases. Bedrock normalised Ni concentrations (Ni_{bed}), as well as Ni concentrations normalised to Ti (Ni_{Ti}), Nb (Ni_{Nb}), and Th (Ni_{Th}), reveal two significant economic Ni enrichments (**Fig. 4.14**) located (1) at the transition between saprock and coarse saprolite, and (2) in the central part of the coarse saprolite, which correlate, respectively, with the presence of Ni–enriched, altered serpentine and Ni–rich smectite.

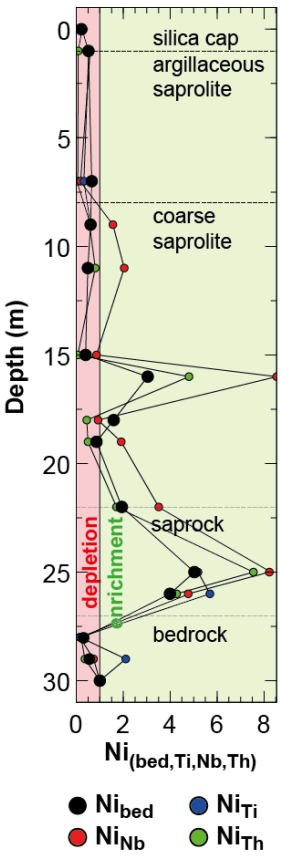

Fig. 4.14. Profiles of bedrock normalised Ni and bedrock normalised Ni corrected for physical effects, such as collapse or dilation, by normalisation to an immobile element. The similar trends shown by the different variables demonstrates that physical effects were insignificant during laterite profile development.

Ni_{bed} = Ni_{sample}(wt%)/Ni_{B1}(wt%), and Ni_X is given by: $[Ni_{sample}(wt\%)/X_{sample}(wt\%)]/[Ni_{B1}(wt\%)/X_{B1}(wt\%)]$ with X = Ti (wt%), Nb (wt%), or Th (wt%).

Ni laterites that form over dunite parent rock material generally develop a strong Ni–rich oxide component (e.g. goethite, hematite) due to the lack of Al in the protolith, and are classified as Ni–oxide–deposits (Brand et al., 1998; Butt and Cluzel, 2013). However, the São João do Piauí Ni laterite is not a classic oxide deposit, because secondary Fe–oxides, such as hematite, are relatively Ni–poor.

Ni in the host laterite units is almost exclusively hosted in variably decomposed serpentine, which is supported by the positive correlation between Ni and Mg and a poor correlation between Ni and Fe (**Fig. 4.15**). The relative stability of serpentine in the laterite profile results from the strong orogenic serpentinisation of the parent rock material prior to exposure and weathering (Wicks and Whittaker, 1977; Salgado et al., 2014, 2016). Nickel mobilised by partial dissolution of serpentine at shallow depths was channelled through intercalated veins and incorporated in Ni–rich smectite and Ni–rich asbolane. Any Ni that remained in solution was transported further downwards and was incorporated in Mg–depleted primary serpentine at the permeability barrier of the profile in the saprock horizon. Supergene Ni enrichment in the lower parts of the profile is further supported by the presence of chrysoprase (Ni–rich chalcedony) that occurs in abundance along fractures that were used as pathways for percolating silica–rich weathering fluids. Therefore, the São João do Piauí Ni laterite can be principally classified as a hydrous Mg–silicate deposit, with a minor Ni–rich smectite component that stems from weathering of Al–rich parent material (troctolite).

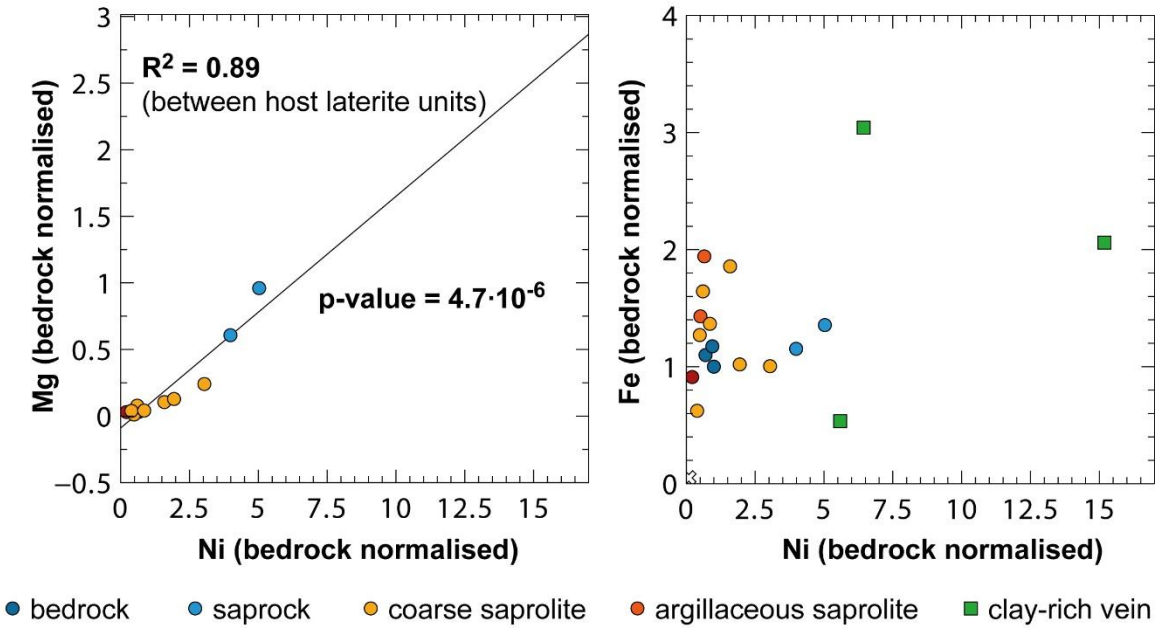

Fig. 4.15 a) Bedrock normalised Mg content vs. Ni content. The host laterite units (including SR, CS, AS, SC) show a significant correlation between Mg and Ni, which demonstrates the loss of Ni from primary serpentine (bedrock normalised Ni < 1) and supergene Ni enrichments (bedrock normalised Ni > 1) in slightly altered, primary serpentine, in particular in the saprock horizon. **b)** A poor correlation between bedrock normalised Fe and Ni shows that Ni enrichments are not due to uptake of Ni by secondary hematite.

4.6.8 Behaviour of Ni isotopes during laterite formation

Fig. 4.16 presents a compilation of δ^{60}Ni values from the São João do Piauí Ni laterite as well as recently reported δ^{60}Ni values for other ultramafic rocks and their lateritic weathering products (Gall et al., 2013; Gueguen et al., 2013; Ratié et al., 2015, 2018). Most samples show δ^{60}Ni values that are lower than the underlying parent rock, which is consistent with a loss of heavy Ni isotopes during ultramafic rock weathering and agrees with observations of positively fractionated δ^{60}Ni values in stream waters, rivers, and the oceans (Cameron and Vance, 2014; Ratié et al., 2018). The overall range of δ^{60}Ni values in the profile is 0.78 ‰ (–0.05 to –0.91 ‰), which is comparable to range observed in the Barro Alto laterite (0.87 ‰; Ratié et al., 2018). However, the São João do Piauí Ni laterite exhibits the lowest yet reported δ^{60}Ni value of –0.91‰ for Ni–enriched saprolite material.

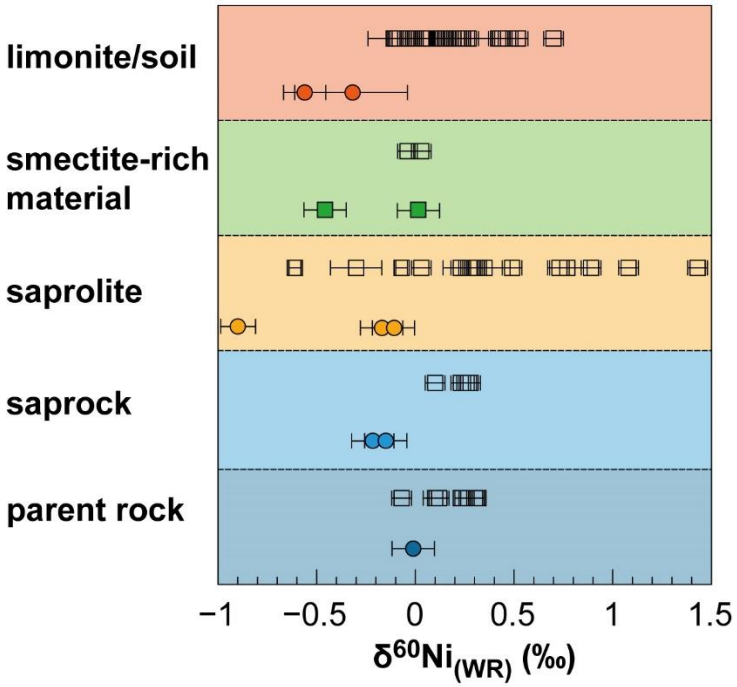

Fig. 4.16. Compilation of δ^{60}Ni values from the São João do Piauí Ni laterite (coloured circles and squares) and from other Ni laterites (open squares). δ^{60}Ni values of some saprolite and smectite–rich samples are lower than values reported for other localities; however, the overall Ni isotope range of this laterite profile is similar to that reported for other laterites, because the bedrock sample B1 has a lower δ^{60}Ni value to start with. Additional data is from Gall et al. (2013), Gueguen et al. (2013), Ratié et al. (2015, 2018).

Weathering of the ultramafic parent rock material appears therefore to be accompanied by Ni isotope fractionation, with enrichment of light Ni isotopes in the residual weathering products. Nevertheless, δ^{60}Ni values are only poorly correlated with the loss of Mg (**Fig. 4.17a**) or with MIA values (**Fig. 4.17b**), which suggests that fractionation of Ni isotopes does not occur during the hydrolysis of Ni–bearing Mg–silicates and supports experimental findings that Ni loss during olivine dissolution does not fractionate Ni isotopes (Ratié et al., 2018). Ni–enriched as well as Ni–depleted laterite samples are both enriched in light Ni isotopes compared to the bedrock.

Ni–enriched samples show a negative correlation between bedrock normalised Ni content and δ^{60}Ni value (**Fig. 4.17c**), which implies that the degree of Ni enrichment may influence the extent of Ni isotope fractionation yielding in low δ^{60}Ni values in highly Ni–enriched samples. Considering the outer to inner–sphere transport as major driving mechanism of light Ni isotope enrichment into the solid (Fujii et al., 2011, 2014; Elliott and Steele, 2017 and references therein), the correlation between high Ni enrichments and low δ^{60}Ni values may indicate that high Ni concentrations in percolating weathering solutions lead to a favourable incorporation of light Ni isotopes into Ni–enriched mineral phases and thus, to low δ^{60}Ni values. Mobile Ni from solution is adsorbed onto the mineral surface during the way of the fluid through the profile, and the higher the concentration of Ni in the fluid, the less concurrent elements can be adsorbed on the mineral surface. According to this assumption, high Ni concentrations in weathering solutions lead to a high Ni adsorption and thus, to more light Ni isotopes diffusing into the inner–sphere crystal lattice, which consequently yields in low δ^{60}Ni values. The deviation of the δ^{60}Ni value of CS4 from the linear trend in **Fig. 4.17c** probably results from the strong re–silicification of the coarse saprolite that leads to a dilution of Ni and thus, to a lower total Ni enrichment. The samples that lie on the trend are not strongly silicified.

The relatively low δ^{60}Ni values of samples CS4 and V2 (**Fig. 4.17c**) likely results from incorporation of isotopically light Ni into smectite (Ratié et al., 2015), and the difference in δ^{60}Ni between the two samples can be attributed to differences in the relative mineral abundances of primary and secondary Ni–bearing phases. Ni in sample V2 is hosted in primary serpentine as well as in secondary smectite and therefore, its Ni isotope composition represents a mixture of ‘unfractionated’ and ‘fractionated’ Ni, whereas the δ^{60}Ni value of CS4 predominantly reflects the Ni isotope composition of Ni–smectite, as the sample principally consists only of secondary silica (Ni–free) and smectite. Negative δ^{60}Ni values in clay–rich samples have been observed in other laterites, for example sepiolite–rich samples from Cerro Matoso and Barro Alto have δ^{60}Ni values of –0.30 ‰ and –0.61 ‰, respectively (Glesson et al., 2004; Ratié et al., 2015).

Retention of light Ni isotopes has so far only been observed in Fe–oxyhydroxides and clays (Elliott and Steele, 2017). However, the negative δ^{60}Ni values of the saprock indicate that light Ni isotopes are also favourably incorporated into partly altered, primary serpentine. Especially, the virtually monomineralic sample SR2 (chrysotile) is highly enriched in Ni (by >400% compared to bedrock), and has a δ^{60}Ni value of –0.21±0.02 ‰.

The incorporation of light Ni isotopes into Fe–oxyhydroxides is considered to be the major driving mechanism for low δ^{60}Ni values in laterites (Gueguen et al., 2018). Indeed, bedrock normalised Fe contents show a negative correlation with δ^{60}Ni values (**Fig. 4.17d**). However, the abundance of hematite in the laterite is generally low (<16 vol%), and some samples that plot on the trend, which is indicated in **Fig. 4.17d**, do not include hematite in their mineral assemblage (e.g. SR1, SR2, V2). This may indicate that Fe–enriched silicates also preferentially incorporate light Ni isotopes compared to their 'unaltered' Mg–rich equivalents. These Fe–rich silicates ultimately alter to hematite, which is supported by lower δ^{60}Ni values of Ni–depleted samples from the argillaceous saprolite compared to Ni–depleted samples of the underlying coarse saprolite.

The argillaceous saprolite formed in a low relief environment with a high standing water table, in which Ni–rich weathering solutions were in contact with the rock for longer, allowing more extensive exchange of Ni isotopes at the fluid–rock interface. The coarse saprolite formed in a high relief environment with a low water table, thus percolating weathering solutions had a shorter residence time in individual horizons that allowed only limited Ni isotope exchange.

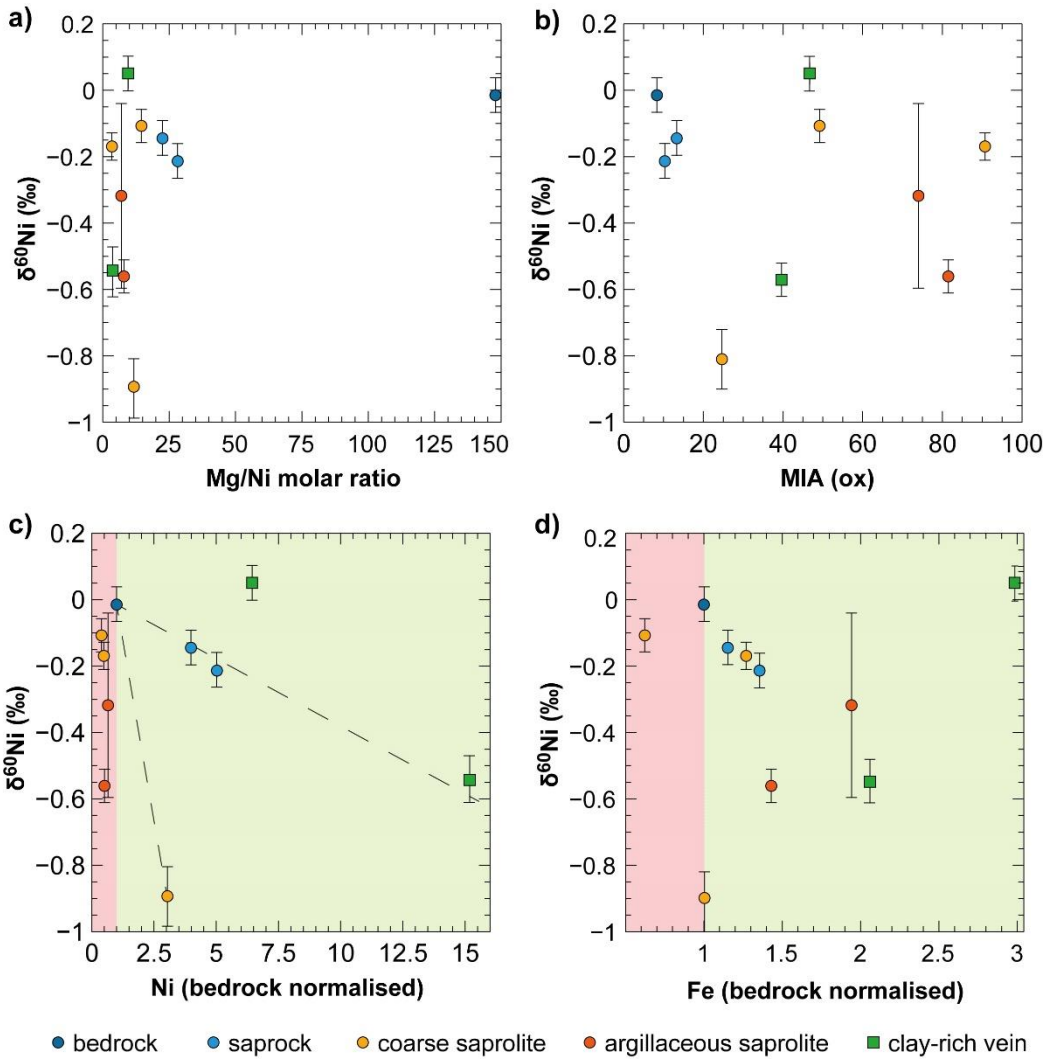

Fig. 4.17. Ni isotope compositions of laterite samples do not show any significant correlations with **a)** the loss of Mg or **b)** the degree of weathering, expressed in MIA values. **c)** Ni–enriched samples from the saprock (blue circles), from one saprolite sample (CS4; yellow circle), and from one smectite–rich vein (V2; green square) show different potential linear correlations. There are two proposed linear trends between Ni–enriched samples and the bedrock sample B1 (deep blue circle). The steep trend between bedrock and saprolite sample CS4 may indicate that the saprolite, which is situated at higher depths within the profile, was more enriched in light Ni isotopes than the saprock and one vein sample, which are situated at lower depths, as light Ni isotopes are continuously extracted from the weathering solution, therefore continuously depleting the mobile Ni pool in light Ni isotopes on its way downward the profile. Another possible explanation includes that the smectite–rich sample CS4 (yellow circle; $\delta^{60}Ni = –0.91$) deviates from the linear trend between saprock, vein sample, and bedrock, due to the high amount of secondary silica that diluted the degree of Ni enrichment. **d)** $\delta^{60}Ni$ vs. bedrock normalised Fe content inferring a linear correlation between increasing Fe contents and decreasing $\delta^{60}Ni$ values.

Vein sample V3 shows the most positively fractionated δ^{60}Ni value of 0.05±0.08 ‰, which is similar to the δ^{60}Ni value of the parent rock (–0.01±0.01 ‰). However, sample V3 has a very high Ni concentration (2.10 wt%) that is consistent with uptake of Ni from percolating fluids. This is supported by the very low δ^{53}Cr value of this sample (–1.57±0.10 ‰), which is indicative of Cr loss due to hydrolysis of primary serpentine and chlorite that dominate the mineralogy of this sample. Therefore, the relatively high δ^{60}Ni value is interpreted to reflect uptake of Ni from a fluid with high δ^{60}Ni (e.g. Spivak-Birndorf et al., 2018).

4.7 Conclusions

The Cr isotopic composition of laterite samples from the São João do Piauí Ni laterite indicate widely variable δ^{53}Cr values, ranging from –0.12 to –1.70 ‰, which is consistent with preferential loss of heavy Cr isotopes during the hydrolysis of primary silicate minerals (i.e. serpentine, chlorite) in the underlying serpentinised dunite parent rock. Interstitial pore water that was sampled at the saprock interface has a relatively high concentration of Cr (~23 ppm), and a very high δ^{53}Cr value (4.31‰), which supports the idea of heavy Cr isotope loss from solid phases and its uptake into percolating fluids. However, the deeper laterite horizons (i.e. saprock, lower saprolite) generally have lower δ^{53}Cr values than the shallower horizons (central and upper saprolite). A simple isotope fractionation model indicates that this can be explained by loss of Cr from primary silicate minerals, with preferential loss of heavy Cr isotopes, in the early to moderate stages of weathering, and retention of Cr in the weathering resistant oxide fraction. Thus, there is a strong mineralogical control on the evolution of the Cr isotopic composition during weathering of mafic and ultramafic rocks.

The Ni isotopic composition of the laterite samples is also widely variable, ranging from δ^{60}Ni = 0.05 ‰ to δ^{60}Ni = –0.91 ‰. These values are generally lower than the δ^{60}Ni value of the bedrock (–0.01±0.09 ‰), which implies preferential loss of isotopically heavy Ni isotopes into the fluid phase during weathering. One Ni–enriched saprolite sample has an extremely low δ^{60}Ni value of –0.91±0.09 ‰ that represents, to our knowledge, the lowest δ^{60}Ni value measured for a natural sample to date. The Ni in this sample is exclusively hosted in secondary formed Ni–rich smectite. δ^{60}Ni values of Ni–enriched samples show a linear correlation to the bedrock normalised Ni content, which indicates that the extent of Ni isotope fractionation may be dependent on the amount of mobile Ni that was scavenged from percolating weathering solutions.

Low δ^{60}Ni values in the highly Ni–enriched saprock horizon, where Ni–enriched, primary serpentine is the main Ni ore, extends the list of Ni–rich minerals that have been reported to favourably incorporate light Ni isotopes. Significant correlations between bedrock normalised Fe contents and the δ^{60}Ni value of individual Ni–enriched laterite samples signal a general tendency that altered, more Fe–rich silicates favourably incorporate light Ni isotopes compared to their ‘unweathered’, more Mg–rich equivalents.

Chapter 5 Conclusions and further work

5.1 Principal outcomes

5.1.1 Behaviour of Cr isotopes during Ni laterite formation

Analyses of the Cr isotopic composition of a series of Ni laterite deposits confirms that oxidative weathering of Cr–bearing rocks leads to preferential loss of heavy Cr isotopes into the fluid phase, thereby enriching the residual rock in light Cr isotopes. These data also demonstrate that the total range of Cr isotopic compositions in modern (Cenozoic to Mesozoic) Ni laterites can be highly variable and is primarily controlled by the mineralogy of the ultramafic parent rock. The range in $\delta^{53}Cr$ values of the three investigated Ni laterite profiles is 0.26 ‰ (Çaldağ), 0.53 ‰ (Karaçam), and 1.58 ‰ (São João do Piauí). The investigation of the São João do Piauí Ni laterite (**Chapter 4**) led to the conclusion that the evolution of the Cr isotopic composition during laterite formation principally depends on the distribution of the whole–rock Cr content between silicates (i.e. serpentine, chlorite) and oxides (chromite, magnetite). The contrasting weathering susceptibilities between silicates and oxides lead to an incongruent mineral dissolution during laterite formation, mobilising silicate–bound Cr in the early to intermediate stages of weathering, whereas oxide–bound Cr is retained. Oxidation of Cr^{3+} derived from silicate breakdown and subsequent removal of Cr^{6+} by fluids is accompanied by a high Cr isotope fractionation ($\varepsilon \approx 5$ ‰), estimated from the $\delta^{53}Cr$ value of soil pore water ($\delta^{53}Cr$ = 4.31 ‰) that was in direct contact with the horizons that are representative of the early stages of weathering. The evolution of the whole–rock Cr isotopic composition can be described in terms of a Rayleigh isotope fractionation process (**Chapter 4**). According to this model, the evolution of the whole–rock Cr isotopic composition follows a ‘u–shaped’ trend, with a local minimum $\delta^{53}Cr$ value associated with loss of Cr from the silicate fraction, and a return to higher $\delta^{53}Cr$ values when most Cr from silicates has been lost and the whole–rock Cr isotopic composition is controlled by the Cr isotopic composition of the residual oxide fraction.

A weak, but statistically significant correlation between the Mn content and the $\delta^{53}Cr$ value of laterites (**Chapter 2**) indicates that the Cr isotopic composition can be controlled by the amount of Mn in the rock. However, this relationship was only observed in the Çaldağ and Karaçam Ni laterite, which formed under a high standing water table. The São João do Piauí Ni laterite formed under a low water table and shows no correlation between Mn and $\delta^{53}Cr$.

This may mean that the Cr isotopic composition of Ni laterites that formed under a low water table is primarily controlled by the Cr mineralogy of the parent rock, whereas the Cr isotopic composition of Ni laterites that formed under a high water table is additionally controlled by the Mn content of the parent rock.

5.1.2 Behaviour of Ni isotopes during Ni laterite formation

The Ni isotopic compositions of the studied laterite profiles are similar to those measured in other laterite studies and show that heavy Ni isotopes are preferentially lost from the rock into the fluid phase during laterite formation (**Chapter 4**). The total range in δ^{60}Ni values in the São João do Piauí Ni laterite is high, with δ^{60}Ni = 0.05 to –0.91 ‰. There is a linear correlation between the Ni content and the δ^{60}Ni value in Ni–enriched laterite samples indicating that extent of Ni isotope fractionation depends on the amount of Ni scavenged from percolating weathering solutions. Low δ^{60}Ni values in the saprock horizon, which consist of Ni–enriched primary serpentine as the main Ni–ore, show that incorporation of light Ni isotopes is not restricted to secondary Fe–oxyhydroxides and secondary clays, as previously reported, and there is a tendency for light Ni isotopes, in general, to become incorporated into altered, Fe–rich minerals including silicates compared to their ‘unweathered’, more Mg–rich equivalents.

5.1.3. Climatic conditions of Ni laterite formation

The investigation of the São João do Piauí Ni laterite deposit (**Chapter 3**) revealed that the climatic conditions under which ultramafic rocks are conducive to develop Ni–rich deposits should be extended to include semi–arid regions that are characterised by low precipitation (~800 mm/yr) in a short but very intense rainy season (2 – 3 months), in an otherwise hot and arid climate. These climatic conditions lead to an episodic progression of the weathering front that results in very low laterite formation rates (0.1 – 0.8 m/Myr); some 10 to 100 times lower than for Ni laterites that formed under tropical conditions. The predominantly arid climate favours the formation of an indurated, weathering resistant siliceous cap that forms in–situ as the residual end–product of weathering. The cap promotes the preservation of the Ni laterite during the dry season, which is dominated by mechanical erosion.

Due to the important role of the silica cap, it can be concluded that only Al–poor ultramafic progenitors (i.e. dunites) can form deep Ni–rich laterite profiles in semi–arid regions, because Al–rich ultramafic rocks (harzburgites, lherzolites, wehrlites) form a clay–mineral rich cap, which is much less resistant to mechanical erosion during the dry season. The laterite formation window (LFW; Thorne et al., 2012) summarises the amount of precipitation and the range of temperatures under which Ni laterites favourably form and can potentially be expanded so that it includes the chemical composition of the ultramafic bedrock as a determining factor for Ni laterite formation.

5.1.2 Forthcoming publications

The findings of **Chapters 2** and **4** will be separately submitted for publication in high impact scientific journals (e.g. *Geochemical Perspectives, Earth and Planetary Science Letters, Geochimica et Cosmochimica Acta, Chemical Geology*). Prospective co–authors for both articles include Rachael H. James (University of Southampton), Christopher Pearce (National Oceanography Centre), and Stephen Roberts (University of Southampton), as they supervised this PhD project. Peter A. Brown and Richard Herrington are proposed co–authors for Chapter 2, as they have contributed, respectively, the major element and trace element data sets of the Çaldağ nickel laterite profile as part of a master thesis as well as the sample material for the Cr isotope measurements. Ghylaine Quitté will be co–authoring Chapter 4, as she provided access and guidance during the Ni isotope analysis at the IRAP, Toulouse, and re–measured critical samples later on. The findings of Chapter 3 will be combined with the investigations of Richard Herrington and Paul Schofield (Natural History Museum London), who intensively focused on the mineralogy of the São João do Piauí Ni laterite deposit, to a joint publication. The author list of for this publication will include the supervisors of this PhD project, Tom Skiggs, who undertook a Master's thesis on the general characterisation of the São João do Piauí Ni laterite deposit, Richard Herrington, and Paul Schofield.

5.2 Further research

5.2.1 Role of Mn–oxides on the behaviour of Cr isotopes

Further research needs to be done in order to fully understand the role of Mn–oxides on the oxidation of Cr in natural systems. It is generally accepted that Mn–oxides are the major oxidants of Cr in ultramafic rocks (Nakayama et al., 1985; Eary and Rai, 1987; Richard and Bourg, 1991; Oze et al., 2007; Economou-Eliopoulos et al., 2014). However, experimental results on Cr isotope fractionation during Cr oxidation by Mn–oxides are very ambiguous and remain poorly understood. To my knowledge, only four experiments have been performed so far that investigated the Cr isotope fractionation during Cr oxidation by Mn–oxides yielding a very broad range of fractionation factors, $\varepsilon = \Delta^{53/52}Cr_{(Cr^{6+} - Cr^{3+})}$, between –2.5 and +0.7 ‰ (Bain and Bullen, 2005; Ellis et al., 2008; Wang et al., 2010; Joshi et al., 2011). These four studies were only presented as conference abstracts and the exact experimental conditions and materials used in these studies are not available. The only peer–reviewed study from Zink et al. (2010) used H_2O_2 as oxidising agent for Cr, which is rather not relevant for natural systems. The relatively high Cr concentration (23 ppm) and strongly fractionated Cr isotopic composition of the collected pore water sample ($\delta^{53}Cr$ = 4.31 ‰, **Chapter 4**) indicate fast Cr dissolution rates and a high Cr isotope fractionation factor during Cr oxidation from silicates in the early stages of laterite formation, because this water was likely in contact with the surrounding rock for about 2 to 3 months. Therefore, I would propose to undertake Cr oxidation experiments on ultramafic rock samples (under varying pH) to investigate Cr isotope fractionation under natural conditions. These experiments could be conducted over a time span of about 1 year in a batch reactor to mimic natural weathering under controlled conditions.

Results presented in **Chapter 2** indicate that the concentration of Mn can correlate with the Cr isotopic composition in Ni laterites. However, the lack of a significant correlation between Mn contents and Cr isotopes in the São João do Piauí Ni laterite (**Chapter 4**) suggests that this is not universal. It would be important to explore under which conditions the Mn concentration may be the controlling factor, and when other factors govern the fractionation behaviour of Cr isotopes. It was also shown that the presence of Mn–oxides can significantly accelerate Cr dissolution rates from chromite, so that chromite may be an important source for Cr^{6+} in later stages of laterite formation (Oze et al., 2007; Garnier et al., 2008). However, there is no data available about the evolution of the Cr isotopic composition during Cr removal from chromite.

Furthermore, it would be useful to investigate how significant the contribution of Cr removal from chromite is on the Cr isotopic composition of the fluid phase to improve our understanding of the global Cr cycle, as Cr–bearing oxides are the most important hosts of Cr on the continental surface and due to their partly extraordinary weathering resistivity, they may have a significant long–term control on the Cr isotope signal that is transported from the continents via rivers into the oceans.

5.2.2 Interstitial pore waters

Further measurements of the Cr isotopic composition of interstitial pore waters from different laterite horizons are needed to estimate the extent of Cr isotope fractionation between weathered rock and percolating fluids during different weathering stages. The δ^{53}Cr value of stream waters from ultramafic catchments, which have been used to discuss the impact of oxidative weathering on the Cr isotopic composition of areas with exposed ultramafic rocks (Farkaš et al., 2013; Novak et al., 2017) and the Cr isotope signal that is transported via rivers into the oceans, rather reflect the sum of Cr isotopic compositions from pore waters integrated over the entire weathering profile. Thus, they do not give a specific indication of Cr isotope fractionation during individual stages of weathering. Direct collection of pore waters can be challenging, in particular from slightly weathered, crystalline rocks. Therefore, I propose collection of seepage waters in specially designed boreholes similar to the method presented in Waber and Smellie (2008). This could be theoretically realised, for instance, at locations where Ni laterite deposits (or parts of the deposit) are already explored and prospected (presence of boreholes), but have not yet been excavated (e.g. São João do Piauí).

5.2.3 Cr isotope fractionation factors

Leaching experiments of single mineral phases need to be conducted in order to estimate Cr isotope fractionation factors during oxidative weathering under natural conditions of individual minerals. As a start, these experiments should focus on the most important Cr–bearing mineral phases in ultramafic rocks, which are chromite and Mg–silicates (i.e. pyroxene, serpentine, olivine). I propose two ways to perform the leaching experiments. First, crushed whole–rock material can be physically separated to obtain individual mineral fractions by methods including vibrating table separation, fluid–based density separation, or magnetic separation. These separation methods are relatively quick, however, the disadvantage is that separated mineral powders do likely not have the same behaviour during dissolution compared to a monomineralic bulk rock, which may have a significant impact on the fractionation behaviour of Cr isotopes.

An alternative way would be to perform leaching experiments on monomineralic mantle xenoliths that consist only of Mg–silicates or chromite, and/or mantle cumulates that originate from segregation processes (e.g. podiform chromitites and olivinites; Arai, 1997; Varela et al., 2017), which minimises a biased Cr isotope fractionation due to textural differences between bulk rock and rock powder. The optimal way, in my opinion, would be in–situ measurements of the Cr isotopic composition of minerals in bulk–rock sections with LA–MC–ICP–MS (Laser ablation MC–ICP–MS), similar to the in–situ measurement of Fe isotopes (e.g. Horn et al., 2006). However, this method has not yet been applied to Cr isotopes due to technical limitations of currently used mass spectrometers (i.e not enough *Faraday* cups to correct for all isobaric interferences).

5.2.4 Evolution of Cr isotopic composition during incongruent mineral dissolution

The simple Cr isotope fractionation model that is presented in **Chapter 4** should be tested on laterite profiles with a very simple mineralogy, such as laterites that overlie dunites. An optimal lateritic weathering profile to test this model will have the following properties; the bedrock and the progenitor units from which the overlying lateritic regolith units formed (1) are of the (very) same rock material, (2) are fine–grained, (3) have a homogenous distribution of the mineral assemblage (i.e. no cumulate structures), (4) are characterised by a well–developed horizontal stratification (i.e. depth of profile correlates with degree of weathering), (5) show a vertical pathway of percolating weathering solutions, and (6) developed under constant external conditions (e.g. relief, precipitation, height of water table).

Furthermore, it would be favourable, if the weathering profile had not collapsed during its formation. Ideally, Cr is hosted in one particular silicate phase and one particular oxide phase. The sample density in the laterite profile should be drastically increased (i.e. sampling each ~10 cm). Given such a high spatial sample resolution, it should be possible to estimate natural Cr isotope fractionation factors without the need for analysis of the Cr isotopic composition of interstitial pore waters. Moreover, this method allows a comparison between the Cr isotope fractionation factor that was deduced from the sample suite of the rock column and the Cr isotope fractionation factor that is approximated from the Cr isotopic composition of the measured interstitial pore water. A comparison between both results will further allow to investigate, if secondary processes may play an important role between initial Cr^{3+} oxidation and uptake of Cr^{6+} into the fluid phase (e.g. partial back–reduction of Cr^{6+}, adsorption of aqueous Cr–species onto mineral surfaces).

5.2.5 Evolution of Ni isotopic composition during supergene Ni enrichment

The major driving factor for Ni isotope fractionation in natural rocks is considered to be the outer to inner–sphere transport/diffusion of Ni into the crystal lattice, favourably incorporating light Ni isotopes (Fujii et al., 2011, 2014; Elliott and Steele, 2017 and references therein). To my knowledge, only Fe–rich oxyhydroxides and secondary clays with a Ni isotopic composition enriched in light Ni isotopes have been reported in the literature to date. However, my results indicate that incorporation of light Ni isotopes may be more widespread, also affecting primary silicates that scavenged Ni from a mobile fluid pool (e.g. Ni–enriched serpentine). It would be valuable to investigate, if this observation is reproducible in experiments.

Appendix A

Table A1. Major, trace, and rare earth element concentrations of processed reference materials.

	JP-1	NIM-P	DTS-2b	JA-2	Chitin (Cat No B21600)
(wt%)					
SiO_2	42.2	50.5			
TiO_2	b.d.	0.176			
Al_2O_3	0.533	4.16			
Fe_2O_3	8.19	12.7			
MnO	0.117	0.221			
MgO	44.1	25.6			
CaO	0.513	2.57			
K_2O	0.002	0.092			
Na_2O	0.179	0.400			
LOI	2.65				
Total C					44.75
(ppm)					
Sr	0.693		0.801	248	
Zr	4.82		0.218	122	
Ni	2410		3760	128	
Cr(ICP–MS)	2070		14900		
Cr(ID)[a]	2270		15400		
Pb	0.092		3.91	22.0	
Zn	45.2	122			
Co	122		125	27.8	
V	33.3	199			
Ba	9.95		11.1	324	
Rb	0.345		0.028	80.0	
Y	0.109		0.044	17.5	
Nb	0.043		0.016	9.30	
Li	1.68		1.31	28.9	
Sc	7.48		2.52	18.3	
Sn	0.040		0.556	1.54	
Cs	0.043		0.002	5.24	
La	0.039		0.026	16.2	
Ce	0.078		0.050	33.6	
Pr	0.009		0.005	3.84	
Nd	0.038		0.022	14.6	
Sm	0.010		0.004	3.13	
Eu	0.002		0.001	0.911	
Gd	0.010		0.005	3.03	
Tb	0.002		0.001	0.476	
Dy	0.015		0.005	2.89	
Ho	0.004		0.001	0.592	
Er	0.012		0.006	1.69	
Tm	0.003		0.001	0.251	
Yb	0.021		0.011	1.68	
Lu	0.004		0.002	0.251	
Hf	0.109		0.006	3.00	
Th	0.014		0.010	4.69	
U	0.025		b.d.	2.18	

b.d. below detection limit
a Determined on MC–ICP–MS by isotope dilution (ID)

Figures A1. XRD patterns of rock samples from the São João do Piauí Ni laterite profile.

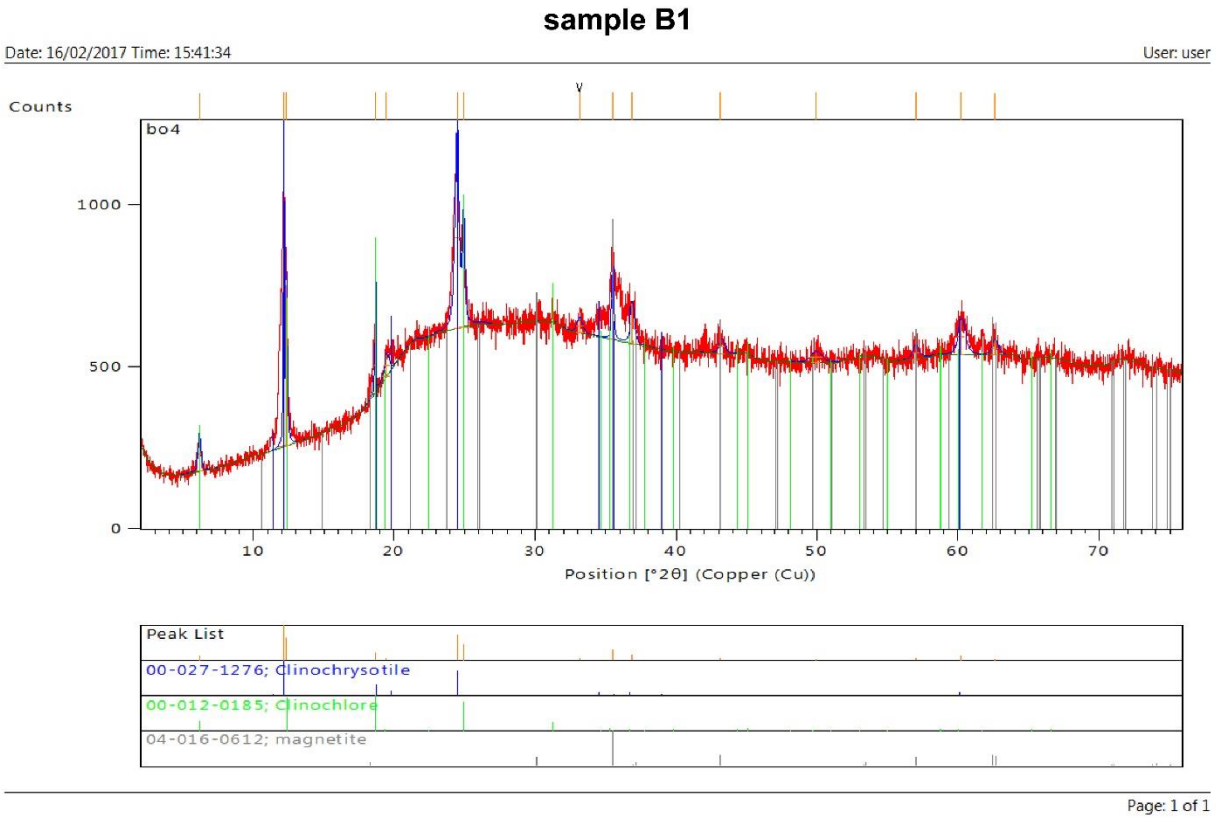

sample B2

Date: 16/02/2017 Time: 15:44:05 User: user

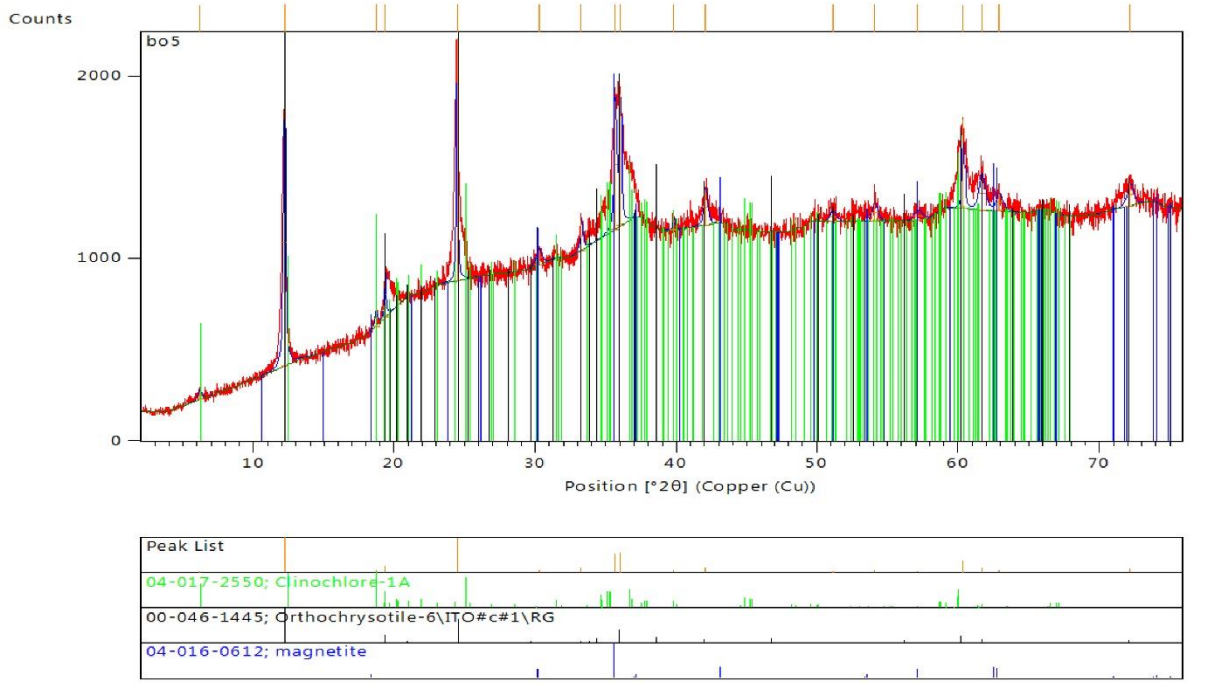

Page: 1 of 1

sample B3

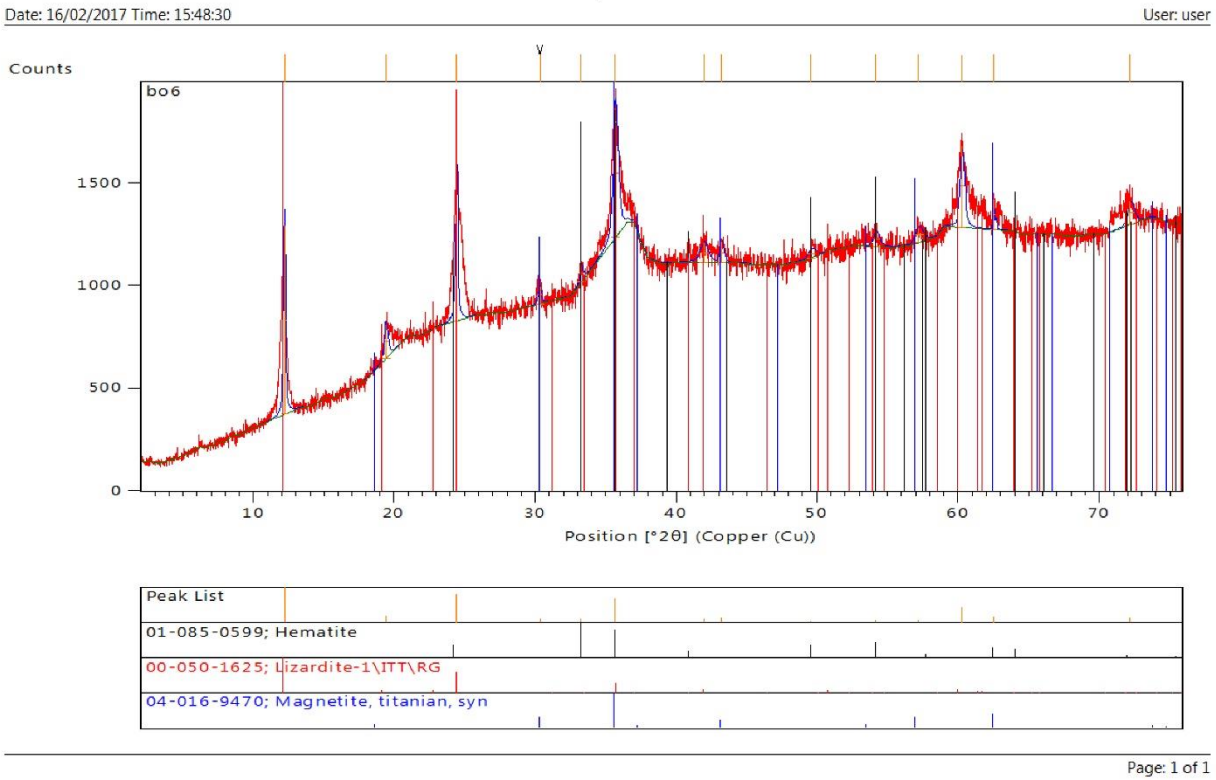
Date: 16/02/2017 Time: 15:48:30
User: user
Counts
bo6
1500
1000
500
0
10
20
30
40
50
60
70
Position [°2θ] (Copper (Cu))
Peak List
01-085-0599; Hematite
00-050-1625; Lizardite-1\ITT\RG
04-016-9470; Magnetite, titanian, syn
Page: 1 of 1

sample SR1

Date: 14/02/2017 Time: 12:44:08 User: user

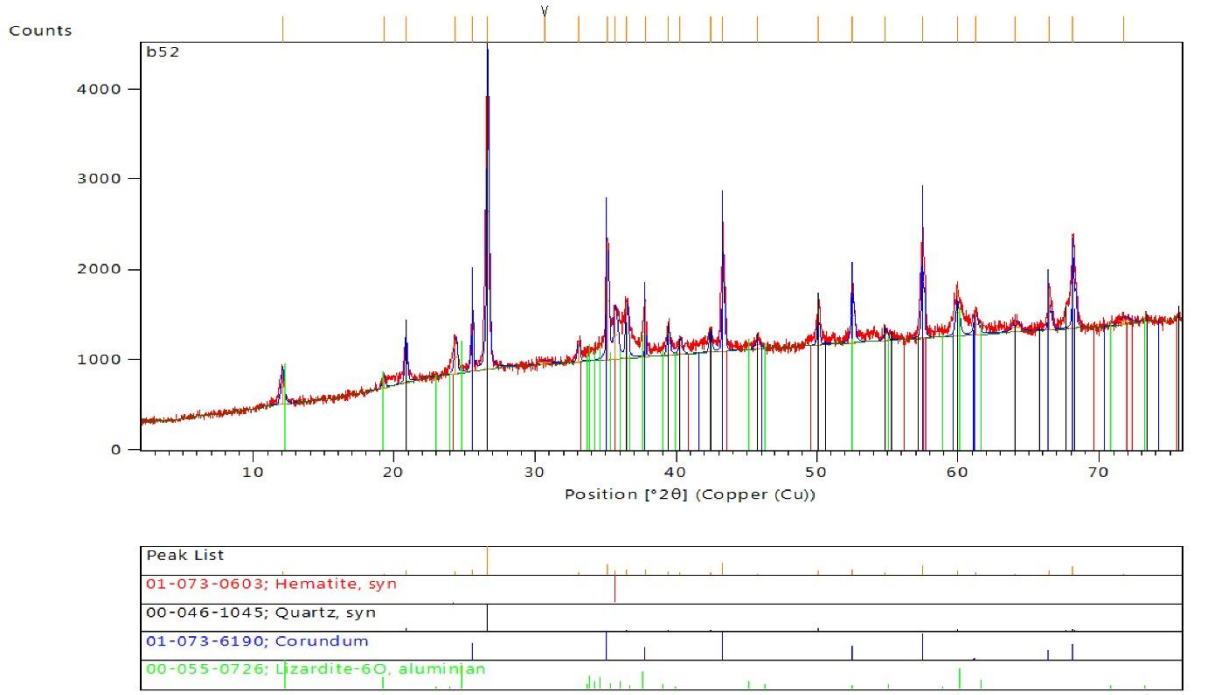

Page: 1 of 1

sample SR2

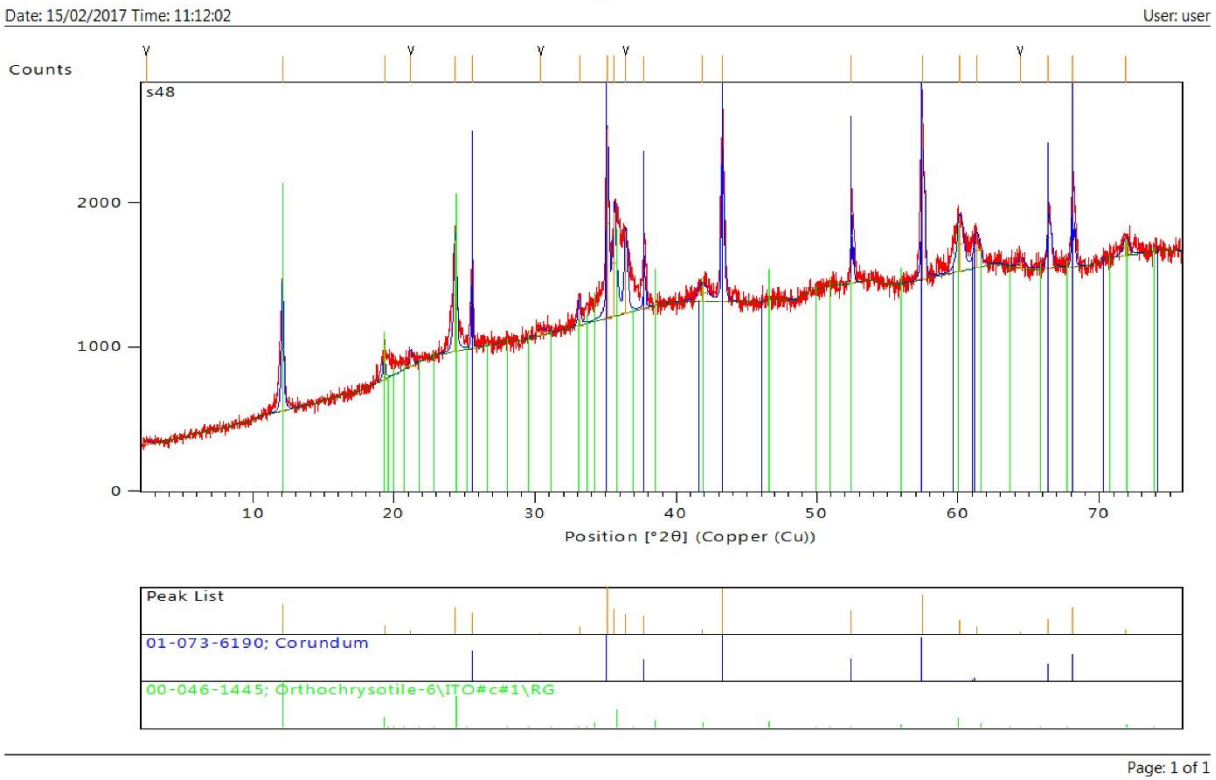
Date: 15/02/2017 Time: 11:12:02
User: user
Counts
s48
2000
1000
0
10
20
30
40
50
60
70
Position [°2θ] (Copper (Cu))
Peak List
01-073-6190; Corundum
00-046-1445; Orthochrysotile-6\ITO#c#1\RG
Page: 1 of 1

sample CS1

Date: 15/02/2017 Time: 11:14:57 User: user

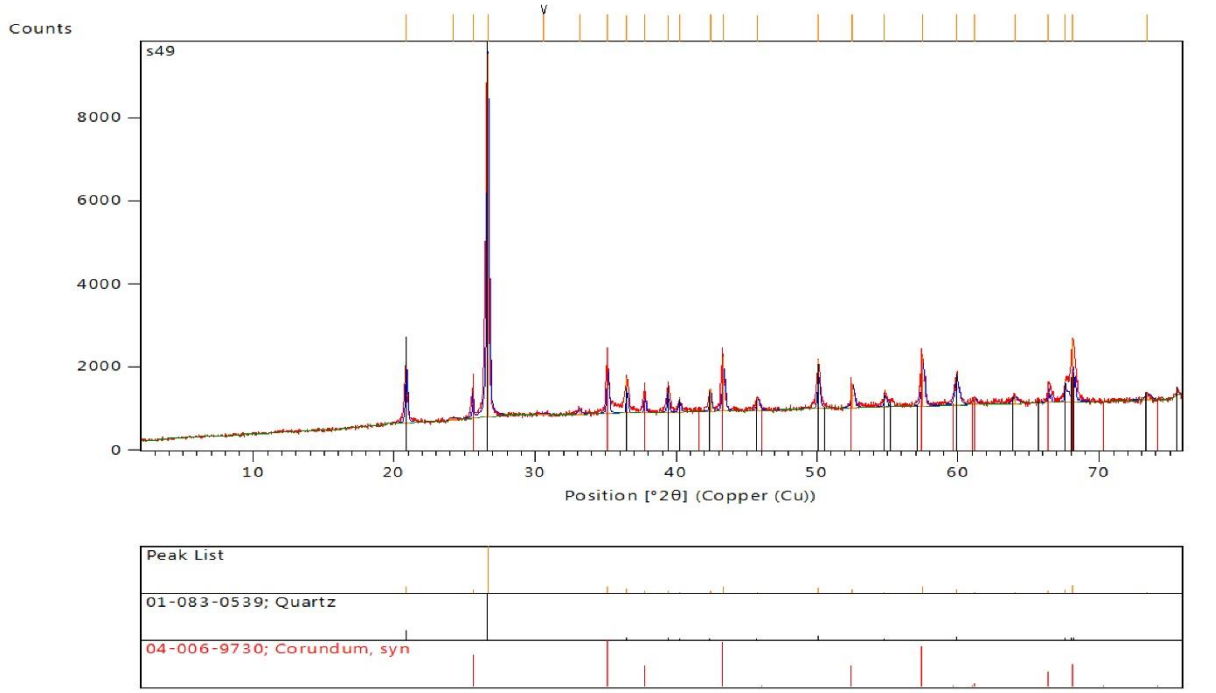

Page: 1 of 1

sample CS2

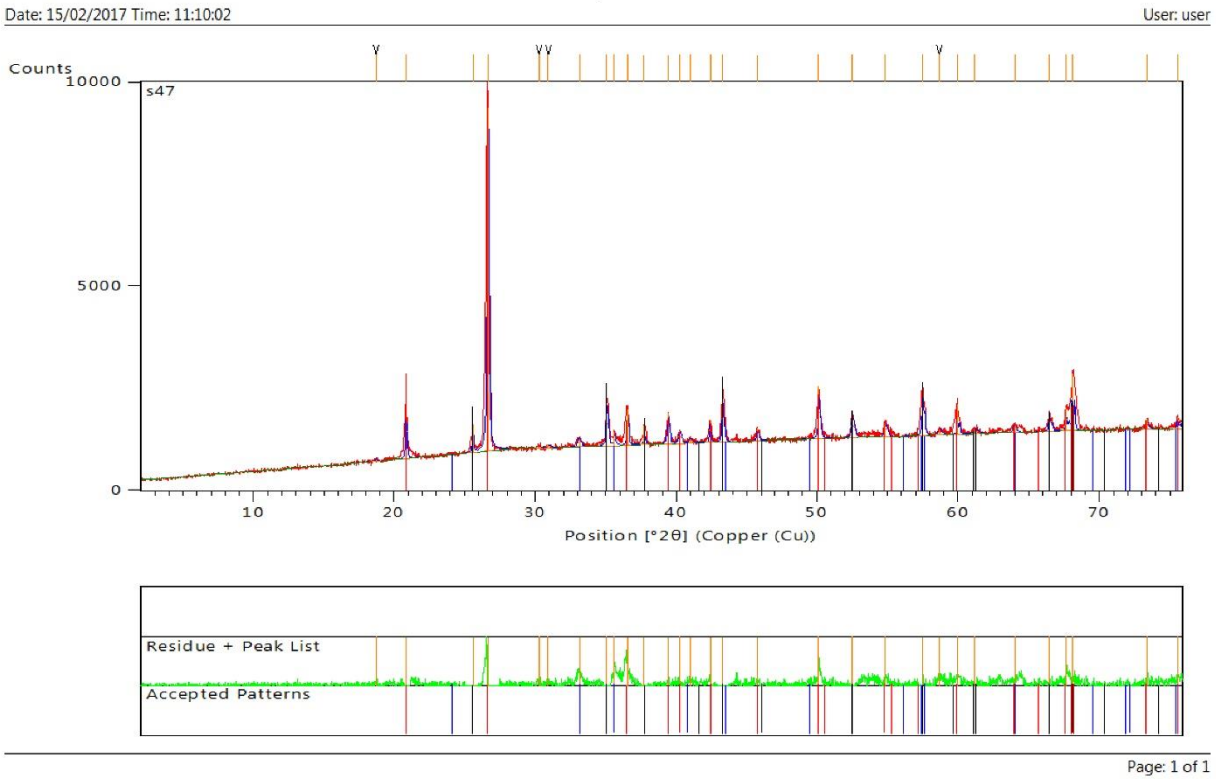
Date: 15/02/2017 Time: 11:10:02
User: user
Counts
10000
5000
0
s47
10
20
30
40
50
60
70
Position [°2θ] (Copper (Cu))
Residue + Peak List
Accepted Patterns
Page: 1 of 1

sample CS3

Date: 14/02/2017 Time: 14:24:31 User: user

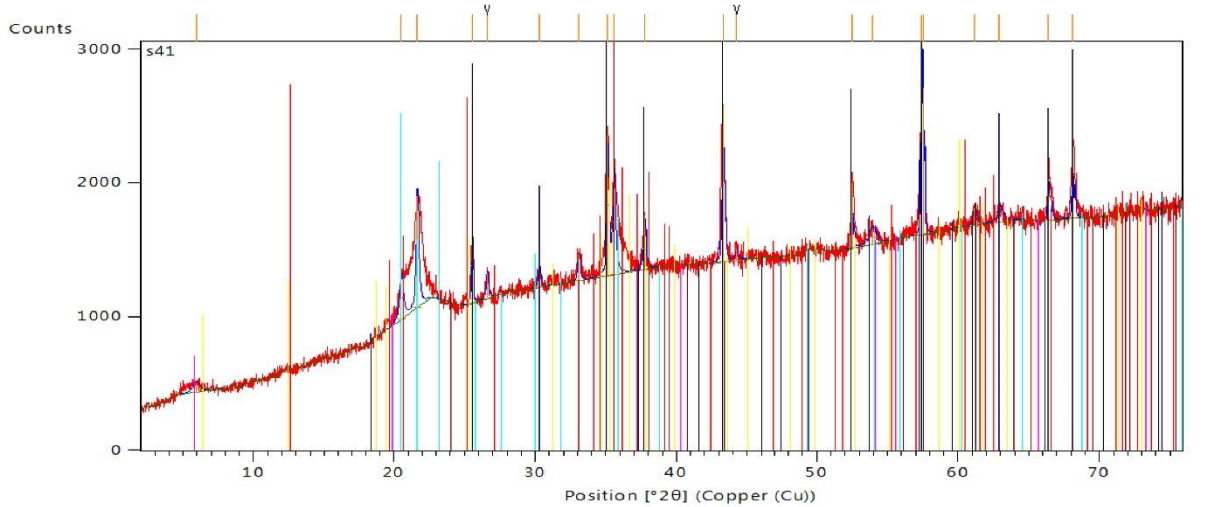

Page: 1 of 1

sample CS4

Date: 14/02/2017 Time: 13:01:24 User: user

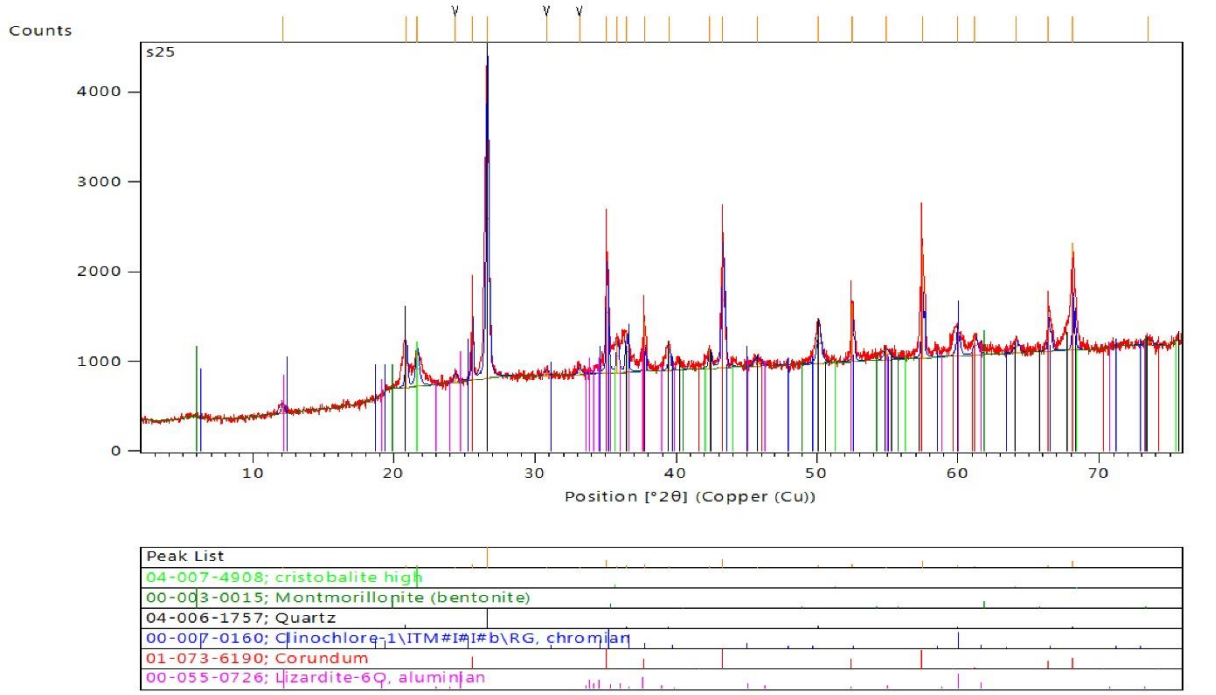

Page: 1 of 1

sample CS5

Date: 16/02/2017 Time: 15:33:33 User: user

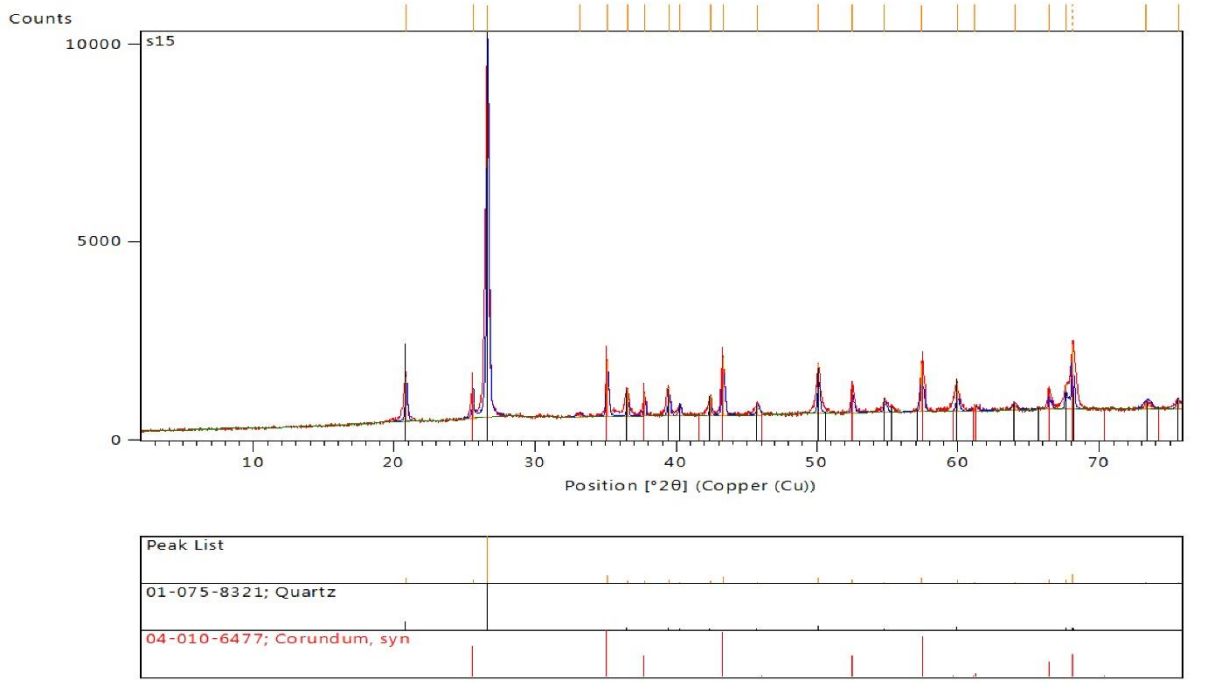

Page: 1 of 1

sample CS6

Date: 16/02/2017 Time: 15:37:39 User: user

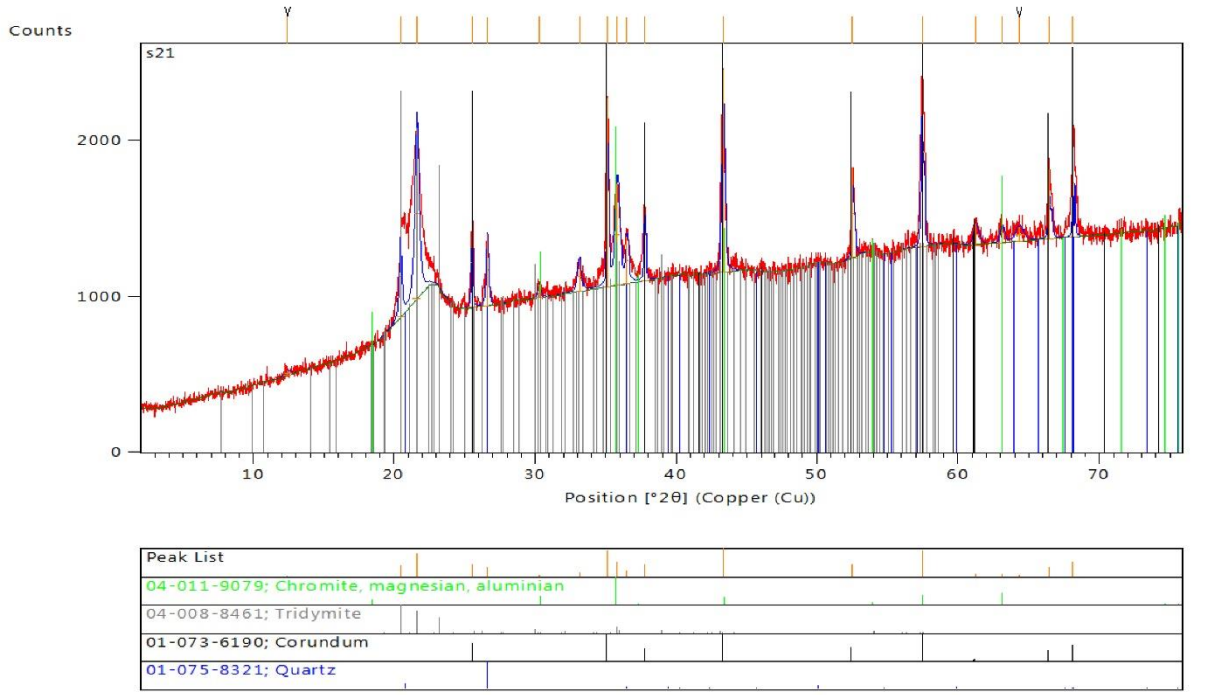

Page: 1 of 1

sample CS7

Date: 16/02/2017 Time: 15:30:36 User: user

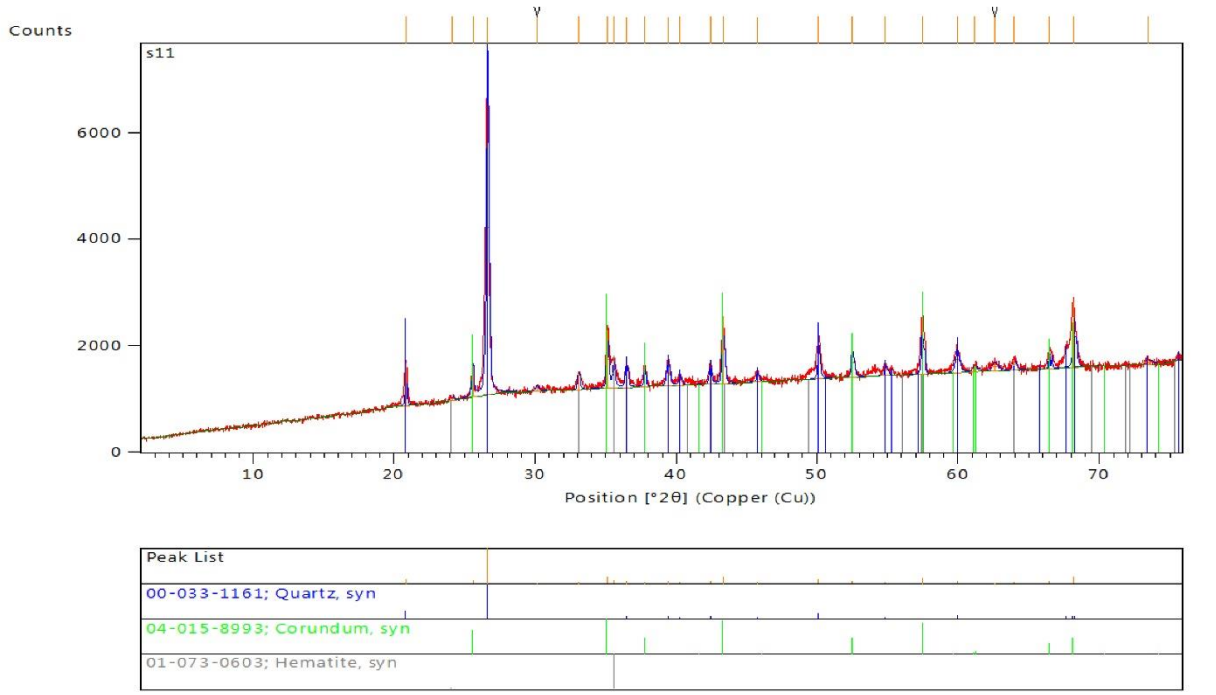

Page: 1 of 1

sample AS1

Date: 15/02/2017 Time: 11:24:26 User: user

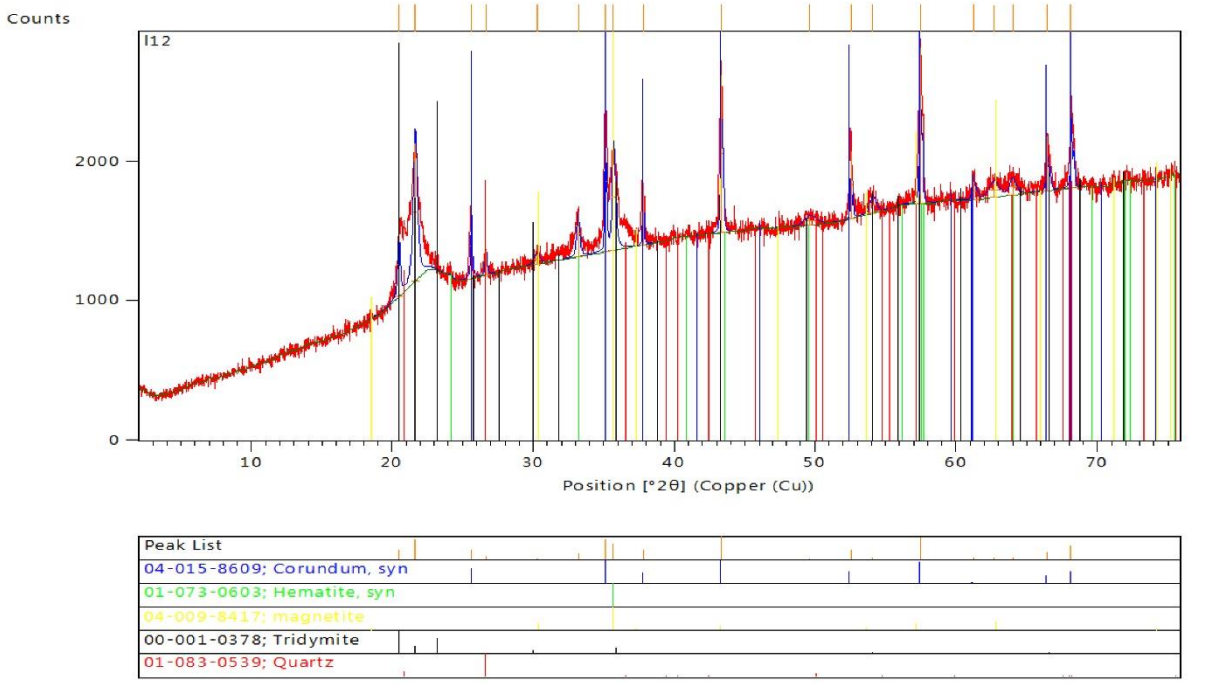

Page: 1 of 1

sample AS2

Date: 15/02/2017 Time: 11:30:22 User: user

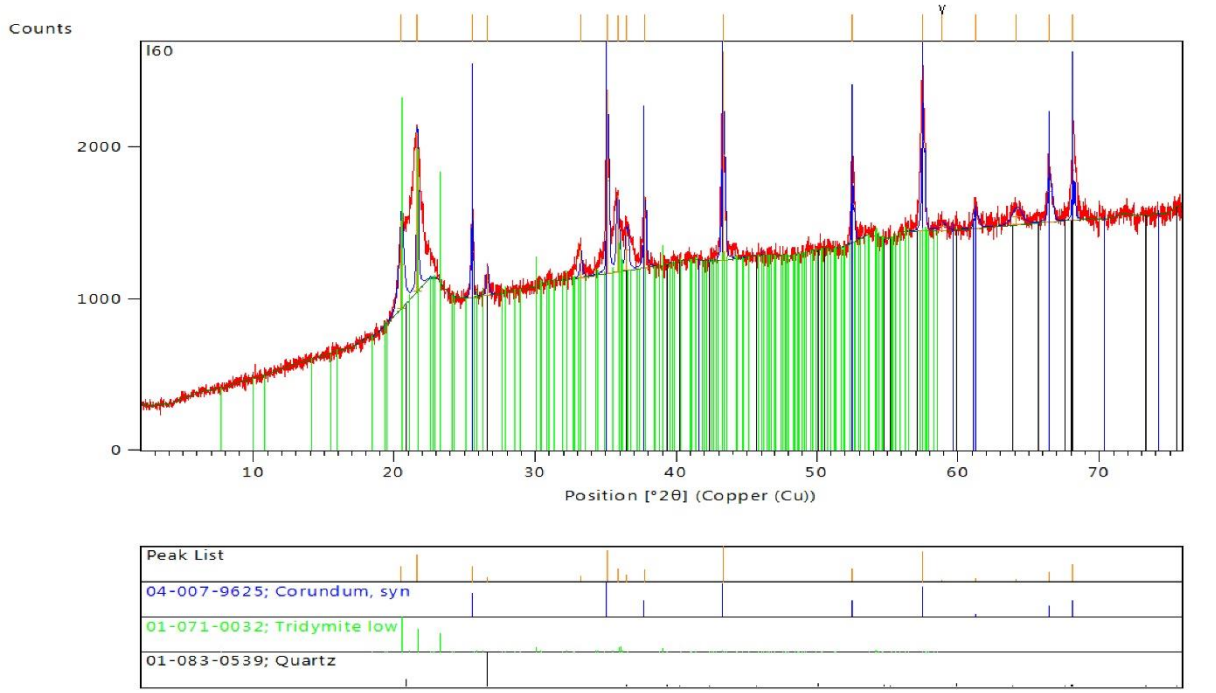

Page: 1 of 1

sample SC

Date: 16/02/2017 Time: 15:28:29 User: user

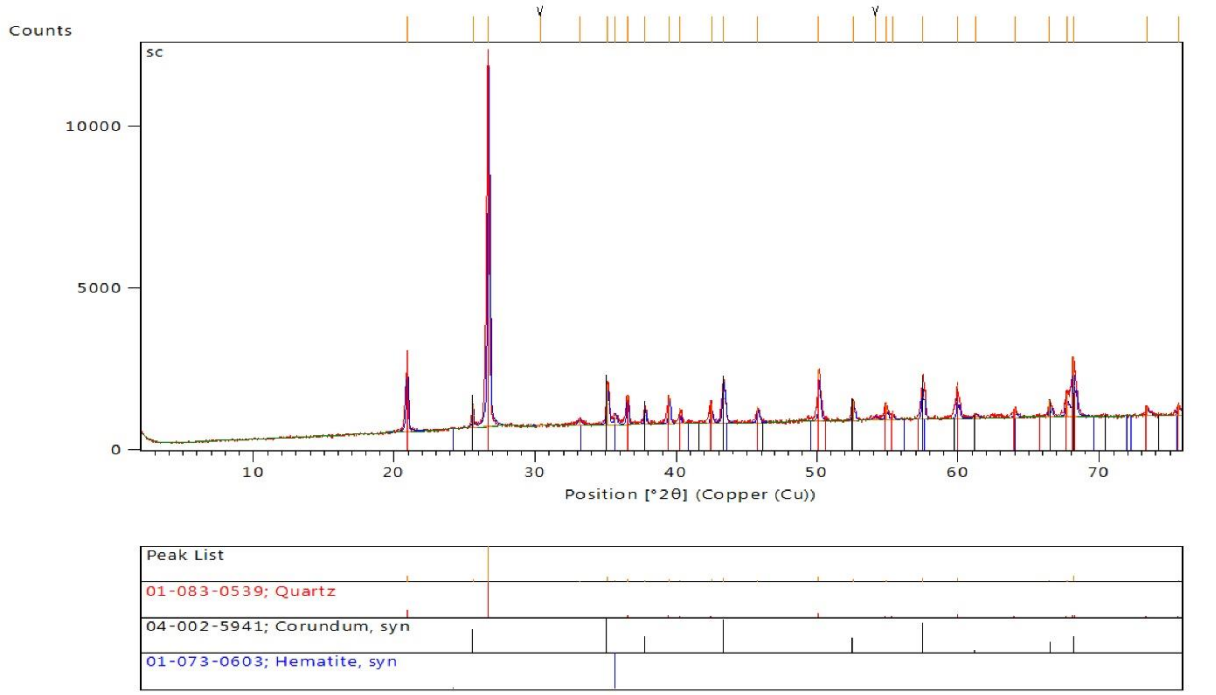

Page: 1 of 1

sample V1

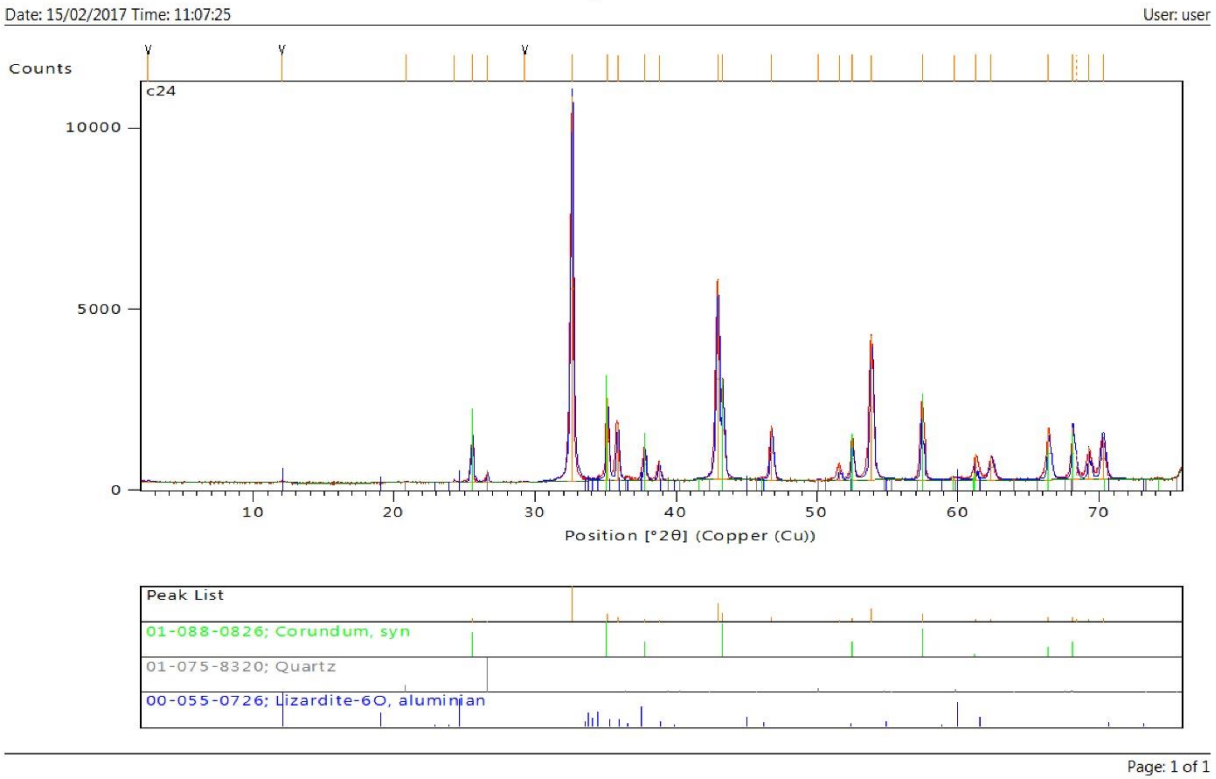
Date: 15/02/2017 Time: 11:07:25
User: user
Counts
c24
10000
5000
0
10
20
30
40
50
60
70
Position [°2θ] (Copper (Cu))
Peak List
01-088-0826; Corundum, syn
01-075-8320; Quartz
00-055-0726; Lizardite-6O, aluminian
Page: 1 of 1

sample V2

Date: 14/02/2017 Time: 12:51:09 User: user

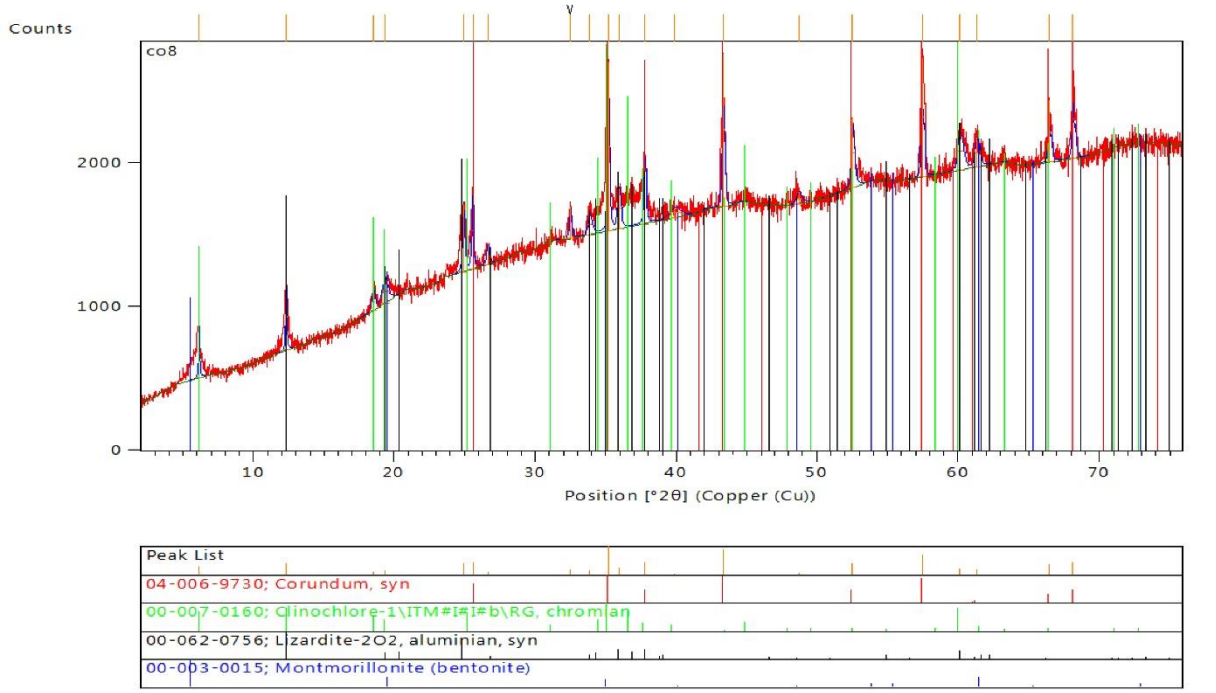

Page: 1 of 1

sample V3

Date: 15/02/2017 Time: 11:17:58 User: user

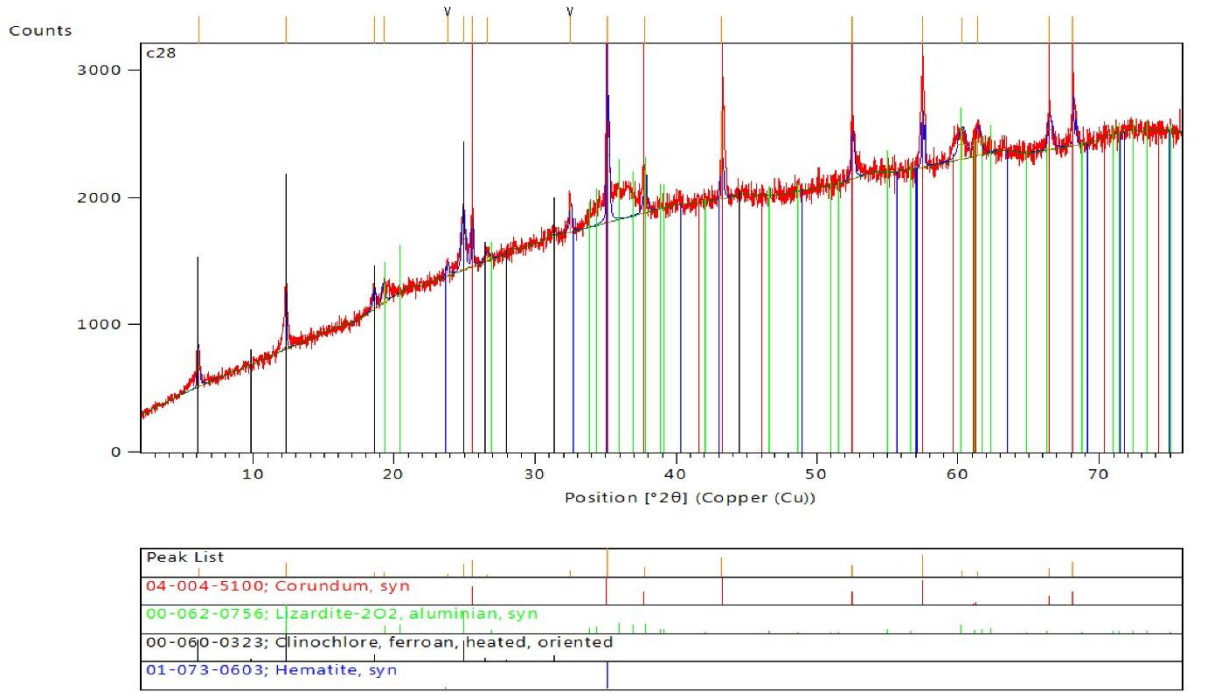

Page: 1 of 1

sample V4

Date: 15/02/2017 Time: 10:57:33 User: user

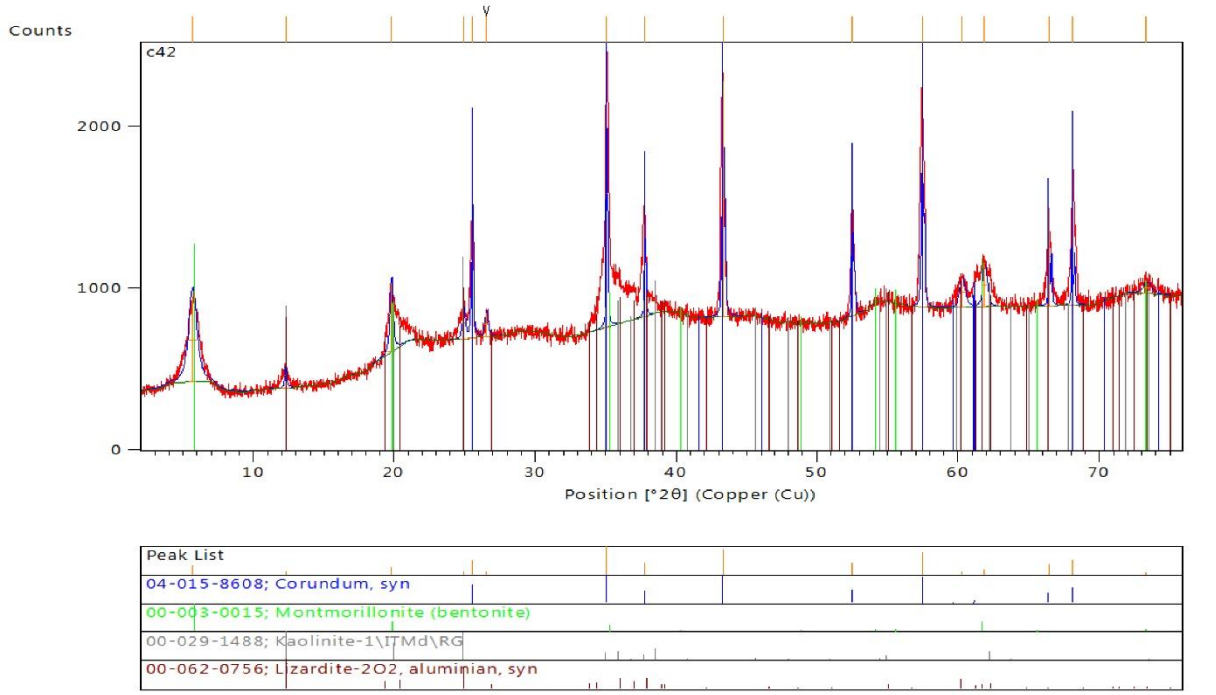

Page: 1 of 1

Table A2. Relative mineral abundances of rock samples from the São João do Piauí Ni laterite profile.

SAMPLE		Initial Analysis			Corundum correction	Corrected Analysis		Analytical Information			
	Mineral Phase ID	Phase	Weight%	Error (±)	Weight%	Weight%	Error (±)	Correction Factor	Global Chi squared	R-Factor	Excluded regions (2θ)
B1	129	Chlorite	7.8	0.19	N/A				4.98	0.529	
	956	Antigorite	87.3	0.28							2-5
	1	Magnetite	4.9	0.15							62-76
		TOTAL	**100.0**								
B2	129	Chlorite	44.6	0.96	N/A				10.9	0.733	2-11
	956	Lizardite	45.2	0.82							64-76
	1	Magnetite	10.2	0.36							
		TOTAL	**100.0**								
B3	41	Hematite	10.1	0.22	N/A						
	896	Magnetite, titanian	11.9	0.39							
	167	Lizardite	78	0.41							
		TOTAL	**100.0**								
SR1		Hematite	6	0.14	7.8	10.4	0.24	173.61			
		Lizardite	24.3	0.46	31.6	42.2	0.80	173.61			
		Quartz	27.3	0.2	35.5	47.4	0.35	173.61			
		Corundum	42.4	0.32	25.0						
		TOTAL			**100.0**	**100.0**					
SR2		Chrysotile	100		N/A						
CS1		Quartz	100		N/A						

Table A2 (continued). Relative mineral abundances of rock samples from the São João do Piauí Ni laterite profile.

SAMPLE		Initial Analysis			Corundum correction	Corrected Analysis		Analytical Information			
	Mineral Phase ID	Phase	Weight%	Error (±)	Weight%	Weight%	Error (±)	Correction Factor	Global Chi squared	R-Factor	Excluded regions (2θ)
CS2		Quartz	62.7	0.29	68.9	91.8	0.42	146.41	5.64	0.317	2-20
		Hematite	5.6	0.24	6.1	8.2	0.35	146.41			22-25
		Corundum	31.7	0.27	25.0						69-76
		TOTAL	**100.0**		**100.0**	**100.0**					
CS3	129	Montmorillonite	3.8	0.14	4.6	6.1	0.23	161.29	8.37	0.474	0-3.5
	956	Chlorite	1.6	0.36	1.9	2.6	0.58	161.29			8-11
	1	Lizardite	3	0.29	3.6	4.8	0.47	161.29			13-18
	40	Magnetite	9.7	0.13	11.7	15.6	0.21	161.29			70-76
		Hematite	5.3	0.15	6.4	8.5	0.24	161.29			
		Tridymite (mono)	38.6	0.34	46.7	62.3	0.55	161.29			
		Corundum	38	0.35	25.0			0.00			
		TOTAL	**100.0**		**100.0**	**100.0**					
CS4	129	Quartz	37.4	0.29	47.0	62.6	0.49	167.50	6.23	0.352	2-11
	956	Cristobalite	9	0.18	11.3	15.1	0.30	167.50			28-34
	1	Montmorillonite	7.6	0.45	9.5	12.7	0.75	167.50			69.5-76
	40	Lizardite	4	0.22	5.0	6.7	0.37	167.50			
		Chlorite	1.7	0.37	2.1	2.8	0.62	167.50			
		Corundum	40.3	0.33	25.0			0.00			
		TOTAL	**100.0**		**100.0**	**100.0**					

Table A2 (continued). Relative mineral abundances of rock samples from the São João do Piauí Ni laterite profile.

SAMPLE		Initial Analysis			Corundum correction	Corrected Analysis		Analytical Information			
	Mineral Phase ID	Phase	Weight%	Error (±)	Weight%	Weight%	Error (±)	Correction Factor	Global Chi squared	R-Factor	Excluded regions (2θ)
CS5		Quartz	68.6	0.16	75.0	100.0	0.23	145.77	4.25	0.223	2-19
		Corundum	31.4	0.16	25.0						28-32
		TOTAL	**100.0**		**100.0**	**100.0**					61-76
CS6	1	Quartz	2.5	0.13	3.3	4.3	0.23	173.91			
	101	Tridymite (mono)	51.9	0.3	67.7	90.3	0.52	173.91			
	1719	Chromite	3.1	0.1	4.0	5.4	0.17	173.91			
	40	Corundum	42.5		25.0						
		TOTAL	**100.0**		**100.0**	**100.0**					
CS7	129	Quartz	52.2	0.18	57.3	76.4	0.26	146.41	5.04	0.297	2-20
	956	Hematite	16.1	0.15	17.7	23.6	0.22	146.41			29-32
	1	Corundum	31.7	0.2	25.0						70-76
	40	**TOTAL**	**100.0**		**100.0**	**100.0**					
AS1		Quartz	0.9	0.14	1.0	1.4	0.22	153.61	11.29	0.514	2-10
		Tridymite	48.6	0.38	56.0	74.7	0.58	153.61			16-19
		Hematite	7.2	0.14	8.3	11.1	0.22	153.61			65-76
		Magnetite	4.4	0.14	5.1	6.8	0.00				
		Chlorite	0	0.36	0.0	0.0	0.00				
		Lizardite	4	0.34	4.6	6.1	0.00				
		Corundum	34.9	0.34	25.0						
		TOTAL	**100.0**		**100.0**	**100.0**					

Table A2 (continued). Relative mineral abundances of rock samples from the São João do Piauí Ni laterite profile.

SAMPLE		Initial Analysis			Corundum correction	Corrected Analysis		Analytical Information			
	Mineral Phase ID	Phase	Weight%	Error (±)	Weight%	Weight%	Error (±)	Correction Factor	Global Chi squared	R-Factor	Excluded regions (2θ)
AS2		Quartz	0.4	0.16	0.5	0.6	0.25	155.04	9.9	0.5	2-10
		Tridymite	61.1	0.39	71.0	94.7	0.60	155.04			60-76
		Lizardite	3.1	0.31	3.6	4.8	0.48	155.04			
		Corundum	35.5	0.34	25.0						
		TOTAL	**100.1**		**100.1**	**100.2**					
SC		Quartz	66.3	0.3	69.1	92.1	0.42	138.89	5.19	0.25	2-20
		Hematite	5.2	0.2	5.4	7.2	0.28	138.89			62-76
		Lizardite	0.5	0.26	0.5	0.7	0.36	138.89			
		Corundum	28	0.23	25.0						
		TOTAL	**100.0**		**100.0**	**100.0**					
V1	129	Magnesite	74.1	0.22	72.6	96.9	0.29	130.72	5.76	0.227	2-23
	956	Lizardite	1.8	0.2	1.8	2.4	0.26	130.72			72-76
	1	Quartz	0.6	0.07	0.6	0.8	0.09	130.72			
	40	Corundum	23.5		25.0						
		TOTAL	**100.0**		**100.0**	**100.0**					
V2	129	Montmorillonite	22	0.39	28.1	37.5	0.66	170.36	6.22	0.533	2-4
	956	Chlorite	28.3	0.62	36.2	48.2	1.06	170.36			8-11
	1	Lizardite	8.4	0.39	10.7	14.3	0.66	170.36			14-17
	40	Corundum	41.3	0.51	25.0						27-33
		TOTAL	**100.0**		**100.0**	**100.0**					63-76

Table A2 (continued). Relative mineral abundances of rock samples from the São João do Piauí Ni laterite profile.

SAMPLE		Initial Analysis			Corundum correction	Corrected Analysis		Analytical Information			
	Mineral Phase ID	Phase	Weight%	Error (±)	Weight%	Weight%	Error (±)	Correction Factor	Global Chi squared	R-Factor	Excluded regions (2θ)
V3	129	Lizardite	16.2	0.44	27.8	37.1	1.01	228.83	7.53	0.636	2-11
	956	Hematite	1.5	0.23	2.6	3.4	0.53	228.83			63-76
	1	Chlorit, Fe	26	0.72	44.6	59.5	1.65	228.83			
	40	Corundum	56.3		25.0						
		TOTAL	**100.0**		**100.0**	**100.0**					
V4	129	Kaolinite	13.1	0.54	17.4	23.2	0.96	176.99	8.19	0.364	2-3
	956	Lizardite	1.6	0.37	2.1	2.8	0.65	176.99			8-10.5
	1	Montmorillonite	41.8	0.37	55.5	74.0	0.65	176.99			14-18.5
	40	Corundum	43.5	0.41	25.0						28-32
		TOTAL	**100.0**		**100.0**	**100.0**					47-51

List of References

Adegoke, H.I., AmooAdekola, F., Fatoki, O.S., Ximba, B.J., 2014. Adsorption of Cr (VI) on synthetic hematite (α-Fe_2O_3) nanoparticles of different morphologies. Korean J. Chem. Eng. 31, 142–154. https://doi.org/10.1007/s11814-013-0204-7

Agrawal, A., Kumar, V., Pandey, B.D., 2006. Remediation options for the treatment of electroplating and leather tanning effluent containing chromium – A review. Miner. Process. Extr. Metall. Rev. 27, 99–130. https://doi.org/10.1080/08827500600563319

Agterberg, F.P., Sampling and analysis of chemical element concentration distribution in rock units and orebodies. 2012. Nonlin. Processes Geophys., 19, 23-44. doi:10.5194/npg-19-23-2012

Aiglsperger, T., Proenza, J.A., Lewis, J.F., Labrador, M., Svojtka, M., Rojas-Purón, A., Longo, F., Ďurišová, J., 2016. Critical metals (REE, Sc, PGE) in Ni laterites from Cuba and the Dominican Republic. Ore Geol. Rev. 73, 127–147. https://doi.org/10.1016/j.oregeorev.2015.10.010

Aiuppa, A., Allard, P., D'Alessandro, W., Michel, A., Parello, F., Treuil, M., Valenza, M., 2000. Mobility and fluxes of major, minor and trace metals during basalt weathering and groundwater transport at Mt. Etna volcano (Sicily). Geochim. Cosmochim. Acta 64, 1827–1841. https://doi.org/10.1016/S0016-7037(00)00345-8

Ajouyed, O., Hurel, C., Ammari, M., Allal, L. Ben, Marmier, N., 2010. Sorption of Cr(VI) onto natural iron and aluminum (oxy)hydroxides: Effects of pH, ionic strength and initial concentration. J. Hazard. Mater. 174, 616–622. https://doi.org/10.1016/j.jhazmat.2009.09.096

Alcock, R.A., 1988. The Character and Resources Available to the Nickel Industry, Extractive Metallurgy of Nickel and Cobalt: Proceedings of a Symposium, The Metallurgical Society, C.P. Tyroler and C. A. Landolt Ed., 117th TMS Annual Meeting, Phoenix, Arizona, 67–89.

Aleva, G.J.J., 1994. Laterites: Concepts, Geology, Morphology and Chemistry. ISRIC, Wageningen.

Almeida, F.F.M. De., 1978. Tectonic map of South America –1/5.000.000 and explanatory note, M.M.E.–D.N.P.M., Brasilia.

Altman, C., King, E.L., 1961. The mechanism of the exchange of chromium(III) and chromium(VI) in acidic solution. J. Am. Chem. Soc. 83, 2825–2830. https://doi.org/10.1021/ja01474a009

Amelin, Y. V., Semenov, V.S., 1996. Nd and Sr isotopic geochemistry of mafic layered intrusions in the eastern Baltic shield: Implications for the evolution of Paleoproterozoic continental mafic magmas. Contrib. to Mineral. Petrol. 124, 255–272. https://doi.org/10.1007/s004100050190

Amundson, R., 2013. Soil Formation, 2nd ed., Treatise on Geochemistry: Second Edition. Elsevier Ltd. https://doi.org/10.1016/B978-0-08-095975-7.00501-5

Anand, R.R., Paine, M., 2002. Regolith geology of the Yilgarn Craton, Western Australia: Implications for exploration. Aust. J. Earth Sci. 49, 3–143. https://doi.org/10.1046/j.1440-0952.2002.00912.x

Anand, R.R., Gilkes, R.J., 1984. Weathering of Ilmenite in a Lateritic Pallid Zone. Clays Clay Miner. 32, 363–374.

April, R., Newton, R., Coles, L.T., 1986. Geological Society of America Bulletin Chemical weathering in two Adirondack watersheds : Past and present-day rates Chemical weathering in two Adirondack watersheds : Past and present–day rates 1232–1238. https://doi.org/10.1130/0016-7606(1986)97<1232

Arai, S., 1997. Origin of podiform chromitites. J. Asian Earth Sci. 15, 303–310.

Arai, S., Matsukage, K., 1996. Petrology of gabbro-troctolite-peridotite complex from Hess Deep, equatorial Pacific: implications for mantle-melt interaction within the oceanic lithosphere. Proc. Ocean Drill. Program, Sci. Results 147, 135–155. https://doi.org/10.2973/odp.proc.sr.147.008.1996

Aumento, F., Loubat, H., 1971. The mid-Atlantic ridge near 45°N. Serpentinized ultramafic intrusions. Can. J. Earth Sci. 8, 631–663. https://doi.org/10.1139/e71-062

Babechuk, M.G., Kleinhanns, I.C., Reitter, E., Schoenberg, R., 2018. Kinetic stable Cr isotopic fractionation between aqueous Cr(III)-Cl-H2O complexes at 25 °C: Implications for Cr(III) mobility and isotopic variations in modern and ancient natural systems. Geochim. Cosmochim. Acta 222, 383–405. https://doi.org/10.1016/j.gca.2017.10.002

Babechuk, M.G., Kleinhanns, I.C., Schoenberg, R., 2017. Chromium geochemistry of the ca. 1.85 Ga Flin Flon paleosol. Geobiology 15, 30–50. https://doi.org/10.1111/gbi.12203

Babechuk, M.G., 2015. Oxidative mafic rock weathering through geological time. PhD Thesis, Trinity College Dublin.

Babechuk, M.G., Widdowson, M., Kamber, B.S., 2014. Quantifying chemical weathering intensity and trace element release from two contrasting basalt profiles, Deccan Traps, India. Chem.

Geol. 363, 56–75.
https://doi.org/10.1016/j.chemgeo.2013.10.027

Babechuk, M.G., Kamber, B.S., Murphy, B., 2013. The Flin Flon paleosol revisited. Can. J. Earth Sci. 50, 1223–1243.
https://doi.org/10.1139/cjes-2013-0076

Babechuk, M.G., Kamber, B.S., Greig, A., Canil, D., Kodolányi, J., 2010. The behaviour of tungsten during mantle melting revisited with implications for planetary differentiation time scales. Geochim. Cosmochim. Acta 74, 1448–1470.
https://doi.org/10.1016/j.gca.2009.11.018

Bain, D.J., Bullen, T.D., 2005. Chromium isotope fractionation during oxidation of Cr(III) by manganese oxides. Geochim. Cosmochim. Acta 69, Supplem. A212.

Banerjee, R., Ray, D., Ishii, T., 2015. Mineral chemistry and alteration characteristics of spinel in serpentinised peridotites from the Northern Central Indian Ridge. J. Geol. Soc. India 86, 41–51.
https://doi.org/10.1007/s12594-015-0279-3

Banerjee, D., Nesbitt, H.W., 1999. Oxidation of aqueous Cr(III) at birnessite surfaces: Constraints on reaction mechanism. Geochim. Cosmochim. Acta 63, 1671–1687.
https://doi.org/10.1016/S0016-7037(99)00003-4

Banfield, J.F., 1990. Analytical Transmission Electron Microscope Studies of Plagioclase, Muscovite, and K-Feldspar Weathering. Clays Clay Miner. 38, 77–89.
https://doi.org/10.1346/CCMN.1990.0380111

Bardossy, G., Aleva, G.J.J., 1990. Lateritic Bauxites: Developments in Economic Geology, Vol. 27. Elsevier, Amsterdam, 624 pp.

Barmina, G., Ariskin, A., 2002. Estimation of chemical and phase characteristics for the initial magma of the Kiglapait troctolite intrusion, Labrador, Canada. Geochemistry Int. 40, 972–983.

Barnes, I., O'Neil, J.R., Rapp, J.B., White, D.E., 1973. Silica-carbonate alteration of serpentine: Wall rock alteration in mercury deposits of the California Coast Ranges. Econ. Geol. 68, 388–398.
https://doi.org/10.2113/gsecongeo.68.3.388

Barnes, S.J., 2000. Chromite in komatiites, II. Modification during greenschist to mid-amphibolite facies metamorphism. J. Petrol. 41, 387–409. https://doi.org/10.1093/petrology/41.3.387

Barros de Oliveira, S.M., Trescases, J.J., Melfi, A.J., 1992. Lateritic nickel deposits of Brazil. Miner. Depos. 27, 137–146.
https://doi.org/10.1007/BF00197099

Basu, A., Johnson, T.M., Sanford, R.A., 2014. Cr isotope fractionation factors for Cr(VI) reduction by a metabolically diverse group of bacteria. Geochim. Cosmochim. Acta 142, 349–361. https://doi.org/10.1016/j.gca.2014.07.024

Basu, A., Johnson, T.M., 2012. Determination of hexavalent chromium reduction using Cr stable isotopes: Isotopic fractionation factors for permeable reactive barrier materials. Environ. Sci. Technol. 46, 5353–5360. https://doi.org/10.1021/es204086y

Becquer, T., Quantin, C., Sicot, M., Boudot, J.P., 2003. Chromium availability in ultramafic soils from New Caledonia. Sci. Total Environ. 301, 251–261. https://doi.org/10.1016/S0048-9697(02)00298-X

Bedson P., 2007. Guidelines for Achieving High Accuracy in Isotope Dilution Mass Spectrometry (IDMS). Royal Society of Chemistry, Cambridge, GBR.

Bénard, A., Arculus, R.J., Nebel, O., Ionov, D.A., McAlpine, S.R.B., 2017. Silica–enriched mantle sources of subalkaline picrite-boninite–andesite island arc magmas. Geochim. Cosmochim. Acta 199, 287–303. https://doi.org/10.1016/j.gca.2016.09.030

Benazir, J.F., Suganthi, R., Rajvel, D., Pooja, M.P., Mathithumilan, B., 2010. Bioremediation of chromium in tannery effluent by microbial consortia. J. Biotechnol. 9, 3140–3143. https://doi.org/10.5897/AJB10.207

Bengtsson, L., Enell, M., 1986. Chemical analysis. In Berglund, B. E. (eds.), Handbook of Holocene Palaeoecology and Palaeohydrology. John Wiley & Sons Ldt., Chichester, 423–451.

Berbert C.O., 1977. Rochas basico–ultrabasicas no Brasil e suas potencialidades economicas. IIa Semana de Estudos Geologicos do Parana. CEGEP-UFPr, 1–51.

Berg, J.H., 1980. Snowflake troctolite in the Hettasch intrusion, Labrador: Evidence for magma-mixing and supercooling in a plutonic environment. Contrib. to Mineral. Petrol. 72, 339–351. https://doi.org/10.1007/BF00371343

Berger, A., Frei, R., 2014. The fate of chromium during tropical weathering: A laterite profile from central Madagascar. Geoderma 213, 521–532. https://doi.org/10.1016/j.geoderma.2013.09.004

Berger, V.I., Mosier, D.L., Bliss, J.D., Moring, B.C., 2011. Ni–Co laterite Deposits of the World–Database and Grade and Tonnage Models. Open-File Rep. 2011, 1058 pp. https://doi.org/10.3133/ofr20141074

Beukes, N.J., Dorland, H., Gutzmer, J., Nedachi, M., Ohmoto, H., 2002. Tropical laterites, life on land, and the history of atmospheric oxygen in the Paleoproterozoic. Geology 30, 491–494. https://doi.org/10.1130/0091-7613(2002)030<0491:TLLOLA>2.0.CO;2

Beukes, J.P., Giesekke, E.W., Elliott, W., 2000. Nickel retention by goethite and hematite. Miner. Eng. 13, 1573–1579. https://doi.org/10.1016/S0892-6875(00)00140-0

Beverskog, B., Puigdomenech, 1997. Revised pourbaix diagrams for chromium at 25–300°C. Corros. Sci. 39, 43–57.

Bezerra, F.H.R., Brito Neves, B.B., Corrêa, A.C.B., Barreto, A.M.F., Suguio, K., 2008. Late Pleistocene tectonic-geomorphological development within a passive margin – The Cariatá trough, northeastern Brazil. Geomorphology 97, 555–582. https://doi.org/10.1016/j.geomorph.2007.09.008

Bigeleisen, J., Mayer, M. G., 1947. Calculation of equilibrium constants for isotopic exchange reactions. J. Chem. Phys. 15, 261–267.

Birck, J. L., Allègre, C.J., 1988. Manganese-chromium isotope systematics and the development of the early Solar System. Nature 357, 57–59.

Birck, J. L., Allègre, C.J., 1984. Chromium isotopic anomalies in Allende Refractory Inclusions. Geophys. Res. Lett. 11, 943–946. https://doi.org/10.1029/GL011i010p00943

Bonnand, P., James, R.H., Parkinson, I.J., Connelly, D.P., Fairchild, I.J., 2013. The chromium isotopic composition of seawater and marine carbonates. Earth Planet. Sci. Lett. 382, 10–20. https://doi.org/10.1016/j.epsl.2013.09.001

Bonnand, P., Parkinson, I.J., James, R.H., Karjalainen, A.M., Fehr, M.A., 2011. Accurate and precise determination of stable Cr isotope compositions in carbonates by double spike MC-ICP-MS. J. Anal. At. Spectrom. 26, 528–535. https://doi.org/10.1039/c0ja00167h

Boultif, A., Louër, D., 1991. Indexing of Powder Diffraction Patterns for Low-Symmetry Lattices by the Successive Dichotomy Method. J. Appl. Crystallogr. 1991, 24, 987–993.

Bourman, R.P., 1993. Perennial problems in the study of laterite: A review. Aust. J. Earth Sci. 40, 387–401. https://doi.org/10.1080/08120099308728090

Boyalı, İ., 1985. Yunusemre Karaçam (Eskişehir–Mihailıççik) Nikel–Kobalt Ceveherleşmesi Etüdü: MTA Maden Etüd Report.

Brand, N.W., Butt, C.R.M., Elias, M., 1998. Nickel Laterites: Classification and Features. J. Aust. Geol. Geophys. 17, 81–88.

Braucher, R., Raisbeck, G.M., Koud, J.M., Bamba, O., Brown, E.T., Yiou, F., Colin, F., Bourlès, D.L., 2002. African laterite dynamics using in situ-produced ^{10}Be. Geochim. Cosmochim.

Acta.
https://doi.org/10.1016/s0016-7037(98)00085-4

Braun, J.J., Pagel, M., 1994. Geochemical and mineralogical behavior of REE, Th and U in the Akongo lateritic profile (SW Cameroon). Catena 21, 173–177.
https://doi.org/10.1016/0341-8162(94)90010-8

Braun, J.J., Pagel, M., Herbilln, A., Rosin, C., 1993. Mobilization and redistribution of REEs and thorium in a syenitic lateritic profile: A mass balance study. Geochim. Cosmochim. Acta 57, 4419–4434.
https://doi.org/10.1016/0016-7037(93)90492-F

Brazilian Nickel Limited, 2017. The Piauí Nickel Project Fact sheet August 2017.

Brimhall, G.H., Christopher J., L., Ford, C., Bratt, J., Taylor, G., Warin, O., 1991. Quantitative geochemical approach to pedogenesis: importance of parent material reduction, volumetric expansion, and eolian influx in lateritization. Geoderma 51, 51–91.
https://doi.org/10.1016/0016-7061(91)90066-3

Brito Neves, B.B., Santos, E.J., Van Schmus, W.R., 2000. Tectonic history of the Borborema Province, northeastern Brazil. In: Cordani, U., Milani, E.J., Thomaz Filho, A., Campos, D.A. (eds.), Tectonic Evolution of South America, Proceedings of the 31st International Geological Congress, Rio de Janeiro, 151–182.

Brown, D.J., Helmke, P.A., Clayton, M.K., 2003. Robust geochemical indices for redox and weathering on a granitic laterite landscape in Central Uganda. Geochim. Cosmochim. Acta 67, 2711–2723.
https://doi.org/10.1016/S0016-7037(03)00104-2

Brown, P.A., 2014. Economically recoverable elements in nickel laterites: distribution, mineral chemistry and implications for exploration and processing of the Çaldağ deposit, W.Turkey. MSci Thesis, Imperial College London.

Brusca, L., Aiuppa, A., D'Alessandro, W., Parello, F., Allard, P., Michel, A., 2001. Geochemical mapping of magmatic gas-water-rock interactions in the aquifer of Mount Etna volcano. J. Volcanol. Geotherm. Res. 108, 199–218.
https://doi.org/10.1016/S0377-0273(00)00286-9

Buchanan, F., 1807. A Journey from Madras Through the Countries of Mysore, Canara, and Malabar. East India Company, London.

Buerge, I.J., Hug, S.J., 1997. Kinetics and pH dependence of chromium(VI) reduction by iron(II). Environ. Sci. Technol. 31, 1426–1432.
https://doi.org/10.1021/es960672i

Butt, C.R.M., 2014. Discussion of 'Silicified serpentinite – a residuum of a Tertiary palaeo–weathering surface in the United Arab Emirates.' Geol. Mag. 151, 1144–1146. https://doi.org/10.1017/S0016756812000325

Butt, C.R.M., Cluzel, D., 2013. Nickel laterite ore deposits: Weathered serpentinites. Elements 9, 123–128. https://doi.org/10.2113/gselements.9.2.123

Butt, C.R.M., Zeegers, H., 1992. Regolith exploration geochemistry in tropical and subtropical terrains. In: Handbook of Exploration Geochemistry 4. Elsevier, Amsterdam.

Cameron, V., Vance, D., 2014. Heavy nickel isotope compositions in rivers and the oceans. Geochim. Cosmochim. Acta. 128, 195–211. https://doi.org/10.1016/j.gca.2013.12.007

Cameron, V., Vance, D., Archer, C., House, C.H., 2009. A biomarker based on the stable isotopes of nickel. Proc. Natl. Acad. Sci. 106, 10944–10948. https://doi.org/10.1073/pnas.0900726106

Cann, J.R., 1970. Rb, Sr, Y, Zr and Nb in some ocean floor basaltic rocks. Earth Planet. Sci. Lett. 10, 7–11. https://doi.org/10.1016/0012-821X(70)90058-0

Cawthorn, R.G., Barnes, S., Ballhaus, C., Malitch, K.N., 2005. Platinum group element, chromium and vanadium deposits in mafic and ultramafic rocks. Econ. Geol. 100th Anniversary, 215–249.

Caxito, F., Uhlein, A., Stevenson, R., Uhlein, G.J., 2014. Neoproterozoic oceanic crust remnants in northeast Brazil. Geology 42, 387–390. https://doi.org/10.1130/G35479.1

Challis, A., Grapes, R.H., Palmer, K., 1995. Chromian muscovite, uvarovite, and zincian chromite: products of regional metasomatism in Northwest Nelson, New Zealand. Can. Mineral. 33, 1263–1284.

Chatterjee, R., Lassiter, J.C., 2016. $^{186}Os/^{188}Os$ variations in upper mantle peridotites: Constraints on the Pt/Os ratio of primitive upper mantle, and implications for late veneer accretion and mantle mixing timescales. Chem. Geol. 442, 11–22. https://doi.org/10.1016/j.chemgeo.2016.08.033

Cleaves, E.T., 1974. Petrological and chemical investigation of chemical weathering in mafic rocks, eastern Piedmont of Maryland. Department of Natural Resources, Report No. 25, 28 pp.

Cocker, M.D., 2014, Lateritic, supergene rare earth element (REE) deposits, in, Conway, F.M., ed., Proceedings of the 48th Annual Forum on the Geology of Industrial Minerals, Phoenix, Arizona, April 30 - May 4, 2012. Arizona Geological Survey Special Paper #9, Chapter 4, 1-18.

Cohen, M.D., Kargacin, B., Klein, C.B., Costa, M., 1993. Mechanisms of chromium carcinogenicity and toxicity. Crit. Rev. Toxicol. 23, 255–281. https://doi.org/10.3109/10408449309105012

Cole, D.B., Wang, X., Qin, L., Planavsky, N.J., Reinhard, C.T., 2018. Chromium Isotopes 1–6. https://doi.org/10.1007/978-3-319-39193-9_334-1

Cole, D.B., Reinhard, C.T., Wang, X., Gueguen, B., Halverson, G.P., Gibson, T., Hodgskiss, M.S.W., Ryan McKenzie, N., Lyons, T.W., Planavsky, N.J., 2016. A shale–hosted Cr isotope record of low atmospheric oxygen during the Proterozoic. Geology 44, 555–558. https://doi.org/10.1130/G37787.1

Compton, J.S., White, R.A., Smith, M., 2003. Rare earth element behavior in soils and salt pan sediments of a semi-arid granitic terrain in the Western Cape, South Africa. Chem. Geol. 201, 239–255. https://doi.org/10.1016/S0009-2541(03)00239-0

Connelly, D.P., Statham, P.J., Knap, A.H., 2006. Seasonal changes in speciation of dissolved chromium in the surface Sargasso Sea. Deep. Res. Part I. Oceanogr. Res. Pap. 53, 1975–1988. https://doi.org/10.1016/j.dsr.2006.09.005

Cornu, S., Lucas, Y., Lebon, E., Ambrosi, J.P., Luizão, F., Rouiller, J., Bonnay, M., Neal, C., 1999. Evidence of titanium mobility in soil profiles, Manaus, central Amazonia. Geoderma 91, 281–295. https://doi.org/10.1016/S0016-7061(99)00007-5

Cottin, J.Y., Lorand, J.P., Agrinier, P., Bodinier, J.L., Liégeois, J.P., 1998. Isotopic (O, Sr, Nd) and trace element geochemistry of the Laouni layered intrusions (Pan-African belt, Hoggar, Algeria): Evidence for post–collisional continental tholeiitic magmas variably contaminated by continental crust. Lithos 45, 197–222. https://doi.org/10.1016/S0024-4937(98)00032-2

Crawford, R.J., Harding, I.H., Mainwaring, D.E., 1993. Adsorption and Coprecipitation of Single Heavy Metal 40, Langmuir 9, 3050–3056.

Cromieres, L., Moulin, V., Fourest, B., Guillaumont, R., Giffaut, E., 1998. Sorption of thorium onto hematite colloids. Radiochimica Acta 82, 249–255.

Crowe, S.A., Døssing, L.N., Beukes, N.J., Bau, M., Kruger, S.J., Frei, R., Canfield, D.E., 2013. Atmospheric oxygenation three billion years ago. Nature 501, 535–538. https://doi.org/10.1038/nature12426

Cullers, R., 1988. Mineralogical and chemical changes of soil and stream sediment formed by intense weathering of the Danburg granite, Georgia, U.S.A. Lithos 21, 301–314. https://doi.org/10.1016/0024-4937(88)90035-7

D'Arcy, J., Babechuk, M.G., Døssing, L.N., Gaucher, C., Frei, R., 2016. Processes controlling the chromium isotopic composition of river water: Constrains from basaltic river catchments. Geochim. Cosmochim. Acta 186, 296–315. https://doi.org/10.1016/j.gca.2016.04.027

Da Costa, M.L., Araújo, E.S., 1996. Application of multi–element geochemistry in Au–phosphate–bearing lateritic crusts for identification of their parent rocks. J. Geochemical Explor. 57, 257–272. https://doi.org/10.1016/S0375-6742(96)00041-6

Dalvi, A.D., Bacon, W.G., Osborne, R.C., 2004b. The Past and the Future of Nickel Laterites. PDAC 2004 Int. Conv. 1–27.

Daugherty, M.L., 1992. Toxicity summary for chromium. Oak Ridge National Laboratory Chemical Hazard Evaluation and Communication Group, Oak Ridge, Tenn.

Day, J.M.D., Barry, P.H., Hilton, D.R., Burgess, R., Pearson, D.G., Taylor, L.A., 2015. The helium flux from the continents and ubiquity of low-3He/4He recycled crust and lithosphere. Geochim. Cosmochim. Acta 153, 116–133. https://doi.org/10.1016/j.gca.2015.01.008

de Chetelat, E., 1947. La genese et l'evolution des gisements de nickel de la Nouvelle–Caledonie. Soc. Geol. Fr. Bull. Ser. 5, 105–160.

de Albuquerque, U.P., de Medeiros, P.M., de Almeida, A.L.S., Monteiro, J.M., de Freitas Lins Neto, E.M., de Melo, J.G., dos Santos, J.P., 2007. Medicinal plants of the caatinga (semi-arid) vegetation of NE Brazil: A quantitative approach. J. Ethnopharmacol. 114, 325–354. https://doi.org/10.1016/j.jep.2007.08.017

de Oliveira, S.M.B., Campos, E.G., 1991. Gold–bearing iron duricrust in Central Brazil. J. Geochemical Explor. 41, 309–323. https://doi.org/10.1016/0375-6742(91)90005-F

Dean, W.E.J., 1974. Determination carbonate and organic matter in calcareous sediments and sedimentary rocks by loss on ignition: comparison with other methods. J. Sediment. Petrol. 44, 242–248.

Deer, W.A., Howie, R.A. and Zussman, J., 2013. An introduction to the rock–forming minerals: Mineralogical Society. 3rd edition. 217–223.

DePaolo, D.J., 2011. Surface kinetic model for isotopic and trace element fractionation during precipitation of calcite from aqueous solutions. Geochim. Cosmochim. Acta 75, 1039–1056. https://doi.org/10.1016/j.gca.2010.11.020

Desai, R. V, Khanapurkar, J. V, Suryawanshi, R.A., 2018. Geochemistry of upland laterites of tarale–thoseghar plateau of bamnoli range of Satara District of Maharashtra, India. J. Appl. Geochemistry 20, 421–431.

Dill, H.G., 2015. Supergene alteration of ore deposits: From nature to humans. Elements 11, 311–316.
https://doi.org/10.2113/gselements.11.5.311

Dong, Z.Y., Huang, W.H., Xing, D.F., Zhang, H.F., 2013. Remediation of soil Co–contaminated with petroleum and heavy metals by the integration of electrokinetics and biostimulation. J. Hazard. Mater. 260, 399–408.
https://doi.org/10.1016/j.jhazmat.2013.05.003

Døssing, L.N., Dideriksen, K., Stipp, S.L.S., Frei, R., 2011. Reduction of hexavalent chromium by ferrous iron: A process of chromium isotope fractionation and its relevance to natural environments. Chem. Geol. 285, 157–166.
https://doi.org/10.1016/j.chemgeo.2011.04.005

Driese, S.G., 2004. Pedogenic translocation of Fe in modern and ancient Vertisols and implications for interpretations of the Hekpoort Paleosol (2.25 Ga). J. Geol. 112, 543–560.
https://doi.org/10.1086/422665

Du, X., Rate, A.W., Gee, M.A.M., 2012. Redistribution and mobilization of titanium, zirconium and thorium in an intensely weathered lateritic profile in Western Australia. Chem. Geol. 330–331, 101–115.
https://doi.org/10.1016/j.chemgeo.2012.08.030

Dupré, B., Dessert, C., Oliva, P., Goddéris, Y., Viers, J., François, L., Millot, R., Gaillardet, J., 2003. Rivers, chemical weathering and Earth's climate. Comptes Rendus - Geosci. 335, 1141–1160.
https://doi.org/10.1016/j.crte.2003.09.015

Eary, L. E., Rai, D., 1987. Kinetics of Chromium(III) Oxidation to Chromium(VI) by Reaction with Manganese Dioxide. Environ. Sci. Technol. 21, 1187–1193.

Economou-Eliopoulos, M., Frei, R., Atsarou, C., 2014. Application of chromium stable isotopes to the evaluation of Cr(VI) contamination in groundwater and rock leachates from central Euboea and the Assopos basin (Greece). Catena 122, 216–228.
https://doi.org/10.1016/j.catena.2014.06.013

Eggleton, R.A., Fitz Gerald, J., Foster, L., 2011. Chrysoprase from Gumigil, Queensland. Aust. J. Earth Sci. 58, 767–776.
https://doi.org/10.1080/08120099.2011.594091

Eggleton, R.A., 2001. The Regolith Glossary, Surficial Geology, Soils and Landscapes.

Eggleton, R.A., Foudoulis, C., Varkevisser, D., 1987. Weathering of Basalt: Changes in Rock Chemistry and Mineralogy. Clays Clay Miner. 35, 161–169. https://doi.org/10.1346/CCMN.1987.0350301

Elias, M., 2002. Nickel laterite deposits – geological overview, resources and exploitation. Giant Ore Depos. Charact. Genes. Explor. CODES Spec. Publ. 4, Hobart, Univ. Tasmania 4, 205–220.

Eliopoulos, D.G., Economou-Eliopoulos, M., 2000. Geochemical and mineralogical characteristics of Fe–Ni– and bauxitic–laterite deposits of Greece. Ore Geol. Rev. 16, 41–58. https://doi.org/10.1016/S0169-1368(00)00003-2

Elliott, T., Steele, R.C.J., 2017. The Isotope Geochemistry of Ni. Rev. Mineral. Geochemistry 82, 511–542. https://doi.org/10.2138/rmg.2017.82.12

Ellis, A., Johnson, T., Villalobos-Aragon, A., Bullen, T., 2008. Environmental Cycling of Cr Using Stable Isotopes: Kinetic and Equilibrium Effects. Am. Geophys. Union, Fall Meet. 2008, Abstr. ID. H53F-08.

Ellis, A.S., Johnson, T.M., Bullen, T.D., 2004. Using chromium stable isotope ratios to quantify Cr(VI) reduction: Lack of sorption effects. Environ. Sci. Technol. 38, 3604–3607. https://doi.org/10.1021/es0352294

Ellis, A.S., Johnson, T.M., Bullen, T.D., 2002. Chromium isotopes and the fate of hexavalent chromium in the environment. Science 295, 2060–2062. https://doi.org/10.1126/science.1068368

Esson, J., 1983. Geochemistry of a nickeliferous laterite profile, Liberdade, Brazil. Geol. Soc. London, Spec. Publ. 11, 91–99. https://doi.org/10.1144/GSL.SP.1983.011.01.11

Estrade, N., Cloquet, C., Echevarria, G., Sterckeman, T., Deng, T., Tang, Y.T., Morel, J.L., 2015. Weathering and vegetation controls on nickel isotope fractionation in surface ultramafic environments (Albania). Earth Planet. Sci. Lett. 423, 24–35. https://doi.org/10.1016/j.epsl.2015.04.018

Fandeur, D., Juillot, F., Morin, G., Livi, L., Cognigni, A., Webb, S.M., Ambrosi, J.P., Fritsch, E., Guyot, F., Brown, G.E., 2009. XANES evidence for oxidation of Cr(III) to Cr(VI) by Mn-oxides in a lateritic regolith developed on serpentinized ultramafic rocks of New Caledonia. Environ. Sci. Technol. 43, 7384–7390. https://doi.org/10.1021/es900498r

Farkaš, J., Chrastný, V., Novák, M., Čadkova, E., Pašava, J., Chakrabarti, R., Jacobsen, S.B., Ackerman, L., Bullen, T.D., 2013. Chromium isotope variations ($\delta^{53/52}$Cr) in mantle–derived sources and their weathering products: Implications for environmental studies and the

evolution of $\delta^{53/52}Cr$ in the Earth's mantle over geologic time. Geochim. Cosmochim. Acta 123, 74–92. https://doi.org/10.1016/j.gca.2013.08.016

Fendorf, S., Wielinga, B.W., Hansel, C.M., 2000. Chromium transformations in natural environments: The role of biological and abiological processes in chromium(VI) reduction. Int. Geol. Rev. 42, 691–701. https://doi.org/10.1080/00206810009465107

Fendorf, S.E., Li, G., 1996. Kinetics of Chromate Reduction by Ferrous Iron 30, 1614–1617.

Fendorf, S.E., 1995. Surface reactions of chromium in soils and waters. Geoderma 67, 55–71. https://doi.org/10.1016/0016-7061(94)00062-F

Frei, R., Døssing, L.N., Gaucher, C., Boggiani, P.C., Frei, K.M., Bech Árting, T., Crowe, S.A., Freitas, B.T., 2017. Extensive oxidative weathering in the aftermath of a late Neoproterozoic glaciation – Evidence from trace element and chromium isotope records in the Urucum district (Jacadigo Group) and Puga iron formations (Mato Grosso do Sul, Brazil). Gondwana Res. 49, 1–20. https://doi.org/10.1016/j.gr.2017.05.003

Frei, R., Crowe, S.A., Bau, M., Polat, A., Fowle, D.A., Døssing, L.N., 2016. Oxidative elemental cycling under the low O_2 Eoarchean atmosphere. Sci. Rep. 6:21058. https://doi.org/10.1038/srep21058

Frei, R., Poiré, D., Frei, K.M., 2014. Weathering on land and transport of chromium to the ocean in a subtropical region (Misiones, NW Argentina): A chromium stable isotope perspective. Chem. Geol. 381, 110–124. https://doi.org/10.1016/j.chemgeo.2014.05.015

Frei, R., Polat, A., 2013. Chromium isotope fractionation during oxidative weathering – Implications from the study of a Paleoproterozoic (ca. 1.9 Ga) paleosol, Schreiber Beach, Ontario, Canada. Precambrian Res. 224, 434–453. https://doi.org/10.1016/j.precamres.2012.10.008

Frei, R., Gaucher, C., Poulton, S.W., Canfield, D.E., 2009. Fluctuations in Precambrian atmospheric oxygenation recorded by chromium isotopes. Nature 461, 250–253. https://doi.org/10.1038/nature08266

Freyssinet, P., Butt, C.R.M., Morris, R.C., Piantone, P., 2005. Ore–forming processes related to lateritic weathering. In: Hedenquist J.W., Thomson J.F.H., Goldfarb R.J., Richards J.P. (eds.), Economic Geology 100th Anniversary Volume. Economic Geology Publishing Company, New Haven, Connecticut, 681–722.

Freyssinet, P., Farah, A.S., 2000. Geochemical mass balance and weathering rates of ultramafic schists in Amazonia. Chem. Geol. 170, 133–151. https://doi.org/10.1016/S0009-2541(99)00245-4

Fu, W., Feng, Y., Luo, P., Zhang, Y., Huang, X., Zeng, X., Cai, Q., Zhou, Y., 2019. Weathering of Ophiolite Remnant and Formation of Ni Laterite in a Strong Uplifted Tectonic Region (Yuanjiang, Southwest China). Minerals 9, 51. 25 pp. https://doi.org/10.3390/min9010051

Fujii, T., Moynier, F., Blichert-Toft, J., Albarède, F., 2014. Density functional theory estimation of isotope fractionation of Fe, Ni, Cu, and Zn among species relevatn to geochemical and biological environments. Geochim. Cosmochim. Acta 140, 553–576.

Fujii, T., Moynier, F., Dauphas, N., Abe, M., 2011. Theoretical and experimental investigation of nickel isotopic fractionation in species relevant to modern and ancient oceans. Geochim. Cosmochim. Acta 75, 469–482. https://doi.org/10.1016/j.gca.2010.11.003

Gall, L., Williams, H.M., Siebert, C., Halliday, A.N., Herrington, R.J., Hein, J.R., 2013. Nickel isotopic compositions of ferromanganese crusts and the constancy of deep ocean inputs and continental weathering effects over the Cenozoic. Earth Planet. Sci. Lett. 375, 148–155. https://doi.org/10.1016/j.epsl.2013.05.019

Garnier, J., Quantin, C., Guimarães, E., Becquer, T., 2008. Can chromite weathering be a source of Cr in soils? Mineral. Mag. 72, 49–53. https://doi.org/10.1180/minmag.2008.072.1.49

Gilleaudeau, G.J., Frei, R., Kaufman, A.J., Kah, L.C., Azmy, K., Bartley, J.K., Chernyavskiy, P., Knoll, A.H., 2016. Oxygenation of the mid-Proterozoic atmosphere: clues from chromium isotopes in carbonates. Geochemical Perspect. Lett. 178–187. https://doi.org/10.7185/geochemlet.1618

Giménez-Forcada, E., Vega-Alegre, M., Timón-Sánchez, S., 2017. Characterization of regional cold–hydrothermal inflows enriched in arsenic and associated trace-elements in the southern part of the Duero Basin (Spain), by multivariate statistical analysis. Sci. Total Environ. 593–594, 211–226. https://doi.org/10.1016/j.scitotenv.2017.03.071

Girgin, I., Obut, A., Üçyildiz, A., 2011. Dissolution behaviour of a Turkish lateritic nickel ore. Miner. Eng. 24, 603–609. https://doi.org/10.1016/j.mineng.2010.10.009

Gleeson, S. a, Herrington, R.J., Durango, J., Velasquez, C. a, Koll, G., 2004. The mineralogy and geochemistry of the Cerro Matoso S. A. Ni laterite deposit, Montelibano, Colombia. Econ.

Geol. 99, 1197–1213.
https://doi.org/10.2113/99.6.1197

Gleeson S. A., Butt C. R. M., Elias M., 2003. Nickel laterites: a review. SEG Newsl. 54, 11–18.

Godgul, G., Sahu, K.C., 1995. Chromium contamination from chromite mine. Environ. Geol. 25, 251–257.
https://doi.org/10.1007/BF00766754

Goldschmidt, V.M., 1937. The Principles of Distribution of Chemical Elements in Minerals and Rocks. J. Chem. Soc. 655–673.
https://doi.org/10.5382/AV100.21

Golightly J.P., 2010. Progress in understanding the evolution of nickel laterites. In: Goldfarb R.J., Marsh E.E., Monecke T (eds.) The Challenge of Finding New Mineral Resources: Global Metallogeny, Innovative Exploration, and New Discoveries Volume II. Society of Economic Geologists Special Publication 15, 451–475.

Golightly J.P., 1981. Nickeliferous laterite deposits. In Econ. Geol. 75th Anniv. Vol. (1905-1980) (eds.) Skinner, B.J., 710–734.

Gong, Q., Deng, J., Yang, L., Zhang, J., Wang, Q., Zhang, G., 2011. Behavior of major and trace elements during weathering of sericite–quartz schist. J. Asian Earth Sci. 42, 1–13.
https://doi.org/10.1016/j.jseaes.2011.03.003

Goring-Harford, H.J., Klar, J.K., Pearce, C.R., Connelly, D.P., Achterberg, E.P., James, R.H., 2018. Behaviour of chromium isotopes in the eastern sub-tropical Atlantic Oxygen Minimum Zone. Geochim. Cosmochim. Acta.
https://doi.org/10.1016/j.gca.2018.03.004

Goring-Harford, H.J., 2017. Chromium Isotope Behaviour in Natural Waters. PhD Thesis, University of Southampton.

Gouveia, M.A., Prudêncio, M.O., Figueiredo, L.C.J., Pereira, L.C.J., Waerenborgh, J.C., Morgado, I., Pena, T., Lopes, A., 1993. Behavior of REE and other trace and major elements during weathering of granitic rocks, Évora, Portugal. Chem. Geol. 107, 293–296.
https://doi.org/10.1177/1522637917750140

Govindaraju, K., 1995. 1995 Working Values With Confidence Limits for Twenty-Six CRPG, ANRT and IWG-GIT Geostandards. Geostand. Newsl. 19, 1–32.
https://doi.org/10.1111/j.1751-908X.1995.tb00164.x

Govindaraju, K., 1994. 1994 Compilation of Working Values and Sample Description for 383 Geostandards. Geostand. Newsl. 18, 1–158.
https://doi.org/10.1046/j.1365-2494.1998.53202081.x-i1

Gramlich, J.W., Machlan, L.A., Barnes, I.L., Paulsen, P.J., 1989. Absolute isotopic abundance ratios and atomic weight of a reference sample of nickel. J. Res. Natl. Inst. Stand. Technol. 94, 347. https://doi.org/10.6028/jres.094.034

Grapes, R.H., 1981. Chromian epidote and zoisite in kyanite amphibolite, Southern Alps, New Zealand. Am. Mineral. 66, 974–975.

Grubb, P.L.C., 1963. Critical factors in the genesis, extent, and grade of some residual bauxite deposits. Econ. Geol. 58, 1267–1277.

Gueguen, B., Sorensen, J. V., Lalonde, S. V., Peña, J., Toner, B.M., Rouxel, O., 2018. Variable Ni isotope fractionation between Fe–oxyhydroxides and implications for the use of Ni isotopes as geochemical tracers. Chem. Geol. 481, 38–52. https://doi.org/10.1016/j.chemgeo.2018.01.023

Gueguen, B., Rouxel, O., Ponzevera, E., Bekker, A., Fouquet, Y., 2013. Nickel isotope variations in terrestrial silicate rocks and geological reference materials measured by MC-ICP-MS. Geostand. Geoanalytical Res. 37, 297–317. https://doi.org/10.1111/j.1751-908X.2013.00209.x

Guillot, S., Hattori, K., 2013. Serpentinites: Essential roles in geodynamics, arc volcanism, sustainable development, and the origin of life. Elements 9, 95–98. https://doi.org/10.2113/gselements.9.2.95

Gunnell, Y., 2003. Radiometric ages of laterites and constraints on long-term denudation rates in West Africa. Geology 31, 131–134. https://doi.org/10.1130/0091-7613(2003)031<0131:RAOLAC>2.0.CO;2

Gurgel, S.P.P., Bezerra, F.H.R., Corrêa, A.C.B., Marques, F.O., Maia, R.P., 2013. Cenozoic uplift and erosion of structural landforms in NE Brazil. Geomorphology 186, 68–84. https://doi.org/10.1016/j.geomorph.2012.12.023

Hamming, E., 1968. On laterites and latsols. Prof. Geogr. 238–241.

Han, R., Qin, L., Brown, S.T., Christensen, J.N., Beller, H.R., 2012. Differential isotopic fractionation during Cr(VI) reduction by an aquifer-derived bacterium under aerobic versus denitrifying conditions. Appl. Environ. Microbiol. 78, 2462–2464. https://doi.org/10.1128/AEM.07225-11

Hanson, B., Jones, J.H., 1998. The systematics of Cr^{3+} and Cr^{2+} partitioning between olivine andliquid in the presence of spinel. Amer. Mineral. 83, 669-684.

Harter, R.D., 1983. Effect of Soil pH on Adsorption of Lead, Copper, Zinc, and Nickel. Soil Sci. Soc. Am. J. 47, 47. https://doi.org/10.2136/sssaj1983.03615995004700010009x

Hausladen, D.M., Fendorf, S., 2017. Hexavalent chromium generation within naturally structured soils and sediments. Environ. Sci. Technol. 51, 2058–2067. https://doi.org/10.1021/acs.est.6b04039

Hayes, J.P., 1994. Analytical accuracy: a review of analyses of standards SY-2 and MRG-1 from departmental records. Curr. Res. Report 94, 117–134.

Herrington, R.J., Kinchington, M., Tavlan, M., Hunter, H., *in preparation*. The Karaçam (Adatepe) Ni-Co laterite deposit Turkey : Evidence for late, low pH fluids to generate silicate-poor goethite-dominated lateritic profiles.

Herrington, R., Mondillo, N., Boni, M., Thorne, R., Tavlan, M., 2016. Bauxite and Nickel-Cobalt Lateritic Deposits of the Tethyan Belt. Society of Economic Geologists, Inc. Special Publication 19, Chapter. 14, 349–387.

Herrington, R., Boni, M., Skarpelis, N., Large, D., 2007. Palaeoclimate, weathering and ore deposits – A European perspective. Proc. Ninth Bienn. SGA Meet.

Hill, I.G., Worden, R.H., Meighan, I.G., 2000a. Yttrium: The immobility-mobility transition during basaltic weathering. Geology 28, 923–926. https://doi.org/10.1130/0091-7613(2000)28<923:YTITDB>2.0.CO;2

Hill, I.G., Worden, R.H., Meighan, I.G., 2000b. Geochemical evolution of a palaeolaterite: The Interbasaltic formation, Northern Ireland. Chem. Geol. 166, 65–84. https://doi.org/10.1016/S0009-2541(99)00179-5

Holmden, C., Jacobson, A.D., Sageman, B.B., Hurtgen, M.T., 2016. Response of the Cr isotope proxy to Cretaceous Ocean Anoxic Event 2 in a pelagic carbonate succession from the Western Interior Seaway. Geochim. Cosmochim. Acta 186, 277–295. https://doi.org/10.1016/j.gca.2016.04.039

Honda, M., Imamura, M., 1971. Half-Life of 53Mn. Phys. Rev. C 4, 1182–1188. https://doi.org/10.1103/PhysRevC.4.1182

Hongxia, Z., Zheng, D., Zuyi, T., 2006. Sorption of thorium(IV) ions on gibbsite: Effects of contact time, pH, ionic strength, concentration, phosphate and fulvic acid. Colloids Surfaces A Physicochem. Eng. Asp. 278, 46–52. https://doi.org/10.1016/j.colsurfa.2005.11.078

Horn, I., von Blanckenburg, F., Schoenberg, R., Steinhoefel, G., Markl, G., 2006. In situ iron isotope ratio determination using UV-femtosecond laser ablation with application to hydrothermal ore formation processes. Geochim. Cosmochim. Acta 70, 3677–3688. https://doi.org/10.1016/j.gca.2006.05.002

Hughes, H.S.R., McDonald, I., Faithfull, J.W., Upton, B.G.J., Loocke, M., 2016. Cobalt and precious metals in sulphides of peridotite xenoliths and inferences concerning their distribution according to geodynamic environment: A case study from the Scottish

lithospheric mantle. Lithos 240, 202–227. https://doi.org/10.1016/j.lithos.2015.11.007

IBGE, 2009. Manual Técnico de Geomorfologia, 2nd ed. Coordenação de Recursos Naturais e Estudos Ambientais, 5, 182 pp.

Imai, N., Terashima, S., Itoh, S., Ando, A., 1995. 1994 Compilation of Analytical Data for Minor and Trace Elements in Seventeen Geochemical Reference Samples, Igneous Rock Series. Geostand. Newsl. 19, 135–213. https://doi.org/10.1111/j.1751-908X.1995.tb00158.x

Impert, O., Katafias, A., Kita, P., Woroniecka, M., 2008. Kinetics of chromate (III) oxidation by hydrogen peroxide in alkaline solutions – Revisited Kinetics of Chromate (III) oxidation by hydrogen peroxide in alkaline solutions – Revisited. Polish J. Chem. 82, 1121–1126.

International, A.F.O.R., 1952. Laterite and Lateritic Soils. Commonwealth. Bur. Soil Sci. Tech. Com. 47.

Jain, J.C., Field, M.P., Neal, C.R., Ely, J.C., Sherrell, R.M., 2000. Determination of the REE in geological reference materials DTS-1 (dunite) and PCC-1 (peridotite) by ultrasonic and microconcentric desolvating nebulisation ICP-MS. J. Geostand. Geoanalysis 24, 65–72.

James, B.R., Petura, J.C., Vitale, R.J., Mussoline, G.R., 1997. Oxidation–reduction chemistry of chromium: Relevance to the regulation and remediation of chromate–contaminated soils. Soil Sediment Contam. 6, 569–580. https://doi.org/10.1080/15320389709383590

Jamieson-Hanes, J.H., Amos, R.T., Blowes, D.W., 2012. Reactive transport modelling of chromium isotope fractionation during Cr(VI) reduction. Environ. Sci. Technol. 46, 13311–13316. https://doi.org/10.1021/es3046235

Japsen, P., Bonow, J.M., Green, P.F., Cobbold, P.R., Chiossi, D., Lilletveit, R., Magnavita, L.P., Pedreira, A., 2012. Episodic burial and exhumation in NE Brazil after opening of the South Atlantic. Bull. Geol. Soc. Am. 124, 800–816. https://doi.org/10.1130/B30515.1

Jochum, K.P., Nohl, U., Herwig, K., Lammel, E., Stoll, B., Hofmann, A.W., 2005. GeoReM: a new geochemical database for reference materials and isotopic standards. Geostand. Geoanal. Res. 29, 333–338.

Joshi, S., Wang, D.T., Ellis, A. S., Johnson, T.M., Bullen, T.D., 2011. Stable isotope fractionation during Cr(III) oxidation by manganese oxides. AGU Fall Meeting, Abstract ID EP41B-0622.

Kaczmarek, M.A., Müntener, O., Rubatto, D., 2008. Trace element chemistry and U–Pb dating of zircons from oceanic gabbros and their relationship with whole rock composition (Lanzo, Italian Alps). Contrib. to Mineral. Petrol. 155, 295–312. https://doi.org/10.1007/s00410-007-0243-3

Karaoğlu, N., Gümüş, A., 1997. Origin of iron–opal–chalcedony deposits near Sivrihisar, Turkey in: Papunen et al. 1997 (eds.), Mineral Deposits: Research and Exploration, Where Do They Meet, Proceedings of the Fourth Biennial SGA Meeting, Turku, Finland, Balkema, Rotterdam, 729–732.

Kastner, M., Keene, J.B., Gieskes, J.M., 1977. Diagenesis of siliceous oozes-I. Chemical controls on the rate of opal-A to opal-CT transformation-an experimental study. Geochim. Cosmochim. Acta 41, 1041–1059. https://doi.org/10.1016/0016-7037(77)90099-0

Katz, S.A., Salem, H., 1993. The toxicology of chromium with respect to its chemical speciation: A review. J. Appl. Toxicol. 13, 217–224. https://doi.org/10.1002/jat.2550130314

Kaya, O., Ünay, E., Saraç, G., Eichhorn, S., Hassenruck, S., Knappe, A., Pekdeğer, A., Mayda, S., 2004. Halitpafla Transpressive Zone : Implications for an Early Pliocene Compressional Phase in Central Western. Turkish J. Earth Sci. 13, 1–13.

Khan, N., Jeong, I.S., Hwang, I.M., Kim, J.S., Choi, S.H., Nho, E.Y., Choi, Kwak, B.-M., Ahn, J.-H., Yoon, T., Kim, K.S., 2013. Method validation for simultaneous determination of chromium, molybdenum and selenium in infant formulas by ICP-OES and ICP-MS. Food. Chem. 141, 3566-3570.

Kierczak, J., Pedziwiatr, A., Waroszewski, J., Modelska, M., 2016. Mobility of Ni, Cr and Co in serpentine soils derived on various ultrabasic bedrocks under temperate climate. Geoderma 268, 78–91. https://doi.org/10.1016/j.geoderma.2016.01.025

Kimbrough, D.E., Cohen, Y., Winer, A.M., Creelman, L., Mabuni, C., 1999. A Critical Assessment of Chromium in the Environment. Crit. Rev. Environ. Sci. Technol. 29, 1–46. https://doi.org/10.1080/10643389991259164

King, L.C., 1956. A gemorphologia do Brasil oriental. Revista Brasileira de Geografia. Rio de Janeiro, 18, 147–265.

Kitchen, J.W., Johnson, T.M., Bullen, T.D., Zhu, J., Raddatz, A., 2012. Chromium isotope fractionation factors for reduction of Cr(VI) by aqueous Fe(II) and organic molecules. Geochim. Cosmochim. Acta 89, 190–201. https://doi.org/10.1016/j.gca.2012.04.049

Knoblowitz M., Morrow J.I., 1976. Kinetic study of an intermediate present in the hydrogen peroxide oxidation of chromium (III) to chromium (VI). Inorg. Chem. 15, 1674−1677.

Konhauser, K.O., Lalonde, S. V., Planavsky, N.J., Pecoits, E., Lyons, T.W., Mojzsis, S.J., Rouxel, O.J., Barley, M.E., Rosìere, C., Fralick, P.W., Kump, L.R., Bekker, A., 2011. Aerobic bacterial pyrite oxidation and acid rock drainage during the Great Oxidation Event. Nature

478, 369–373.
https://doi.org/10.1038/nature10511

Kuck, P.H., 2010. Nickel. In: U.S. Geological Survey; Mineral Commodity Summaries.

Kynicky, J., Smith, M.P., Xu, C., 2012. Diversity of rare earth deposits: The key example of China. Elements 8, 361–367.
https://doi.org/10.2113/gselements.8.5.361

Lacinska, A.M., Styles, M.T., 2013. Silicified serpentinite – A residuum of a Tertiary palaeo–weathering surface in the United Arab Emirates. Geol. Mag. 150, 385–395.
https://doi.org/10.1017/S0016756812000325

Larsen, K.K., Wielandt, D., Schiller, M., Bizzarro, M., 2016. Chromatographic speciation of Cr(III)-species, inter-species equilibrium isotope fractionation and improved chemical purification strategies for high-precision isotope analysis. J. Chromatogr. A 1443, 162–174.
https://doi.org/10.1016/j.chroma.2016.03.040

Leblanc, M., 1986. Co–Ni arsenide deposits, with accessory gold, in ultramafic rocks from Morocco. Can. J. Earth Sci. 23, 1592–1602.
https://doi.org/10.1139/e86-149

Lee, B.D., Graham, R.C., Laurent, T.E., Amrhein, C., 2004. Pedogenesis in a wetland meadow and surrounding serpentinitic landslide terrain, northern California, USA. Geoderma 118, 303–320.
https://doi.org/10.1016/S0016-7061(03)00214-3

Lima, M. da G., 2008. Centro de Ciências Exatas e da Terra – A História do Intemperismo na Província Borborema Oriental, Nordeste do Brasil Impl. Cent. Ciências Exatas e da Terra PhD, 251 pp.

Losi, M.E., Amrhein, C., Frankenberger, W.T., 1994. Factors affecting chemical and biological reduction of hexavalent chromium in soil. Environ. Toxicol. Chem. 13, 1727–1735.
https://doi.org/10.1002/etc.5620131103

Louise Jeffery, M., Poulsen, C.J., Ehlers, T.A., 2012. Impacts of Cenozoic global cooling, surface uplift, and an inland seaway on South American paleoclimate and precipitation $\delta^{18}O$. Bull. Geol. Soc. Am. 124, 335–351.
https://doi.org/10.1130/B30480.1

Lovering, T.S., 1959. Significance of accumulator plants in rock weathering. Geol. Soc. Am. Bull. 70, 781–800.
https://doi.org/10.1130/0016-7606(1959)70

Mackenzie F.T., Gees R., 1971. Quartz: Synthesis at earth surface conditions. Science 173, 533–535.

MacLean, W.H., Bonavia, F.F., Sanna, G., 1997. Argillite debris converted to bauxite during karst weathering: evidence from immobile element geochemistry at the Olmedo Deposit, Sardinia. Miner. Depos. 32, 607–616. https://doi.org/10.1007/s001260050126

Marker, A., Friedrich, G., Carvalho, A., Melfi, A., 1991. Control of the distribution of Mn, Co, Zn, Zr, Ti and REEs during the evolution of lateritic covers above ultramafic complexes. J. Geochemical Explor. 40, 361–383. https://doi.org/10.1016/0375-6742(91)90048-Y

Marsh, E.E., Anderson, E.D., 2011. Ni–Co laterite deposits: U.S. Geological Survey Open File Report 2011, 1259–1268.

Martin, S., Foulonneau, M., Turki, S., Ihadjadene, M., 2013. Open Data: Barriers, risks and opportunities. Proc. Eur. Conf. e-Government, ECEG 37, 301–309. https://doi.org/10.1088/1751-8113/44/8/085201

Matos, R.M.D., 1992. The Northeast Brazil rift system. Tectonics 11, 766–791.

Maynard, J.B., 1992. Chemistry of modern soils as a guide to interpreting Precambrian paleosols. J. Geol. 100, 279-289. J. Geol. 100, 279–289. https://doi.org/10.1086/629632

McAlister, J.J., Smith, B.J., 1997. Geochemical trends in Early Tertiary palaeosols from northeast Ireland: a statistical approach to assess element behaviour during weathering. Geol. Soc. London, Spec. Publ. 120, 57–65. https://doi.org/10.1144/GSL.SP.1997.120.01.05

McClain, C.N., Maher, K., 2016. Chromium fluxes and speciation in ultramafic catchments and global rivers. Chem. Geol. 426, 135–157. https://doi.org/10.1016/j.chemgeo.2016.01.021

McDonough, W.F., Sun, S.-S., 1995. The chemical composition of the Earth. Chem. Geol. 120, 223–253. https://doi.org/10.1016/0012-821X(95)00123-T

McLennan, S.M., Xiao, G., 1998. Composition of the upper continental crust revisited: insights from sedimentary rocks. Mineral. Mag. 62A, 983–984. https://doi.org/10.1180/minmag.1998.62A.2.182

Melfi, A.J., Trescases, J.J., Carvalho, A., Barros De Oliveira, S.M., Ribeiro Filho, E., Laquintine Formoso, M.L., 1988. The lateritic ore deposits of Brazil. Sci. Geol. Bull. 41, 5–36.

Merlini, A., Giovanni, G., Valeria, D., 2009. Ferritchromite and chromian–chlorite formation in mélange–hosted Kalkan chromitite (Southern Urals, Russia). Am. Mineral. 94, 1459–1467. https://doi.org/10.2138/am.2009.3082

Middelburg, J.J., van der Weijden, C.H., Woittiez, J.R.W., 1988. Chemical processes affecting the mobility of major, minor and trace elements during weathering of granitic rocks. Chem. Geol. 68, 253–273. https://doi.org/10.1016/0009-2541(88)90025-3

Milliot, G. Bonifas, M., 1955. Transformations isovolumétriques dans les phénomènes de latéritisation et de bauxitisation. Bull. Serv. Carte Geol. Als. Lorr. 8, 3–20.

Mohan, D., Pittman, C.U., 2006. Activated carbons and low cost adsorbents for remediation of tri– and hexavalent chromium from water. J. Hazard. Mater. 137, 762–811. https://doi.org/10.1016/j.jhazmat.2006.06.060

Moody, J.B., 1976. Serpentinization: a review. Lithos 125–138. https://doi.org/10.1016/0024-4937(76)90030-X

Morrey, D.R., Balkwill, K., Balkwill, M.-J., Williamson, S. 1992. A review of some studies of the serpentine flora of Southern Africa. In R.D. Reeves, Ed. The Vegetation of Ultramafic (Serpentine) Soils, p. 147–157.

Mücke, A., Raphael Cabral, A., 2005. Redox and non–redox reactions of magnetite and hematite in rocks. Chemie der Erde 65, 271–278. https://doi.org/10.1016/j.chemer.2005.01.002

Mudd, G.M., 2010. Global trends and environmental issues in nickel mining: Sulfides versus laterites. Ore Geol. Rev. 38, 9–26. https://doi.org/10.1016/j.oregeorev.2010.05.003

Mudd, G.M., 2009. Nickel Sulfide versus Laterite: The Hard Sustainability Challenge Remains. 48th Conf. Metall. 1–10.

Mukherjee, R., Mondal, S.K., Frei, R., Rosing, M.T., Waight, T.E., Zhong, H., Kumar, G.R.R., 2012. The 3.1 Ga Nuggihalli chromite deposits, Western Dharwar craton (India): Geochemical and isotopic constraints on mantle sources, crustal evolution and implications for supercontinent formation and ore mineralization. Lithos 155, 392–409. https://doi.org/10.1016/j.lithos.2012.10.001

Nag, N.G., 2004. Final Summary of Research Report to the National Aeronautics and Space Administration Cosmochemistry Program. NASA Grant NAG541912 1–5.

Nahon D.B., 1986. Evolution of iron crusts in tropical landscapes. In Rates of Chemical Weathering in Rocks and Minerals (eds. Coleman, S.M., Dethier, D.P.), 169–192.

Nakayama, E., Kuwamoto, T., Tsurubo, S., Fujinaga, T., 1985. Speciation of chromium in sea water. Part 2 effects of manganese oxides and reducible organic materials on the redox processes of chromium. Anal. Chim. Acta 175, 147–151. https://doi.org/10.1016/S0003-2670(00)82726-9

Nesbitt, H.W., Wilson, R.E., 1992. Recent Chemical Weathering of Basalts. Am. J. Sci. 292, 740–777.

Nesbitt, H.W., Young, G.M., 1982. Early Proterozoic climates and plate motions inferred from major element chemistry of lutites. Nature. https://doi.org/10.1038/299715a0

Nesbitt, H.W., Markovics, G., Price, R.C., 1980. Chemical processes affecting alkalis and alkaline earths during continental weathering. Geochim. Cosmochim. Acta 44, 1689–1666. https://doi.org/10.5710/AMGH.02.02.2016.2971

Nesbitt H. W., 1979. Mobility and fractionation of rare earth elements during weathering of a granodiorite. Nature 279, 206–210.

Ningthoujam, P.S., Dubey, C.S., Guillot, S., Fagion, A.S., Shukla, D.P., 2012. Origin and serpentinization of ultramafic rocks of Manipur Ophiolite Complex in the Indo-Myanmar subduction zone, Northeast India. J. Asian Earth Sci. 50, 128–140. https://doi.org/10.1016/j.jseaes.2012.01.004

Nriagu, J.O., Nieboer, E., 1988. Chromium in the natural and human environments. Wiley–Interscience, New York.

Norton, S.A., 1973. Laterite and bauxite formation. Econ. Geol. 68, 353–361.

Novak, M., Kram, P., Sebek, O., Andronikov, A., Chrastny, V., Martinkova, E., Stepanova, M., Prechova, E., Curik, J., Veselovsky, F., Myska, O., Stedra, V., Farkas, J., 2017. Temporal changes in Cr fluxes and δ^{53}Cr values in runoff from a small serpentinite catchment (Slavkov Forest, Czech Republic). Chem. Geol. 472, 22–30. https://doi.org/10.1016/j.chemgeo.2017.09.023

Odom, I.E., 1984. Smectite clay Minerals: Properties and Uses. Philos. Trans. R. Soc. A Math. Phys. Eng. Sci. 311, 391–409. https://doi.org/10.1098/rsta.1984.0036

Oh, N.H., Richter, D.D., 2005. Elemental translocation and loss from three highly weathered soil-bedrock profiles in the southeastern United States. Geoderma 126, 5–25. https://doi.org/10.1016/j.geoderma.2004.11.005

Okay, A.I., 2011. Tavşanlı Zonu: Antolid–Torid Bloku`nun dalma–batmaya uğramış kuzey ucu: Maden Tetkik ve Arama Dergisi, MTA Dergisi, 142, 195–226.

Okay, A.I., Tansel, İ., Tüysüz, O., 2001. Obduction, subduction and collision as reflected in the Upper Cretaceous – Lower Eocene sedimentary record of western Turkey. Geol. Mag. 138, 117–142.

Olesik, J.W., 1991. Elemental analysis using ICP-OES and ICP/MS. An Evaluation and Assessment of Remaining Problems. Anal. Chem. 63, 12-21.

Önen, A.P., Hall, R., 2000. Sub–ophiolite metamorphic rocks from NW Anatolia, Turkey. J. Metamorph. Geol. 18, 483–495. https://doi.org/10.1046/j.1525-1314.2000.00276.x

Ottonello, G., Zuccolini, M.V., 2005. Ab–initio structure, energy and stable Cr isotopes equilibrium fractionation of some geochemically relevant H–O–Cr–Cl complexes. Geochim. Cosmochim. Acta 69, 851–874. https://doi.org/10.1016/j.gca.2004.06.045

Oxley, A., Smith, M.E., Caceres, O., 2016. Why heap leach nickel laterites? Miner. Eng. 88, 53–60. https://doi.org/10.1016/j.mineng.2015.09.018

Oxley, A., Smith, M.E., 2013. The Best Nickel Laterite Heap Leach in the World.

Oze, C., Bird, D.K., Fendorf, S., 2007. Genesis of hexavalent chromium from natural sources in soil and groundwater. PNAS 104, 6544–6549. https://doi.org/https://doi.org/10.1073/pnas.0701085104

Oze, C., 2004. Chromium geochemistry in serpentinized ultramafic rocks and serpentine soils from the Franciscan complex of California. Am. J. Sci. 304, 67–101. https://doi.org/10.2475/ajs.304.1.67

Oze, C., Fendorf, S., Bird, D.K., Coleman, R.G., 2004. Chromium Geochemistry of Serpentine Soils. Int. Geol. Rev. 46, 97–126. https://doi.org/10.2747/0020-6814.46.2.97

Oze, C., 2003. Chromium geochemistry of serpentinites and serpentine soils. PhD Thesis, Stanford University.

Palmer, C.D., Puls, R.W., 1994. EPA Ground Water Issue: Natural Attenuation of Hexavalent Chromium in Groundwater and Soils, EPA.

Park, A.H.A., Fan, L.S., 2004. CO_2 mineral sequestration: Physically activated dissolution of serpentine and pH swing process. Chem. Eng. Sci. 59, 5241–5247. https://doi.org/10.1016/j.ces.2004.09.008

Paton, T.R., Williams, M.A.J., 1972. The concept of laterite. Ann. Assoc. Am. Geogr. 62, 42–56.

Patterson, R.R., Fendorf, S., Fendorf, M., 1997. Reduction of hexavalent chromium by amorphous iron sulfide. Environ. Sci. Technol. 31, 2039–2044. https://doi.org/10.1021/es960836v

Paulukat, C., Døssing, L.N., Mondal, S.K., Voegelin, A.R., Frei, R., 2015. Oxidative release of chromium from Archean ultramafic rocks, its transport and environmental impact – A Cr isotope perspective on the Sukinda valley ore district (Orissa, India). Appl. Geochemistry 59, 125–138. https://doi.org/10.1016/j.apgeochem.2015.04.016

Peacock, C.L., Sherman, D.M., 2007. Sorption of Ni by birnessite: Equilibrium controls on Ni in seawater. Chem. Geol. 238, 94–106. https://doi.org/10.1016/j.chemgeo.2006.10.019

Pearce, J.A., 2014. Immobile element fingerprinting of ophiolites. Elements 10, 101–108. https://doi.org/10.2113/gselements.10.2.101

Peek, E., Åkre, T., Asselin, E., 2009. Technical and Business Considerations of Cobalt Hydrometallurgy. JOM. 61, 43-53.

Pelleter, E., Fouquet, Y., Etoubleau, J., Cheron, S., Labanieh, S., Josso, P., Bollinger, C., Langlade, J., 2017. Ni–Cu–Co–rich hydrothermal manganese mineralization in the Wallis and Futuna back–arc environment (SW Pacific). Ore Geol. Rev. 87, 126–146. https://doi.org/10.1016/j.oregeorev.2016.09.014

Peltier, L.C., 1950. The Geographic Cycle in Periglacial Regions as It is Related to Climatic Geomorphology. Annals of the Association of American Geographers, 40, 214–236.

Peralta-Videa, J.R., Lopez, M.L., Narayan, M., Saupe, G., Gardea-Torresdey, J., 2009. The biochemistry of environmental heavy metal uptake by plants: Implications for the food chain. Int. J. Biochem. Cell Biol. 41, 1665–1677. https://doi.org/10.1016/j.biocel.2009.03.005

Peterson, L.C., Haug, G.H., 2006. Variability in the mean latitude of the Atlantic Intertropical Convergence Zone as recorded by riverine input of sediments to the Cariaco Basin (Venezuela). Palaeogeogr. Palaeoclimatol. Palaeoecol. 234, 97–113. https://doi.org/10.1016/j.palaeo.2005.10.021

Peulvast, J.-P., Claudino Sales, V., Bétard, F., Gunnell, Y., 2008. Low post–Cenomanian denudation depths across the Brazilian Northeast: Implications for long–term landscape evolution at a transform continental margin. Glob. Planet. Change 62, 39–60. https://doi.org/10.1016/j.gloplacha.2007.11.005

Peulvast, J.-P., Sales, V.C., Bezerra, F.H.R., Betard, F., 2006. Landforms and Neotectonics in the Equatorial Passive Margin of Brazil. Geodin. Acta 19, 51–71. https://doi.org/10.3166/ga.19.51-71

Planavsky, N.J., Reinhard, C.T., Wang, X., Thomson, D., McGoldrick, P., Rainbird, R.H., Johnson, T., Fischer, W.W., Lyons, T.W., 2014. Low mid–proterozoic atmospheric oxygen levels and

the delayed rise of animals. Science 346, 635–638. https://doi.org/10.1126/science.1258410

Prescott, J.A., Pendleton, R.L., 1952. Laterite and lateritic soils. Commonw. Bur. Soil Sci. Tech. Com. 47 pp.

Pope, G.A., Meierding, T.C., Paradise, T.R., 2002. Geomorphology's role in the study of weathering of cultural stone. Geomorphology 47, 211–225. https://doi.org/10.1016/S0169-555X(02)00098-3

Post, J.E., 1999. Manganese oxide minerals: Crystal structures and economic and environmental significance. Proc. Natl. Acad. Sci. 96, 3447–3454. https://doi.org/10.1073/pnas.96.7.3447

Price, R.C., Gray, C.M., Wilson, R.E., Frey, F.A., Taylor, S.R., 1991. The effects of weathering on rare–earth element, Y and Ba abundances in Tertiary basalts from southeastern Australia. Chem. Geol. 93, 245–265. https://doi.org/10.1016/0009-2541(91)90117-A

Prider, R.T., 1970. Nickel in Western Australia. Nature 226, 691–693.

Qin, L., Wang, X., 2017. Chromium Isotope Geochemistry. Rev. Mineral. Geochemistry 82, 379–414. https://doi.org/10.2138/rmg.2017.82.10

Qin, L., Carlson, R.W., Alexander, C.M.O.D., 2011. Correlated nucleosynthetic isotopic variability in Cr, Sr, Ba, Sm, Nd and Hf in Murchison and QUE 97008. Geochim. Cosmochim. Acta 75, 7806–7828. https://doi.org/10.1016/j.gca.2011.10.009

Quitté, G., Oberli, F., 2006. Quantitative extraction and high precision isotope measurements of nickel by MC-ICPMS. J. Anal. At. Spectrom. 21, 1249–1255. https://doi.org/10.1039/b607569j

Ramos, R.P.L., 1975. Precipitation characteristics in the Northeast Brazil dry region. J. Geophys. Res. 80, 1665–1678. https://doi.org/10.1029/JC080i012p01665

Rasmussen, C., Dahlgren, R.A., Southard, R.J., 2010. Basalt weathering and pedogenesis across an environmental gradient in the southern Cascade Range, California, USA. Geoderma 154, 473–485. https://doi.org/10.1016/j.geoderma.2009.05.019

Ratié, G., Garnier, J., Calmels, D., Vantelon, D., Guimaraes, E., Monvoisin, G., Nouet, J., Ponzevera, E., Quantin, C., 2018. Nickel distribution and isotopic fractionation in a Brazilian lateritic regolith: coupling Ni isotopes and Ni K-edge XANES. Geochim.

Cosmochim. Acta.
https://doi.org/10.1016/j.gca.2018.03.026

Ratié, G., Jouvin, D., Garnier, J., Rouxel, O., Miska, S., Guimarães, E., Cruz Vieira, L., Sivry, Y., Zelano, I., Montarges-Pelletier, E., Thil, F., Quantin, C., 2015. Nickel isotope fractionation during tropical weathering of ultramafic rocks. Chem. Geol. 402, 68–76.
https://doi.org/10.1016/j.chemgeo.2015.02.039

Rauch, J.N., Pacyna, J.M., 2009. Earth's global Ag, Al, Cr, Cu, Fe, Ni, Pb, and Zn cycles. Global Biogeochem. Cycles 23, 1–16.
https://doi.org/10.1029/2008GB003376

Reagan, M.K., Meijer, A.I., 1984. Geology and geochemistry of early arc-volcanic rocks from Guam. Geol. Soc. Am. Bull. 95, 701–713.
https://doi.org/10.1130/0016-7606(1984)95<701:GAGOEA>2.0.CO;2

Reiller, P., Moulin, V., Casanova, F., Dautel, C., 2002. Retention behaviour of humic substances onto mineral surfaces and consequences upon thorium (IV) mobility: Case of iron oxides. Appl. Geochemistry 17, 1551–1562.
https://doi.org/10.1016/S0883-2927(02)00045-8

Reinhard, C.T., Planavsky, N.J., Wang, X., Fischer, W.W., Johnson, T.M., Lyons, T.W., 2014. The isotopic composition of authigenic chromium in anoxic marine sediments: A case study from the Cariaco Basin. Earth Planet. Sci. Lett. 407, 9–18.
https://doi.org/10.1016/j.epsl.2014.09.024

Reinhard, C.T., Planavsky, N.J., Robbins, L.J., Partin, C.A., Gill, B.C., Lalonde, S. V., Bekker, A., Konhauser, K.O., Lyons, T.W., 2013. Proterozoic ocean redox and biogeochemical stasis. Proc. Natl. Acad. Sci. 110, 5357–5362.
https://doi.org/10.1073/pnas.1208622110

Retallack, G.J., 2010. Lateritization and bauxitization events. Econ. Geol. 105, 655–667.
https://doi.org/10.2113/gsecongeo.105.3.655

Richard, F.C., Bourg, A.C.M., 1991. Aqueous geochemistry of chromium: A review. Water Res. 25, 807–816.
https://doi.org/10.1016/0043-1354(91)90160-R

Righter, K., Campbell, A.J., Humayun, M., Hervig, R. L., 2003. Partitioning of Ru, Rh, Pd, Re, Ir, and Au between Cr-bearing spinel, olivine, pyroxene and silicate melts. Geochim. Cosmochim. Acta, 68, 867-880.
doi:10.1016/j.gca.2003.07.005

Roberts, B.A., Proctor, J., 1992. The Ecology of Areas with Serpentinized Rocks. A World View. Kluwer Academic Publication, Netherlands.

Robin-Popieul, C.C.M., Arndt, N.T., Chauvel, C., Byerly, G.R., Sobolev, A. V, Wilson, A., 2012. A New Model for Barberton Komatiites : Deep Critical Melting with High Melt Retention 53. https://doi.org/10.1093/petrology/egs042

Robinson, G.R., 1997. Portaying chemical properties of bedrock for water quality and ecosystem analysis: an approach for the New England region. USGS Open-File Rep. 97–154.

Rosman, K.J.R., Taylor, P.D.P., 1998. Isotopic compositions of the elements 1997. J. Phys. Chem. Ref. Data 27, 1275–1287. https://doi.org/10.1063/1.556031

Ross, J.L.S., 2013. Brasilian Relief: Structures and Forms. Rev. do Dep. Geogr. 25, 20–36. https://doi.org/10.7154/RDG.2013.0025.0002

Rotaru, M., Birck, J.L., Allègre, C.J., 1992. Clues to early Solar System history from chromium isotopes in carbonaceous chondrites. Nature 358, 465–470. https://doi.org/10.1038/358465a0

Rye, R., Holland, H.D., 1998. Paleosols and the evolution of atmospheric oxygen: A critical review. Am. J. Sci. https://doi.org/10.2475/ajs.298.8.621

Salemi, E., Tessari, U., Colombani, N., Mastrocicco, M., 2010. Applied Clay Science Improved gravitational grain size separation method. Appl. Clay Sci. 48, 612–614. https://doi.org/10.1016/j.clay.2010.03.014

Salgado, S.S., Ferreira Filho, C.F., Caxito, F. de A., Uhlein, A., Dantas, E.L., Stevenson, R., 2016. The Ni–Cu–PGE mineralized Brejo Seco mafic-ultramafic layered intrusion, Riacho do Pontal Orogen: Onset of Tonian (ca. 900 Ma) continental rifting in Northeast Brazil. J. South Am. Earth Sci. 70, 324–339. https://doi.org/10.1016/j.jsames.2016.06.001

Salgado, S.S., Fonseca, C., Filho, F., Uhlein, A., 2014. Geologia, Estratigrafia E Petrografia Do Complexo De Brejo Seco, Faixa Riacho Do Pontal, Sudeste Do Piauí. Geonomos 22, 10–21.

Salgado, S.S., 2014. Geologia , Contexto Geotectônico e Potencial Metalogenético para Depósitos de Ni–Cu– (EGP) do Complexo máfico–ultramáfico de Brejo Seco, Faixa Riacho do Pontal , Sudeste do Piauí Geologia , Contexto Geotectônico e Potencial Metalogenético para Depósit. PhD Thesis, Universidade Federal de Minas Gerais.

Sanematsu, K., Moriyama, T., Sotouky, L., Watanabe, Y., 2011. Mobility of Rare Earth Elements in Basalt-Derived Laterite at the Bolaven Plateau, Southern Laos. Resour. Geol. 61, 140–158. https://doi.org/10.1111/j.1751-3928.2011.00155.x

Schandl, E.S., Wicks, F.J., 1993. Carbonate and associated alteration of ultramafic and rhyolitic rocks at the Hemingway Property, Kidd Creek volcanic complex, Timmins, Ontario. Econ. Geol. 88, 1615–1635. https://doi.org/10.2113/gsecongeo.88.6.1615

Schauble, E., Rossman, G.R., Taylor, H.P., 2004. Theoretical estimates of equilibrium chromium-isotope fractionations. Chem. Geol. 205, 99–114. https://doi.org/10.1016/j.chemgeo.2003.12.015

Scheiderich, K., Amini, M., Holmden, C., Francois, R., 2015. Global variability of chromium isotopes in seawater demonstrated by Pacific, Atlantic, and Arctic Ocean samples. Earth Planet. Sci. Lett. 423, 87–97. https://doi.org/10.1016/j.epsl.2015.04.030

Schellmann, W., 1994. Geochemical differentiation in laterite and bauxite formation. Catena 21, 131–143. https://doi.org/10.1016/0341-8162(94)90007-8

Schellmann, W., 1989. Allochthonous surface alteration of Ni–laterites. Chem. Geol. 74, 351–364. https://doi.org/10.1016/0009-2541(89)90044-2

Schellmann, W., 1986. On the geochemistry of laterites. Chem. Erde 45, 39–52.

Schellmann, W., 1983. Geochemical principles of lateritic nickel ore formation. In proceedings of the International Sem. Lateritization Processes (eds. Melfi, A.J., Carvalho, A.), 119–135. Univ. Sao Paulo.

Schellmann, W., 1982. Eine neue Lateritdefinition. Geol. Jahrb., Reihe D, 58: 31–47.

Schellmann, W., 1981. Considerations on the definition and classification of laterites. Proceedings of the International Seminar on Lateritisation Processes, IGCP 129 and IAGC, Trivandrum, India. Oxford and IBH Publishing Company, New Delhi, 1–10.

Schnebele, E.K., 2017. Nickel. USGS Miner. Commod. Summ. 114–115.

Schobbenhaus, C., 1976. Carta geológica do Brasil ao milionésimo. Folha Aracaju, SC. 24. D.N.P.M., Brasilia, 226 pp.

Schoenberg, R., Merdian, A., Holmden, C., Kleinhanns, I.C., Haßler, K., Wille, M., Reitter, E., 2016. The stable Cr isotopic compositions of chondrites and silicate planetary reservoirs. Geochim. Cosmochim. Acta 183, 14–30. https://doi.org/10.1016/j.gca.2016.03.013

Schoenberg, R., Zink, S., Staubwasser, M., von Blanckenburg, F., 2008. The stable Cr isotope inventory of solid Earth reservoirs determined by double spike MC-ICP-MS. Chem. Geol. 249, 294–306. https://doi.org/10.1016/j.chemgeo.2008.01.009

Schorin, H., Puchelt, H., 1987. Geochemistry of a ferruginous bauxite profile from southeast Venezuela. Chem. Geol. 64, 127–142.

Schroeder, P.A., Le Golvan, J.J., Roden, M.F., 2002. Weathering of ilmenite from granite and chlorite schist in the Georgia Piedmont. Am. Mineral. 87, 1616–1625. https://doi.org/10.2138/am-2002-11-1211

Seco, F., Hennig, C., De Pablo, J., Rovira, M., Rojo, I., Martí, V., Giménez, J., Duro, L., Grivé, M., Bruno, J., 2009. Sorption of Th(IV) onto iron corrosion products: Exafs study. Environ. Sci. Technol. 43, 2825–2830. https://doi.org/10.1021/es803608a

Sedlak, D.L., Chan, P.G., 1997. Reduction of hexavalent chromium by ferrous iron. Geochim. Cosmochim. Acta 61, 2185–2192. https://doi.org/10.1016/S0016-7037(97)00077-X

Shaver, J.P., 1993. What statistical significance testing is, and what it is not. J. Exp. Educ. 61, 293–316. https://doi.org/10.1080/00220973.1993.10806592

Shen, J., Liu, J., Qin, L., Wang, S.J., Li, S., Xia, J., Ke, S., Yang, J., 2015. Chromium isotope signature during continental crust subduction recorded in metamorphic rocks. Geochemistry, Geophys. Geosystems 16, 3840–3854. https://doi.org/10.1002/2015GC005944

Shields, W.R., Murphy, T.J., Catanzaro, E.J., Garner, E., 1966. Absolute Isotopic Abundance Ratios and the Atomic Weight of a Reference Sample of Chromium. J. Res. Natl. Bur. Stand. A. Phys. Chem. 70A, 193–197.

Shiraki, K., 1997. Geochemical Behaviour of Chromium. Resour. Geol. 47, 319–330.

Siivola, J., Schmid, R., 2007. List of Mineral abbreviations. IUGS Subcomm. Syst. Metamorph. Rocks 1–14.

Šillerová, H., Chrastný, V., Čadková, E., Komárek, M., 2014. Isotope fractionation and spectroscopic analysis as an evidence of Cr(VI) reduction during biosorption. Chemosphere 95, 402–407. https://doi.org/10.1016/j.chemosphere.2013.09.054

Silvester, E., Charlet, L., Manceau, A., 1995. Mechanism of Chromium(III) Oxidation by Na-Buserite. J. Phys. Chem. 99, 16662–16669.

Skiggs, T.J., 2017. Formation and evolution of the São João do Piauí Ni laterite deposit. MSci Thesis, University of Southampton.

Som, S.K., Joshi, R., 2002. Chemical weathering of serpentinite and Ni enrichment in Fe oxide at Sukinda area, Jajpur district, Orissa, India. Econ. Geol. 97, 165–172. https://doi.org/10.2113/gsecongeo.97.1.165

Spivak-Birndorf, L.J., Wang, S.J., Bish, D.L., Wasylenki, L.E., 2018. Nickel isotope fractionation during continental weathering. Chem. Geol. 476, 316–326. https://doi.org/10.1016/j.chemgeo.2017.11.028

Stebbins, J.F., Carmichael, I.S.E., Moret, L.K., 1984. Heat capacities and entropies of silicate liquids and glasses. Contrib. Mineral. Petrol., 86, 131–148.

Stephens, C.G., 1971. Laterite and silcrete in Australia: A study of the genetic relationships of laterite and silcrete and their companion materials, and their collective significance in the formation of the weathered mantle, soils, relief and drainage of the Australian continent. Geoderma 5, 5–52. https://doi.org/10.1016/0016-7061(71)90023-1

Stueber, A.M., Goles, G.G., 1967. Abundances of Na, Mn, Cr, Sc and Co in ultramafic rocks. Geochim. Cosmochim. Acta 31, 75–93. https://doi.org/10.1016/0016-7037(67)90099-3

Su, B.X., Qin, K.Z., Sun, H., Tang, D.M., Sakyi, P.A., Chu, Z.Y., Liu, P.P., Xiao, Q.H., 2012. Subduction-induced mantle heterogeneity beneath Eastern Tianshan and Beishan: Insights from Nd–Sr–Hf–O isotopic mapping of Late Paleozoic mafic–ultramafic complexes. Lithos 134, 41–51. https://doi.org/10.1016/j.lithos.2011.12.011

Tandarich, J.P., Darmody, R.G., Follmer, L.R., 1994. The pedo–weathering profile: A paradigm for whole-regolith pedology from the glaciated midcontinental United States of America. SSSASP 34, 97–117.

Tardy, Y., 1993. Pétrologie des latérites et des sols tropicaux. Paris. Masson, 1993, 459 pp.

Tardy, Y., Mazaltarim, D., Boeglin, J.-L., Roquin, C., Pion, J.-C., Paquet, H., Milliot, G., 1988. Lithodépendance et homogénéisation de la composition minéralogique et chimique des cruirasses ferrugineuses latéritiques. Comptes rendus l'Académie des Sci. Série 2, Mécanique, Phys. Chim. Sci. l'univers, Sci. la Terre 307, 1765–1772.

Tardy, Y., Nahon, D., 1985. Geochemistry of laterites, stability of Al-goethite, Al hematite, and Fe^{3+}–kaolinite in bauxites and ferricretes; an approach to the mechanism of concretion formation. Am. J. Sci. 285, 865–903.

Tavlan, M., Thorne, R., Herrington, R.J., 2011. Uplift and lateritization history of the Caldag ophiolite in the context of Neo-Tethyan ophiolite obduction and uplift : implications for the

Cenozoic weathering history of western Anatolia. J. Geol. Soc. 168, 927–940. https://doi.org/10.1144/0016-76492010-086.

Taylor, G., Eggleton, R.A., Holzhauer, C.C., Maconachie, L.A., Gordon, M., Brown, M.C., McQueen, K.G., 1992. Cool Climate Lateritic and Bauxitic Weathering. J. Geol. 100, 669–677. https://doi.org/10.1086/629620

Taylor, J.C., 1991. Computer Programs for Standardless Quantitative Analysis of Minerals Using the Full Powder Diffraction Profile. Powder Diffr. 6, 2–9. https://doi.org/10.1017/S0885715600016778

Taylor, R.M., 1984. The Rapid Formation of Crystalline Double Hydroxy Salts and Other Compounds by Controlled Hydrolysis. Clay Miner. 19, 591–603. https://doi.org/10.1180/claymin.1984.019.4.06

Tebo, B.M., Bargar, J.R., Clement, B.G., Dick, G.J., Murray, K.J., Parker, D., Verity, R., Webb, S.M., 2004. Biogenic Manganese Oxides: Properties and Mechanisms of Formation. Annu. Rev. Earth Planet. Sci. 32, 287–328. https://doi.org/10.1146/annurev.earth.32.101802.120213

Théveniaut, H., Freyssinet, P., 1999. Paleomagnetism applied to lateritic profiles to assess saprolite and duricrust formation processes: The example of Mont Baduel profile (French Guiana). Palaeogeogr. Palaeoclimatol. Palaeoecol. 148, 209–231. https://doi.org/10.1016/S0031-0182(98)00183-7

Thorne, R.L., Roberts, S., Herrington, R., 2012. Climate change and the formation of nickel laterite deposits. Geology 40, 331–334. https://doi.org/10.1130/G32549.1

Thorne, R.L., 2011. Nickel Laterites, Origin and Climate. PhD Thesis, University of Southampton.

Thorne, R., Herrington, R., Roberts, S., 2009. Composition and origin of the Çaldağ oxide nickel laterite, W. Turkey. Miner. Depos. 44, 581–595. https://doi.org/10.1007/s00126-009-0234-6

Tipping E., 1984. Temperature dependence of Mn(II)oxidation in lakewaters: a test of biological involvement. Geochim. Cosmochim. Acta. 48, 1353-1356.

Traoré, D., Beauvais, A., Chabaux, F., Peiffert, C., Parisot, J.C., Ambrosi, J.P., Colin, F., 2008. Chemical and physical transfers in an ultramafic rock weathering profile: Part 1. Supergene dissolution of Pt–bearing chromite. Am. Mineral. 93, 22–30. https://doi.org/10.2138/am.2008.2605

Treloar, P.J., 1987. The Cr–minerals of Outokumpu – Their chemistry and significance. J. Petrol. 28, 867–886. https://doi.org/10.1093/petrology/28.5.867

Trescases, J.J., Melfi, A.J., Barros De Oliveira, S.M., 1981. Nickeliferous laterites of Brazil. Lateritisation Process. Proc. Int. Semin. Trivandrum, India, 1979 170–184.

Trinquier, A., Birck, J., Allègre, C.J., 2007. Widespread ^{54}Cr Heterogeneity in the Inner Solar System. Astrophys. J. 655, 1179–1185. https://doi.org/10.1086/510360

Uren, N.C., 1992. Forms, reactions, and availability of nickel in soils. Adv. Agron. 48, 141–203. https://doi.org/10.1016/S0065-2113(08)60937-2

Urey, H., 1947. The thermodynamic properties of isotopic substances. J. Chem. Soc., 562–581.

van Baalen, M.R., 1993. Titanium mobility in metamorphic systems: a review. Chem. Geol. 110, 233–249. https://doi.org/10.1016/0009-2541(93)90256-I

van der Weijden, C.H., van der Weijden, R.D., 1995. Mobility of major, minor and some redox-sensitive trace elements and rare-earth elements during weathering of four granitoids in central Portugal. Chem. Geol. 125, 149–167. https://doi.org/10.1016/0009-2541(95)00071-S

van der Weijden, C.H., Reith, M., 1982. Chromium (III)-chromium (VI) interconversions in seawater. Mar. Chem. 11, 565–572.

Varela, M.E., Hwang, S.L., Shen, P., Chu, H.T., Yui, T.F., Iizuka, Y., Brandstätter, F., Abdu, Y.A., 2017. Olivinites in the angrite D'Orbigny: Vestiges of pristine reducing conditions during angrite formation. Geochim. Cosmochim. Acta 217, 349–364. https://doi.org/10.1016/j.gca.2017.08.027

Velbel, M.A., 1999. Bond strength and the relative weathering rates of simple orthosilicates. Am. J. Sci. 299, 679–696. https://doi.org/10.2475/ajs.299.7-9.679

Velbel, M.A., 1993. Constancy of silicate-mineral weathering-rate ratios between natural and experimental weathering: implications for hydrologic control of differences in absolute rates. Chem. Geol. 105, 89–99.

Venturelli, G., 1997. Weathering of Ultramafic Rocks and Element Mobility at Mt. Prinzera, Northern Apennines, Italy. Mineral. Mag. 61, 765–778. https://doi.org/10.1180/minmag.1997.061.409.02

Verma, S.K., Oliveira, E.P., 2015. Tectonic setting of basic igneous and metaigneous rocks of Borborema Province, Brazil using multi-dimensional geochemical discrimination diagrams. J. South Am. Earth Sci. 58, 309–317. https://doi.org/10.1016/j.jsames.2014.08.010

Villanova-de-Benavent, C., Proenza, J.A., Galí, S., García-Casco, A., Tauler, E., Lewis, J.F., Longo, F., 2014. Garnierites and garnierites: Textures, mineralogy and geochemistry of garnierites in the Falcondo Ni–laterite deposit, Dominican Republic. Ore Geol. Rev. 58, 91–109. https://doi.org/10.1016/j.oregeorev.2013.10.008

Waber, H.N., Smellie, J.A.T., 2008. Characterisation of pore water in crystalline rocks. Appl. Geochemistry 23, 1834–1861. https://doi.org/10.1016/j.apgeochem.2008.02.007

Wang, X., Planavsky, N.J., Reinhard, C.T., Zou, H., Ague, J.J., Wu, Y., Gill, B.C., Schwarzenbach, E.M., Peucker-Ehrenbrink, B., 2016. Chromium isotope fractionation during subduction–related metamorphism, black shale weathering, and hydrothermal alteration. Chem. Geol. 423, 19–33. https://doi.org/10.1016/j.chemgeo.2016.01.003

Wang, X., Johnson, T.M., Ellis, A.S., 2015. Equilibrium isotopic fractionation and isotopic exchange kinetics between Cr(III) and Cr(VI). Geochim. Cosmochim. Acta 153, 72–90. https://doi.org/10.1016/j.gca.2015.01.003

Wang, H., Wu, Y.B., Gao, S., Liu, X.C., Liu, Q., Qin, Z.W., Xie, S.W., Zhou, L., Yang, S.H., 2013. Continental origin of eclogites in the North Qinling terrane and its tectonic implications. Precambrian Res. 230, 13–30. https://doi.org/10.1016/j.precamres.2012.12.010

Wang D.T., Fregoso D.C., Ellis A.S., Johnson T.M., Bullen T.D., 2010. Stable isotope fractionation during chromium(III) oxidation by δ-MnO_2. 2010 Fall Meeting, AGU, San Francisco. Abstract ID H53F−1109.

Wanner, C., Sonnenthal, E.L., 2013. Assessing the control on the effective kinetic Cr isotope fractionation factor: A reactive transport modelling approach. Chem. Geol. 337–338, 88–98. https://doi.org/10.1016/j.chemgeo.2012.11.008

Wasylenki, L.E., Howe, H.D., Spivak-Birndorf, L.J., Bish, D.L., 2015. Ni isotope fractionation during sorption to ferrihydrite: Implications for Ni in banded iron formations. Chem. Geol. 400, 56–64. https://doi.org/10.1016/j.chemgeo.2015.02.007

Wells, M.A., Butt, C.R.M., 2006. Geology, geochemistry and mineralogy of the Murrin Murrin Nickel Laterite Deposit. Open File Rep. 207.

Wentworth, C.K., 1922. A scale of grade and class terms for clastic sediments. Journ. Geol. 30, 377–392.

Wicks, F.J., & Whittaker, E.J.W., 1977. Serpentine textures and serpentinization, Can. Mineral. 15, 459–488.

Widdowson, M., 2007. Laterite and ferricretes, In: Nash, D.J., McLaren, S.J. (Eds.), Geochemical Sediments and Landscapes, RGS-IBG Book Series, Blackwell Publishing, Oxford, 46–94.

Wille, M., Babechuk, M.G., Kleinhanns, I.C., Stegmaier, J., Suhr, N., Widdowson, M., Kamber, B.S., Schoenberg, R., 2018. Silicon and chromium stable isotopic systematics during basalt weathering and lateritisation: A comparison of variably weathered basalt profiles in the Deccan Traps, India. Geoderma 314, 190–204. https://doi.org/10.1016/j.geoderma.2017.10.051

Wilson, M.J., 2004. Weathering of the primary rock–forming minerals: processes, products and rates. Clay Miner. 39, 233–266. https://doi.org/10.1180/0009855043930133

Xia, J., Qin, L., Shen, J., Carlson, R.W., Ionov, D.A., Mock, T.D., 2017. Chromium isotope heterogeneity in the mantle. Earth Planet. Sci. Lett. 464, 103–115. https://doi.org/10.1016/j.epsl.2017.01.045

Xu, F., Ma, T., Zhou, L., Hu, Z., Shi, L., 2015. Chromium isotopic fractionation during Cr(VI) reduction by Bacillus sp. under aerobic conditions. Chemosphere 130, 46–51. https://doi.org/10.1016/j.chemosphere.2015.02.033

Xue, S., Morse, S.A., 1993. Geochemistry of the Nain massif anorthosite, labrador: Magma diversity in five intrusions. Geochim. Cosmochim. Acta 57, 3925–3948. https://doi.org/10.1016/0016-7037(93)90344-V

Yongue-Fouateu, R., Ghogomu, R.T., Penaye, J., Ekodeck, G.E., Stendal, H., Colin, F., 2006. Nickel and cobalt distribution in the laterites of the Lomié region, south-east Cameroon. J. African Earth Sci. 45, 33–47. https://doi.org/10.1016/j.jafrearsci.2006.01.003

Young, E.D., Galy, A., Nagahara, H., 2002. Kinetic and equilibrium mass-dependent isotope fractionation laws in nature and their geochemical and cosmochemical significance. Geochim. Cosmochim. Acta 66, 1095–1104. https://doi.org/10.1016/S0016-7037(01)00832-8

Zasoski, R.J., Fendorf, S.E., 1992. Chromium(III) Oxidation by Δ–Manganese Oxide (MnO_2). 1. Characterization. Environ. Sci. Technol. 26, 79–85. https://doi.org/10.1021/es00025a006

Zeissink, H.E., 1969. The mineralogy and geochemistry of a nickeliferous laterite profile (Greenvale, Queensland, Australia). Miner. Depos. 4, 132–152. https://doi.org/10.1007/BF00208049

Zheng Y., 2008. A perspective view on ultrahigh–pressure metamorphism and continental collision in the Dabie–Sulu orogenic belt. Chin. Sci. Bull. 53, 3081−3104.

Zink, S., Schoenberg, R., Staubwasser, M., 2010. Isotopic fractionation and reaction kinetics between Cr(III) and Cr(VI) in aqueous media. Geochim. Cosmochim. Acta 74, 5729–5745. https://doi.org/10.1016/j.gca.2010.07.015